ATOMIC STRUCTURE AND CHEMICAL ANALYSIS OF METAL NANOPARTICLES BY SCANNING TRANSMISSION ELECTRON MICROSCOPY

by

Jian Liu

A Thesis Submitted to the University of Birmingham for the Degree of

DOCTOR OF PHILOSOPHY

Nanoscale Physics Research Laboratory

School of Physics & Astronomy

University of Birmingham

April 2017

UNIVERSITY OF
BIRMINGHAM

University of Birmingham Research Archive

e-theses repository

This unpublished thesis/dissertation is copyright of the author and/or third parties. The intellectual property rights of the author or third parties in respect of this work are as defined by The Copyright Designs and Patents Act 1988 or as modified by any successor legislation.

Any use made of information contained in this thesis/dissertation must be in accordance with that legislation and must be properly acknowledged. Further distribution or reproduction in any format is prohibited without the permission of the copyright holder.

Abstract

This thesis explores the use of aberration-corrected Scanning Transmission Electron Microscope (ac-STEM) to characterise the size, atomic structure and chemical composition of different types of nanoparticles, including Ag clusters produced in a matrix assembly cluster source (MACS), chemically-synthesised monolayer-protected Au clusters, metal oxide nanoparticles and bimetallic nanoparticles. The size and density of clusters produced in the MACS with different experimental parameters are characterised by STEM High-Angle Annular Dark Field (HAADF) imaging, shedding light on the capabilities of this new cluster source. A statistical investigation is conducted into the size and atomic structure of nominally $Au_{144}(SR)_{60}$ clusters synthesised by two different research groups. The clusters are "weighed" against size-selected clusters (i.e. atom counting) and the structures are compared to several model structure simulations. A ring-dot feature, characteristic of a local icosahedral order, is frequently observed. The oxidation states of CeO_x, CuO_x, CoO_x and FeO_x nanoparticles are investigated by Electron Energy Loss Spectroscopy (EELS) in the STEM. All these samples show a mixing oxidation states. HAADF images are used to analyse the elemental distribution of Cr-Pt bimetallic nanoparticles. Comparison between the experimental and simulated HAADF intensity profiles indicates that Cr and Pt atoms are mixed. EELS mapping and energy dispersive X-ray spectroscopy (EDX) are used to characterise hydrothermally-prepared FeCo oxide nanoparticles. The results show that the Fe-Co nanoparticles synthesised with iron nitrate precursors are less crystallised and the elemental distributions of Fe and Co are not uniform. While the nanoparticles synthesised with ammonium iron citrate are well crystallised and the elemental distributions are homogenous.

Acknowledgements

I praise the Lord Jesus, the Creator of all things and the Saviour of my life. He leads my way to study abroad, provides me my daily needs, and shapes my characters. His love for me never fails.

I would like to thank Prof. Richard Palmer for providing me with the opportunity to study in his group and his instructive guidance during this work. I thank Prof. Eugenia Valsami-Jones of the School of Geography for encouraging me to collaborate in her projects. I'm grateful to Dr Wolfgang Theis for his supervision during my thesis writing-up stage and his valuable comments and corrections.

Special thanks are due to Dr Nan Jian for training me on the electron microscope and Dr Kuo-Juei Hu for solving many problems I met when I was using the microscope. Also, I would like to thank Dr Dogan Ozkaya from Johnson Matthey for teaching me how to use EDX and EELS.

I'm grateful to Dr Feng Yin, William Terry, Dr Lu Cao, and Dr Ahmed Abdela for their guidance and help with the work on the MACS cluster source. I would like to thank Dr Sung Jin Park, Alexander Pattison, and Megan Grose for reading and correcting my thesis. I would like to thank Dawn Foster for many helpful discussions. I thank all my colleagues, past and present, for their companionship, help and friendship.

I acknowledge the Chinese Scholarship Council and the School of Physics & Astronomy for funding of my doctorate studies.

Last but not the least, I would like to thank my parents for their great love and support in my life. I'm glad that I can honour them. Great thanks also to my brothers and sisters in the church for their unceasing prayers and encouragements.

The Lord is my shepherd, I shall not want. —Psalm 23

Author's Publications

[1] P. Ellis, C. M. Brown, P. T. Bishop, J. Yin, K. Cooke, W. D. Terry, J. Liu, F. Yin, R. E. Palmer. The cluster beam route to model catalysts and beyond, *Faraday Discuss*, 2016,188, 39-56.

[2] V. T. A. Oiko, T. Mathieu, L. Cao, J. Liu, and R. E. Palmer. Note: Production of silver nanoclusters using a Matrix-Assembly Cluster Source with a solid CO_2 matrix, J. Chem. Phys., 2016, 145, 166101.

[3] J. Liu, N. Jian, I. Ornelas, A. J. Pattison, T. Lahtinen, K. Salorinne, H. Häkkinen and R. E. Palmer. Exploring the Atomic Structure of 1.8 nm Monolayer-Protected Gold Clusters with Aberration-Corrected STEM, *Ultramicroscopy*, 2016, doi: 10.1016/j.ultramic. 2016.11.021.

[4] S. M. Briffa, I. Lynch, V. Trouillet, M. Bruns, D. Hapiuk, J. Liu, R. E. Palmer and E. Valsami-Jones. Development of scalable and versatile nanomaterial libraries for nanosafety studies: Polyvinylpyrrolidone (PVP) Capped Metal Oxide Nanoparticles, *RCS Advance*, 2017, **7**, 3894-3906.

[5] G. Gupta, P. Iqbal, F. Yin, J. Liu, R.E. Palmer, S. Sharma, K.C.F. Leung and P.M. Mendes, Pt Diffusion Dynamics for the Formation Cr–Pt Core–Shell Nanoparticles, *Langmuir*, 2015, 31, 6917-6923.

Table of Contents

Chapter 1 Introduction and Background

This thesis is focused on studying the atomic structure and chemical analysis of nanoparticles: deposited Ag clusters, monolayer-protected (MP) Au clusters, metal oxides and bimetallic nanoparticles. The principal tool employed is the aberration-corrected Scanning Transmission Electron Microscope (ac-STEM). In this chapter, I introduce the types of nanoparticles investigated and the specific ac-STEM techniques used. These techniques are High Angle Annular Dark Field (HAADF) imaging, Energy Dispersive X-ray spectroscopy (EDX) and Electron Energy Loss Spectroscopy (EELS). They enable atom counting (i.e. size determination), atomic structure identification, elemental mapping and oxidation state investigations.

1.1 Monolayer-protected Au clusters

1.1.1 Introduction to monolayer-protected Au clusters

Monolayer-protected (MP) nanoparticles are usually prepared by the reduction of metal salts using appropriate reducing agents in the presence of ligand molecules. A monolayer of ligand molecules will form on the surface of the metal core and prevent the nanoparticles from sintering [1]. MP Au nanoparticles are the most interesting and widely investigated systems, due to their chemical stability and the numerous potential applications in the fields of catalysis [2,3], biological imaging [4,5], cancer therapy [6], etc. The typical ligand molecules used for Au nanoparticles protection are thiolates (-SR) [7,8], phosphines (-PR) [9-11] and amines (-NH_2R) [12,13], among which thiolate-Au systems are the most intensively investigated because of the strong Au-SR bond and the generated magic size clusters with respect to phosphines and amines.

Brust et al. [7] reported the chemical preparation of thiolate-protected Au clusters for the first time in 1994. The synthesising strategy of the Au-SR clusters consisted of growing the metallic clusters with the simultaneous attachment of thiol molecules on the growing nuclei. The clusters were grown in a two-phase system to allow the surface reaction (attachment of thiols) to take place during metal nucleation and growth. In Brust's report, $AuCl_4^-$ was transferred from aqueous to toluene using tetraoctylammonium bromide and was then reduced with aqueous sodium borohydride in the presence of dodecanethiol ($C_{12}H_{25}SH$). The colour of the organic layer changed from orange to deep brown indicating the formation of Au-SR clusters (The colour change of the solution reflects the nature of the electronic states of the clusters. Small Au-SR clusters are believed to have discrete electronic energy levels [14] and these discrete levels start to develop into bands when the size increases to bulk materials). The precipitate was washed with ethanol to remove excess thiols. Au-SR clusters with a diameter in the range 1-3 nm were then synthesised. This synthesis strategy was then modified by different research groups to have better control on the size and purity of the clusters produced. The optimised reaction conditions for producing ultrasmall Au-SR clusters include increasing the thiol-to-Au ratio, using a large excess reducing agent, enhancing reaction temperatures and changing the thiol type to ensure adequate etching and increase the yield of a certain size of Au-SR clusters [15-17].

Besides the reaction conditions and choice of ligand molecules, the most challenging question is to determine the composition and atomic structure of the Au-SR clusters, which affect their optical and electronic properties. Early work [16,18] by the Whetten group has shown the formation of a discrete sequence of Au-SR nanoclusters by the

measurements of laser desorption ionisation mass spectrometry (LDI-MS). Au core masses of the isolated Au-SR fractions measured by the LDI-MS [16] were 27-29 k (k = 1000amu), 45-46 k, ~57 k, and, 92-93 k, respectively, containing ~100 to ~460 Au atoms. Smaller species with core masses of 14-15 k (~ 75 atoms) and 8 k (~38 atoms) were obtained in subsequent work [18]. However, due to lower control of clusters at the atomic level and the severe fragmentation during the laser ionisation process, the precise determination of the formula of several discrete species was not achieved.

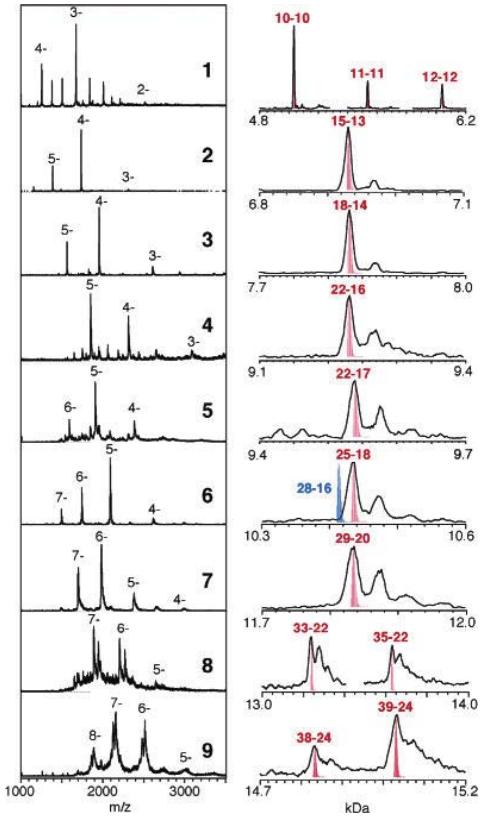

Figure 1.1 Low- (left) and high-resolution (right) ESI mass spectra of the fractionated $Au_n(SG)_m$ nanoclusters. The coloured peaks show the calculated spectra of clusters with corresponding n-m values. From reference [19]

Electrospray ionisation (ESI) is a soft ionisation technique, which allows an accurate determination of compositions of the isolated clusters. By improving the

polyacrylamide gel electrophoresis (PAGE) separation of the Au-SG (SG, glutathione) clusters and suppressing the fragmentation with a soft ionisation procedure, Negishi et al. [19] obtained very clean ESI-MS spectra (Figure 1.1). Discrete clusters, including $Au_{15}(SG)_{13}$, $Au_{18}(SG)_{14}$, $Au_{22}(SG)_{16}$, $Au_{22}(SG)_{17}$, $Au_{25}(SG)_{18}$, $Au_{29}(SG)_{20}$, $Au_{33}(SG)_{22}$, and $Au_{39}(SG)_{24}$, were identified. Furthermore, the definitive formula for $Au_{25}(SR)_{18}$ was corrected from earlier $Au_{25}(SR)_{16}$ formula by Whetten and co-workers [20].

The formation of discrete sizes of Au-SR clusters, rather than a continuous distribution of sizes, indicates a size-dependent stability. The geometric and electronic shell closings are often invoked to explain the stability of the magic-sized nanoclusters [21, 22]. A highly symmetrical core-atom packing structure leads to higher binding energies and, hence, higher stabilities. The geometric symmetry balances the interatomic forces, i.e. the forces tangential to the surface of a sphere sum to zero. The stability of $Au_{25}(SR)_{18}^{x}$ is attributable to geometric rather than electronic factors, since $Au_{25}(SR)_{18}^{x}$ is found to be stable regardless of the charge state for x=1-, 0 and 1+ [23]. The "superatom electronic theory" [22] is analogous to the atomic theory and predicts the stability and chemical nature of simple clusters. The electron energy levels of magic-size clusters with a filled-electronic shell correspond to $1S^2|1P^6|1D^{10}|2S^2\ 1F^{14}|2P^6\ 1G^{18}|2D^{10}\ 3S^2\ 1H^{22}|\ldots$ where S, P, D, F, G, H denote the angular momentum characters. The delocalised orbitals are derived mainly from atomic 6s orbitals, representing a finite-system analogy to the bulk conduction electron states. A stable configuration is associated with a total number of 2, 8, 18, 34, 58, 92, ... shell-closing electron count. For a cluster with formula $(L_s{\cdot}A_NX_M)^z$, where A and X denote metal atoms and electron-withdrawing ligands with numbers of N and M, L represents weak dative ligands that do not withdraw electrons from the core atoms, s the number of dative ligands, and z is the overall charge on the complex. Then

the number of superatomic electrons is $n^* = NV_A - M - Z$, where V is the valence of the metal atom (V=1 for Au, denoting its 6s electron). The superatom theory has explained the stability of several cluster species, such as $Au_{25}(SR)_{18}^-$, $Au_{39}(PPh_3)_{14}Cl_6^-$, $Au_{68}(SR)_{34}$, and $Au_{102}(SR)_{44}$, which have shell-closing electron counts of 8, 34, 34, and 58, respectively. However, clear trends were not observed for $Au_{25}(SR)_{18}$ [24], $Au_{38}(SR)_{24}$ [25], $Au_{144}(SR)_{60}$ [26], etc.

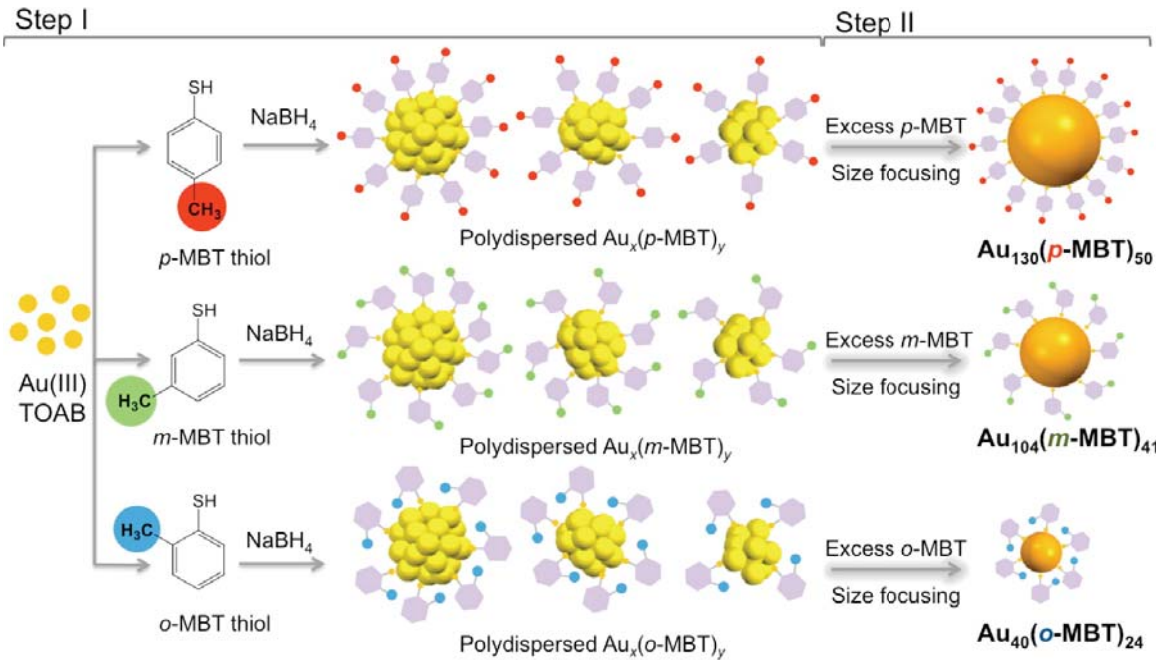

Figure 1.2 The synthetic strategy of different magic-sized Au-SR clusters by exploring the three isomeric ligands: *p*-MBT, *m*-MBT, and *o*-MBT. Taken from reference [27].

The effect of ligands on the magic-size selection was largely overlooked in the early studies of MP Au clusters. However, the effects of the ligands on the cluster sizes and structures have been revealed recently. Jin's group [27] reported that the magic sizes of Au-SR clusters are sensitive to the subtle change of surface protecting ligand structure. By the selection of isomeric methylbenzenethiols (para-, meta-, and ortho- MBT), Au-SR clusters with sizes of $Au_{130}(p\text{-MBT})_{50}$, $Au_{104}(m\text{-MBT})_{41}$ and $Au_{40}(o\text{-MBT})_{24}$ were

successfully prepared. The trend of cluster size decreasing from Au_{130} to Au_{104} to Au_{40} was ascribed to the Au-S interfacial bond stress changing. The Au-S bond stress increases when the methyl group of MBT ligand goes from para- to meta- to ortho-position. Figure 1.2 illustrates the synthetic strategy of different size Au-SR clusters.

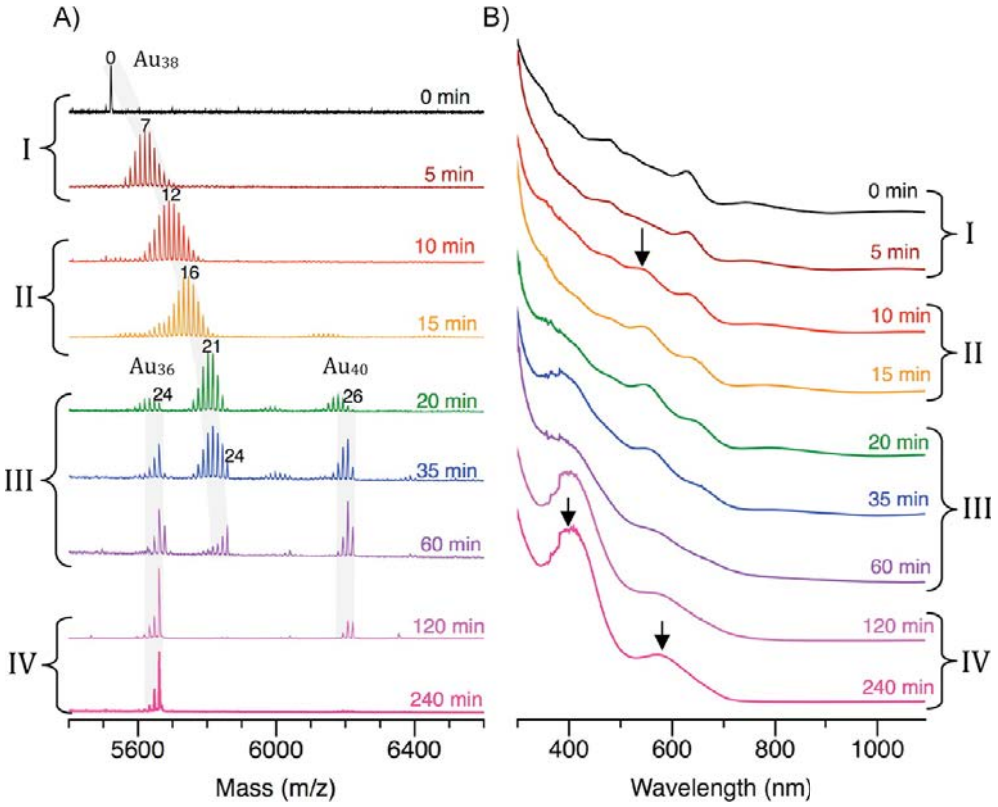

Figure 1.3 (A) Time-dependent ESI mass spectra for the $Au_{36}(PET)_{24}$ clusters' LEIST reaction products at four different stages. The number of TBBT ligands (m) exchanged onto the clusters ($Au_{36}(TBBT)_m(PET)_{24-m}$) is labelled on the top of the mass peaks. (B) Corresponding UV-vis spectra of the reaction products at different times. From reference [30].

Magic-sized Au-SR clusters can be transformed from one stable size to another by ligand-exchange-induced size/structure transformation (LEIST for short) [28]. Notable examples include the transformation of $Au_{25}(PET)_{18}$ to $Au_{28}(TBBT)_{20}$ [29], $Au_{38}(PET)_{24}$ to

$Au_{36}(TBBT)_{24}$ [30,31], and $Au_{144}(PET)_{60}$ to $Au_{133}(TBBT)_{52}$ [32] (where PET = SC_2H_4Ph and TBBT= 4-*tert*-butylbenzenelthiol). To fulfil the LEIST reaction, a very high molar ratio of incoming TBBT to the original PET (~160:1) and thermal conditions (to overcome the energy barrier between stable sizes) are needed. To figure out how the size and structure transform along with ligand exchange, Zeng et al. [30] conducted time-dependent mass spectrometry and optical spectroscopy analyses of the $Au_{38}(PET)_{24}$ to $Au_{36}(TBBT)_{24}$ transformation reaction, and a disproportionation reaction was revealed. Figure 1.3 shows the time-dependent ESI mass spectra and the corresponding UV-vis spectra of the LEIST reaction products of $Au_{36}(PET)_{24}$ clusters.

The size-transformation process can be divided into four stages. The first stage (0-5 min) indicates ligand exchange without any size or structure transformation, evidenced by the optical spectra being nearly the same as the starting point. The second stage (10-15 min) demonstrates that more TBBT ligands attach on the Au_{38} core, which induces structural distortion of the clusters. The absorption spectra of the metastable cluster show a new absorption peak at ~550nm. During the third stage (20-60 min), a disproportionation reaction takes place. Via internal reconstruction and releasing and capturing processes, original $Au_{38}(TBBT)_m(PET)_{24-m}$ (m = 19 to 24) clusters transform to Au_{36} and Au_{40} clusters. After all the $Au_{38}(TBBT)_m(PET)_{24-m}$ clusters are transformed (stage IV), the $Au_{40}(TBBT)_{m+2}(PET)_{24-m}$ species are gradually converted to Au_{36} clusters. The experimental yield of $Au_{36}(SR)_{24}$ is 90%, which is consistent with the above reaction mechanism. The driving force leading to the size and structural transformation from $Au_{38}(SCH_2CH_2Ph)_{24}$ to $Au_{36}(TBBT)_{24}$ is not clear. However, the steric bulkiness and electronic conjugation factors of the ligand are believed to trigger the initial

transformation process. Joint efforts between theory and experiment are still needed to map out more details of the ligand's effects role.

The current reports indicate that the stability of magic-sized Au-SR clusters depends on a complex interplay of multiple factors, such as the core atom packing structure, carbon tail of the protecting ligands and number of superatomic electrons. A good understanding of these factors on the size and structure of the Au-SR clusters is of great importance to produce high purity clusters and discover new magic-sized species.

1.1.2 Crystal structure of Au-SR clusters

Determination of the total structure of the Au-SR clusters, including the arrangements of the Au kernel and the protecting ligands, is an outstanding experimental challenge. Due to their small size, softness and no atomic mono-dispersibility, the atomic structures of the magic-sized Au-SR clusters remained unknown until the first reported structure by the Kornberg group of the Au_{102}(p-MBA)$_{44}$ (p-MBA, p-mercaptobenzoic acid) cluster in 2007 [33]. The structure was solved by single crystal X-ray diffraction, which can provide reliable details of both the gold-core structures and the ligand arrangements. The structure of the $Au_{102}(SR)_{44}$ cluster (Figure 1.4) can be dissected into a Marks decahedral (The structural schemes of classic decahedron, Ino's decahedron and Marks' decahedron are shown in Figure A10. Ino's decahedral is derived by truncating a classic decahedron to generate five {100} faces. The Marks decahedron is constructed by introducing 10 additional re-entrant {111} surfaces at the five twin boundaries [34]) Au_{49} kernel (yellow, Figure 1.4b), two 20-atom caps (green, Figure 1.4b) with C_5 symmetry on opposite poles, and a 13-atom band (blue, Figure 1.4b) on the equator [33].

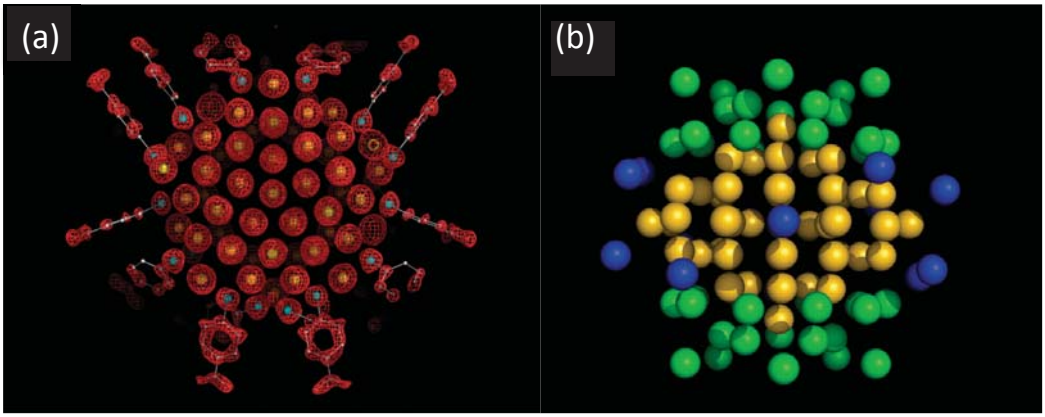

Figure 1.4 (a) $Au_{102}(p\text{-}MBA)_{44}$ structure determined by single crystal X-Ray diffraction. Yellow: Au atoms; cyan: S atoms; framework: p-MBA. (b) Packing of Au atoms in the cluster. Reproduced from reference [33].

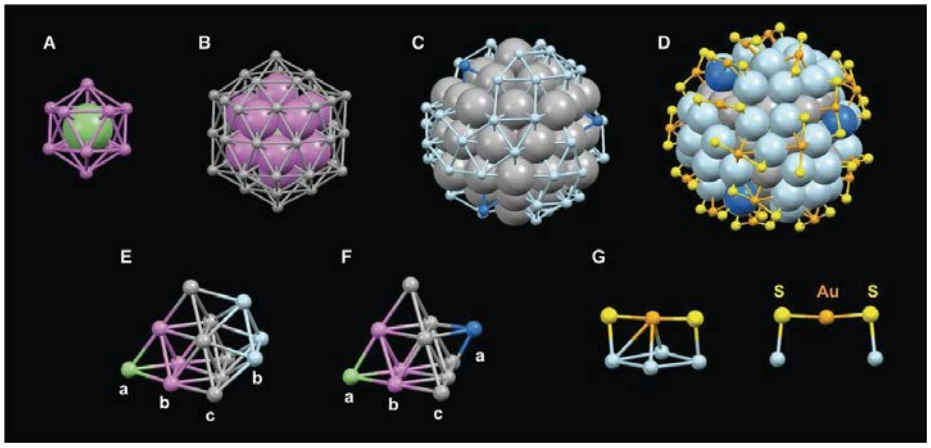

Figure 1.5 The four-shell structure of $Au_{133}(SR)_{52}$. (A) The first shell, pink; (B) The second shell, gray; (C) The third shell, blue and cyan; (D) The fourth shell with Au (orange) and S (yellow). (E) a-b-c-a packing of atoms; (F) a-b-c-b packing of atoms; (G) Monomeric –SR–Au–SR– motifs. Figure and caption from reference [32].

Through the growth of single crystals, more structures of Au-SR clusters have been obtained. The most recently determined clusters are $Au_{130}(SR)_{50}$ [35] and $Au_{133}(SR)_{52}$ [32, 36] clusters. $Au_{133}(SR)_{52}$ is the largest Au-SR cluster that has been solved by the single

crystal diffraction method so far. The total structure of the $Au_{133}(SR)_{52}$ is constructed in a shell-by-shell manner, based on a 55-atom Mackay icosahedron (two shells, Figure 1.5A,B). The third layer caps the 20 triangular {111} facets of the Au_{55} icosahedron. 16 {111} facets are capped by three Au atoms (Figure 1.5E) and 4 are capped by one Au atom (Figure 1.5F), resulting in a Au_{107} kernel, which is then protected by 26 -SR–Au–SR– monomeric staples (Figure 1.5G). The monomeric staples forms four aesthetic helical stripes (consisting of 6 staples) on the surface of the Au_{107} kernel (Figure 1.6), and different rotation directions of the four helical stripes give rise to chirality in the $Au_{133}(SR)_{52}$ cluster.

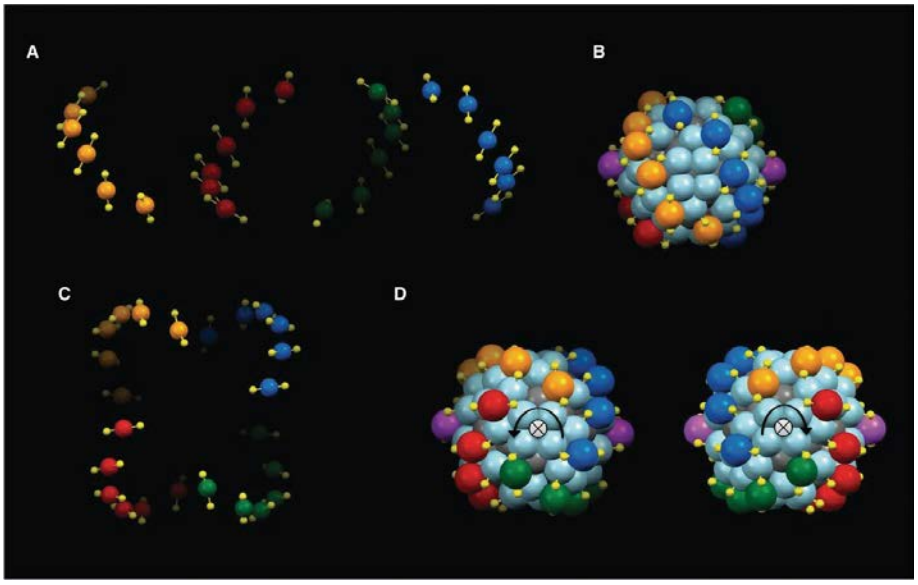

Figure 1.6 Helical stripes on the Au_{107} kernel formed from monomeric staples giving rise to the chirality of $Au_{133}(SR)_{52}$. From reference [32].

Crystal structures of MP AuAg alloy clusters and MP Au cluster isomers determined by single crystal X-ray diffraction have also been reported somewhere [37, 38]. The Dass group reported the first X-ray crystal structure of $Au_{38-x}Ag_x(SCH_2CH_2Ph)_{24}$ alloy, where x ranges from 1 to 5. The determined structure of $Au_{38-x}Ag_x(SCH_2CH_2Ph)_{24}$ has an

identical core structure to $Au_{38}(SR)_{24}$ [25], which is a 23-atom face-shared bi-icosahedra (Figure 1.7). Ag atoms were likely to occupy nine selected sites, which are the vertex edges and the middle face-shared ring (gray locations in Figure 1.7a). No Ag atom was found in the $Au_2(SR)_3$ and $Au(SR)_2$ staples.

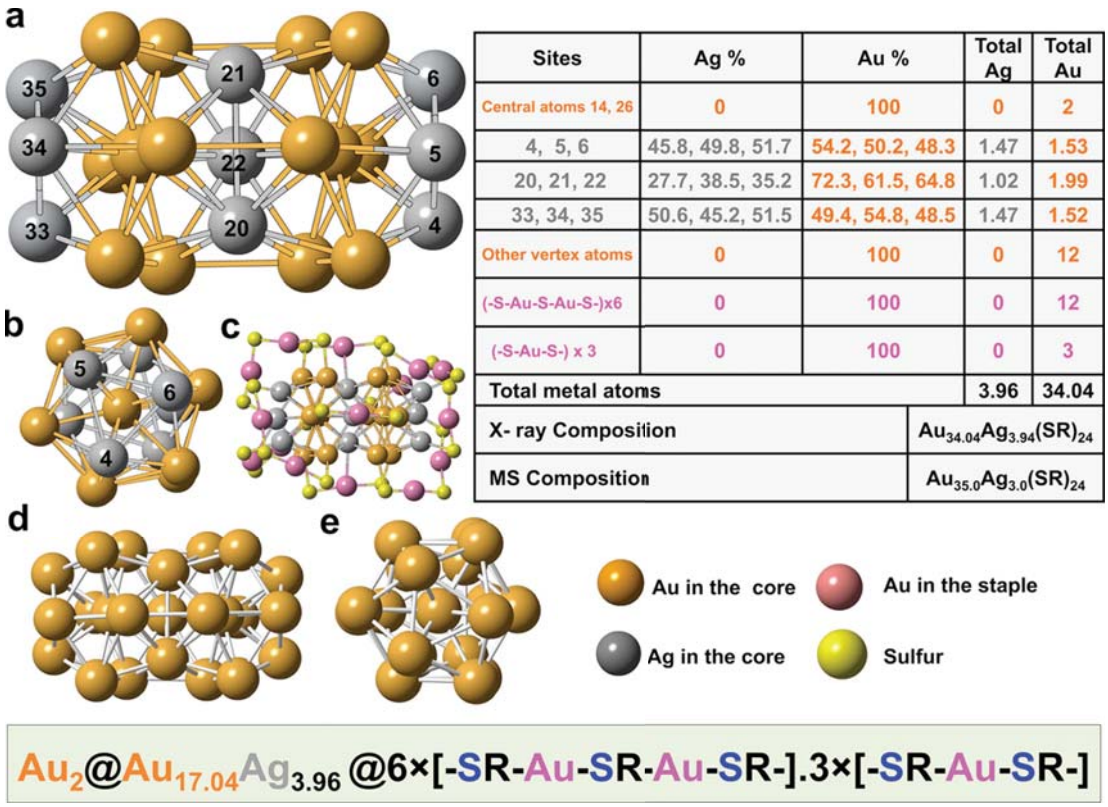

Sites	Ag %	Au %	Total Ag	Total Au
Central atoms 14, 26	0	100	0	2
4, 5, 6	45.8, 49.8, 51.7	54.2, 50.2, 48.3	1.47	1.53
20, 21, 22	27.7, 38.5, 35.2	72.3, 61.5, 64.8	1.02	1.99
33, 34, 35	50.6, 45.2, 51.5	49.4, 54.8, 48.5	1.47	1.52
Other vertex atoms	0	100	0	12
(-S-Au-S-Au-S-)x6	0	100	0	12
(-S-Au-S-) x 3	0	100	0	3
Total metal atoms			3.96	34.04
X- ray Composition			$Au_{34.04}Ag_{3.94}(SR)_{24}$	
MS Composition			$Au_{35.0}Ag_{3.0}(SR)_{24}$	

Figure 1.7 (a-c) X-ray crystal structure of $Au_{38-x}Ag_x(SCH_2CH_2Ph)_{24}$. (d-e) Front and side view of the 23-atom bi-icosahedra $Au_{38}(SCH_2CH_2Ph)_{24}$ core. The table shows the possibility of Au and Ag atoms occupying different sites. From reference [37].

Tian and co-workers [38] reported a pair of structural isomers of Au_{38Q} and Au_{38T} (where Q and T are the surname initial of the first author) clusters revealed by X-ray crystallography. These two clusters have the same formula but completely different structures (Figure 1.8). The main differences are the structures of the Au_{23} kernels and the surface capping of the staples. The Au_{38Q} cluster has a face-shared bi-icosahedra

core [25], while the Au_{23} core of Au_{38T} can be considered as one Au_{12} cap and one Au_{13} icosahedron fused together (Figure 1.8a, b). Au_{38T} is unstable at high temperature (50 °C) in toluene and transforms to Au_{38Q}. Optical and catalytic analysis of two isomer clusters showed very different absorption peaks and catalytic activity, which indicate a strong structure-property correlation.

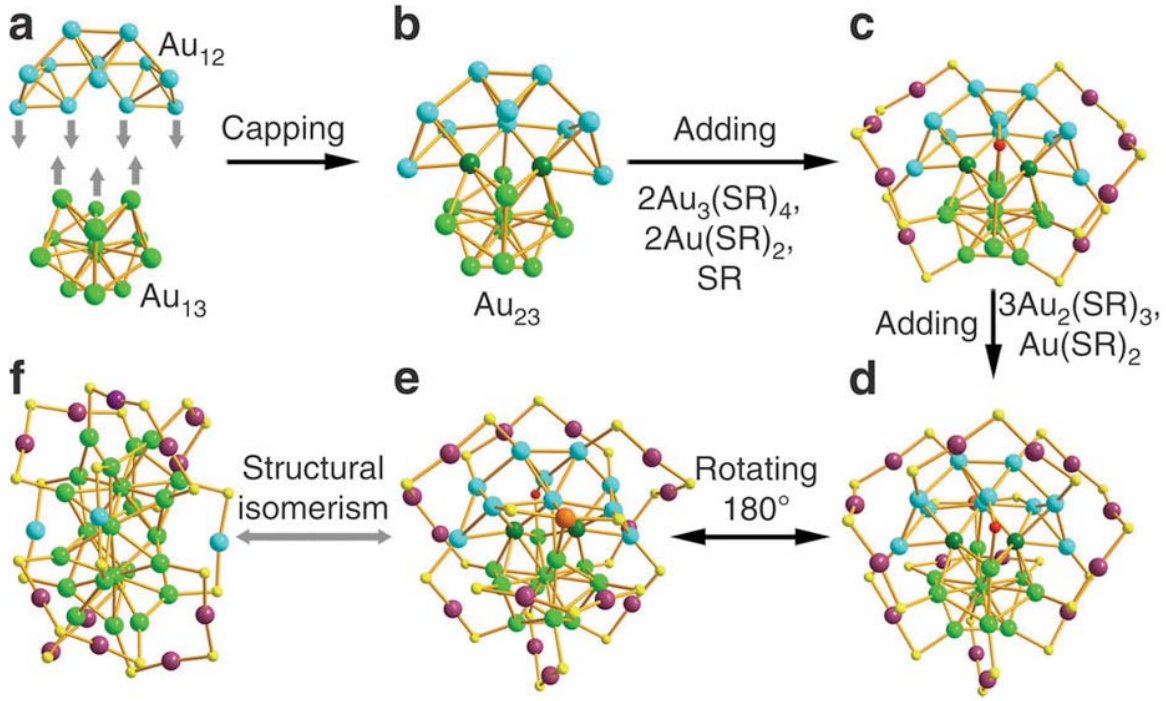

Figure 1.8 X-ray crystal structures of (a-e) Au_{38T}; (f) Au_{38Q}. From reference [38].

A number of Au-SR clusters have been well characterised both in size and crystal structure, and they are reviewed in Ref. [21]. Worth noting that the growth of single crystals is very difficult for the majority of the Au-SR clusters, since high-quality clusters with atomically precise and molecular purity are essential to enable the crystallisation of these clusters. $Au_{144}(SR)_{60}$ is extremely stable at ambient and elevated temperature. However, its crystal structure remains unresolved since it was synthesised in 1996 (known as 28-29 kDa species in the LDI-MS), even though several research groups have

obtained crystals [39-41]. Therefore, it is of great importance to characterise the structure of Au-SR clusters with alternative approaches.

1.2 Investigation of MP Au clusters by (S)TEM

1.3.1 Atom counting for MP Au clusters

Atomic resolution high-angle annular dark field (HAADF) scanning transmission electron microscopy (STEM) has become a popular technique, not only because it provides directly interpretable images, but also the HAADF image intensities show Z-contrast and are highly sensitive to the number of atoms [42-44]. The signals detected by the HAADF detected are high-angle (>50 mrad) scattered electrons, which follow the Rutherford scattering model. The HAADF intensity (I) of an atom is found to be proportional to the atomic number to the power n ($I \sim Z^n$). Therefore, for pure Au clusters, the HAADF intensity has a linear relationship with the number of atoms in a cluster.

Li and co-workers [45] studied the relationship between HAADF intensities and the number of atom in the size-selected Au clusters experimentally. Figure 1.9 shows that the integrated HAADF intensity of the size-selected Au clusters increases linearly with the number of atoms up to about 1500 or even higher [46]. Taking advantage of the HAADF intensity analyses, Young et al. [46] studied the relationship of HAADF intensity against the diameter of thermally evaporated Au and colloidal Au nanoparticles. They found that the relationship between particle diameter and HAADF intensity of the thermally evaporated Au nanoparticles agrees with a hemispherical model, and that the data from the colloidal Au nanoparticles are consistent with a spherical model

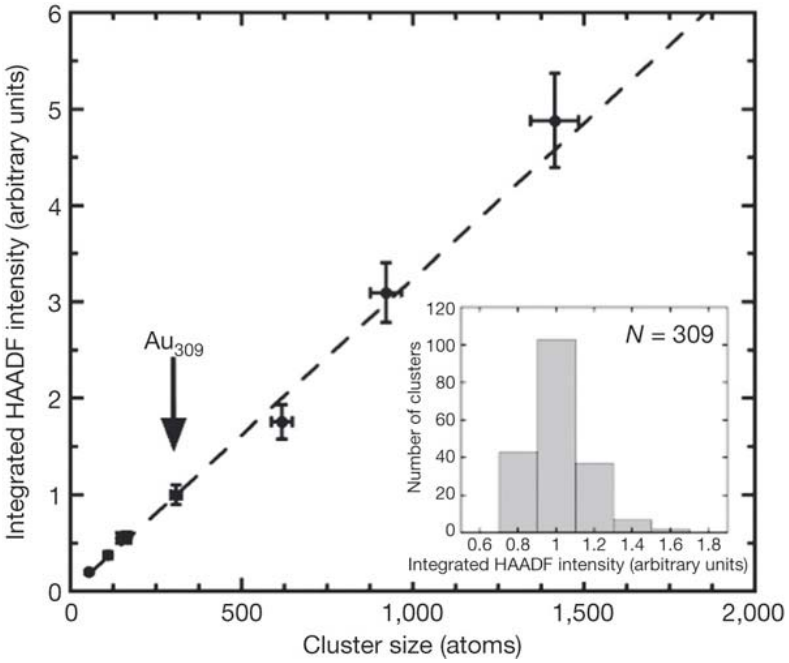

Figure 1.9 Relationship between integrated HAADF intensity and cluster size. From reference [45].

The HAADF intensity of a MP Au cluster consists of the intensities from the Au atoms and the protecting ligands. To count the number of Au atoms in MP Au clusters, we need to remove the intensity that accounts for the ligands. Therefore, the value of the exponent n needs to be calibrated. The calibration can be obtained by comparing the integrated HAADF intensities of size-selected Au_{923} and Pd_{923} clusters [47, 48]. Figure 1.10a illustrates the integrated HAADF intensity of size-selected clusters as a function of the inner acceptance angle and the relationship between the exponent and the acceptance angle is shown in Figure 1.10b. The calibrated value of *n* increases from 1.2 to 1.8 as the acceptance angle varies from 14 to 103 mrad. This means that the intensity contributed by crystalline diffraction decreases at higher acceptance angles (θ) and becomes more *Z*-dependent. The fitting line in Figure 1.10b follows the trend of $n=2-Ae^{B\theta}$ (A and B are fitting parameters) from the theoretical model by Hartel et al. [49]. The

exponent n is always smaller than 2, for the nucleus charge is partially shielded by the surrounded electrons.

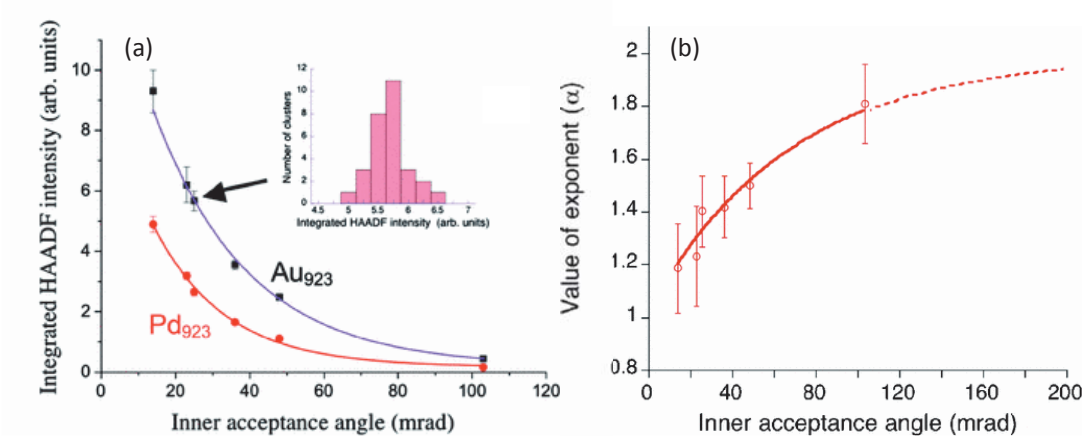

Figure 1.10 (a) Integrated HAADF intensities of Au_{923} and Pd_{923} clusters and (b) the values of the exponent as a function of inner acceptance angle. Reproduced from reference [47].

It is possible to determine the number of Au atoms in a MP cluster by using size-selected Au clusters as mass standard and knowing the exponent *n* with the above calibrations. This atom counting method was tested on $Au_{38}(SC_2Ph)_{24}$ clusters by Wang et al. [50]. Size-selected Au_N clusters, with N=25, 38, and 55 (mass resolution M/ΔM=20), were produced in a magnetron, gas aggregation cluster source by a lateral time-of-flight mass filter. Figure 1.11 shows the HAADF intensity distributions of Au_{38}, Au_{25} and MP Au_{38} clusters. To extract the number of Au atoms, the intensity contributed by the 24 SC_2Ph ligands was calculated by the following equation,

$$E = N_S\left(\frac{Z_S}{Z_{Au}}\right)^n + N_C\left(\frac{Z_C}{Z_{Au}}\right)^n + N_H\left(\frac{Z_H}{Z_{Au}}\right)^n \quad (1.1)$$

where E is the equivalent number of Au atoms due to the intensity of ligands, Z is the atomic number, N is the number of S, C and H atoms in the attached 24 ligands. After the

subtraction of *E*, which was found to be 8.7 ± 2.6 Au atoms, the numbers of Au atoms calculated from the HAADF intensity of the MP Au_{38} clusters are 38.6 ± 2.8, 38.4 ± 2.9, and 37.5 ± 2.9 Au atoms, respectively, when the intensity of Au_{25}, Au_{38} and Au_{55} is used for the calibration. The size of single clusters can be easily determined with this atom counting method and images of clusters with a certain size can then be fractionated. Nan et al. [51] weighed the chemically prepared $Au_{55}(PPh_3)_{12}Cl_6$ clusters against size-selected Au_{309} clusters. Clusters with four main sizes were fractionated and the atomic structure of clusters with ~ 55 Au atoms was then investigated.

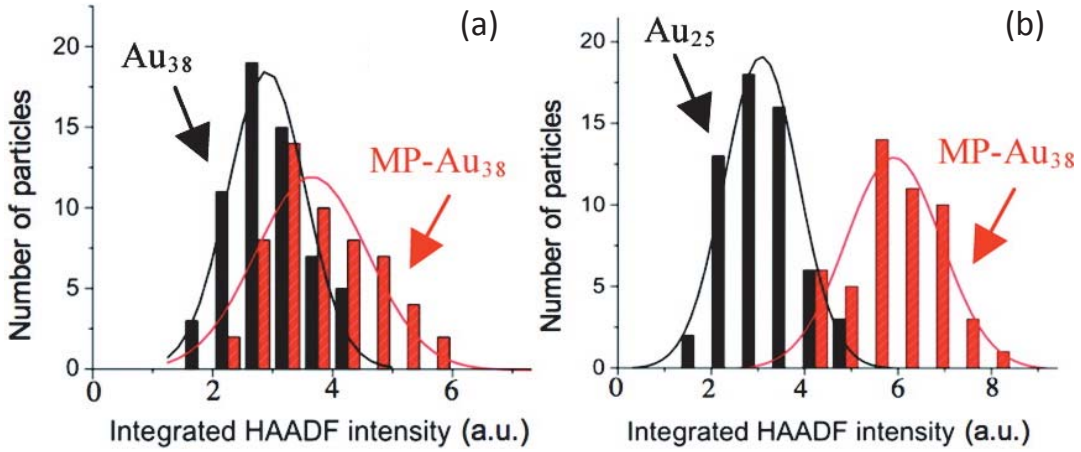

Figure 1.11 Integrated HAADF intensity distributions of (a) MP Au_{38} and Au_{38}, (b) MP Au_{38} and Au_{25}. Figure is taken from reference [50].

Composition analysis of small clusters (<5 nm) by EDX and EELS is very difficult because of the small amount of materials and a few signals generated. Quantitative Z-contrast imaging in STEM can also provide chemical composition information of a single bimetallic cluster. Nan and co-workers [52] determined the Au-Ag compositions of single thiolated $(Au_xAg_{1-x})_{312\pm55}$ cluster by calibrating the HAADF intensity of AuAg clusters against size-selected Au_{923} clusters. Determination of the Au-Ag composition of each cluster enables them to reveal the change of cluster structures as a function of

composition, in which they found that the dominant structure of the clusters changes from icosahedron to face-centred cubic (FCC) gradually as the Au proportion increases. By simulating the HAADF intensity profiles of Cu-Au core-shell clusters, Yin et al. [53] roughly determined the Cu-Au compositions in the core and shell.

Overall, these works demonstrate that STEM HAADF imaging technique is a powerful approach to determine cluster size and compositions quantitatively. However, there are several factors that may significantly affect the accuracy of the quantitative analysis, such as cluster size, orientation, detector asymmetry, brightness/contrast, emission current fluctuation, etc. Among these factors, the detector asymmetrical response could cause a significant error in the quantitative analysis due to the non-equal sensitivity [54]. For the size effect, as the cluster size increases, the relationship between the HAADF intensity and cluster size (>6000 atoms) is no longer linear [46]. Cluster orientation can cause electron-channelling effect, which occurs when electrons pass through a crystal near zone axis. The atom columns acting as small lenses can focus the electron beam due to the positive electrostatic potential of the atoms and keep the intensity on an atomic column as it propagates through the sample [55,56]. Small mis-tilts away from the near zone axis will cause a certain intensity difference. Therefore, these factors must be treated carefully to do a reliable quantitative analysis with STEM-HAADF images.

1.2.2 Atomic structure of MP Au clusters by (S)TEM

Due to the difficulty of growing high quality single crystals, structure determination of MP Au clusters by electron microscopy is of great value. The advantage of atomic resolution HAADF images is that one can obtain the size and structure information at the same time. Since the structures of small size MP Au clusters are very complicated [33,

[35], simulations from proposed models are usually used for comparison with the experimental HAADF images and NBD patterns for structural identification.

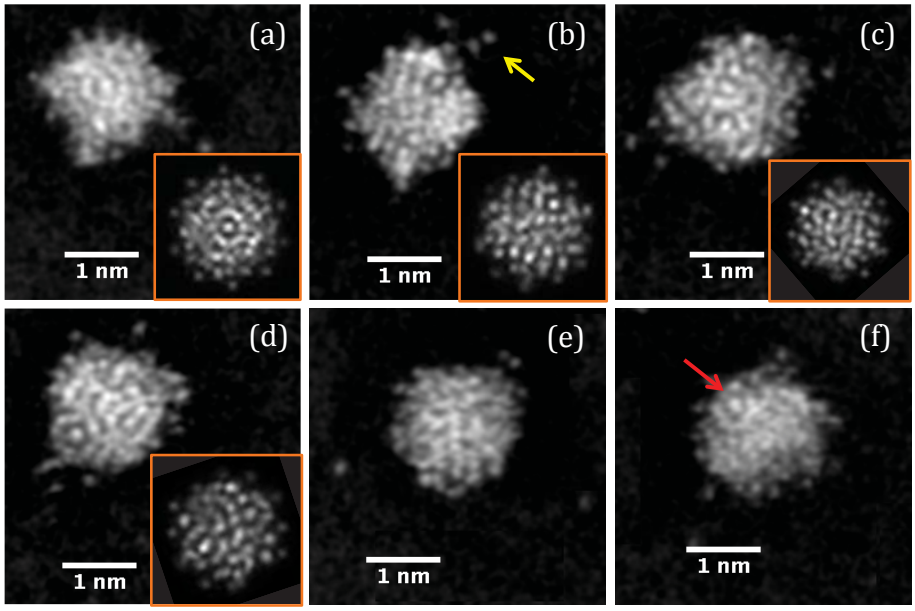

Figure 1.12 HAADF images of nominally "$Au_{144}(SR)_{60}$" clusters (a~f). The insets are the simulations at different orientations, which show a good agreement with the experimental images. The yellow and red arrows indicate the ejected Au atoms and a ring-dot feature, respectively. From reference [57].

The Palmer group reported the size and structure investigations of MP Au_{55} [51], Au_{144} [57], and $(Au_xAg_{1-x})_{312\pm55}$ [52] clusters. In these works, size-selected Au clusters were used as mass standards to fractionate the MP Au cluster with expected sizes for structure identification, since the chemically prepared clusters are not pure in size, even though these clusters are dissolved from crystals [57]. Simulations of different models (full-shell icosahedron, cuboctahedron, decahedron and theoretically predicted models) were used for structural comparison. The structure determination of MP Au_{55} was quite successful, in which they found 42% of the clusters fit best to a hybrid model and the

rest were amorphous [51]. Figure 1.12 shows some examples of the structural comparison of nominally "$Au_{144}(SR)_{60}$" clusters between the HAADF images and simulations. A few percentage of clusters were found to match the theoretical MP Au_{144} model [60], while a large proportion was not identified. However, a ring-dot feature was frequently (20-30%) observed in the clusters, which is a characteristic of local icosahedral order. Knowing the cluster size is important since the atomic structure of the MP Au clusters is size-dependent. For example, MP Au_{133} has an icosahedron core, which is entirely different from the MP Au_{130} (a decahedron core), even though the difference is only three Au atoms.

Combining atomic resolution HAADF images with nanobeam electron diffraction (NBD), the Jose-Yacaman group studied the structure of the $Au_{144}(SR)_{60}$ [58] and $Au_{130}(SR)_{50}$ [59] clusters. In this method, simulations of NBD patterns and structures from $Au_{144}(SR)_{60}$ model [60] at different orientations were calculated for further comparison with the experimental data. NBD patterns and HAADF images were recorded at a reduced accelerating voltage of 80 kV to minimise the radiation damage from the electron beam.

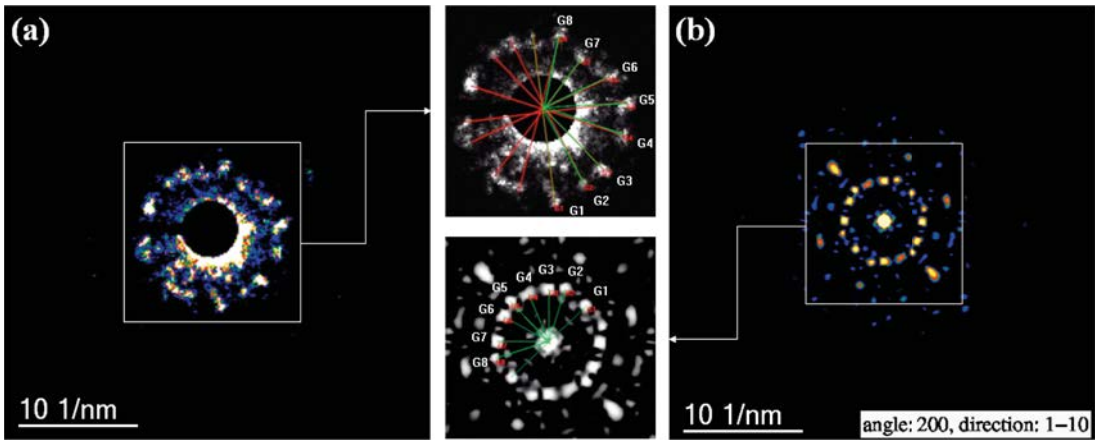

Figure 1.13 Comparison between experimental (a) and simulated (b) NBD patterns. From reference [58].

Figure 1.13 illustrates the experimental and simulated NBD patterns. The comparison was conducted by comparing the spot reflections on the patterns and angles between the reflections (Figure 1.13). The difference of angles measured from the experimental and theoretical patterns is within 2°, which indicates a good match. An atomic resolution HAADF image and its power spectra were also used to match the simulations shown in Figure 1.14. Their results revealed that the structure of the MP Au_{144} clusters is consistent with the theoretical model proposed by Lopez-Acevedo et al. [60]. With the same method, they studied the structure of the $Au_{130}(SR)_{50}$ cluster [59] by comparing the simulations of the theoretical model suggested by Negishi et al. [61]. The suggested $Au_{130}(SR)_{50}$ structure consists of a Au_{75} Marks decahedron core, protected by two Au_{15} motifs and 25 monomeric staples. The experimental results showed a good agreement with the simulations [59]. The crystal structure of $Au_{130}(SR)_{50}$ was resolved recently [35] and is similar to the theoretical model. The structure of MP Au clusters remained for several seconds before it was damaged by the electron beam exposure; this was identified by the changing of time-resolved NBD patterns.

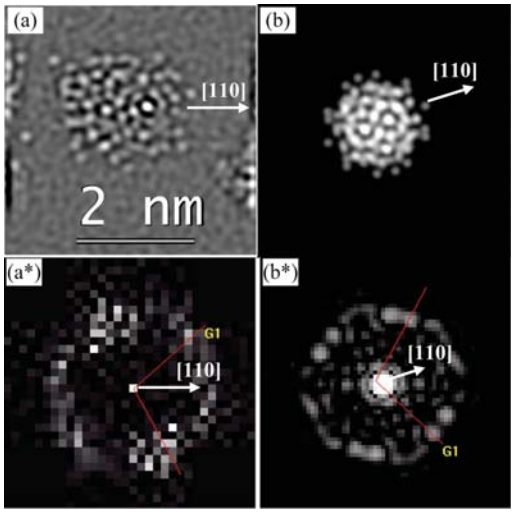

Figure 1.14 (a) HAADF image of a $Au_{144}(SR)_{60}$ cluster and (b) simulated HAADF image from a model. (a*) and (b*) are the power spectra of (a) and (b) images, respectively. From reference [58].

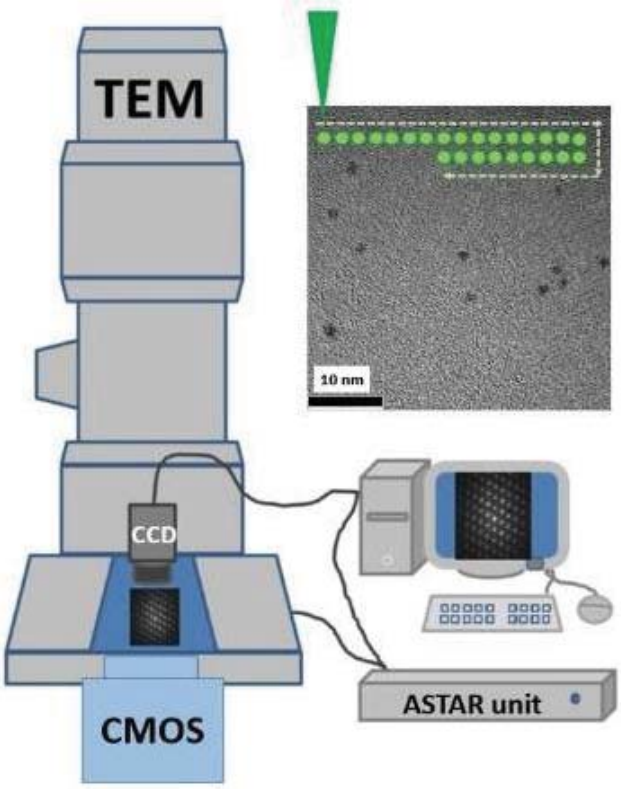

Figure 1.15 Schematic representation of the experimental setup. A TEM was coupled with a NANOMEGAS ASTAR system. From reference [62].

This method was improved recently by coupling with a NANOMEGAS ASTAR system to fulfil the fast scan of the electron beam on a pre-established area. A series of NBD patterns was then collected simultaneously by a CCD camera [62]. The advantage of this method is the fast and sequential scanning of 0.1 nm point-to-point step (probe size 3 nm) and 0.1s of acquisition time, which can largely reduce the irradiation time and the radiation damage of the MP clusters. The schematic of the experimental setup is illustrated in Figure 1.15. $Au_{102}(SR)_{44}$ clusters were used to test this method. The experimental NBD patterns were then compared with the simulations of its crystal structure [33].

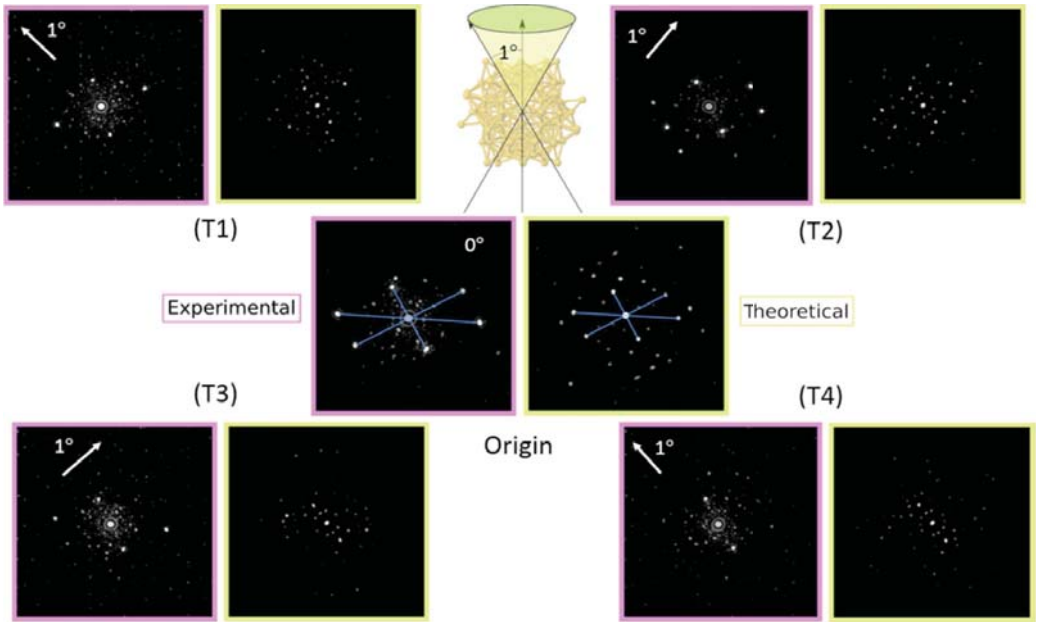

Figure 1.16 Experimental and the corresponding simulated NBD patterns at 0°, and 1° disoriented out of its axial axis. From reference [62].

Structure comparison between atomic resolution HAADF images and structure simulations was usually conducted by eye [51, 52, 57]. This means that the structure comparison is very subjective and many structural details may be ignored. The NBD method proposed by the Yacaman group [58, 59, 62] provide a quantitative criterion for structural comparison, e.g. distances and angles between the diffraction spots. However, the NBD patterns seem to be very sensitive to the cluster orientations, and the patterns are quite different even the cluster is one degree disoriented out of its axis (Figure 1.16). Additionally, extra spots were also introduced because of the presence of carbon substrate and noise in the images. Since the mass spectra and diameter distribution of these MP clusters given in the literature is very broad, the size of these clusters is not pure. Therefore, it would be very difficult to find the right size clusters and the corresponding simulations to the experimental data.

In the above two methods, prior knowledge about atom packing and model simulation are needed for structure determination. To reveal the atomic structure of a MP Au cluster without any prior knowledge could be of great value. Kornberg and co-workers [63] proposed a three-dimensional reconstruction method for the determination of the atomic structure of MP Au_{68} cluster without comparing with simulations from a predicted model. Atomic-resolution EM images were taken by an ac-TEM at a very low electron dose ((~800 $e^-/Å^2$), which is much lower than that taken from a traditional ac-STEM [57, 58, 59]. Images of 939 clusters (Figure 1.17A) were used for 3-D reconstruction, and an electron density map with 68 peaks (Figure 1.17B, C) was yielded. The peaks were assigned as Au atoms justified by their numbers, distances and the high intensity, which could be attributed only to heavy atoms. The packing was FCC-like and has a 13-atom cuboctahedral core, surrounded by 24 atoms extending the fcc-like framework and an additional 31 atoms deviating from FCC packing. The reconstructed structure was supported by comparison of absorption spectra with the calculations.

The low-dose technique of ac-TEM adapted from biological studies would largely decrease the damage from the electron beam radiolysis. While the great advantage of structural 3-D reconstruction of atomic-resolution TEM images could make it a general method for determining the structure of any size MP Au clusters, since it doesn't need any prior knowledge or fittings to predicted models. However, the studied clusters must be of a high order of purity both in size and structure for the structural reconstruction, for a large number (over 900) of TEM images are needed. In the ESI mass spectra [63], the number of attached ligands varies from 30 to 34 (may cause structure distortion or transformation [30]), and other size clusters were also observed. The impurity of the

clusters probably introduces some errors into the reconstructed structure, and only the structure of MP Au_{68} has been resolved by this method so far.

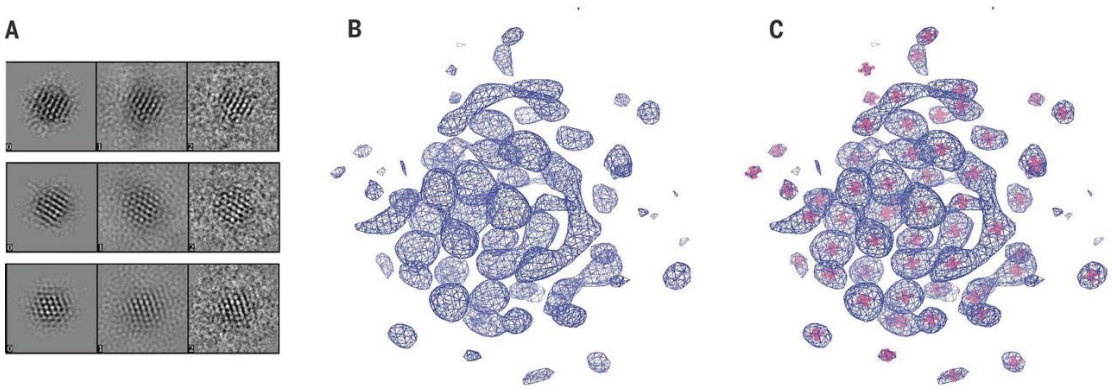

Figure 1.17 (A) Representative components of the reconstruction. (Left) Back projection of the reconstruction; (middle) corresponding class average of the EM images; (right) EM images. (B-C) Electron density map (blue mesh) and Au atoms (pink stars). From reference [63].

1.3 Chemical analysis of metal nanoparticles by (S)TEM

1.3.1 Elemental analysis of bimetallic nanoparticles

Bimetallic nanoparticles are being investigated in many research fields, such as fuel cell electrocatalysts [64], alcohol oxidation [65], and preferential oxidation of CO [66]. Their catalytic activities are usually related to the arrangement of the metals. Enache et al. [65] showed that the addition of Au to Pd nanoparticles (Au-rich core surrounded a Pd-rich shell) had higher selectivity in the oxidation of alcohols to aldehydes than the pure Au and Pd catalysts. They believe that the surface of the Au/Pd nanoparticles contains some Au atoms, which act as an electronic promoter for Pd and improves the catalytic selectivity. Alayoglu and co-workers reported that Ru@Pt core-shell nanoparticles were more active and selective in the preferential oxidation of CO than the PtRu alloy and

monometallic mixture catalysts. The oxidation of CO can be completed below 20 °C with the presence of Ru@Pt core-shell catalyst, while the PtRu alloy and monometallic mixture catalysts show complete CO conversion at 85 °C and 93 °C, respectively, for H_2 feeds containing 1000 p.p.m. CO. The enhanced catalytic activity was ascribed to the electronic structure change of the Pt shell with Ru as the core [66]. Wand et al. studied the catalytic activity of structurally ordered intermetallic Pt-Co core-shell nanoparticle in the oxygen reduction reaction (ORR). It is found that the mass activity of the Pt-Co core-shell nanocatalysts is over two times higher than the Pt-Co alloy nanoparticles as well as Pt/C, and over three times enhancement in catalytic selectivity.

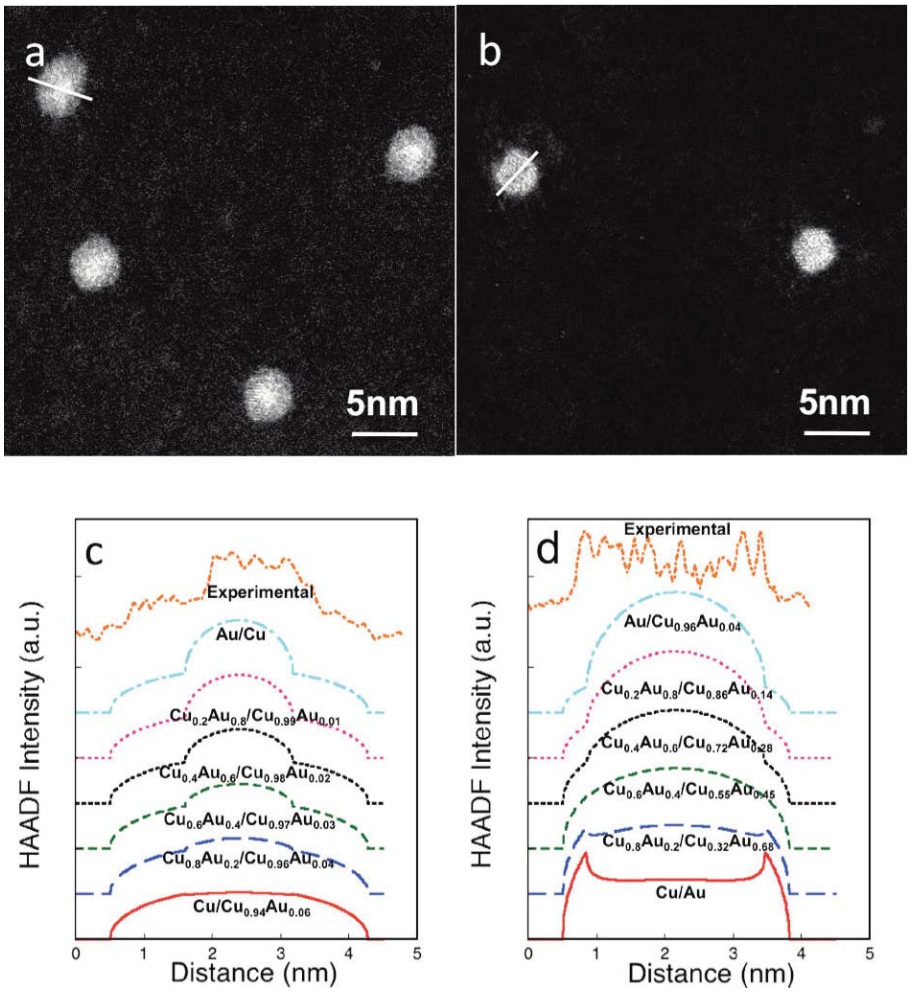

Figure 1.18 (a, b) HAADF images of mass-selected Au-Cu clusters; (c, d) experimental and simulated HAADF intensity line profiles. From reference [53].

It is of great value to characterise the chemical arrangements of alloy nanoparticles. STEM HAADF, EDX and EELS are possible ways to fulfil the characterisation of the elemental distribution. As mentioned in section 1.2.1, STEM uses the Z-contrast imaging technique and the image HAADF intensity is related to the atomic number so that the chemical contrast can be obtained in the HAADF images. Yin et al. [53] prepared Cu-rich/Au-rich and Au-rich/Cu-rich mass selected core/shell clusters in a magnetron sputtering cluster source. Bright and dark cores can be observed in the HAADF images (Figure 1.18 a,b), indicating the formation Au-rich and Cu-rich cores, respectively. HAADF intensity line profiles were simulated from models with different compositions (Figure 1.18 c,d). The Au and Cu compositions in the shell and core can be roughly determined by comparing the intensity change around the central area in the simulated and experimental line profiles.

The chemical contrast of bimetallic nanoparticles can be easily obtained with STEM-HAADF, for it uses Z-contrast imaging and only takes a few seconds to acquire a HAADF image. However, there are some limitations on chemical analysis with HAADF images. First, it needs some assumptions in the model to simplify the calculations for quantification. For example, simple geometrical structures and uniform elemental distribution in the core and shell were assumed in the above work [53]. Sometimes mass balance may be needed [52]. Second, the HAADF intensity contrast of two elements with close atomic numbers is very low in the HAADF images. It is harder to distinguish the distribution of the elements when more elements are in the specimen. Third, there are many factors can affect the HAADF intensity, e.g. electron channelling effect, detector asymmetry, detector angle mismeasurement, etc [56]. These will cause variations of the HAADF intensity and introduce some errors in the quantification. EDX and EELS are

widely used methods for elemental analysis to determine the elemental composition and distribution.

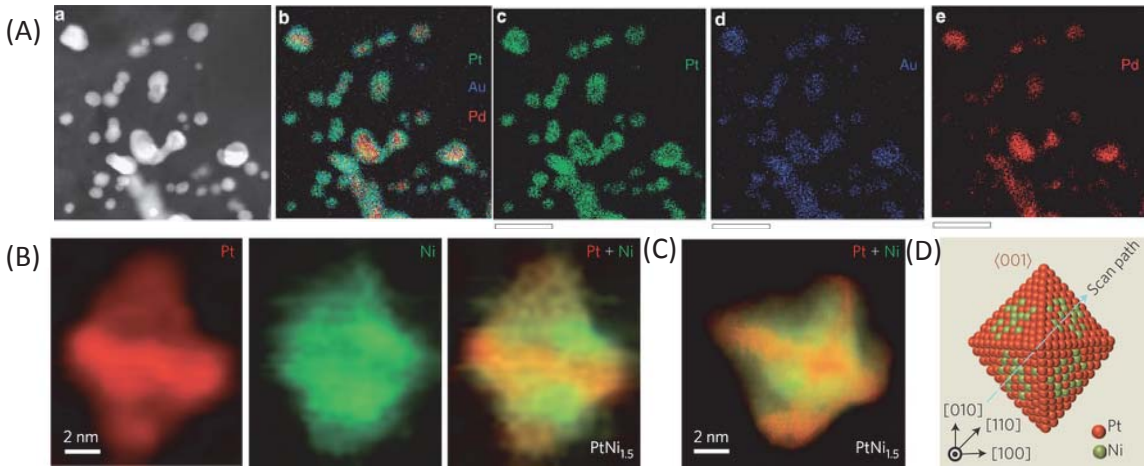

Figure 1.19 (A) STEM-EDX maps of Pt/PdAu nanoparticles. From (a) to (e) are HAADF image, EDX elemental maps overlapping, Pt (green), Au (blue) and Pd (red). Bar sizes, 20 nm. From reference [68]. (B) STEM-EELS maps of PtNi nanoparticles close to the ⟨110⟩ zone axis; from left to right are the EELS maps of Pt (red), Ni (green) and composite map, respectively. (C) Composite image of a particle close to the ⟨100⟩ zone axis. (D) A particle model along the ⟨001⟩ zone axis. Reproduced from reference [69].

The EDX detector was developed in the late 1960s and measures the number and energy of the characteristic X-rays emitted after the interaction between the electron beam and a specimen. The application of EELS can be traced back to the 1940s [67], which detects the energy loss of the incident electrons during the electron-specimen interaction. (More details about EDX and EELS are shown in Chapter 2). After decades of development, its stability, collection efficiency and spatial resolution have been largely improved nowadays. Elemental mapping can be obtained by EDX and EELS spectrum imaging, which records a full spectrum at every pixel in the digital image; therefore, this

only can be done in STEM mode. Figure 1.19 shows examples of EDX and EELS elemental mapping of Pt/PdAu [68] and PtNi nanoparticles [69]. Revealing the element distribution of alloy nanoparticles is essential to have a good understanding of the catalytic mechanism and to find the active sites for maximising the catalytic performance. However, the characterisation of core-monolayer shell nanoparticles [65, 68], doped nanoclusters [70] by EDX and EELS is still very challenging considering the small volume of material, especially when the particle size is small (~2nm).

Both EDX and EELS have advantages and disadvantages in the elemental analysis. EDX is simple to operate and collects different energy range peaks at the same time. The signal of almost all of the elements in the specimen can be presented in one spectrum. But it is limited by its poor energy resolution, which is ~ 120 eV at Mn Kα line. There is a significant peak overlap in the low-energy range (<500 eV), so EDX is suitable for analysing heavy elements. The energy resolution of EELS is much higher than EDX, which ranges from 0.5 to 1.5 eV when a field-emission gun is used. The characteristic energy edges of light elements can easily be separated in an EELS spectrum. However, the intensity drops exponentially when the energy-loss increases and the energy-loss feature of heavy elements at high-energy range (>1000 eV) is very weak. The low-loss region is typically 10^4-10^6 times more intense than the core-loss region. Due to the huge intensity variation across the spectrum and the limited number of channels, in certain cases, it's not possible to measure the low loss spectrum and high loss spectrum at the same time for a conventional EELS detector. Additionally, the collection efficiency of EELS (~80%) is much greater than that of EDX (<30%) [71], since most of the energy-loss electrons are forward-scattered and can be efficiently collected with a small EELS

collection angles. In contrast, an EDX detector receives only a small fraction of the isotropically emitted characteristic X-rays.

Significant improvements have been made to push these limitations further. The implementation of a DualEELS detector makes it possible to collect both the low and core loss regions near-simultaneously [72,73]. In this system, three ultrafast electrostatic deflectors are synchronized to fulfil the dual energy range EELS imaging: beam-blanking control (down to 1 μs for low-loss spectrum collection), energy shift control (changing energy range for recording core-loss spectrum), and lateral spectrum shift control to isolate two portions of the spectrum on the detector. The full energy range acquisition of electron energy-loss signals allows full processing of the EELS data, e.g. deconvolution, thickness mapping, etc. To increase the collection efficiency of EDX, Super-X™ system [74] was designed. It integrates four silicon drift EDX detectors with a total active area of 120 mm^2. The detectors are windowless, which allows higher collection efficiency and better sensitivity for light elements detection.

With the application of newly designed detectors and the implementation of spherical aberration correction in STEM, the resolution in chemical mapping was pushed into the atomic length scale [75, 76]. Figure 1.20 shows examples of atomic-resolution EDX and EELS maps of $SrTiO_3/LaMnO_3$ Multilayers. The atomic chemical imaging not only demonstrates the arrangement of different elements at the atomic scale but also the local bonding states [76] and valence states [77]. Turner and co-workers [77] studied the surface of CeO_{2-x} nanoparticles using atomic-resolution EELS mapping. They found that the surface cerium ions were reduced to Ce^{3+}, and that 1-2 underlying atomic layers for the {111} surfaces were mixed-valency. While the thickness of Ce^{3+} shell for {100}

surfaces was extended to over 6 layers. This finding may explain the higher catalytic activity of the {100} surface facets in ceria.

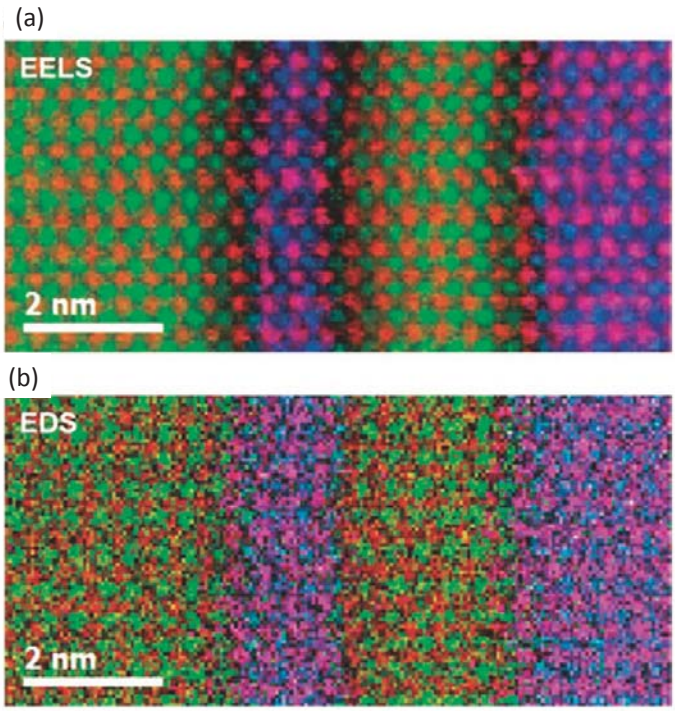

Figure 1.20 Atomic-resolution EELS (a) and EDX (b) elemental maps of Ti in green, Sr in red, La in purple, and Mn in blue. From reference [78].

1.3.2 Oxidation state analysis by EELS

Compared to EDX, EELS can obtain more information from the specimen, such as the specimen thickness, plasmon excitations, electronic band structure, and valence state, etc. A thorough analysis of the valence state of metal nanoparticles leads to an accurate and full understanding of the fundamental nature of the catalytic and toxic reactivity [79-82]. In the mimic superoxide dismutase catalytic activity, ceria nanoparticles with high Ce^{3+}/Ce^{4+} (~40 at.%) ratio were found to be more active than those with low Ce^{3+}/Ce^{4+} (~20 at.%) ratio [79]. White et al. [80] reported that the active catalyst state of Cu nanoparticles is Cu^{+} in the CO oxidation reaction, because of the valence variations of

Cu_2O and thus its ability to seize and release surface lattice oxygen. In the toxicity assessment of cobalt ferrite nanoparticles, the toxic effect was detected for these nanoparticles due to the Co^{2+} ions released from the particles, which causes a hypoxia-like response [81]. Pulido-Reyes et al. [82] concluded that the toxicity of ceria nanoparticles was related to the concentration of surface Ce^{3+} sites. Particles with 40% and 58% Ce^{3+} were found to be toxic, while samples having 26, 28 and 36% Ce^{3+} were non-toxic. This could be ascribed to the high concentration of oxygen vacancies near the Ce^{3+} sites and the damaging oxygen radicals generated. In this thesis, the valence states of cerium oxide, iron oxide and cobalt oxide were studied; therefore, we will introduce the EELS spectra of these materials in this section.

The valence state determination by EELS can be obtained by observing the chemical shift of the energy-loss edge or comparing the energy-loss near edge structure (ELNES). In EELS, the L or M edge of transition metal and rare-earth elements is usually characterised by two strong peaks (known as white lines) resulting from the transition of an electron from 2p (or 3d) state to unoccupied 3d (or 4f) states. Their intensities are related to the occupation number of 3d (or 4f) orbits leading to the possibility of identifying the valence state of cations.

Figure 1.21a shows the Ce $M_{4,5}$ edges of Ce^{4+} and Ce^{3+} bearing materials [83].The EELS spectra of cerium are characterised by two sharp peaks due to the transition of a core electron to an unbound state. One peak is due to the $3d_{3/2} \rightarrow 4f_{5/2}$ transition indicated as M_4, and the other is due to $3d_{5/2} \rightarrow 4f_{7/2}$ transition denoted as M_5 [84]. The Ce^{4+} M_5 and M_4 edges consist of two main peaks at 880.4 eV (B) and 901.6 eV (B') followed by two lower intensity maxima at 889.2 eV (Y) and 906.7 eV (Y'). The Ce^{3+} $M_{4,5}$ edges have

different energies, edge shapes and intensities to those of Ce^{4+}. The M_5 edge is at about 882 eV and the broad peak can be separated into two peaks (D and D') within high-resolution EELS spectra [77]. The Ce^{3+} M_4 edge is asymmetrical with features E, F and G at 896.6, 898.4, and 899.7 eV. Additionally, the intensity of M_5 edge is higher than that of M_4 edge in Ce^{3+} and reversed in Ce^{4+}. The O K-edges of CeO_2 and Ce_2O_3 also have different shapes (Figure 1.21b). The O edge of CeO_2 has three distinct peaks at 529.3, 532.0, and 536.2 eV, respectively. While the peaks in the Ce_2O_3 O K-edge are at 531, 533.7, and 536.2 eV, respectively.

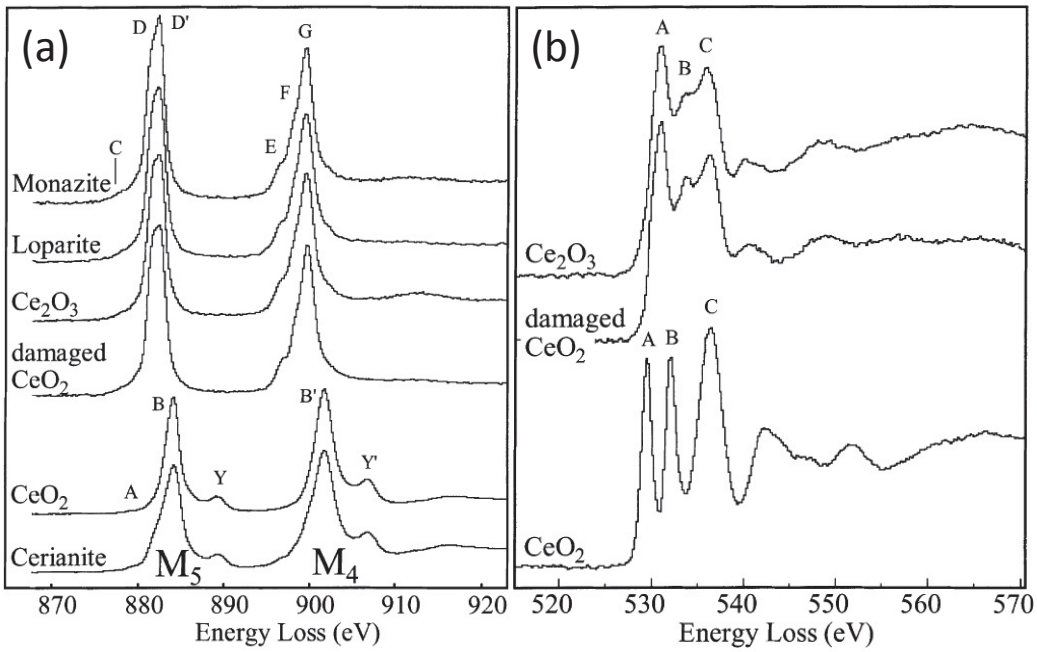

Figure 1.21 (a) Ce $M_{4,5}$ edges of Ce^{4+} and Ce^{3+} bearing materials; (b) Comparison of O K-edges of CeO_2, Ce_2O_3 and electron-damaged CeO_2. Reproduced from reference [83].

Two methods are usually used to determine the Ce^{4+}/Ce^{3+} ratio considering the changes in ELNES shape and M_5/M_4 intensity ratio. First, the studied spectra can be simulated by a multiple linear least-square fitting (MLLS) method with Ce^{4+} and Ce^{3+} single-valence spectra as references. Figure 1.22 demonstrates an example of the MLLS fitting for

determining the Ce^{4+}/Ce^{3+} ratio. The fitting weights of each spectrum are the fractions of Ce^{4+} and Ce^{3+} ions [83]. Second, the valence of Ce ions can also be estimated using a linear interpolation between the M_5/M_4 ratio for Ce^{4+} (0.91) and Ce^{3+} (1.31), because of the linear relationship between the M_5/M_4 ratio and the occupancy of the 4*f* level [85]. In both methods, spectra from reference materials are needed. However, in some materials, the relationship between the white-line ratio and valence states is not linear [86,87]; the quantification would then be more complicated.

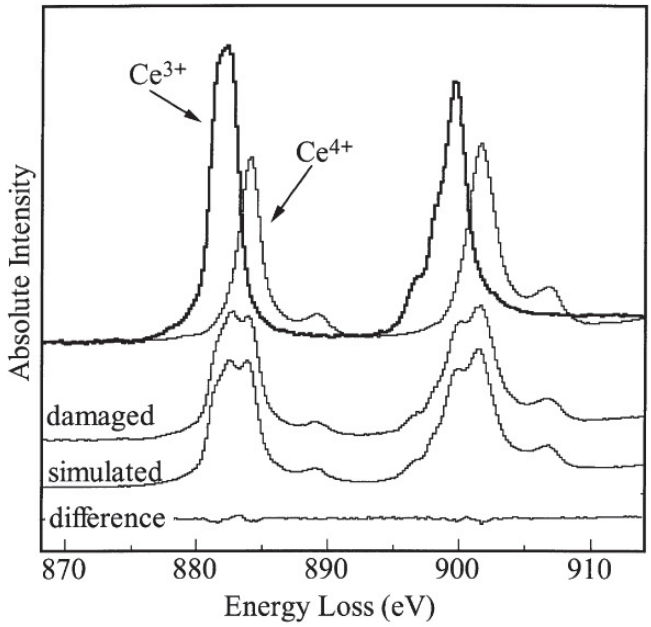

Figure 1.22 Simulation of an intermediate spectrum using MLLS fitting of the $M_{4,5}$ edges from CeO_2 and Ce_2O_3. From reference [83].

There are three methods that have been proposed to measure the white-line ratio. First, the subtraction method where the continuous L or M edge contribution is removed and then the intensity ratio is taken within a given energy window of 3 to 5 eV. Second, the maximum intensity method, the total intensities are measured within a given energy window without removing the continuous L or M edge contribution. Third, the second

derivative method, it measures the positive contribution from the second derivative of the spectra under each peak [87].

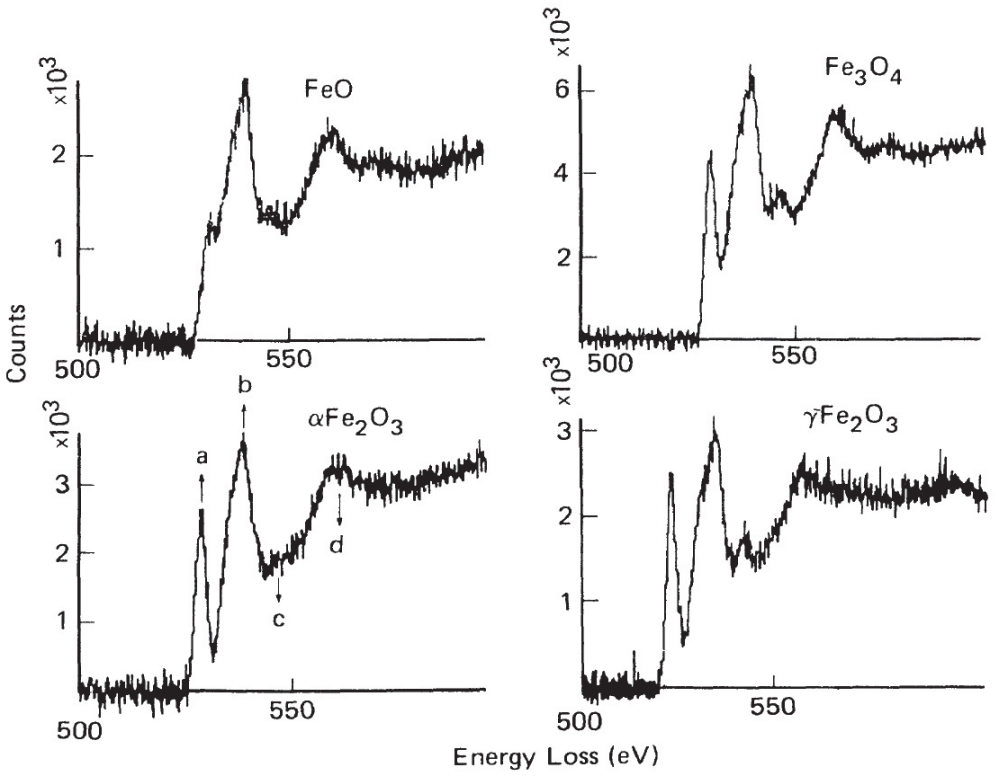

Figure 1.23 O K-edges of FeO, Fe_3O_4, α-Fe_2O_3, and γ-Fe_2O_3. From reference [88].

The EELS spectra of four Iron oxide compounds (FeO, Fe_3O_4, α-Fe_2O_3, and γ-Fe_2O_3) display distinct features in their O K-edges (Figure 1.23). First, the relative intensity of the pre-peak (a, see Figure 1.23, α-Fe_2O_3) at about 530 eV increases gradually from FeO to Fe_2O_3. Second, the dominant peak (b) around 540 eV remains rather similar for all spectra. Third, there is a weak maximum at about 545-550 eV and its shape and position vary between different compounds. The fourth major feature around 560-565 eV is a rather broad profile. To quantitatively characterise the O K-edges between these compounds, Colliex et al. [88] measured the energy difference between peak (a) and (b) and the relative intensity of peak (a) with respect to (b). They found that the energy difference increased from 9.0 to 11.0 eV when the compounds changed from FeO to

Fe_3O_4, γ-Fe_2O_3, and α-Fe_2O_3. A similar trend was observed in the relative intensity, which increased from 0.09 to 0.20.

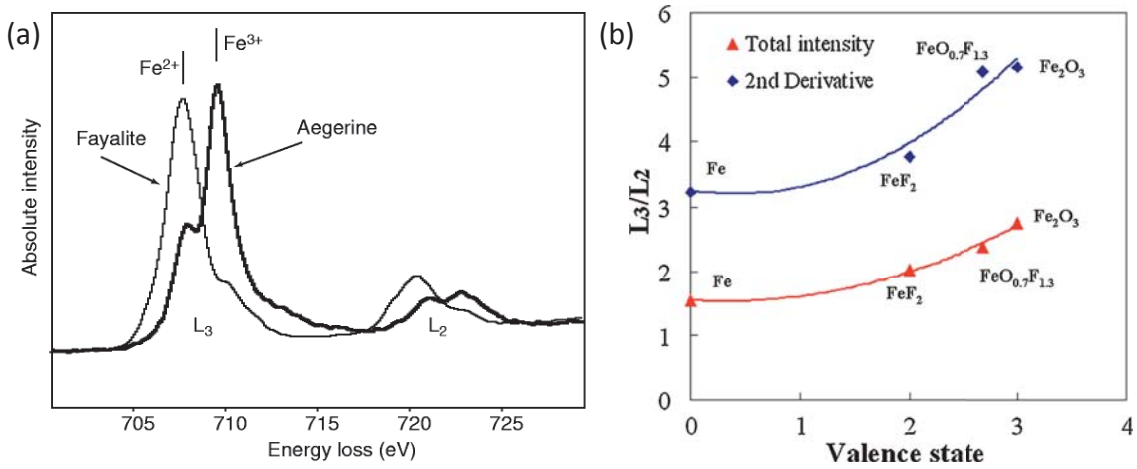

Figure 1.24 (a) Comparison of the Fe $L_{2,3}$ edges of fayalite (Fe_2SiO_4, Fe^{2+}) and aegirine ($NaFeSi_2O_6$, Fe^{3+}) Reproduced from reference [89]; (b) Fe L_3/L_2 intensity ratio for various standards. Reproduced from reference [87].

The spectra of Fe L-edges for Fe^{2+}- and Fe^{3+}-bearing materials are shown in Figure 1.24a, which illustrates distinct chemical shifts and $L_{2,3}$ edge shapes. The Fe^{2+} L_3 peak is at about 707.5 eV, while the peak maximum of Fe^{3+} L_3 is at 709.5 eV with a pre-peak at 708.0 eV. The separations of the L_3 and L_2 maxima for Fe^{2+} and Fe^{3+} are 12.8±0.1 and 13.2±0.1 eV, respectively. The white-line ratio (L_3/L_2) increases as the valence state of Fe goes up, however, the relationship between the white-line ratio and the valence state is not linear. The white-line ratio was measured in its second derivative and total intensity methods, and this value increases from about 3.2 to 5.4 and 1.5 to 2.8, respectively, when the valence state of Fe changes from 0 to 3+.

The EELS spectra of cobalt oxides are shown in Figure 1.25a. The O K-edges for CoO and Co_3O_4 have three pre-peaks labelled by a, b and c. The main difference is that peak a in

Co_3O_4 is sharper and more separated than in CoO. The energy difference between peak a and c is about 11 eV in Co_3O_4 and around 8 eV in CoO. The Co L_3 and L_2 lines correspond to the $2p^{3/2} \rightarrow 3d^{3/2}$ $3d^{5/2}$ and $2p^{1/2} \rightarrow 3d^{3/2}$ transitions, respectively. The relative intensity of Co L_3 with respect to the intensity of L_2 is higher in CoO than in Co_3O_4, indicating a higher white line ratio. The relationship between the Co valence states and the Co L_3/L_2 ratio has been investigated by studying the Co white lines from standard samples of known Co valences (shown in Figure 1.25b) [86]. The Co L_3/L_2 ratio is about 5 when the Co valence is 2+ and this value goes down to about 3.3 for $Co^{2.67+}$ and finally decreases to about 2 at the valence state of 4+.

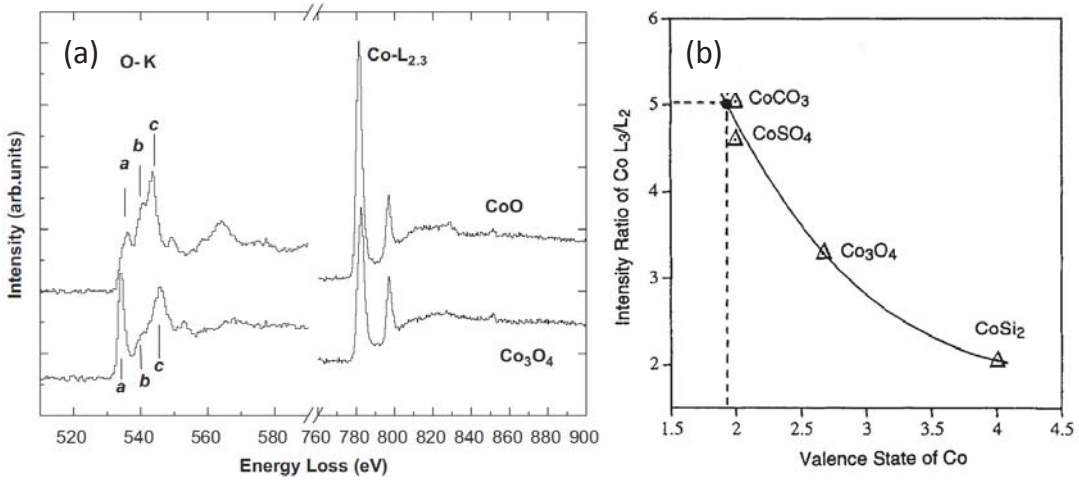

Figure 1.25 (a) O K-edge and Co L-edges for CoO and Co_3O_4. Pre-peaks in O K-edge are labelled by a, b and c. Reproduced from reference [90]. (b) Intensity ratio of Co L_3/L_2 obtained from known Co valences of standard samples. From reference [86].

Overall, EELS is a sensitive and efficient method to detect the variation of valence states, especially for transition metals and rare-earth elements. The changes in O K-edge features, white line ratio and energy position usually reflect the different valence states of the studied element. To qualitatively or quantitatively determine the valence state of

some elements, several standard specimens with known valence states are usually needed either for multiple linear fitting or white line ratio calibrations. However, there are several things need to be noted. First, energy drift often occurs during the acquisition of EELS spectra arising from the change in the accelerating voltage or spectrometer current. This causes inaccuracy in the position of energy-loss edge and affects the identification of chemical shift and the fitting result from the reference spectra. This can either be calibrated by the energy position of reference material, e.g. amorphous carbon or can be corrected by the zero-loss peak in a DualEELS system. Second, a poor energy resolution (i.e. full-width half maximum of the zero-loss peak) may blur some features in the ELNES. For example, the pre-peak in Fe L_3 was not obvious when the energy resolution is above 1 eV [88], but can be clearly seen when the resolution increases to 0.7 eV [89]. The energy resolution of the electron beam is mainly determined by the electron gun (a cold field emission gun has a better energy resolution of ~0.3 eV) and can be improved to be better than 0.1 eV by coupling with a monochromator [91]. Third, the valence state of reference material can be changed by the irradiation of electron beam [83], which may make the reference spectra less reliable. To minimise the electron beam induced damage on the samples, the spectrum acquisition time should be short.

1.4 Electron beam effects

In an electron microscope, all the useful signals as discussed above come from the interaction between the electron beam and specimen; however, the electron beam irradiation also brings a side effect, electron-beam damage. The damage can affect the structure and the chemistry of the specimen. The Palmer group investigated the ground-state atomic structure of size-selected Au clusters and found that the metastable

icosahedral clusters can be transformed into decahedral or FCC clusters under the electron beam irradiation [92,93]. Under the irradiation of highly focused electron beam, clusters with a few metal atoms can be split from their larger crystals [94]. Garvie et al. [83] studied the electron-beam effect on the valence state of Ce cations in CeO_2 by determining the Ce^{4+}/Ce^{3+} ratio with EELS. They found that the Ce^{3+} content increases after about ten seconds and the final ELNES features of the electron-damaged material are consistent with Ce_2O_3.

There are two common assumptions for the electron-beam damage. First, the amount of radiation damage is proportional to the electron dose. Second, the extent of the damage is proportional to the amount of energy transferred to the target. The primary radiation effects are sputtering the atoms from the surface, displacement of atoms in the bulk of the specimen, heating the target, and breakage of bonds or cross-linking. The displacement and sputtering damages are caused by the direct energy transfer from the electron beam to atoms, knocking them out of their atomic sites when the transferred energies exceed the displacement energy or surface binding energy. Displacement and surface sputtering is generally referred to inelastic scattering, and only high-angle scattered electrons can transfer enough momentum to an atomic nucleus to eject an atom. The transferred energy (E) is negligible when the scattering angle θ is small. The equation of transferred energy is given below [95],

$$E = E_{max} sin^2(\theta/2) = E_{max}\,(1 - cos\theta)/2 \qquad (1.2)$$

where E_{max} is the maximum energy transfer, when θ=180°. The maximum transferred energy of a relativistic electron (energy E_0, mass m) to a nucleus (mass M) when θ=180° is [95]

$$E_{max} = \frac{2ME_0(E_0 + 2mc^2)}{(m+M)^2c^2 + 2ME_0} \approx \frac{2E_0(E_0 + 2mc^2)}{Mc^2} \tag{1.3}$$

where c is the speed of light. Since $m \ll M$ and $E_0 \ll Mc^2$, equation 1.2 can be simplified.

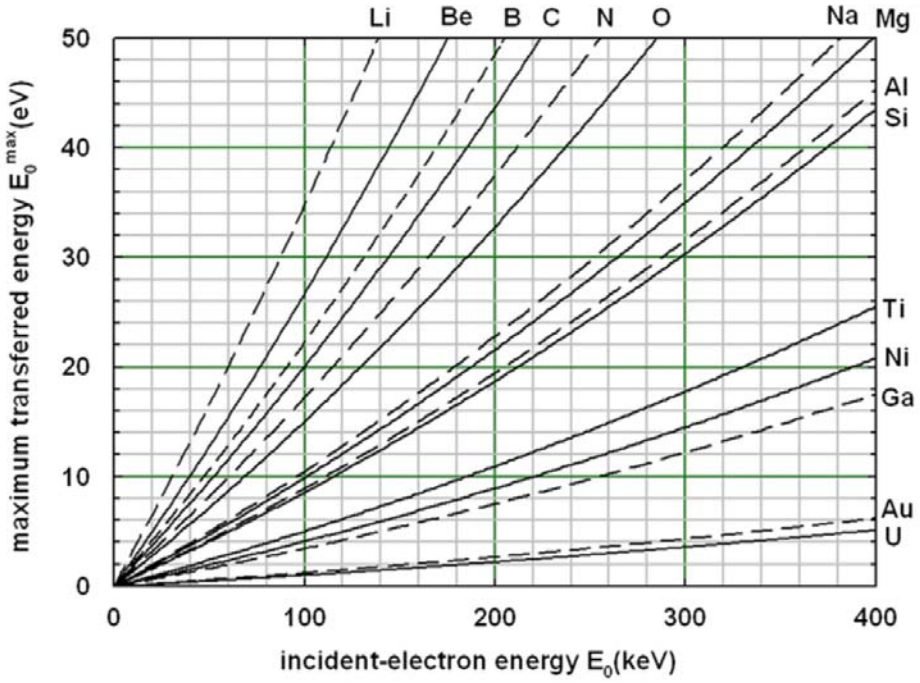

Figure 1.26 Maximum transferred energy against the incident-electron energy in various elements. From reference [96].

From equation 1.3 and Figure 1.26, we can see that E_{max} increases almost linearly as the electron beam energy increases. At the same incident electron energy, E_{max} decreases when the nucleus mass or atomic number increases, which mean that lighter atoms will need less energy to be displaced by the electron beam. In the studies of MP Au clusters by electron microscopy, the sublimation energy of Au is 3.8 eV [96] and the corresponding sputtering threshold energy is above 200 keV. Therefore, no significant sputtering of Au atoms will occur under normal imaging condition as is reported [51, 97]. But the lighter elements (H, C, O, and S) in the ligands can all be damaged even using

low voltages of 80 kV [62], so the knock-on damage of ligands in the MP Au clusters cannot be avoided by reducing the beam energy. The displacement energy (E_d) in bulk specimen is about 10 to 50 eV, and the energy for surface sputtering is usually below 10 eV [96]. Elastic electron scattering can also lead to diffusion of atoms at the surface, which require an energy of the order of 1 eV or less [95, 96]. Therefore, heavy atoms are mobilised even though the incident-electron energy is below their sputtering threshold energies [98].

Heating of the target is governed by the dissipation of plasmons caused by the collision between the incident electrons and the atomic electrons. In the process of this inelastic scattering, the transferred energy ends up as heat within the specimen [99]. The heat generation is balanced by the heat loss through thermal conduction; therefore, the temperature rise induced by the electron beam is mainly governed by the electron beam current and thermal conductivity of the specimen. In a TEM, common metals can be melted under a high beam current, even though they have a good thermal conductivity (>100 W/m/K). The thermal conductivity of polymers is usually very poor (0.2-2 W/m/K); so these materials are vulnerable at moderately elevated temperature even under a relatively low beam current. Current density has a little effect on specimen heating. Egerton et al [99] reported that the temperature rise of an amorphous carbon film (~1.6 W/m/K) increases from 0.5 K to 1.4 K when the current density in a 5 nA stationary probe increases by a factor of 10^6. The temperature rise is even lower when the beam is scanned at a video rate since the beam dwell time per pixel is typically less than the thermal equilibration time. Therefore, imaging in a STEM mode can reduce the beam heating effect on the specimen.

Radiolysis implies electron beam-induced breakage of bonds or cross-linking through inelastic scattering. Radiolysis damage in organic material is caused by electron excitation within each molecule but do not return to its original state in the subsequent de-excitation. In this way, chemical bonds are broken, and the molecule changes in crystallinity and structure. This damage is related to the electron dose $D=jT$, where j is the beam current density, and T is the irradiation time. A critical dose is defined as a complete destruction of the crystallinity or loss of mass. The critical dose for different materials varies widely, and it is reported that the critical dose for aromatic compounds is higher than the aliphatic ones due to the stable ring structures [99]. The mechanism for radiolysis of inorganic materials varies between different materials. In the case of metal oxides, radiolysis damage happens by creating an inner-shell vacancy on the metal site. Followed by Auger decay from the oxygen, a positive O atom is generated. The positive O atom is then repelled by the surrounding metal ions and ejected into the vacuum [99]. This process generates O vacancies and changes surface properties (composition, oxidation states, etc.) of the metal oxides.

Beam-induced damage is unavoidable in electron microscopy analysis; however, there are several methods one can use to minimize the damage, such as reducing knock-on effects by using a lower beam energy, cooling the specimen to lower temperature to reduce the heating effects, using low-dose imaging techniques to minimise the radiolysis damage, and so on. Worth noting that some methods may be useful to minimise one effect but increase another effect. For example, the best way to minimize the radiolysis damage is to lower the cross section for the electron-electron interactions by using higher voltages, but this will increase the knock-on effect at the same time.

1.5 Summary and conclusions

In this chapter, I introduced the recent studies of structure identification of MP Au clusters, elemental distribution by HAADF imaging, EDX and EELS, and oxidation state analysis by EELS. The MP Au clusters are of a great variety in size and structures. Due to the difficulty to grow high quality single crystals, a large number of MP Au cluster species remain unsolved. The application of high-resolution electron microscopy is of great importance to characterise the atom number and structure of individual MP clusters. Other information such as elemental composition, elemental distribution and valence state can also be obtained by analytical electron microscopy. With the application of spherical aberration correction, the resolution of HAADF imaging and chemical mapping can be pushed into the atomic level. Despite the great information an electron microscope can obtain, it also produces side effects. The specimen suffers from knock-on effect, specimen heating and radiolysis damages under the irradiation of high-energy electron beam. Beam-induced damages may not be very significant in certain cases, but efforts should be taken to minimise the damage, and their effects should be considered in the interpretation of the information obtained.

References

[1] Olmos-Asar, J. A.; Ludueña, M.; Mariscal, M. M. Monolayer Protected Gold Nanoparticles: The Effect of the headgroup–Au Interaction. *Phys. Chem. Chem. Phys.*

[2] Liu, Y.; Tsunoyama, H.; Akita, T.; Tsukuda, T. Efficient and Selective Epoxidation of Styrene with Tbhp Catalyzed by Au_{25} Clusters on Hydroxyapatite. *Chem. Commun.* **2010**, *46*, 550–552.

[3] Nie, X.; Qian, H.; Ge, Q.; Xu, H.; Jin, R. CO Oxidation Catalyzed by Oxide-Supported $Au_{25}(SR)_{18}$ Nanoclusters and Identification of Perimeter Sites as Active Centers. *ACS Nano* **2012**, *6*, 6014–6022.

[4] Tan, X.; Jin, R. Ultrasmall Metal Nanoclusters for Bio-Related Applications. WIREs Nanomed. *Nanobiotechnol*. **2013**, *5*, 569–581.

[5] Goswami, N.; Zheng, K.; Xie, J. Bio-NCs—The Marriage of Ultrasmall Metal Nanoclusters with Biomolecules. *Nanoscale* **2014**, *6*, 13328–13347.

[6] Zhao, T.; Zhou, T.; Yao, Q.; Hao, C.; Chen, X. Metal Nanoclusters: Applications in Environmental Monitoring and Cancer Therapy. *J. Environ. Sci. Health C* **2015**, *33*, 168–187.

[7] Brust, M.; Walker, M.; Bethell, D.; Schiffrin, D. J.; Whyman, R. Synthesis of Thiol-Derivatised Gold Nanoparticles in a Two-Phase Liquid–Liquid System. *J. Chem. Soc., Chem. Commun.* **1994**, 801–802.

[8] Qian, H.; Jin, R. Ambient Synthesis of $Au_{144}(SR)_{60}$ Nanoclusters in Methanol. *Chem. Mater.* **2011**, *23*, 2209–2217.

[9] Weare, W. W.; Reed, S. M.; Warner, M. G.; Hutchison, J. E. Improved Synthesis of Small (d_{Core} ≈ 1.5nm) Phosphine-Stabilized Gold Nanoparticles. *J. Am. Chem. Soc.* **2000**, *122*, 12890–12891.

[10] Fairbanks, M. C.; Benfield, R. E.; Newport, R. J.; Schmid, G. An Exafs Study of the Cluster Molecule $Au_{55}(PPh_3)_{12}Cl_6$. *Solid State Commun.* **1990**, *73*, 431–436

[11] Qian, H.; Eckenhoff, W. T.; Bier, M. E.; Pintauer, T.; Jin, R. Crystal Structures of Au_2 Complex and Au_{25} Nanocluster and Mechanistic Insight into the Conversion of Polydisperse Nanoparticles into Monodisperse Au_{25} Nanoclusters. *Inorg. Chem.* **2011**, *50*, 10735–10739.

[12] Leff, D. V; Brandt, L.; Heath, J. R. Synthesis and Characterization of Hydrophobic, Organically-Soluble Gold Nanocrystals Functionalized with Primary Amines. *Langmuir* **1996**, *12*, 4723–4730.

[13] Aslam, M.; Fu, L.; Su, M.; Vijayamohanan, K.; Dravid, V. P. Novel One-Step Synthesis of Amine-Stabilized Aqueous Colloidal Gold Nanoparticles. *J. Mater. Chem.* **2004**, *14*, 1795.

[14] Weissker, H. C.; Escobar, H. B.; Thanthirige, V. D.; Kwak, K.; Lee, D.; Ramakrishna, G.; Whetten, R. L.; López-Lozano, X. Information on Quantum States Pervades the Visible Spectrum of the Ubiquitous $Au_{144}(SR)_{60}$ Gold Nanocluster. *Nat. Commun.* **2014**, *5*, 3785.

[15] Alvarez, M. M.; Khoury, J. T.; Schaaff, T. G.; Shafigullin, M.; Vezmar, I.; Whetten, R. L. Critical Sizes in the Growth of Au Clusters. *Chem. Phys. Lett.* **1997**, *266*, 91–98.

[16] Whetten, R. L.; Khoury, J. T.; Alvarez, M. M.; Murthy, S.; Vezmar, I.; Wang, Z. L.; Stephens, P. W.; Cleveland, C. L.; Luedtke, W. D.; Landman, U. Nanocrystal Gold Molecules. *Adv. Mater.* **1996**, *8*, 428–433.

[17] Qian, H.; Jin, R. Controlling Nanoparticles with Atomic Precision: The Case of $Au_{144}(SCH_2CH_2Ph)_{60}$. *Nano Lett.* **2009**, *9*, 4083–4087.

[18] Schaaff, T. G.; Shafigullin, M. N.; Khoury, J. T.; Vezmar, I.; Whetten, R. L.; Cullen, W. G.; First, P. N.; Gutierrez-Wing, C.; Ascensio, J.; Jose-Yacaman, M. J. Isolation of Smaller Nanocrystal Au Molecules: Robust Quantum Effects in Optical Spectra. *J. Phys. Chem. B* **1997**, *101*, 7885–7891.

[19] Negishi, Y.; Nobusada, K.; Tsukuda, T. Glutathione-Protected Gold Clusters Revisited: Bridging the Gap between Gold(I)–Thiolate Complexes and Thiolate-Protected Gold Nanocrystals. *J. Am. Chem. Soc.* **2005**, *127*, 5261–5270.

[20] Schaaff, T. G.; Knight, G.; Shafigullin, M. N.; Borkman, R. F.; Whetten, R. L. Isolation and Selected Properties of a 10.4 kDa Gold:Glutathione Cluster Compound. *J. Phys. Chem. B* **1998**, *102*, 10643–10646.

[21] Jin, R.; Zeng, C.; Zhou, M.; Chen, Y. Atomically Precise Colloidal Metal Nanoclusters and Nanoparticles: Fundamentals and Opportunities. *Chem. Rev.* **2016**, *116*, 10346–10413.

[22] Walter, M.; Akola, J.; Lopez-Acevedo, O.; Jadzinsky, P. D.; Calero, G.; Ackerson, C. J.; Whetten, R. L.; Gronbeck, H.; Hakkinen, H. A Unified View of Ligand-Protected Gold Clusters as Superatom Complexes. *Proc. Natl. Acad. Sci.* **2008**, *105*, 9157–9162.

[23] Negishi, Y., Chaki, N. K., Shichibu, Y., Whetten, R. L., and Tsukuda, T. Origin of Magic Stability of Thiolated Gold Clusters: A Case Study on $Au_{25}(SC_6H_{13})_{18}$. *J. Am. Chem. Soc.* **2007**, *129*, 11322 –11323.

[24] Zhu, M.; Eckenhoff, W. T.; Pintauer, T.; Jin, R. Conversion of Anionic $[Au_{25}(SCH_2CH_2Ph)_{18}]^-$ Cluster to Charge Neutral Cluster Via Air Oxidation. *J. Phys. Chem. C* **2008**, *112*, 14221–14224.

[25] Qian, H.; Eckenhoff, W. T.; Zhu, Y.; Pintauer, T.; Jin, R. Total Structure Determination of Thiolate-Protected Au38 Nanoparticles. *J. Am. Chem. Soc.* **2010**, *132*, 8280–8281.

[26] Tofanelli, M. a; Ackerson, C. J. Superatom Electron Configuration Predicts Thermal Stability of Au 25 (SR) 18 Nanoclusters. *J. Am. Chem. Soc.* **2012**, *134*, 16937–16940.

[27] Chen, Y.; Zeng, C.; Kauffman, D. R.; Jin, R. Tuning the Magic Size of Atomically Precise Gold Nanoclusters Via Isomeric Methylbenzenethiols. *Nano Lett.* **2015**, *15*, 3603–3609.

[28] Zeng, C.; Chen, Y.; Das, A.; Jin, R. Transformation Chemistry of Gold Nanoclusters: From One Stable Size to Another. *J. Phys. Chem. Lett.* **2015**, *6*, 2976–2986.

[29] Zeng, C.; Li, T.; Das, A.; Rosi, N. L.; Jin, R.Chiral Structure of Thiolate-Protected 28-Gold-Atom Nanocluster Determined by X-ray Crystallography. *J. Am. Chem. Soc.* **2013**, *135*, 10011– 10013.

[30] Zeng, C.; Liu, C.; Pei, Y.; Jin, R. Thiol Ligand-Induced Transformation of $Au_{38}(SC_2H_4Ph)_{24}$ to $Au_{36}(SPh\text{-}t\text{-}Bu)_{24}$. *ACS Nano* **2013**, *7*, 6138– 6145.

[31] Zeng, C.; Qian, H.; Li, T.; Li, G.; Rosi, N. L.; Yoon, B.; Barnett, R. N.; Whetten, R. L.; Landman, U.; Jin, R. Total Structure and Electronic Properties of the Gold Nanocrystal $Au_{36}(SR)_{24}$. *Angew. Chem. Int. Ed*. **2012**, *51*, 13114– 13118.

[32] Zeng, C.; Chen, Y.; Kirschbaum, K.; Appavoo, K.; Sfeir, M. Y.; Jin, R. Structural Patterns at All Scales in a Nonmetallic Chiral $Au_{133}(SR)_{52}$ Nanoparticle. *Sci. Adv.* **2015**, *1*, e1500045.

[33] Jadzinsky, P. D.; Calero, G.; Ackerson, C. J.; Bushnell, D. A.; Kornberg, R. D. Structure of a Thiol Monolayer-Protected Gold Nanoparticle at 1.1 Å Resolution. *Science* **2007**, *318*, 430–433.

[34] Jiang, H.; Cai, W.; Shao, X. New Lowest Energy Sequence of Marks' Decahedral Lennard-Jones Clusters Containing up to 10 000 Atoms, *J. Phys. Chem. A*, **2003**, *107*, 4238–4243

[35] Chen, Y.; Zeng, C.; Liu, C.; Kirschbaum, K.; Gayathri, C.; Gil, R. R.; Rosi, N. L.; Jin, R. Crystal Structure of Barrel-Shaped Chiral Au_{130}(p-MBT)$_{50}$ Nanocluster. *J. Am. Chem. Soc.* **2015**, *137*, 10076–10079.

[36] Dass, A.; Theivendran, S.; Nimmala, P. R.; Kumara, C.; Jupally, V. R.; Fortunelli, A.; Sementa, L.; Barcaro, G.; Zuo, X.; Noll, B. C. Au_{133}(SPh-tBu)$_{52}$ Nanomolecules: X-Ray Crystallography, Optical, Electrochemical, and Theoretical Analysis. *J. Am. Chem. Soc.* **2015**, *137*, 4610–4613.

[37] Kumara, C.; Aikens, C. M.; Dass, A. X-Ray Crystal Structure and Theoretical Analysis of $Au_{25-X}Ag_X(SCH_2CH_2Ph)_{18}^-$ Alloy. *J. Phys. Chem. Lett.* **2014**, *5* (3), 461–466.

[38] Tian, S.; Li, Y.-Z.; Li, M.-B.; Yuan, J.; Yang, J.; Wu, Z.; Jin, R. Structural Isomserism in Gold Nanoparticles Revealed by X-Ray Crystallography. *Nat. Commun.* **2015**, *6*, 8667.

[39] Schaaff T. G.; Shafigullin M. N.; Khoury J. T.; Vezmar I.; Whetten R. L. Properties of a Ubiquitous 29 kDa Au:SR Cluster Compound, *J. Phys. Chem. B* **2001**,*105*, 8785–8796.

[40] Ackerson C. J.; Jadzinsky P. D.; Sexton J. Z.; Bushnell D. A.; Kornberg R. D. Synthesis and Bioconjugation of 2 and 3 nm-Diameter Gold Nanoparticles, *Bioconjugate Chem.* **2010**, *21*, 214–218.

[41] Koivisto J.; Salorinne K.; Mustalahti S.; Lahtinen T.; Malola S.; Pettersson M. Vibrational Perturbations and Ligand–Layer Coupling in a Single Crystal of $Au_{144}(SC_2H_4Ph)_{60}$ Nanocluster. *J. Phys. Chem. Lett.* **2014**, *144*, 1–6.

[42] Pennycook S. J.; Boatner L. A. Chemically sensitive structure-imaging with a scanning transmission electron microscope, *Nature* **1988**, *336*, 565–567.

[43] Singhal A.; Yang J. C.; Gibson J. M. STEM-based mass spectroscopy of supported Re clusters, *Ultramicroscopy* **1997**, *67*, 191–206.

[44] LeBeau J. M.; Findlay S. D.; Allen L. J.; Stemmer S. Standardless atom counting in scanning transmission electron microscopy, *Nanoletters* **2010**, *10*, 4405–4408.

[45] Li, Z. Y.; Young, N. P.; Di Vece, M.; Palomba, S.; Palmer, R. E.; Bleloch, a L.; Curley, B. C.; Johnston, R. L.; Jiang, J.; Yuan, J. Three-Dimensional Atomic-Scale Structure of Size-Selected Gold Nanoclusters. *Nature* **2008**, *451*, 46–48.

[46] Young, N.; Li, Z.; Chen, Y.; Palomba, S.; Di Vece, M.; Palmer, R. Weighing Supported Nanoparticles: Size-Selected Clusters as Mass Standards in Nanometrology. *Phys. Rev. Lett.* **2008**, *101*, 246103.

[47] Wang, Z. W.; Li, Z. Y.; Park, S. J.; Abdela, a.; Tang, D.; Palmer, R. E. Quantitative Z-Contrast Imaging in the Scanning Transmission Electron Microscope with Size-Selected Clusters. *Phys. Rev. B* **2011**, *84*, 073408.

[48] Wang, Z. W.; Palmer, R. E. Intensity Calibration and Atomic Imaging of Size-Selected Au and Pd Clusters in Aberration-Corrected HAADF-STEM. *J. Phys. Conf. Ser.* **2012**, *371*, 012010.

[49] Hartel P.; Rose H.; Dinges C. Conditions and reasons for incoherent imaging in STEM. *Ultramicroscopy* **1996**, *63*, 93-114.

[50] Wang, Z. W.; Toikkanen, O.; Yin, F.; Li, Z. Y.; Quinn, B. M.; Palmer, R. E. Counting the Atoms in Supported, Monolayer-Protected Gold Clusters. *J. Am. Chem. Soc.* **2010**, *132*, 2854–2855.

[51] Jian, N.; Stapelfeldt, C.; Hu, K.-J.; Fröba, M.; Palmer, R. E. Hybrid Atomic Structure of the Schmid Cluster $Au_{55}(PPh_3)_{12}Cl_6$ Resolved by Aberration-Corrected STEM. *Nanoscale* **2015**, *7*, 885–888.

[52] Jian, N.; Palmer, R. E. Variation of the Core Atomic Structure of Thiolated ($Au_xAg_{1-x})_{312\pm55}$ Nanoclusters with Composition from Aberration-Corrected HAADF STEM. *J. Phys. Chem. C* **2015**, *119*, 11114–11119.

[53] Yin F.; Wang Z. W.; Palmer R. E. Controlled Formation of Mass-Selected Cu–Au Core–Shell Cluster Beams. *J. Am. Chem. Soc.*, **2011**, *133*, 10325–10327

[54] MacArthur K. E.; Jones L. B.; Nellist P. D. How flat is your detector? Non-uniform annular detector sensitivity in STEM quantification. *J. Phys.: Conf. Ser*. **2014**, *522*, 012018.

[55] Van Dyck D.; Op de Beeck M. A simple intuitive theory for electron diffraction. *Ultramicroscopy*, **1996**, *64*, 99-107.

[56] Jones, L. Quantitative ADF STEM: Acquisition, Analysis and Interpretation. *IOP Conf. Ser. Mater. Sci. Eng.* **2016**, *109*, 012008.

[57] Liu J; Jian N; Ornelas I; Pattison A. J.; Lahtinen T., Salorinne K.; Häkkinen H.; Palmer, R. E. Exploring the Atomic Structure of 1.8 nm Monolayer-Protected Gold Clusters with Aberration-Corrected STEM. *Ultramicroscopy* **2016**, *176*, 146-150.

[58] Bahena, D.; Bhattarai, N.; Santiago, U.; Tlahuice, A.; Ponce, A.; Bach, S. B. H.; Yoon, B.; Whetten, R. L.; Landman, U.; Jose-yacaman, M. STEM Electron Diffraction and High-Resolution Images Used in the Determination of the Crystal Structure of the $Au_{144}(SR)_{60}$ Cluster. *J. Phys. Chem. Lett.* **2013**, *4*, 975–981.

[59] Tlahuice-flores, A.; Santiago, U.; Bahena, D.; Vinogradova, E.; Conroy, C. V; Ahuja, T.; Bach, S. B. H.; Ponce, A.; Wang, G.; Jose, M.; et al. Structure of the Thiolated Au 130 Cluster. *J. Phys. Chem. A* **2013**, *117*, 10470–10476.

[60] Lopez-Acevedo, O.; Akola, J.; Whetten, R. L.; Grönbeck, H.; Häkkinen, H.Structure and Bonding in the Ubiquitous Icosahedral Metallic Gold Cluster $Au_{144}(SR)_{60}$. *J. Phys. Chem. C* **2009**, *113*, 5035– 5038.

[61] Negishi, Y.; Sakamoto, C.; Tatsuya, O.; Tsukuda, T. Synthesis and the Origin of the Stability of Thiolate-Protected Au_{130} and Au_{187} Clusters. *J. Phys. Chem. Lett.* **2012**, *3*, 1624–1628.

[62] Bruma, A.; Santiago, U.; Alducin, D.; Plascencia Villa, G.; Whetten, R. L.; Ponce, A.; Mariscal, M.; José-Yacamán, M. Structure Determination of Superatom Metallic Clusters Using Rapid Scanning Electron Di Ff Raction. *J. Phys. Chem. C* **2015**, *102*, 1902–1908.

[63] Azubel, M.; Koivisto, J.; Malola, S.; Bushnell, D.; Hura, G. L.; Koh, A. L.; Tsunoyama, H.; Tsukuda, T.; Pettersson, M.; Häkkinen, H.; et al. Nanoparticle Imaging. Electron Microscopy of Gold Nanoparticles at Atomic Resolution. *Science* **2014**, *345*, 909–912.

[64] Maroun, F., Ozanam, F., Magnussen, O. M. & Behm, R. J. The Role of Atomic Ensembles in the Reactivity of Bimetallic Electrocatalysts. *Science* **2001**, *293*, 1811–1814.

[65] Enache, D. I. et al. Solvent-Free Oxidation of Primary Alcohols to Aldehydes Using Au–Pd/TiO_2 Catalysts. *Science* **2006**, *311*, 362–365.

[66] Alayoglu, S.; Nilekar, A. U.; Mavrikakis, M.; Eichhorn, B. Ru–Pt Core–Shell Nanoparticles for Preferential Oxidation of Carbon Monoxide in Hydrogen. *Nat. Mater.* **2008**, *7*, 333 – 338.

[67] Hillier, J.; Baker, R. F. Microanalysis by Means of Electrons. *J. Appl. Phys.* **1944**, *15*, 663.

[68] Sasaki, K.; Naohara, H.; Choi, Y.; Cai, Y.; Chen, W.-F.; Liu, P.; Adzic, R. R. Highly Stable Pt Monolayer on PdAu Nanoparticle Electrocatalysts for the Oxygen Reduction Reaction. *Nat. Commun.* **2012**, *3*, 1115.

[69] Cui, C.; Gan, L.; Heggen, M.; Rudi, S.; Strasser, P. Compositional Segregation in Shaped Pt Alloy Nanoparticles and Their Structural Behaviour during Electrocatalysis. *Nat. Mater.* **2013**, *12*, 765–771.

[70] Zhang, H.; Watanabe, T.; Okumura, M.; Haruta, M.; Toshima, N. Catalytically Highly Active Top Gold Atom on Palladium Nanocluster. *Nat. Mater.* **2012**, *11*, 49–52.

[71] Williams, D. B.; Carter, C. B. Transmission Electron Microscopy: A Textbook for Materials Science. Springer, 2009.

[72] Scott, J.; Thomas, P. J.; MacKenzie, M.; McFadzean, S.; Wilbrink, J.; Craven, A. J.; Nicholson, W. A. P. Near-simultaneous dual energy range EELS spectrum imaging. *Ultramicroscopy* **2008**, *108*, 1586.

[73] GATAN DualEELS, http://www.eels.info/about/techniques/dual-eels

[74] von Harrach, H.S.; Dona, P.; Freitag, B.; Soltau, H.; Niculae, A.; Rohde, M. An integrated Silicon Drift Detector System for FEI Schottky Field Emission Transmission Electron Microscopes. *Microsc. Microanal.* **2009**, *15*, 208-209.

[75] Kotula, P.G.; Klenov, D.O.; von Harrach, H.S. Challenges to quantitative multivariate statistical analysis of atomic-resolution x-Ray spectral. *Microsc. Microanal.* **2012**, *18*, 691–698.

[76] Muller D. A.; Fitting Kourkoutis L.; Murfitt M.; Song J. H.; Hwang H. Y.; Silcox J.; Krivanek O. L. Atomic-scale chemical imaging of composition and bonding by aberration-corrected microscopy. *Science* **2008**, *319*, 1073–1076.

[77] Turner, S.; Lazar, S.; Freitag, B.; Egoavil, R.; Verbeeck, J.; Put, S.; Strauven, Y.; Van Tendeloo, G. High Resolution Mapping of Surface Reduction in Ceria Nanoparticles. *Nanoscale* **2011**, *3*, 3385–3390.

[78] Longo, P.; Thomas, P. J.; Aitouchen, A.; Rice, P.; Topuria, T.; Twesten, R. D. Atomic Elemental and Chemical Analysis of $SrTiO_3/LaMnO_3$ Multilayers Using Fast Simultaneous EELS and EDS Analysis in DigitalMicrograph. *Microsc. Today* **2015**, *23*, 44-53.

[79] Korsvik, C.; Patil, S.; Seal, S.; Self, W. T. Superoxide Dismutase Mimetic Properties Exhibited by Vacancy Engineered Ceria Nanoparticles. *Chem. Commun.* **2007**, *10*, 1056–1058.

[80] White, B.; Yin, M.; Hall, A.; Le, D.; Stolbov, S.; Rahman, T.; Turro, N.; O'Brien, S. Complete CO Oxidation over Cu_2O Nanoparticles Supported on Silica Gel. *Nano Lett.* **2006**, *6*, 2095–2098.

[81] Mariani, V.; Ponti, J.; Giudetti, G.; Broggi, F.; Marmorato, P.; Gioria, S.; Franchini, F.; Rauscher, H.; Rossi, F. Online Monitoring of Cell Metabolism to Assess the Toxicity of Nanoparticles: The Case of Cobalt Ferrite. *Nanotoxicology* **2012**, *6*, 272–287.

[82] Pulido-Reyes, G.; Rodea-Palomares, I.; Das, S.; Sakthivel, T. S.; Leganes, F.; Rosal, R.; Seal, S.; Fernández-Piñas, F. Untangling the Biological Effects of Cerium Oxide Nanoparticles: The Role of Surface Valence States. *Sci. Rep.* **2015**, *5*, 15613.

[83] Garvie, L. A. J.; Buseck, P. R. Determination of Ce^{4+}/Ce^{3+} in Electron-Beam-Damaged CeO 2 by Electron Energy-Loss Spectroscopy. *J. Phys. Chem. Solids* **2000**, *60*, 1943–1947.

[84] Manoubi, T.; Colliex, C.; Rez, P., Quantitative electron energy loss spectroscopy on M45 edges in rare earth oxides. *J. Electron. Spectrosc. Relat. Phenom.* **1990,** *50*, 1-18

[85] Wu, L.; Wiesmann, H. J.; Moodenbaugh, A. R.; Klie, R. F.; Zhu, Y.; Welch, D. O.; Suenaga, M. Oxidation State and Lattice Expansion of CeO_{2-x} Nanoparticles as a Function of Particle Size. *Phys. Rev. B* **2004**, *69*, 125415.

[86] Wang, Z. L.; Yin, J. S. Cobalt Valence and Crystal Structure of $La_{0.5}Sr_{0.5}CoO_{2.25}$. *Philos. Mag. B* **1998**, *77*, 49–65.

[87] Cosandey, F.; Su, D.; Sina, M.; Pereira, N.; Amatucci, G. G. Fe Valence Determination and Li Elemental Distribution in Lithiated $FeO_{0.7}F_{1.3}$/C Nanocomposite Battery Materials by Electron Energy Loss Spectroscopy (EELS). *Micron* **2012**, *43*, 22–29.

[88] Colliex, C.; Manoubi, T.; Ortiz, C. Electron-Energy-Loss-Spectroscopy near-Edge Fine Structures in the Iron-Oxygen System. *Phys. Rev. B* **1991**, *44*, 11402–11411.

[89] Garvie, L. J.; Buseck, P. R. Ratios of Ferrous to Ferric Iron from Nanometer-Sized Areas in Minerals. *Nature* **1998**, *396*, 667–670.

[90] Zhang, Z. Surface Effects in the Energy Loss near Edge Structure of Different Cobalt Oxides. *Ultramicroscopy* **2007**, *107*, 598–603.

[91] Mitterbauer, C.; Kothleitner, G.; Grogger, W.; Zandbergen, H.; Freitag, B.; Tiemeijer, P.; Hofer, F. Electron Energy-Loss near-Edge Structures of 3d Transition Metal Oxides Recorded at High-Energy Resolution. *Ultramicroscopy* **2003**, *96*, 469–480.

[92] Wang, Z. W.; Palmer, R. E. Determination of the Ground-State Atomic Structures of Size-Selected Au Nanoclusters by Electron-Beam-Induced Transformation. *Phys. Rev. Lett.* **2012**, *108* (24), 245502.

[93] Wells, D. M.; Rossi, G.; Ferrando, R.; Palmer, R. E. Metastability of the Atomic Structures of Size-Selected Gold Nanoparticles. *Nanoscale* **2015**, *7*, 6498–6503.

[94] Cretu, O.; Rodríguez-Manzo, J. A.; Demortire, A.; Banhart, F. Electron Beam-Induced Formation and Displacement of Metal Clusters on Graphene, Carbon Nanotubes and Amorphous Carbon. *Carbon N. Y.* **2012**, *50*, 259–264.

[95] Banhart, F. Irradiation Effects in Carbon Nanostructures Irradiation Effects in Carbon Nanostructures. *Rep. Prog. Phys.* **1999**, *62*, 1181–1221.

[96] Egerton, R. F. F.; McLeod, R.; Wang, F.; Malac, M. Basic Questions Related to Electron-Induced Sputtering in the TEM. *Ultramicroscopy* **2010**, *110*, 991–997.

[97] Wang, Z. W.; Palmer, R. E. Direct Atomic Imaging and Dynamical Fluctuations of the Tetrahedral Au(20) Cluster. *Nanoscale* **2012**, *4*, 4947–4949.

[98] Surrey, a; Pohl, D.; Schultz, L.; Rellinghaus, B. Quantitative Measurement of the Surface Self-Diffusion on Au Nanoparticles by Aberration-Corrected Transmission Electron Microscopy. *Nano Lett.* **2012**, *12*, 6071–6077.

[99] Egerton, R. F.; Li, P.; Malac, M. Radiation Damage in the TEM and SEM. *Micron* **2004**, *35*, 399–409.

Chapter 2 Experimental Methods

The Scanning Transmission Electron Microscope (STEM) is a powerful and widely used instrument in the field of nanoscience and nanotechnology. A significant advantage that it offers is a range of complementary characterisation techniques with high spatial and spectroscopic resolution, providing for atomic structure determination, elemental analysis, etc. In this chapter, I will introduce the basic STEM technique, the theoretical background to spherical aberration and correction, Z-contrast imaging, Energy Dispersive X-ray spectroscopy (EDX) and Electron Energy Loss Spectroscopy (EELS).

2.1 Aberration-corrected STEM

2.1.1 Comparison of TEM, SEM and STEM

Different from the light microscopes, electron microscopy uses a beam of accelerated electrons as an illumination source and uses electrostatic and electromagnetic lenses to control the electron beam to magnify and form an image. Since the first electron microscope was built in 1931 by Ruska and Knoll, different types of electron microscope have been developed, such as Transmission Electron Microscope (TEM), Scanning Electron Microscopy (SEM) and Scanning Transmission Electron Microscopy (STEM) and the performance of electron microscopes have also been greatly improved by coupling with aberration correctors and different imaging and analysing detectors.

TEM is the original form of electron microscopy, which adopts an imaging method by using Fourier transformation through a convex objective lens, followed by intermediate and projection lenses for magnifying the images (Figure 2.1a). On the other hand, a scanning

electron probe is used in a SEM; secondary electrons are excited from the sample surface by the electron beam and are collected to form an image (Figure 2.1b). As illustrated in Figure 2.1c, a STEM has a combination of a TEM and a SEM imaging characteristics. STEM uses a convergent electron beam as a scanning probe and scans a selected region of the sample in a raster pattern, which is similar to the imaging method of a SEM. Instead of collecting secondary electrons, transmitted electrons are used for forming images, and this is the same as a TEM. It is also worthy to note that the STEM images are not magnified by lenses like the TEM, but appear on a computer screen at a magnification that is controlled by the scanning dimensions on the specimen.

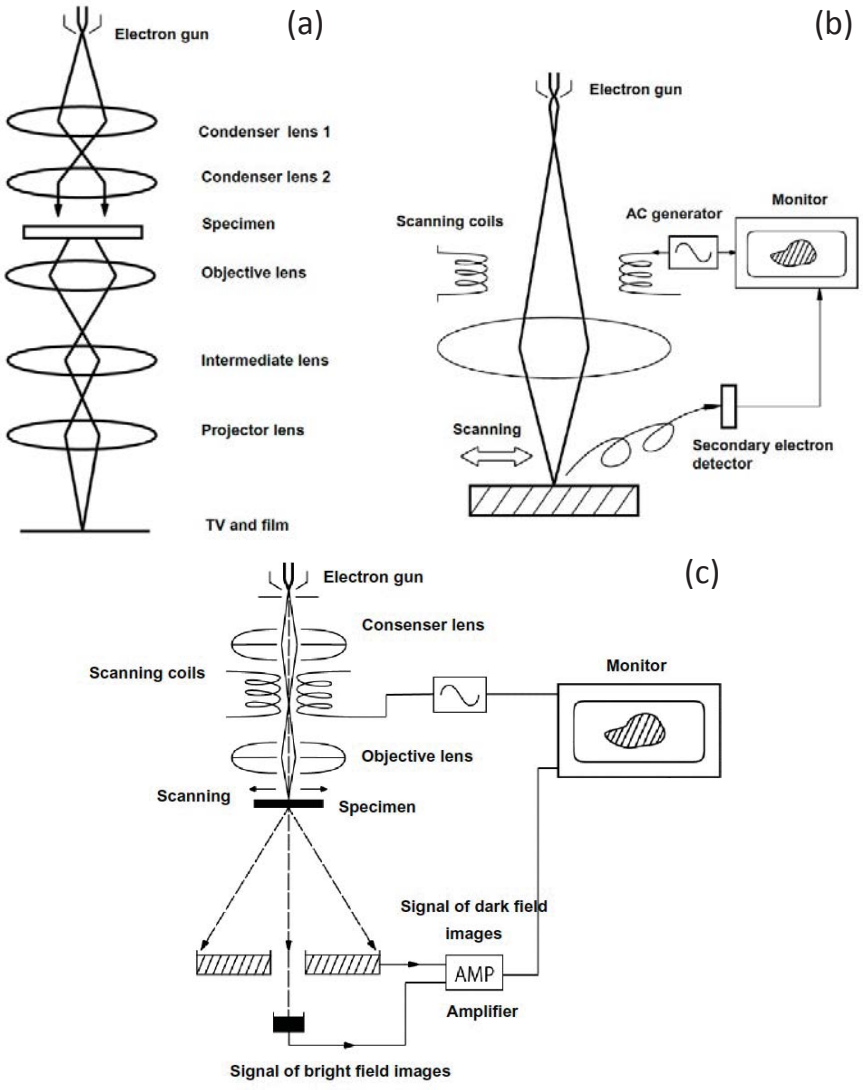

Figure 2.1 Basic schematics of (a) TEM, (b) SEM, and (c) STEM. From reference [1].

STEM has several advantages over TEM. In terms of image contrast, high-resolution TEM uses phase contrast imaging method. As electron waves pass through a sample, the waves may be absorbed (changed in amplitude) and/or refracted (changed their phase). With thin samples, amplitude contrast is not obvious and contrast arises through phase alteration [2]. Because the combination of contrasts is complex, the recorded phase-contrast images are not a direct representation of the samples structure, i.e., the high intensity might or might not indicate the presence of an atom column. On the other hand, high angle annular dark field (HAADF) STEM adopts the "Z-contrast" imaging method, where elastically scattered electrons at high-angle (>50 mrad) are collected and diffracted electrons are avoided. The intensity of an atom independently relies on the scattering cross section, which has a Z^n (n<2) dependence on atomic number. This provides a way to count the number of atoms in relatively small and thin samples [3,4]. In addition, the size of the convergent electron probe in a STEM can go down to the sub-Angstrom scale when aberration-corrected electron lenses are used [5]. Thus, various kinds of local analyses can be performed in STEM, such as point analysis, line scan and elemental mapping with the coupling of EDX and EELS detectors.

Taking advantage of the HAADF STEM imaging method, atom counting, atomic structure identification, elemental mapping and oxidation state analysis were applied in this study to characterise different types of nanoparticles. The model of the electron microscope used was JEOL-2100F equipped with a spherical aberration corrector (CEOS GmbH). Figure 2.2 shows a photograph of the instrument and the schematic diagram of the main components.

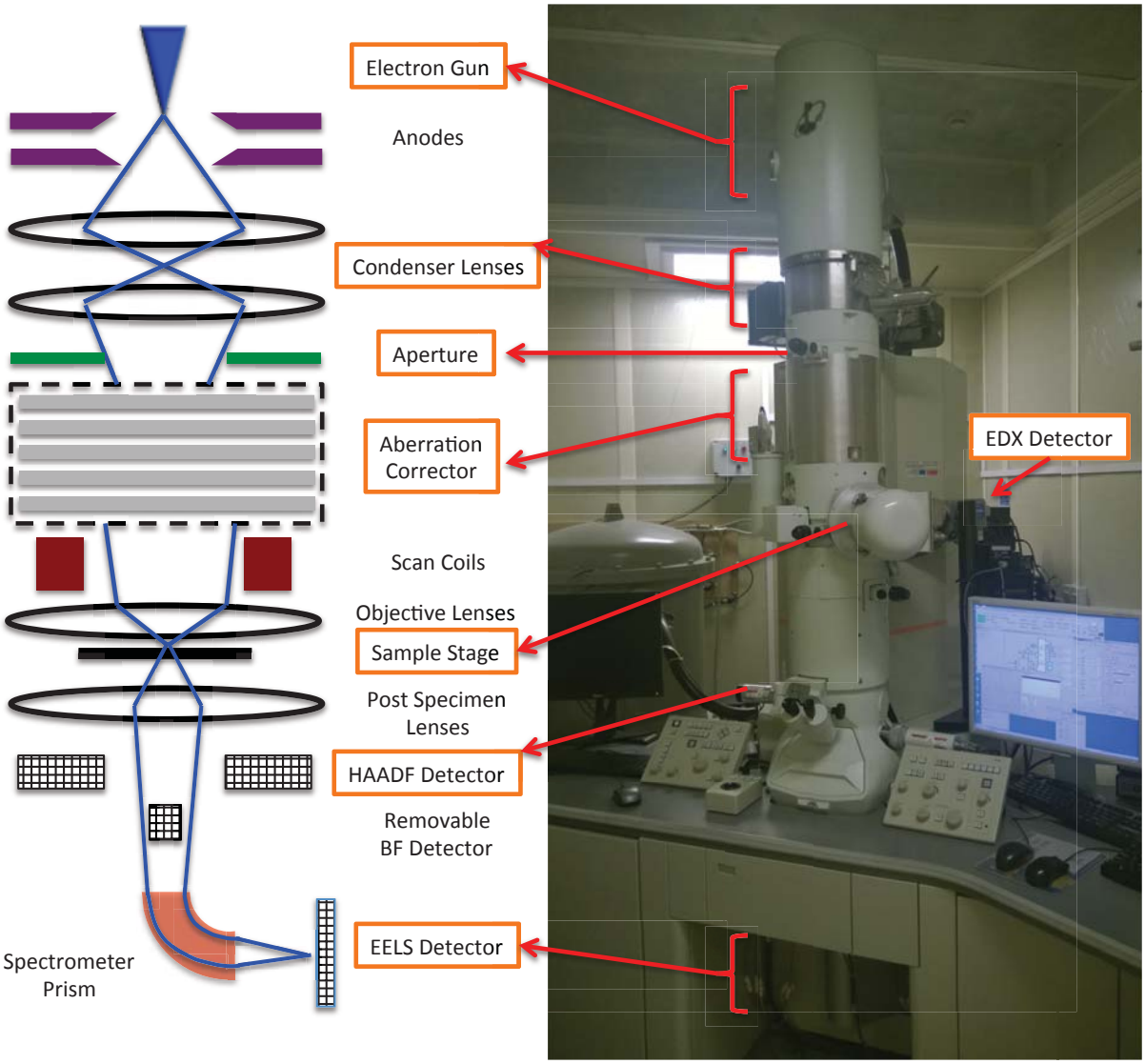

Figure 2.2 Simplified schematic diagram of an aberration corrected STEM and a photograph of our JEOL 2100F electron microscope equipped with a CEOS aberration corrector.

Electrons are extracted from a field emission gun (FEG, working as a cathode) by the first anode, which is positively charged by several kV. Then, the electrons are accelerated by seven electron accelerators to 200 kV or more. The FEG in our STEM is a Schottky FEG, which is made of a Lanthanum hexaboride (LaB_6) crystal. Because the electron gun is very sensitive to oxygen and contamination absorption on the gun tip surface, the operation of the electron gun should be in a proper high vacuum condition. But even in an ultra-high vacuum (UHV) condition, contaminants build up on the tip of a gun in a short time. This will cause the

emission current to drop and the extraction voltage to increase to compensate. For a Schottky FEG, the operational vacuum is about 10^{-6} Pa, but, because the gun is continuously heated (~1700 K) to increase the efficiency of field emission, no surface contamination layer will form on the gun. But the heating will cause a wider energy spread of the emitted electrons, which will decrease the energy resolution (full width half maximum of the zero loss peak, ~1 eV) of EELS and also the spatial resolution by increasing the chromatic aberration. By contrast, a cold FEG made of a tungsten tip is operated in UHV conditions (~10^{-9} Pa) and at relatively low temperatures (~300K). The cold FEG has a smaller energy spread of ~0.3 eV.

After the extraction and acceleration of the electrons from the electron gun, the electron beam passes through the condenser lenses. The condenser lenses are responsible for forming parallel or convergent probes, controlling the beam size and adjusting the convergence angle for a convergent probe to illuminate the specimen. Other coils are used to tilt and shift the beam and to align it with the detectors. The objective lens (a round magnetic lens) in an electron microscope suffers from spherical aberration, chromatic aberration, coma and astigmatism, which are the main defects that can seriously limit the image resolution. The correction of coma and astigmatism can be achieved by using a combination of two lenses. However, because the round magnetic lens cannot form a concave lens, the spherical and chromatic aberrations cannot be corrected by any combination of round magnetic lenses. A multipole that consists of several magnetic poles and can deflect electrons in the convergent and divergent directions to an optical axis, which makes it possible to compensate the spherical and chromatic aberrations. After passing through the condenser lenses, the electron beam enters a spherical aberration corrector consists of multipoles, in which most of the spherical aberration can be removed.

After the spherical aberration correction, the electron beam is focused to form a very fine probe (~0.1 nm) by a pre-specimen objective lens and scan coils are used to scan the probe across a certain area of the sample. Many kinds of signals are generated by the interaction of the electron beam and the specimen. High-angle elastically scattered electrons are collected by the HAADF detector to form HADDF-STEM images. The bright field (BF) image is obtained by using a small acceptance angle; the BF-STEM image is equivalent to a conventional high-resolution TEM image based on the principle of reciprocity. The signal of electron energy loss can be recorded by an EELS detector at the bottom of the microscope for chemical analysis. An EDX detector (shown in figure 2.2) is also installed near to the sample stage to record the generated characteristic X-rays. The details of HAADF imaging, EELS and EDX are described in the following sections.

2.1.2 Resolution and aberration-correction

If no aberrations are considered in an electron microscope, the resolution of any lens can be defined in terms of the Rayleigh criterion (equation 2.1) referring to the spacing between two overlapping images of the probe,

$$d_r = 1.22\,{}^{\lambda}/_{\beta} \tag{2.1}$$

where d_r is the diameter of an Airy disk, which is formed from a source point broadened by the diffraction of the electron beam, λ is the wavelength of the electron beam and β is the collection angle. The factor 1.22 is derived from a calculation of the position of the first dark circular ring surrounding the central Airy disc diffraction pattern. From equation 2.1 we can see that higher resolution can be obtained by using shorter illumination rays. According to the de Broglie theory, electrons have wave-like characteristics. Thus, the electron beam has a

wavelength and depends on its energy. The de Broglie wavelength λ of a moving electron can be found in equation 2.2,

$$\lambda = {}^{h}/_{p} \tag{2.2}$$

Where h is the Planck constant and p is the momentum of an electron. Considering the energy-momentum conservation of a free electron in special relativity theory, the de Broglie wavelength of the electron can be written in the following form,

$$\lambda = h/\sqrt{2m_0eV(1+\frac{eV}{2m_0c^2})} \tag{2.3}$$

where e is the elemental charge, m_0 is the rest mass of an electron, V is the accelerating voltage in the electron microscope, and c is the speed of light.

The accelerating voltage of our electron microscope is 200 kV, and the corresponding wavelength of the electron beam is 0.00251 nm. According to equation 2.1, the spatial resolution can easily go down to sub-Angstrom. However, because of the imperfections of the electromagnetic lenses, spherical and chromatic aberrations and astigmatism primarily limit the spatial resolution.

Spherical aberration occurs when the field of the electromagnetic lenses behaves differently for off-axis and near-axis electrons. Off-axis electrons are bent more than those close to the axis. Therefore, a point object will be blurred to be a finite size disc. Figure 2.3a shows the effects of spherical aberration. Chromatic aberration appears because the electrons extracted from the electron gun are not monochromatic, in which case, electrons with certain energy spread will not be focused to the same focal point (shown in Figure 2.3b). As mentioned above, the energy spread in the beam varies from ~0.3 eV (cold FEG) to ~ 1 eV (LaB_6). However, chromatic aberration could get worse if the specimen is thick, since the interaction

between the electron beam and the specimen will cause energy loss, so it is essential to have thin specimens. When electrons transmit through a round magetic lens, the coefficients of sphereical and chromatic aberrations cannot be negative. This is because of that these two coefficients are determined integrals that consists of squares of the fields, the position of an electron in a trajectory, and their differentials [6]. Astigmatism arises because of the non-uniform magnetic field of the lenses. Electrons then spiral around the optic axis. The misalignment or contamination of the objective aperture can also cause astigmatism.

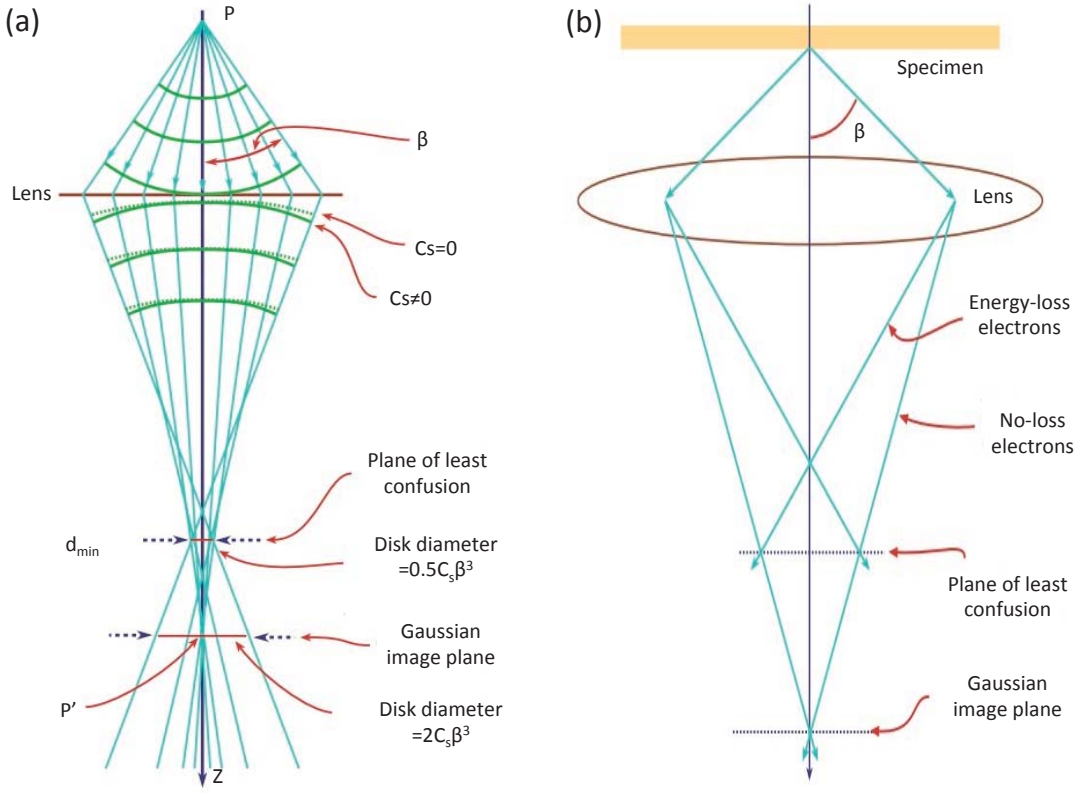

Figure 2.3 Schematic of spherical aberration (a) and chromatic aberration (b). β is the objective-lens collection angle and C_s is the spherical coefficient. From reference [7].

Because the STEM images are not magnified by lenses, the resolution of STEM image is not affected by the aberrations in the imaging lenses, but by the aberrations in the probe itself. The diameter of the probe size (d_p) is expressed by the following formulae [8],

$$d_p = \sqrt{0.5^2 {C_s}^2 \alpha^6 + 0.43^2 {C_c}^2 (\frac{\Delta E}{E_0})^2 \alpha^2 + (\frac{1.22\lambda}{\alpha})^2} \quad (2.4)$$

where α is the convergent angle of the beam shown in Figure 2.4, C_s and C_c are spherical and chromatic aberration coefficients, respectively, E_0 and ΔE are accelerated energy and energy spread of electrons. In equation 2.4, the first two terms are due to the spherical and chromatic aberrations, respectively. The third term is from the diffraction-limited error.

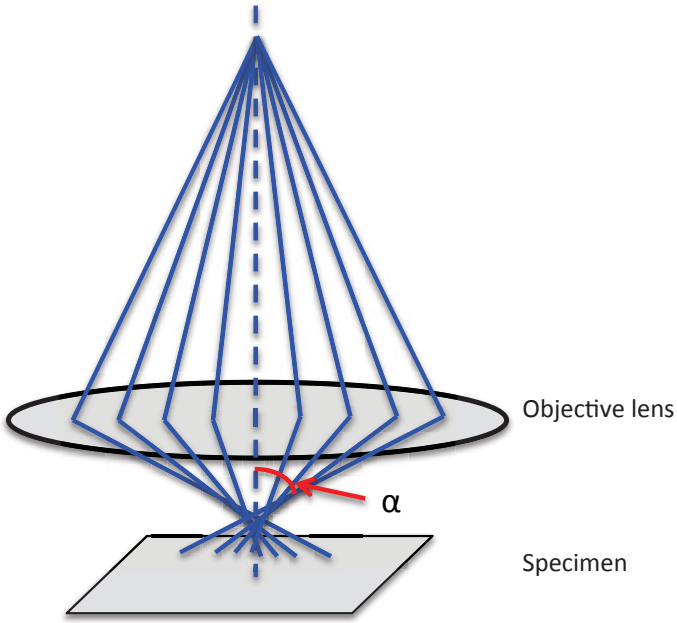

Figure 2.4 Spherical aberration caused blur of the objective lens in STEM. α is the convergent angle.

The wave aberration function $\chi(\theta, \varphi)$ expresses the difference between the ideal and actual wave-fronts in the diffraction plane, which is a function of the diffraction angles θ (radial) and φ (azimuthal). The aberration function is as follows [9]:

$$\chi(\theta, \varphi) = \sum_{m,n} \frac{1}{m+n} \mid C_{n,m} \mid \theta^{n+1} \cos\left(m\varphi - \varphi_{C_{n,m}}\right) \quad (2.5)$$

where m and n are integers and $C_{n,m}$ are the aberration coefficients in the notation of Haider et al. The wave aberration function with a third order spherical aberration can be written as follow [9,10],

$$\chi(\theta,\varphi) = \frac{1}{2}A_1\theta^2\cos\left(2\varphi - \varphi_{A_1}\right) + \frac{1}{2}C_1\theta^2 + \frac{1}{3}A_2\theta^3\cos\left(3\varphi - \varphi_{A_2}\right)$$
$$+ B_2\theta^3\cos\left(\varphi - \varphi_{B_2}\right) + \frac{1}{4}C_3\theta^4 + \frac{1}{4}A_3\theta^4\cos\left(4\varphi - \varphi_{A_3}\right)$$
$$+ S_3\theta^4\cos\left(2\varphi - \varphi_{S_3}\right) \qquad (2.6)$$

where A_1, A_2, and A_3, are the second-, third- and fourth-order astigmatism, respectively. C_1 and C_3 are defocused and the third-order spherical aberration (i.e. C_s), B_2 is the third-order coma (When the incoming electrons enter the lens at an angle, individual electrons are not reflected to the same point) and S_3 is the fourth-order star aberration.

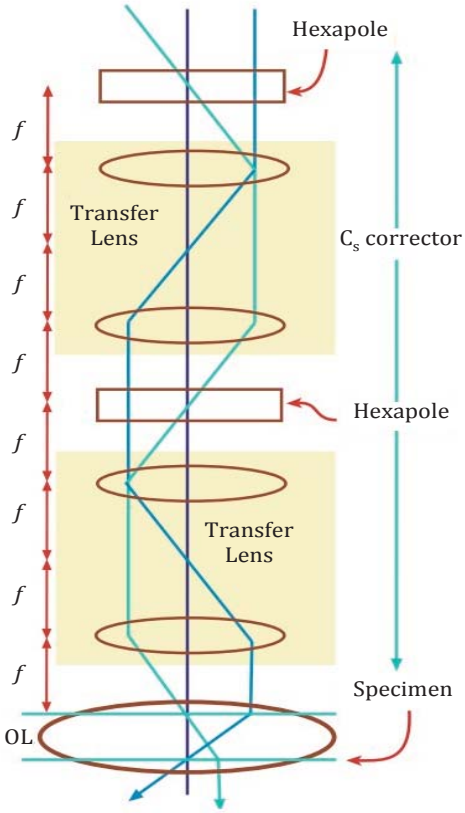

Figure 2.5 Schematic of a CEOS aberration correction consists of two hexaploes and other transfer lenses. From reference [7].

Approaches to aberration corrections in electron microscopy were proposed by Scherzer as early as 1947 [11]. After about fifty years of attempts and studies, spherical aberration correctors have been designed to reduce the aberrations. The quadrupole-octupole corrector and double hexapole corrector for STEM were designed by O.L. Krivanek et al [12, 13] in 1997 and M. Haider et al [14] in 1998, respectively. With the installation of a spherical aberration correction, an improvement of point resolution from 0.25 nm to better than 0.14 nm was obtained [14]. The spherical aberration correction installed on our STEM is a CEOS double hexapole spherical aberration correction.

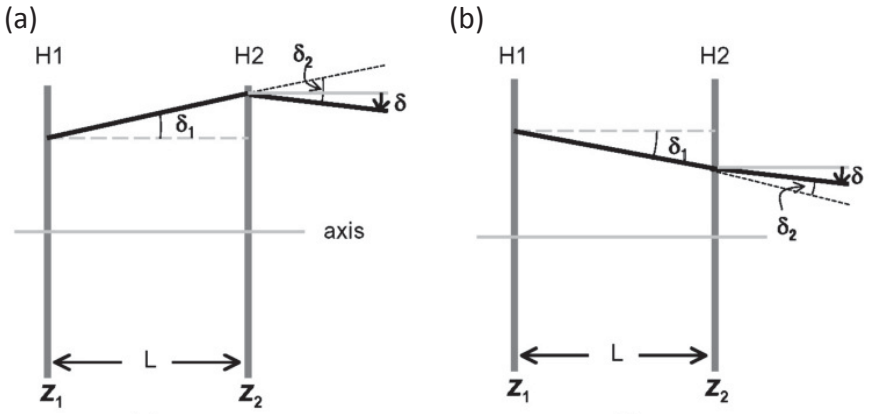

Figure 2.6 Third-order aberration derived from two hexapoles (Z_1 and Z_2) separated by L. Electrons deflected by the first hexapole in (a) divergent and (b) convergent directions. The amplitudes of the two hexapole fields are H_1 and H_2. Reproduced from reference [15].

A hexapole-type spherical aberration corrector consists of two electromagnetic hexapoles and other transfer lenses as shown in Figure 2.5. The principle of aberration correction is based on the fact that the primary second-order aberrations of the first hexapole can be compensated by the second hexapole element. In Figure 2.6, the electron that is deflected divergently by the first hexapole Z_1 (H_1) converges toward the axis at the second hexaple, because the field at Z_2 (H_2) is opposite to H_1. Since the position of the electron at Z_2 is further

from the axis than that at Z_1, the deflection power is stronger at Z_2, i.e., $|\delta_2| > |\delta_1|$. On the other hand, the deflection effect is relatively smaller when an electron is deflected in the convergent direction (Figure 2.6b). By using transfer lens doublets, a residual third-order spherical aberration that is opposite to the third-order spherical aberration caused by the objective lens is induced by the two hexapoles. Therefore, the spherical aberration of the entire system can be removed by appropriately exciting the hexapoles [16].

The routine work with a CEOS spherical corrector follows iterative steps: First, measuring and correcting the first- and second-order aberrations (A_1, B_2, A_2); Second, measure and correct the third- order aberrations (C_s, A_3 and S_3) [17]. Two probe tableaux in under- and over-focus are acquired in the second step. Two probe tableaux are acquired in the second step by shifting the probe between under- and over-focus and through a succession of tilt angles. The measurements are fed back to the aberration corrector control software. The software works out the coefficients of the aberrations and suggests the correction that should be made. The STEM tableau was obtained with a beam tilt angle of 18 mrad and azimuthal angles varying from 0 to 2π in steps of $\pi/6$.

2.1.3 HAADF-STEM imaging

Electrons that pass through a thin specimen can be scattered by interacting with the electron cloud and nucleus of the specimen atoms. Depending on the change of kinetic energy of an incident electron, the scattered electrons can be divided into elastic and inelastic scattering electrons. In the elastic scattering process, the kinetic energy of an incident electron is conserved, while an inelastically scattered electron usually loses some energy during the electron-specimen interaction. The signals (e.g. energy loss, characteristic X-rays) generated during the inelastic scattering process can be used for different chemical analyses, such as

EDX and EELS, while the high-angle elastically scattered electrons can be used for HAADF-STEM imaging. HAADF images are also termed Z-contrast images, and the image intensity is proportional to Z^n (n<2). This can be explained by the Rutherford scattering model.

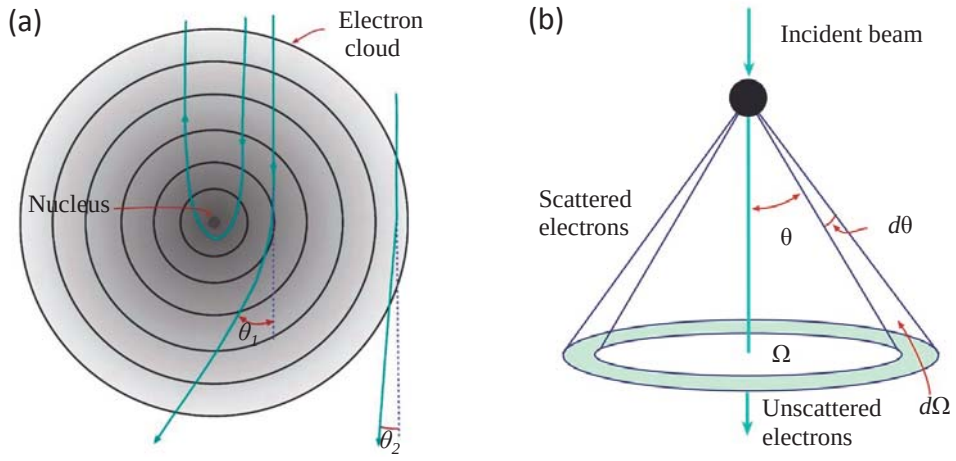

Figure 2.7 (a) Schematic diagram representing high (θ_1) and low (θ_2) angle elastic scattering from an atom; (b) Rutherford scattering parameters. Reproduced from reference [7].

Figure 2.7a shows that an atom can scatter an electron by a small angle by the Coulombic force within the electron cloud and also by a higher angle due to the electron-nucleus interaction. The differential cross section ($\sigma_R(\theta)$) for high-angle scattering by nucleus alone was derived by Rutherford as follows:

$$\sigma_R(\theta) = \frac{e^4 Z^2}{16(4\pi\varepsilon_0 E_0)^2} \frac{d\Omega}{sin^4(\theta/2)} \qquad (2.7)$$

where Z is the atomic number, θ is the scattering angle and Ω is the solid angle scattering, ε_0 is the dielectric constant and E_0 is the energy of the electrons. The definition of the angles is shown in Figure 2.7b.

In a STEM, the high-angle scattered electrons can be collected by the HAADF detector at certain inner and outer collection angles. In this case, according to equation 2.7, the number of high-angle scattered electrons collected by a detector is proportional to Z^2. However, the power of Z is usually less than 2 because of the screening effect of electrons, which reduces the differential cross section. Considering the screening effect and the relativity, equation 2.7 can be modified as follows,

$$\sigma_R(\theta) = \frac{Z^2 \lambda_R^4}{64\pi^4 a_0^2} \frac{d\Omega}{[sin^2(\theta/2) + \theta_0^2/4]^2} \tag{2.8}$$

where λ_R is the relativistically corrected electron wavelength (equation 2.3), θ_0 is the screening parameter given by equation 2.9 and a_0 is the Bohr radius of the scattering atom given by equation 2.10.

$$\theta_0 = \frac{0.117 Z^{1/3}}{E_0{}^{1/2}} \tag{2.9}$$

$$a_0 = \frac{h^2 \varepsilon_0}{\pi m_0 e^2} \tag{2.10}$$

A HAADF detector usually has a larger central aperture than a normal ADF detector. Since the conventional ADF detector always collects some Bragg diffracted electrons, it was not suitable to study crystalline specimens. To avoid collecting Bragg electrons, HAADF detectors were designed to have a collection angle larger than 50 mrad (~3°). In this work, the HAADF images were acquired with inner and outer detector angles of 62 and 164 mrad at the camera length of 10 cm.

2.2 Energy Dispersive X-ray Spectroscopy

The properties of nanoscale materials depend not only on their morphologies, such as particle structure, size and defects, but also on the elemental compositions. Energy dispersive X-ray

spectroscopy (EDX) is an analytical technique used for chemical analysis of a sample. It makes use of the characteristic X-ray spectrum emitted by a sample bombarded with a focused electron beam.

An atom within the sample contains ground state electrons in discrete energy levels. When a high-energy beam electron penetrates through the outer-shell electrons and inelastically interacts with the inner-shell electrons, a critical amount of energy can be transferred to an inner-shell electron and that electron is ejected, i.e. ionised. The ejection of an inner-shell electron leaves the atom in an excited state. One of the ways that the ionised atom can return to the ground state is by filling the inner-shell vacation with an electron from an outer shell and at the same time emitting an X-ray with an energy equal to the difference in energy between the two states of the atom (shown in Figure 2.8). The characteristic X-rays appear as sharp peaks and have a narrow energy range.

The number of X-rays generated of energy E (n_E) can be expressed as follows [18],

$$n_E = Q\omega N i_p \tag{2.11}$$

where ω is the fluorescent yield (i.e. the probability of the ionised atom returning to the ground state by emitting X-rays), N is the number of atoms in the irradiated volume, and Q is the ionisation cross section. The expression of Q is proposed by Bethe,

$$Q = \frac{\pi e^4}{E_0 E_c} z b \ln\left(\frac{cE_0}{E_c}\right) \tag{2.12}$$

where E_0 is incident electron energy, E_c is the critical ionisation energy, z is the number of electrons in the shell and b and c are constants related to the atomic structure.

Figure 2.8 also shows the interaction of an incident electron with the nucleus. Some electrons travelling close to the nucleus would be deflected by the electric field of the nucleus, and a portion or all of the kinetic energy of the electron would be lost during the deceleration. The lost energy can be emitted as X-ray photons, which is Bremsstrahlung X-ray (or braking radiation). Since the electron can suffer any amount of energy loss, the Bremsstrahlung X-ray forms a continuous spectrum, which contributes to the background of the EDX spectrum. Different from the emission of the characteristic X-rays, the emission of Bremsstrahlung X-rays is anisotropic and the intensity becomes the highest in the forward direction, which is the direction of the incident beam. The Kramers cross-section is used to estimate the production of Bremsstrahlung photons,

$$N(E) = \frac{KZ(E_0 - E)}{E} \tag{2.13}$$

where N(E) is the number of Bremsstrahlung photons of energy E and K is Kramers' constant.

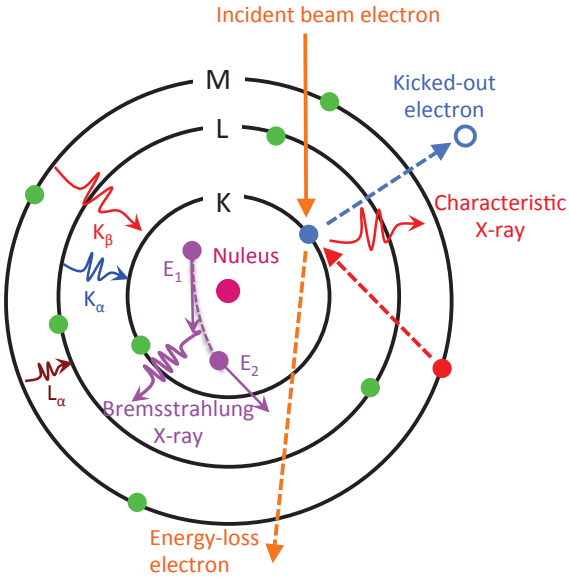

Figure 2.8 A schematic diagram of the mechanism of characteristic X-ray generation from electron-electron interaction and Bremsstrahlung X-rays from the interaction of electron-nucleus.

An EDX detector is usually made of a single crystal semiconductor and used to collect the X-ray signals. When an X-rays photon enters the Si detector, it will produce electron-hole pairs. The average energy required to excite each electron-hole pair is ~3.8 eV, and the number of the created pairs is directly proportional to the energy of the X-ray. The electron-hole pairs are subsequently separated by the electric field applied across the crystal and a charge pulse is generated and amplified. The energy of the X-ray can be then identified by the magnitude of the charge pulse.

It is of great value to know how much of each element the sample contains, once we know what it consists of. The Cliff-Lorimer ratio technique is a quantitative measurement method to obtain the relative concentration of each element in an EDX spectrum. In a binary system, the concentration ratio of element A and element B (C_A/C_B) can be obtained from equation (2.14),

$$\frac{C_A}{C_B} = k_{AB}\frac{I_A}{I_B} \tag{2.14}$$

where I_A and I_B are the intensity of the characteristic X-ray peaks of element A and B, respectively, and k_{AB} is a proportionality factor, which is determined by many factors, such as the ionisation cross sections, fluorescent yields of the elements, accelerating voltage and so on. k_{AB} can be obtained from characteristic X-ray measurement of standard specimens. Nowadays, many k_{AB} factors have been measured and tabulated in commercial EDX software. Therefore, quantitative analysis of the elements can be performed by referring to these k_{AB} values without measuring standard specimen.

The Cliff-Lorimer method is used under the assumption that the specimen is thin enough so that X-ray absorption by the specimen itself and fluorescence effect can be ignored. X-rays generated at different depths travel different distances in the specimen to reach the detector.

The absorption path is relatively short in a thin specimen, which reduces the possibility of absorption. The fluorescence effect means that X-rays emitted from non-target element are absorbed by target element and results in an enhancement in X-ray intensity. For a thick specimen, the ZAF correction method is used, in which the absorption and fluorescence of X-rays within the specimen are considered. In this thesis, nanoparticles with a diameter of less than 20 nm were investigated, so only the Cliff-Lorimer method was used in this study.

Though EDX detection of small nanoparticles can reduce the absorption effect of the specimen itself, a lower X-ray intensity will be generated, since a small number of atoms are excited by the incident beam electrons. To increase the detection efficiency of the detector, one can use a larger solid angle for collection. The solid angle is determined by the active area of the detector and the distance between the specimen and the detector. A bigger solid angle can be obtained by tilting the sample stage closer to the EDX detector. The other way to increase the X-ray signals is to increase the probe current by using a large spot size. Unavoidably, a high probe current will cause serous sample damage, especially for point analysis. EDX mapping is an optional method to minimise the electron beam damage since the dwelling time at each pixel is relatively short. Recently, a super-X EDX detector system was developed [19], which has four windowless silicon drift detectors (SDD) around the specimen providing a very large solid angle (0.9 sr) for X-ray collection. The acquisition time for EDX-mapping then drops from hours to minutes and the sensitivity is also largely improved [20]. Atomic-scale chemical mapping [21] and 3D EDX tomography [22] have been obtained by using the super-X EDX system.

The main advantage of EDX is that the collection of X-rays has a very large energy range, indicating that most of the elements can be detected simultaneously. However, the energy

resolution of the detector is very poor, which is about 130 eV at the Mn K_α peak. This is mainly caused by the electronic noise in the EDX system. The poor energy resolution causes many overlaps in the low energy range, especially for the light elements. Because of the poor energy resolution, structure and valence state information cannot be achieved.

In this study, a Bruker XFlash 4030 detector is fitted on the STEM, as indicated in Figure 2.2. The detector area is 30 mm^2 and the solid angle is 0.16 sr. The energy resolution at Mn K_α peak is 133 eV.

2.3 Electron Energy-Loss Spectroscopy

2.3.1 Overview

Electron energy-loss spectroscopy (EELS) measures the energy distribution of electrons after they have passed through a specimen. Some of the electrons will be inelastically scattered because of the Coulombic interactions with the electrons in the specimen as is shown in Figure 2.8 (orange arrows). The energy loss from these incident electrons is gained by the electrons in the specimen and the amount of energy loss is dependent on the nature of materials. The transmitted electrons can be separated by an electron spectrometer according to their kinetic energy and produce an energy-loss spectrum of electron counts versus energy loss. The fundamental difference between EDX and EELS is that EELS detects the initial excitation of an atom to an excited or ionised state, while EDX measures the X-rays generated from the decay of this excited state. Comparing with EDX, EELS offers much more physical insight, not only elemental composition, but also specimen thickness, electronic structure, oxidation state, plasmon, and so on.

Figure 2.9 presents a typical EELS spectrum of Fe_2O_3. The first sharp and intense peak on the most left peak refers to the zero-loss peak (ZLP), which is from those electrons that travel through the specimen without losing energy. The ZLP is used to calibrate the spectrometer by placing the ZLP at 0 eV. The energy resolution of the EELS system is also defined from the ZLP, which is the full width half maximum (FWHM) of the ZLP. The energy resolution is determined mainly by the energy width of the primary beam and the energy resolution of the spectrometer. An energy resolution of less than 0.1 eV can be obtained by monochromating the primary beam, and thus makes the studies of detailed energy-loss structures and band gaps possible [23, 24].

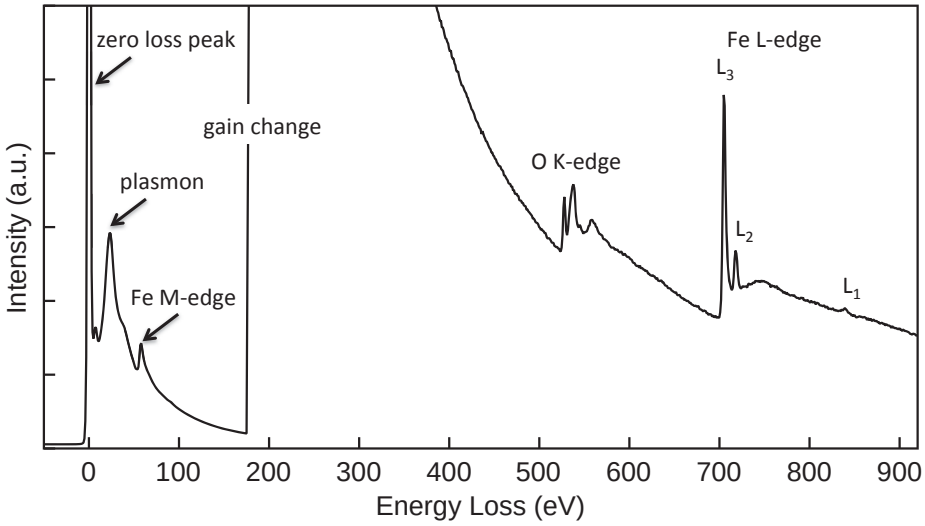

Figure 2.9 A typical EELS spectrum of Fe_2O_3 showing zero loss peak, plasmon, Fe M-edge, O K-edge, and Fe L-edge. Reproduced from reference [25].

The second dominant feature in Figure 2.9 is the plasmon peak, which occurs when incident electrons interact with the weakly bound electrons in the conduction or valence band and the energy range of plasmons is about 7 to 30 eV [25]. Following the plasmon peak are the features of Fe M-edge, O K-edge and Fe L-edges. These edges belong to the core-loss region of the

spectrum, which is above ~50 eV. The jump in intensity at characteristic energy losses is caused by the excitation of electrons at O K-, Fe L- and M- shells out of the atoms. In an EELS spectrum, some edges appear as sharp peaks, such as the Fe L_3- and L_2-edges in Figure 2.9. These edges are known as "white lines", which are typical features for the transition metals and rare-earth elements. The white lines arise because of the excitation of inner-shell electron from 2p (or 3d) state to unoccupied 3d (or 4f) state.

The background intensity drops rapidly as the energy loss increases in the EELS spectrum. There are several contributions to the background intensity, such as lower energy core excitations, plural scattering, Bremsstrahlung energy loss, spurious electron scattering in the spectrometer (detector noise) and so on. Though the reasons for the increase in background is complicated, the energy dependence of the background is usually found to follow a simple power law,

$$J(E) = Ae^{-r} \tag{2.15}$$

where *J(E)* is the intensity in the channel of energy loss *E*, and *A* and *r* are constants. For quantitative analysis, the background needs to be subtracted.

2.3.2 EELS quantitative analysis

As we mention in section 2.2, the quantification of EDX needs reference spectra to find the k factors and then determine the elemental compositions. However, the quantification of EELS can be performed within a single spectrum by measuring the intensities of the characteristic core-loss edges and knowing the partial ionisation cross-sections of the studied elements. In order to accurately measure the elemental concentration, it is crucial to separate the background reliably, for the core edge intensities are sensitive to the background subtraction.

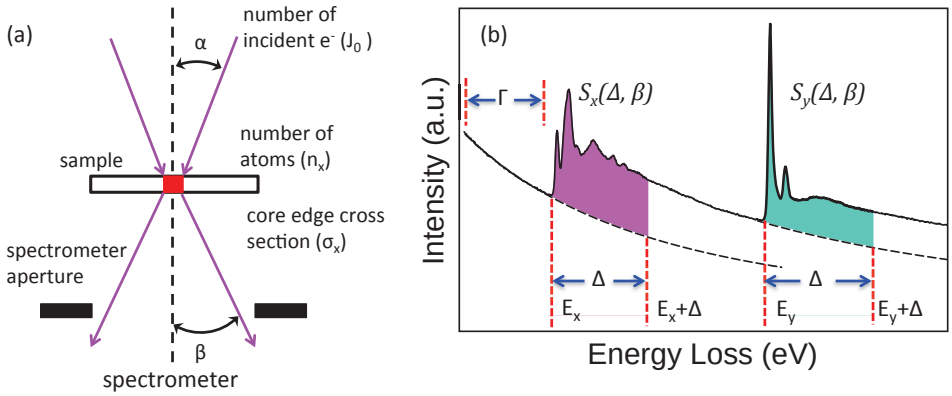

Figure 2.10 Definition of experimental parameters (a) and measured intensities for quantification. Reproduced from reference [25].

Two important parameters in EELS quantification are the probe convergence semi-angle (α) and the collection semi-angle (β) of the spectrometer, shown in Figure 2.10a. The intensity of the core-loss edge of element *x* can be written as follows [26],

$$S_x(\Delta,\beta) = J_0 n_x \sigma_x(\Delta,\beta) \tag{2.16}$$

where J_0 is the total number of incident electrons, n_x is the number of atoms per unit area and $\sigma_x(\Delta,\beta)$ is the partial ionisation cross-section per atom within an energy loss window of Δ and for the collection angles up to β. The definition of these symbols is shown in Figure 2.10a. J_0 is usually corrected as $J_1(\Delta,\beta)$, which is the integrated intensity of the zero- and low-loss electrons over an energy window Δ. This is because some electrons that have excited inner shells can be elastically scattered out of the spectrometer collection angle and other electrons may lose energy again by inelastic scattering and transfer outside the energy window Δ. So the equation (2.16) is modified as,

$$S_x(\Delta,\beta) = J_1(\Delta,\beta) n_x \sigma_x(\Delta,\beta) \tag{2.17}$$

Then the absolute number of atoms in an area of A is given by,

$$N_x = \frac{S_x(\Delta,\beta)A}{J_1(\Delta,\beta)\sigma_x(\Delta,\beta)} \tag{2.18}$$

Therefore, the atomic ratio of element x and y is given by,

$$\frac{N_x}{N_y} = \frac{S_x(\Delta,\beta)\sigma_y(\Delta,\beta)}{S_y(\Delta,\beta)\sigma_x(\Delta,\beta)} \tag{2.19}$$

The accuracy of this method is limited by the uncertainties in the ionisation cross-sections. In practice, it is necessary to accurately subtract the background and choose the signal windows Δ carefully. The background fitting window Γ is usually 10 - 30% of the edge energy, and the signal window Δ should be approximately 10% of the edge energy and also cover the near edge fine structure, hence about 40 – 60 eV. The plural scattering effects tend to be cancelled if the same size signal windows for all edges are used. Using the same edge type (K, L, M…) for quantification is helpful to minimise the cross-section errors.

2.3.3 Multiple linear least-square fitting

The conventional background fitting method would not work in the cases of quantifying difference spectra phases or severely overlapping core edges. The alternative approach is to fit reference spectra from standard samples using a multiple linear least-square fitting (MLLS) routine. The MLLS fitting program forms a model function consisting of a linear combination of specified spectra and then fits that model function to the unknown spectrum by adjusting the coefficients of each linear term to minimise the square deviation between the model and the studied spectrum. The model function is given by [26]

$$J(E) = Ae^{-r} + \sum_n B_n S_n(E) \tag{2.20}$$

The first term on the right of equation (2.20) represents background, $S_n(E)$ terms represent core-loss reference spectra, B_n terms are the scaling coefficients.

To perform MLLS fitting the unknown spectrum and standard spectra should be taken under the same conditions (aperture size, channel dispersion etc.). The energy scales of the spectra must be accurately calibrated first, and then the spectra are isolated by subtracting the background. MLLS fitting can be performed using the DigitalMicrograph software.

MLLS fitting is a very useful tool not only for the separation of overlapping edges, but also for chemical state identification, anisotropic studies and so on. In this thesis, MLLS fitting was used for oxidation state determination.

2.4 Summary and conclusions

In this chapter, I introduced some of the key components in a STEM to establish a basic understanding of how the STEM works. By contrast with a TEM imaging, STEM exploits Z-contrast imaging (HAADF imaging), which means that the image intensity is proportional to Z^n (and the number of atoms in a column). The HAADF images thus provide not only structural information, but also elemental contrast in a specimen. It is also easier to interpret a HAADF image than a TEM phase-contrast image, since the peaks in intensity in a TEM image might or might not imply the real location of atom columns. Since a STEM does not use imaging lenses to form images, the image resolution is then limited by the aberrations of the focused beam. Spherical aberration, chromatic aberration and astigmatism are the main sources of aberrations in an electron microscope. To reduce the spherical aberration, an aberration corrector is introduced. The working principal of a CEOS double hexapole aberration corrector has been discussed. EDX and EELS are two widely used approaches for chemical analysis. I reviewed the theories for the generation of characteristic signals and elemental quantification. Compared to EDX, EELS is particularly suitable for studying valence states and near edge structures because of the high-energy resolution that is possible.

References

[1] Tanaka, N. Scanning Transmission Electron Microscopy of Nanomaterials: Introduction, **2014**, 1-8.

[2] Nagayama, K.; Danev, R. Phase contrast electron microscopy: development of thin-film phase plates and biological applications. *Philos. Trans. R. Soc., B* **2008**, *363*, 2153-2162.

[3] Wang, Z. W.; Toikkanen, O.; Yin, F.; Li, Z. Y.; Quinn, B. M.; Palmer, R. E. Counting the Atoms in Supported, Monolayer-Protected Gold Clusters. *J. Am. Chem. Soc.* **2010**, *132*, 2854–2855.

[4] Lebeau, J. M.; Findlay, S. D.; Allen, L. J.; Stemmer, S. Standardless Atom Counting in Scanning Transmission Electron Microscopy. *Nano Lett.* **2010**, *10*, 4405–4408.

[5] Batson, P. E.; Dellby, N.; Krivanek, O. L. Sub-Ångstrom Resolution Using Aberration Corrected Electron Optics. *Nature* **2002**, *418*, 617–620.

[6] Hawkes, P. W.; Kasper, E. Principles of Electron Optics, Academic Press: London, **1989**.

[7] Williams, D. B.; Carter, C. B. Transmission Electron Microscopy: A Textbook for Materials Science, 2nd ed.; Springer: New York, **2009**.

[8] Tanaka, N.; Saitoh K. Scanning Transmission Electron Microscopy of Nanomaterials: Basics of STEM, **2014**, 41-108.

[9] Hsiao, C.; Kuo, S.; Lai, F.; Chen, W. Interfacial Atomic Structure Analysis at Sub-Angstrom Resolution Using Aberration- Corrected STEM. *Nanoscale Res. Lett.* **2014**, **9**, 578.

[10] Kirkland, A. I.; Meyer, R. R. " Indirect " High-Resolution Transmission Electron Microscopy : Aberration Measurement and Wavefunction Reconstruction. *Microsc. Microanal.* **2004**, *10*, 401–413.

[11] Scherzer, O. Sparische und chromatische Korrektur von Electronen-linsen. *Optik* **1947**, *2*, *114*–132.

[12] Krivanek O.L., Dellby N., Spence A.J., Camps R.A., and Brown L.M. (1997) “Aberration correction in the STEM”, in: Inst. Phys. Conf. Ser. 153 (Proceedings 1997 EMAG meeting) Ed. Rodenburg JM, 35

[13] Krivanek, O. L.; Dellby, N.; Lupini, A. R. Towards Sub-Å Electron Beams. *Ultramicroscopy* **1999**, *78*, 1-11

[14] Haider, M.; Uhlemann, S.; Schwan, E.; Rose, H.; Kabius, B.; Urban, K. Electron microscopy image enhanced. *Nature*, **1998**, *392*, 768-769.

[15] Sawada H. Scanning Transmission Electron Microscopy of Nanomaterials: Aberration Correction in STEM, **2014**, 283-305.

[16] Urban, K.; Kabius, B.; Haider, M.; Rose, H.; A Way to Higher Resolution : Spherical-Aberration Correction in a 200 kV Transmission Electron Microscope. *J. Electron Microsc.* **1999**, *48*, 821–826.

[17] Biskupek J.; Hartel P., Haider M.; Kaisera U. Effects of residual aberrations explored on single-walled carbon nanotubes. *Ultramicroscopy* **2012**, *116*, 1-7.

[18] Loretto, M.H. Electron Beam Analysis of Materials. New York ,1984.

[19] von Harrach, H.S.; Dona, P.; Freitag, B.; Soltau, H.; Niculae, A.; Rohde, M. An integrated Silicon Drift Detector System for FEI Schottky Field Emission Transmission Electron Microscopes. *Microsc. Microanal.* **2009**, *15*, 208-209.

[20] P. Schlossmacher, D. O. Klenov, B. Freitag, S.von Harrach, and A. Steinbach, Nanoscale Chemical Compositional Analysis with an Innovative S/TEM-EDX System, *Microscopy and Analysis (Nanotechnology Suppl.)*, **2010**, *24* , S5–S8.

[21] Ping Lu; L. Zhou; M.J. Kramer; D.J. Smith. Atomic-Scale Chemical Imaging and Quantification of Metallic Alloy Structures by Energy-Dispersive X-ray Spectroscopy. *Scientific Reports*, **2014**, *4*, 3945.

[22] Genc, A.; Kovarik, L.; Gu, M.; Cheng, H.; Plachinda, P.; Pullan, L.; Freitag, B.; Wang, C. Ultramicroscopy XEDS STEM Tomography for 3D Chemical Characterization of Nanoscale Particles. *Ultramicroscopy*, **2013**, *131*, 24–32.

[23] Krivanek, O. L.; Ursin, J. P.; Bacon, N. J.; Corbin, G. J.; Dellby, N.; Hrncirik, P.; Murfitt, M. F.; Own, C. S.; Szilagyi, Z. S. High-Energy-Resolution Monochromator for Aberration-Corrected Scanning Transmission Electron Microscopy/Electron Energy-Loss Spectroscopy. *Phil. Trans. R. Soc. A* **2009**, *367*, 3683–3697.

[24] Su, D.S.; Zandbergen, H.W.; Tiemeijer, P.C.; Kothleitner, G.; Hävecker, M.; Hébert, C.; Knop-Gericke, A.; Freitag, B.H.; Hofer, F.; Schlögl, R. High Resolution Eels Using Monochromator And High Performance Spectrometer: Comparison Of V_2O_5 ELNES with Nexafs And Band Structure Calculations. *Micron*. **2003**, *34*, 235–238

[25] B. Fultz, Transmission Electron Energy Loss Spectroscopy in Materials Science and the EELS Atlas. Wiley, Weinheim, 2004.

[26] Egerton, R. F. Electron Energy-Loss Spectroscopy in the Electron Microscope. Plenum, New York, 1996.

Chapter 3 Generation of Clusters in the Matrix Assembly Cluster Source

Feng Yin and William Terry constructed the cluster source system. I was involved in the preparation of the samples for STEM and collected and analysed the STEM data explored in this chapter. Some data in this work has been published in the paper *The Cluster Beam Route to Model Catalysts and beyond* (*Faraday Discuss.* 2016, 188, 39-56). Some text and figures are adapted from this paper.

3.1 Introduction to cluster sources

Nanomaterials have many potential applications in the fields of catalyst, biology, and new energies [1-3]. The performance of the nanomaterials is related to their size, shape, and composition (core-shell). A good control of these parameters is extremely important for the nanomaterial preparation strategies to optimise their performance. There are several commonly used chemical synthesis methods, such as chemical reduction of metal salt precursors, electrochemical synthesis, and decomposition of metal-surfactant complexes. Since "bare" nanoparticles are thermodynamically unstable in solution and tend to be aggregated, thus stabilizing agents, which absorb at the surface of the nanoparticles, are usually used to prevent agglomeration. The stabilizing agents can be polymers and thiols, which are also very important to control the size, shape and composition of the nanoparticles. However, the attachment of ligands may block the active sites. The stabilizer-ligands can be removed by thermal and oxidative treatments [4, 5], but this would lead to extensive changes in the size and morphology of the nanoparticles.

The other approach is the physical strategy, such as evaporation, magnetron sputtering, and cluster beam technique. Comparing to the chemical synthesis methods, there are several advantages for the physical methods. First, stabilisers are not used during the synthesising procedure, and the active sites can be preserved [6]. Second, the size of the nanoparticles can be selected with a mass filter even to single atom precision [7, 8]. Third, the landing energy of the particles can be tuned to have a different impact on the support. The particles can either be impregnated or soft-landed.

Cluster beam sources were developed in the early 1980s, and with the coupling of mass selection techniques, magic numbers in metal and rare gas clusters were discovered [9,10]. After over 30 years development, different types of cluster beam source have designed, such as seeded supersonic nozzle source [11], gas-aggregation cluster source [12], laser vaporization cluster source [13], sputtering source [14] and magnetron plasma sputtering and gas condensation source [8] etc. The beam current for these cluster sources ranges from a few tens of picoamperes to about tens of nanoamperes [15]. The maximum beam current after mass selection could be as high as tens of picoamperes under optimal conditions for some materials, which means that the production rate of clusters (containing a few hundred atoms) is in the scale of microgram per hour. This is not sufficient for catalysis or medical studies.

To scale up the production rate of clusters for industry and commercial applications, a matrix assembly cluster source (MACS) was developed by the Palmer group [16,17, 6]. In this cluster source, a copper TEM grid (400 mesh) was cooled down to about 15 K by a liquid helium cryostat. A metal loaded rare gas matrix was then formed on the copper grid by exposing the grid in the metal vapour (Au, Ag) and Ar (or CO_2 [17]) gas

atmosphere. An ion gun was then used to sputter the matrix in a perpendicular direction to the matrix (transmission mode) to generate clusters. It is believed that the incident ions will enhance the rate of metal-metal atom collisions in the matrix and transfer energies to the clusters to fly out of the matrix. The mechanism of MACS is different from a sputtering source [14], which sputters clusters out of a target directly. A sputtering efficiency (the number of clusters produced per argon ion incident) of ~3% was obtained, indicating great potential for scaling up cluster production by orders of magnitude.

In this chapter, a reflection mode MACS (the clusters were collected in a reflected direction) was developed. The effects of the incident angle of the ion beam, collection angle of the cluster flux and metal loading in the matrix on the clusters size and flux were studied.

3.2 Experimental details

In order to increase the production of clusters in a cluster source, the reflection mode MACS is proposed and designed to demonstrate the possibility of scaling up the cluster beam flux. The principle of MACS is shown in figure 3.1. In this source, a matrix support (cold finger, a copper plate) is cooled to a low temperature (less than 20K) by liquid helium. The inert gas atoms (Ar) and vaporized metal atoms (Ag) flies onto the cold finger and will be co-condensed and form a matrix. A high-energy ion beam is then used to sputter the matrix at a specific incident angle (α) and clusters are bombarded out and collected in a direction of reflection (β).

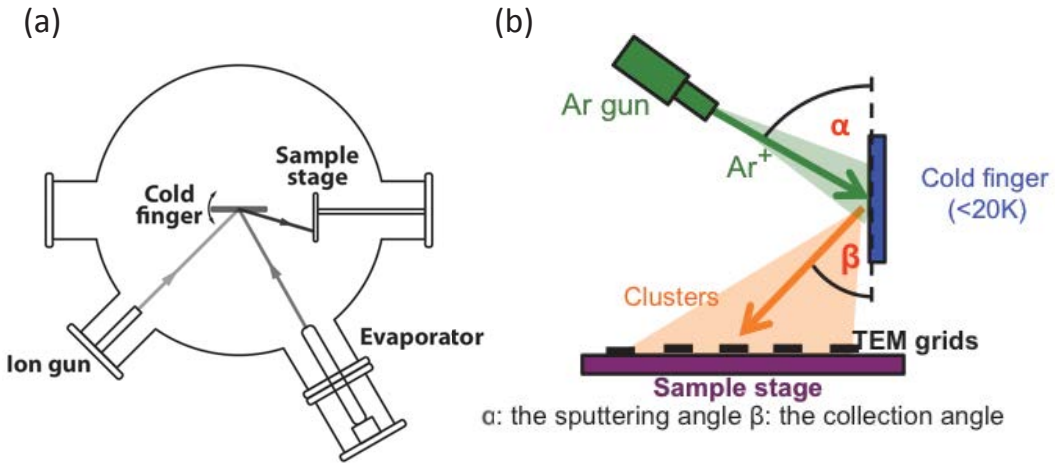

Figure 3.1 (a) A schematic of the reflection MACS instruments. Ion gun, evaporator, sample stage and cold finger (a copper plate) are indicated. (b) A schematic of the principle of the MACS. α and β are the sputtering angle of Ar^+ beam and collecting angle of the cluster beam. Reproduced from reference [6].

The cluster production process is performed in a vacuum chamber pumped down by a turbo pump. The cold finger (a copper plate, 15 × 40 mm) is mounted on a copper pillar and cooled down by liquid helium. A cryogenic temperature monitor with a temperature range of 0.1 K to 420 K is used to monitor the temperature of the matrix. The cold finger is connected to a picoammeter to record the sputtering current from the ion beam. The position of cold finger is adjusted through a XYZ sample manipulator and a rotary platform is used to rotate the cold finger to specific angles.

A sample stage is designed to collect the reflection cluster beam. Eight slots were drilled on the surface of the sample holder to mount TEM grids. The distances between each slot are different, in this way, clusters that fly out at different reflection angles are collected. The sample holder is grounded to avoid charge accumulation. The shaft of the

sample holder is mounted on a sample manipulator to adjust the distance between the sample holder and the centre of the cold finger. The distance between the centre of the cold finger and surface of the sample stage is 12.5 mm when producing clusters.

The metal material (Ag) is evaporated by an effusion cell and the evaporation rate is monitored with a quartz crystal microbalance (QCM) by putting it at the position of the cold finger. Inert gas (Ar) flows into the chamber through a leak valve; the growth rate of inert gas atoms on the cold finger is controlled by keeping the chamber pressure at $\sim 5\times10^{-6}$ torr, which is about 2 layer/s (calculated from the ideal gas equation). The dosing time for Ar gas and Ag vapour mixture is 200s.

Ion beam source (Omicron ISE-5) is mounted on the side of the chamber with an angle of 120° with respect to the axis of the sample holder. They are all aligned with the cold finger. The spot size of the Ar+ ion beam generated from the ion source is ~40 mm in diameter. The current sputtering on the matrix is read from a picoammeter. The current used during the sputtering process is kept at around 10 μA and the ion energy is set to 2.5 keV. Since the ion beam sputters the matrix at a specific angle, part of the Ar+ ions would sputter the back of the cold finger, which has no contribution to the cluster yield. The current received at the front side and backside of the cold finger was measured at the same time by inserting a thin insolating plate between the cold finger and another metal sheet that connected to a picoammeter. The sputtering process is performed at a pressure of 9.6×10^{-7} torr. In order to get rid of the effect of the ion beam fluctuation, we keep the charge sputtered on the cold finger at a constant (2.2×10^{-4} C) and the sputtering time is recorded. The prepared samples were kept in the load lock in a high vacuum before imaging.

The prepared samples were imaged in in a STEM (JEOL 2100F) equipped with a CEOS spherical aberration corrector. HAADF images were acquired with the inner and outer collection angles of 62 and outer 164 mrad, at the camera length of 10 cm. The probe convergence angle is 19 mrad. Cluster size and density were measured from the HAADF images.

3.3 Results and discussion

3.3.1 Effect of collection angle

Figure 3.2 shows the HAADF images (left) of Ag clusters collected at different collection angles when the incident angle of the Ar ion beam is 10°. The corresponding size distributions of the clusters are also presented in Figure 3.2 (on the right side). The size of clusters spans the range from ~50 to over 5000 atoms and the main peak positions in the size distribution shift a little when the collection angles changes, and the size peaks are at about 200 to 400 atoms. The main proportion (over 65%) of the clusters contains 150 to 450 atoms; as the cluster size increases the number of large clusters decreases rapidly.

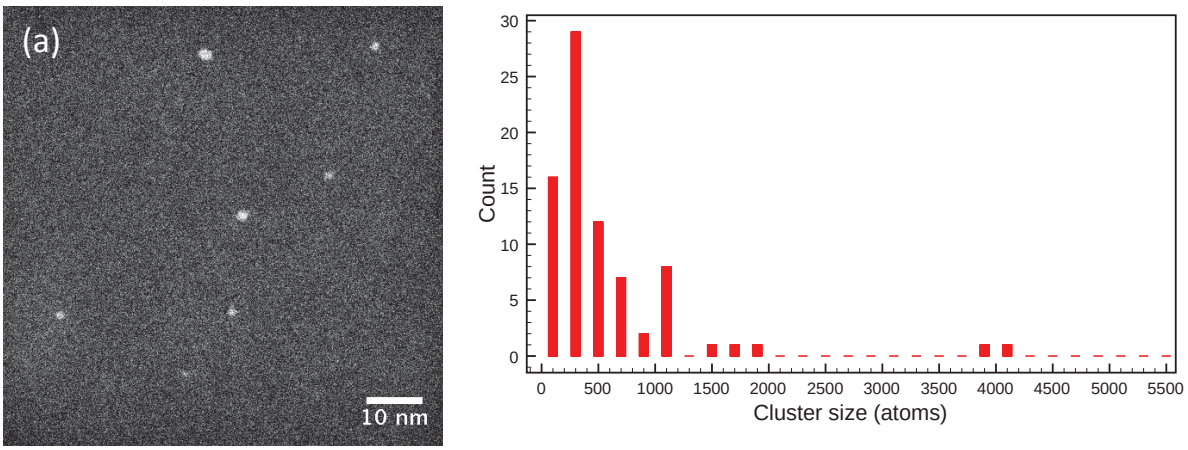

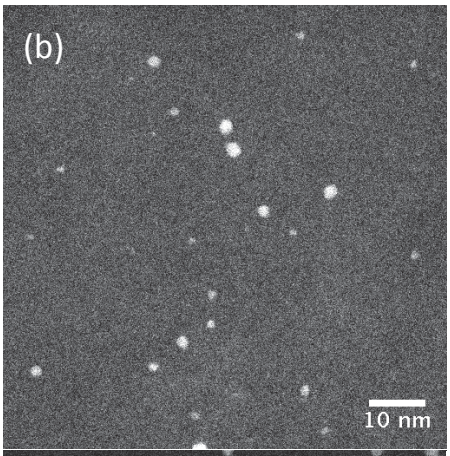
(b)
10 nm

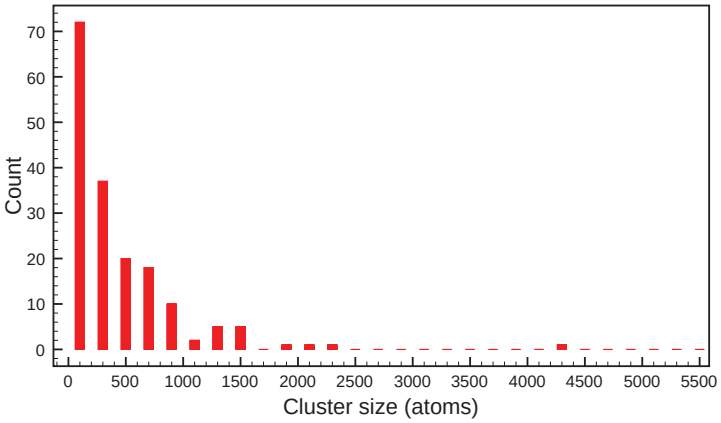
Count
Cluster size (atoms)

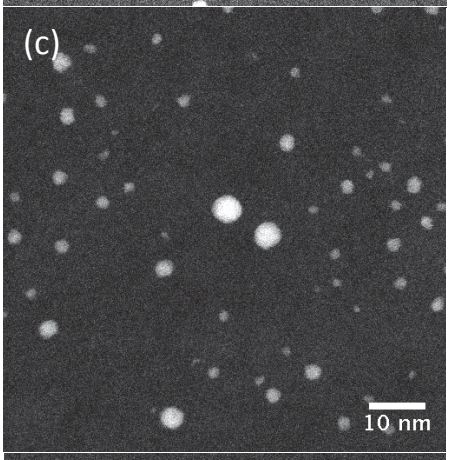
(c)
10 nm

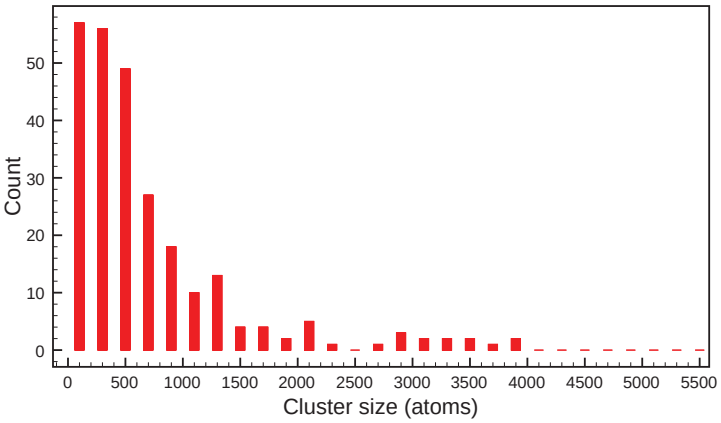
Count
Cluster size (atoms)

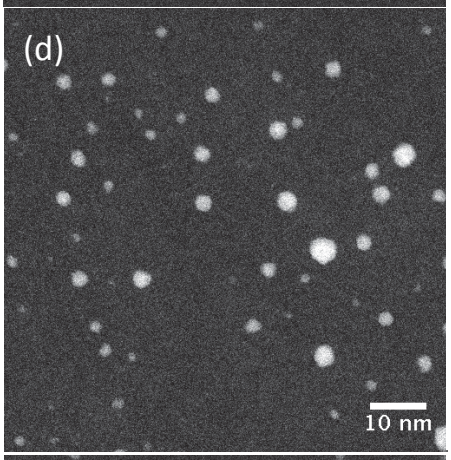
(d)
10 nm

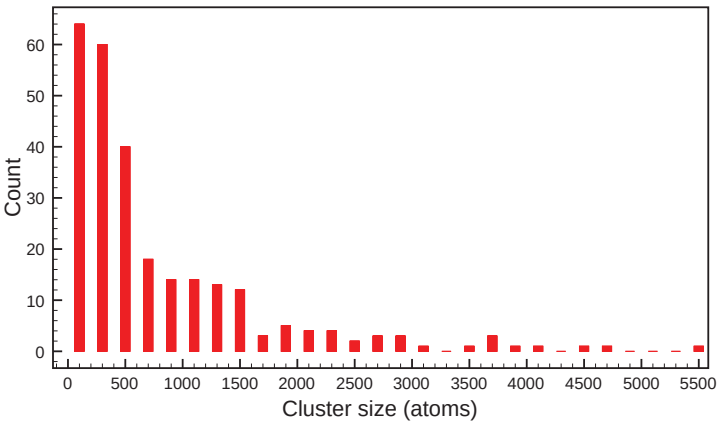
Count
Cluster size (atoms)

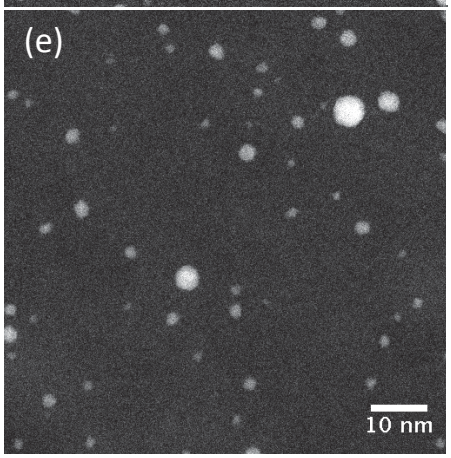
(e)
10 nm

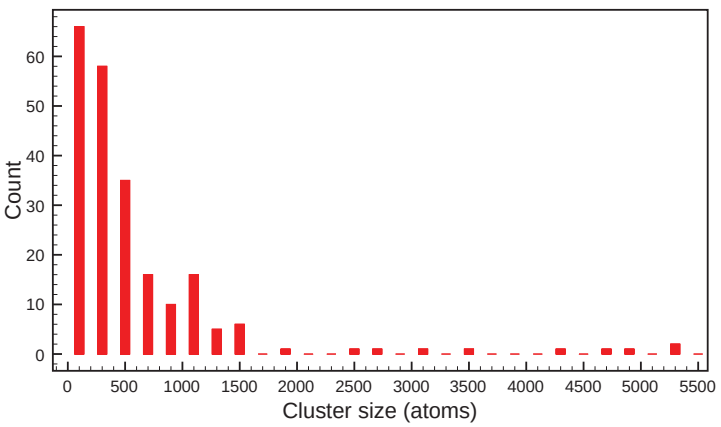
Count
Cluster size (atoms)

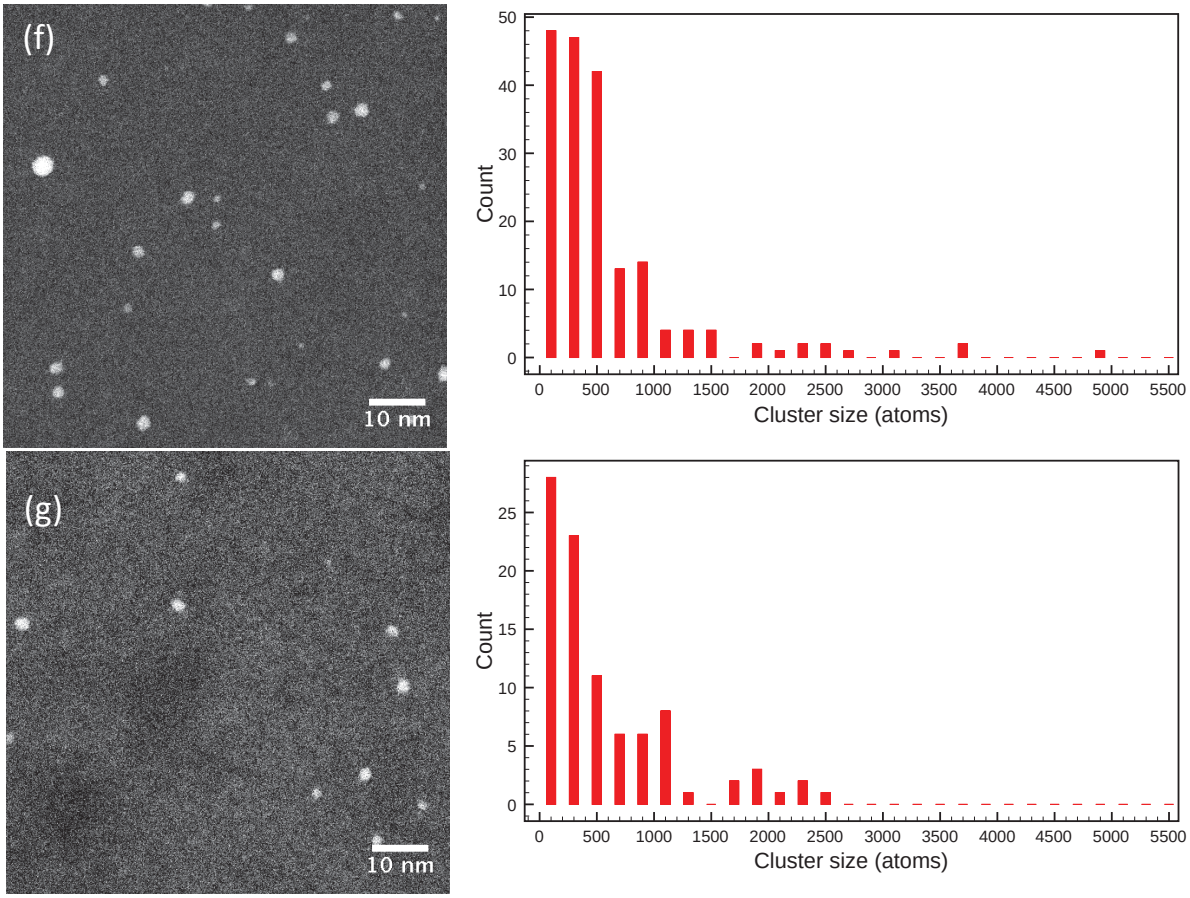

Figure 3.2 Examples of HAADF images of Ag clusters produced in the reflection mode MACS (left) at different collection angles of (a) 8.2°, (b) 24.6°, (c) 43.6°, (d) 62.1°, (e) 78.3°, (f) 91.2°, and (g) 101.4°. The corresponding size distributions of the clusters are presented on the right. The vacuum of the chamber during matrix formation is 5×10^{-6} torr, and the Ag deposition rate is 0.05 Å/s, therefore, the metal loading is ~0.8%. The incident angle of the Ar ion is 10° with respect to the surface of the cold finger, and the ion energy is 2.5 keV.

The diagram of cluster flux against collection angle is given in Figure 3.3(a), and the error is calculated from the standard derivation. As we can see that the cluster flux varies a lot as the collection angle changes and is maximised at an angle of ~62°, which is about 5.2 nA/cm^2 by assuming that each cluster is singly charged. No cluster is

collected when β is larger than 110°. Since the clusters are sputtered out of the matrix by the incident ion beam, it's worthy to know the sputtering yield of the MACS, which is the number of clusters produced per argon ion. In order to calculate the intrinsic efficiency of the ion beam, the cluster beam profile is drawn in Figure 3.3(b). We assumed that the number of clusters sputtered out from the matrix is isotropic and that the amount of clusters collected from the bottom and upper sides of the matrix is half of that collected in the center of the matrix and decreases linearly.

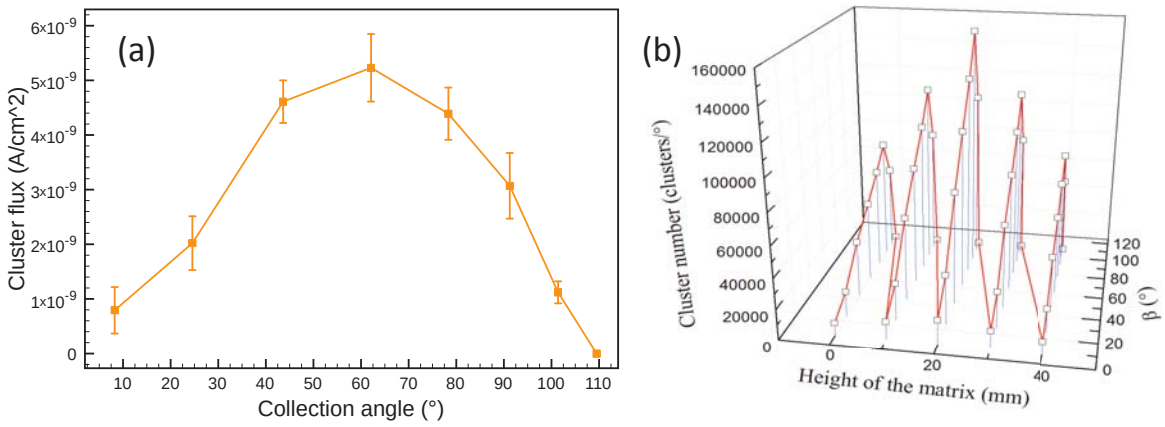

Figure 3.3 (a) Diagram of cluster flux against the collection angle; (b) cluster beam profile.

The integrated number of clusters is ~5.2×10^{12}, equals to ~28 nA. The sputtering current on the cold finger is ~6.9 μA (calculated from the total charge and sputtering time). About 47.7% of the Ar^+ ions were found to sputter the front side, which means real sputtering current is ~3.2 μA. Thus, the cluster yield from the ion beam is close to 1%. In principal, the efficiency estimated here implies that a cluster beam current equivalent to 20 mA can be reached, if an ion beam source with a current up to 2 A is

used (a powerful cooling system is therefore needed, because of the huge amount of energy injected).

3.3.2 Effect of incident angle

In order to find the optimal sputtering angle and to have a good knowledge of the cluster formation mechanism, we studied the effect of incident angles of the ion beam on the cluster flux. The incident angle of the ion beam is adjusted by rotating the cold finger with a rotary platform. The clusters were prepared under the same dosing and sputtering conditions, and only the incident angle is changed.

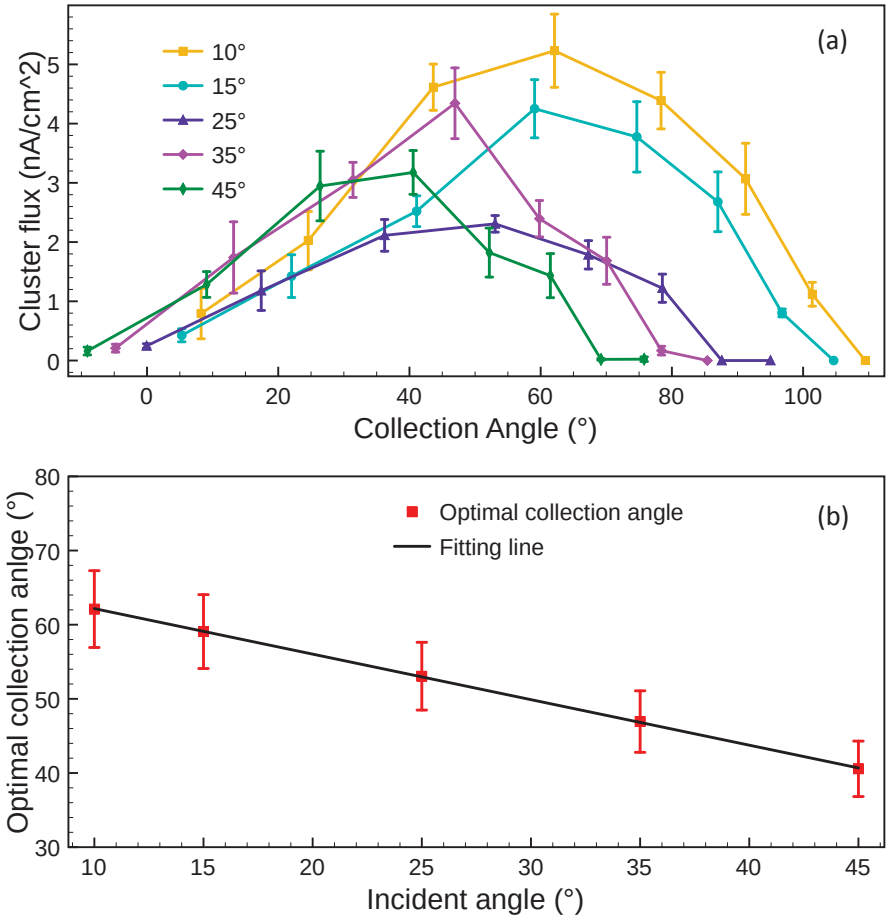

Figure 3.4 (a) Cluster flux against collection angle with incident angle at 10°, 15°, 25°, 35°, and 45°; (b) The relationship between the optimal collection angle and incident angles.

Figure 3.4(a) shows the cluster flux versus collection angles with the incident angle changes from 10° to 45°. As we can see that the maximum cluster flux tends to decrease as the incident angle increases. This may be accounted for the maximum momentum transfer of the ion beam at a smaller incident angle, thus more clusters are sputtered out. The optimal collection angle, where the cluster flux is the highest, shifts to smaller angles as the incident angle increases. Figure 3.4(b) shows the relationship between the optimal collection angle and the incident angles, demonstrating that the optimal collection angle decreases linearly as the incident angle increases. The angle between the incident ion beam and the maximum cluster beam is almost constant, which is close to 110°.

The cluster flux at incident angle of 25° is lower than that at the angle of 35°. This might because of that the evaporated metal gas forms a conductive metal film on the insulating layer, which is used to protect the ion beam from sputtering the metal shaft. When the isolating layer and the shaft are conductively connected, the Ar ions sputtered on the insulating layer were also recorded. Thus the total charge collected on the copper support is less than expected and cluster flux is a bit lower.

Figure 3.5 shows the size distributions of the samples prepared at different sputtering angles. The cluster size distributions are very similar to each other and the main peaks of the cluster size are at about 200 to 400 atoms. The size distribution is relatively narrow, since over 80% of the clusters are in the range of tens to one thousand atoms, which is about 1 to 3 nm in diameter. Worthy noting that both the incident and collection angles have little effect on the cluster size distribution, but will affect the cluster flux.

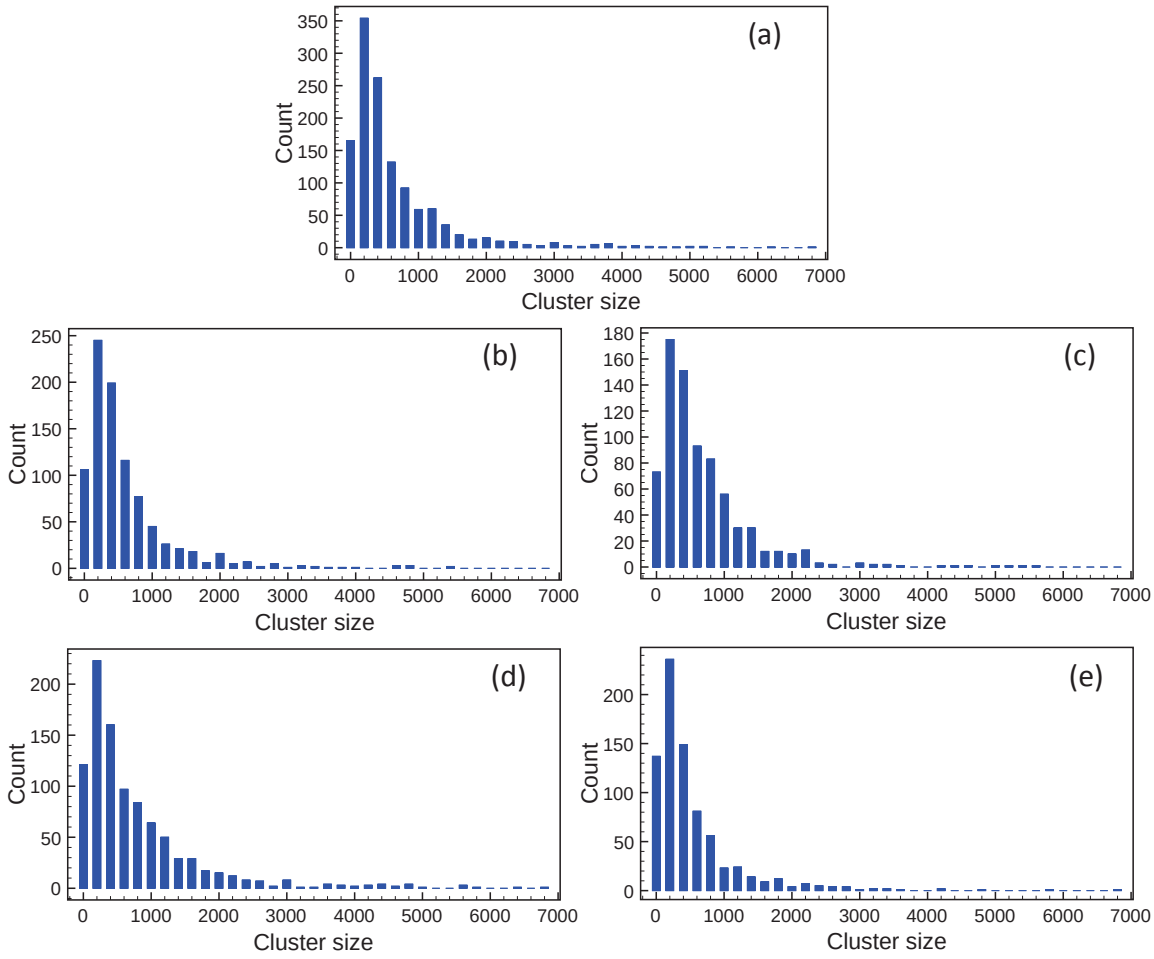

Figure 3.5 Cluster size distribution at incident angle of (a) 10°; (b) 15°; (c) 25°; (d) 35°; and (e) 45°.

The principle of MACS is sputtering clusters out of a matrix, which is different from the traditional sputtering cluster sources. In a sputtering source, a target of cluster material is sputtered by heavy high-energy ions. Katakuse et al [14] and Fayet et al [18] produced Ag, Cu and Pt clusters using a 10 to 30 keV xenon ion beam. The produced clusters are relatively small containing only a few tens of atoms and the cluster flux tails off exponentially with cluster size. The exact mechanism for the sputtering source is unclear. In the MACS, the diffusion of metal atoms was expected to be slowed down in the cold matrix and metal-metal collision was then enhanced by the ion bombardment

[16]. Therefore, we can produce relatively large clusters with hundreds to thousands of atoms. The cluster size could be determined by the mixing state of Ag and Ar in the matrix and the incident ion energy. In the transmission mode MACS [16], it has been found that the cluster size increase rapidly as the metal concentration in the matrix increases. The structure of the Ag/Ar matrix is not clear in this work. However, some literature mentioned that the structure of metal/rare-gas composite is an admixture of hexagonal close packing (HCP) and FCC structures [19] and that the variation of metal concentration does affects the mixing state of the matrix [20].

3.3.3 Effect of metal concentration

The key procedure for producing cluster in MACS is forming the metal and inert gas co-condensed matrix. In this section, we studied the effect of metal concentration in the matrix. The matrix formation time was kept at the same, but the metal evaporation rate was changed by adjusting the evaporation temperatures. Three batches of samples were prepared at evaporation rates of 0.01 Å/s (1200 °C), 0.05 Å/s (1260°C), 0.3 Å/s (1360 °C) and the corresponding Ag concentrations in the matrix are about 0.37%, 0.80% and 3.56%.

The cluster flux produced with different metal concentration matrix is given in Figure 3.6(a). The cluster fluxes drops a lot when the Ag concentration increases to 3.56%. But the cluster flux is possibly underestimated, since small clusters containing a few atoms are observed at high magnification (inset of the Figure 3.6b). The cluster flux profile and size distribution (Figure 3.5 and 3.6e) of the two samples produced with Ag concentrations of 0.37% and 0.80% are very close to each other. This is probably

because of that the sputtering condition and the matrix structure (the mixing state of the Ag and Ar atoms) are very similar.

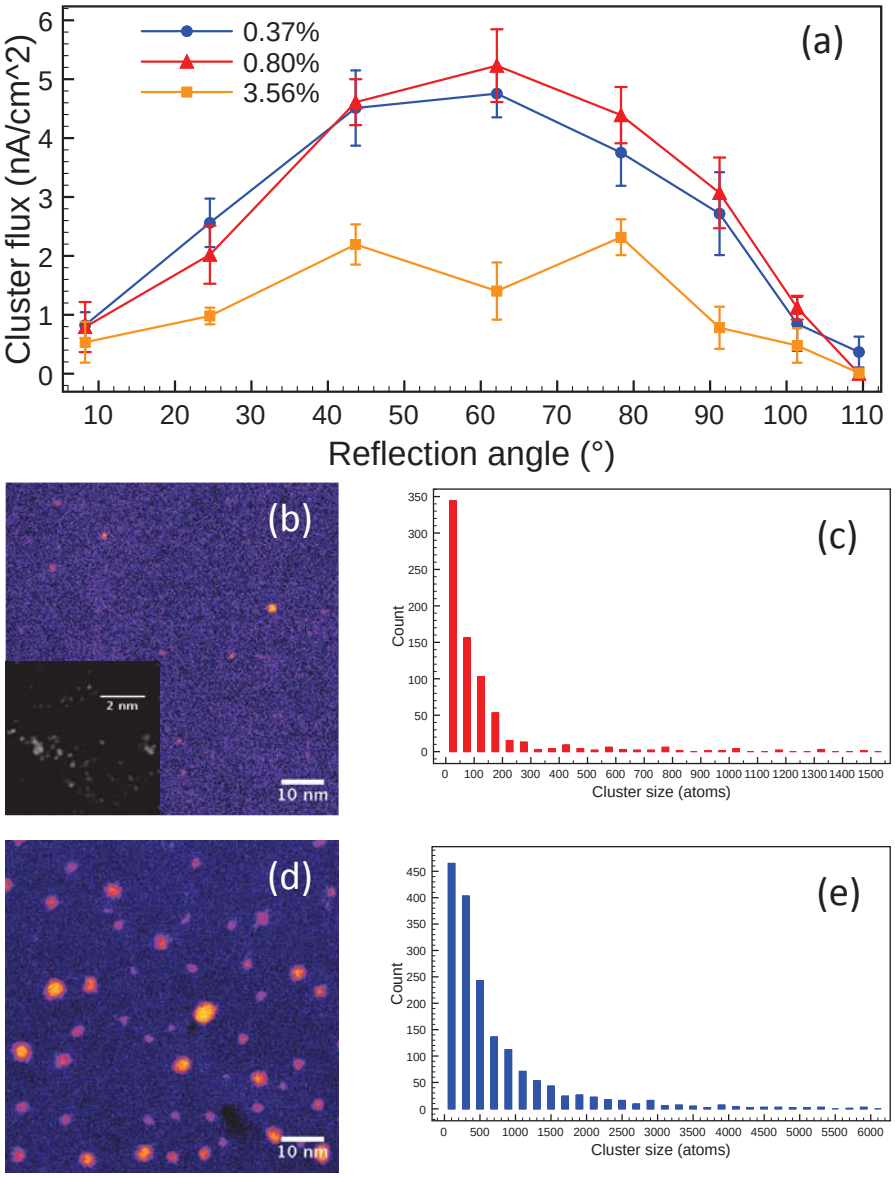

Figure 3.6 Cluster flux produced with different Ag concentration (a), and HAADF images and size distribution histograms of clusters produced with Ag concentrations of 3.56% (b, c) and 0.37% (d, e). The inset of (b) is a high magnification HAADF image.

Figure 3.6 (b) and (d) are the HAADF images of the sample produced with Ag concentrations of 3.56% and 0.37%, and the corresponding size distribution histograms

are shown in Figure 3.6 (c) and (e), respectively. The cluster size decreases a lot when the metal concentration in the matrix increases to 3.56%. The main peak of the cluster size occurs at ~50 atoms and most of the clusters are less than 300 atoms. This may be caused by the changing of the matrix structure. For a higher metal loading, a higher evaporation temperature (1360 °C) was applied. Fast Ag evaporation rate and high thermal radiation onto the matrix could increase the temperature of the matrix and form large clusters or even Ag film on the cold finger. If so, the sputtering of the matrix is more like a sputtering source and only small clusters can be produced.

3.4 Summary and Conclusions

In this chapter, I reported the characterisation of clusters produced by a new type of cluster source, in which Ag clusters were produced by sputtering a matrix formed by co-condensing Ar and evaporated Ag onto a liquid Helium cooled copper plate. An integrated cluster flux of 28 nA was obtained when the incident angle of the ion beam was 10° with respect to the copper plate, and the sputtering yield is nearly 1%. This implies that the cluster flux could be potentially scaled up to milliamps, which would be a massive enhancement over the presently available sources. We also studied the parameters that may affect the cluster flux and sizes. The results show that the cluster flux will drop when the incident angle of the ion beam increases. The highest cluster flux was obtained when the incident angle is 10°. The clusters were collected at different collection angles and the cluster density was maximised at a specific collection angle. This collection angle has a linear relationship with the incident angle. The angle between the incident ion beam and the cluster flux was found to be approximately constant at about 110°. The cluster size distribution showed little change when the incident angle and collection angle varies. The main peak of the cluster size distribution

is at about 200 to 400 atoms. But when the metal loading in the matrix increases from about 0.8% to 3.6%, the peak of cluster size distribution shifts to about 50 atoms. This maybe because of that the structure or mixing state of the matrix is very different from that when the metal loading is low.

For the further improvement of the MACS, there are still several important problems one needs to solve. Firstly, what is the mechanism of the cluster formation? A better understanding of the mechanism can help us to increase the efficiency and have a better control of the produced clusters. Secondly, how to collect the clusters when the cluster flux is enhanced to milliamps? In that case, the deposition rate will be very high and the produced clusters will form a thin film in a few seconds. Additionally, the surfaces of clusters produced in the cluster source are unprotected, so they will tend to aggregate. Therefore, it is also very important to find a way to protect the clusters from agglomeration. Thirdly, how to optimise the configuration of the cold finger is important in decreasing the material loss during the matrix formation and maximising the utilisation of the incident ions during the sputtering. To answer these questions, studies of ion-induced photoluminescence, molecule dynamic simulation, and multilayer deposition system coupled to a high current ion gun have all been or currently being undertaken in the group.

Reference

[1] Hu, K. J.; Plant, S. R.; Ellis, P. R.; Brown, C. M.; Palmer, R. E. Atomic Resolution Observation of a Size-Dependent Change in the Ripening Modes of Mass-Selected Au Nanoclusters Involved in CO Oxidation. *J. Am. Chem. Soc.* **2015**, *137*, 15161–15168.

[2] Salata, O. V. Applications of Nanoparticles in Biology and Medicine. *J. Nanobiotechnology* **2014**, *2*, 3.

[3] Chen, X.; Li, C.; Grätzel, M.; K. Robert.; Mao, S. S. Nanomaterials for Renewable Energy Production and Storage. *Chem. Soc. Rev.* **2012**, *41*, 7909-7937.

[4] Jia, C.J.; Schuth, F. Colloidal Metal Nanoparticles as A Component of Designed Catalyst. *Phys. Chem. Chem. Phys*. **2011**, *13*, 2457-2487.

[5] Lopez-Sanchez, J.A.; Dimitratos, N.; Hammond, C.; et al. Facile Removal of Stabilizer-Ligands from Supported Gold Nanoparticles. *Nature Chem.* **2011**, *3*, 551-556.

[6] Ellis, P.; Brown, C. M.; Bishop, P. T.; Yin, J.; Cooke, K.; Terry, W. D.; Liu, J.; Yin, F.; Palmer, R. E. The Cluster Beam Route to Model Catalysts and Beyond. *Faraday Discuss.* **2016**, *188*, 39-56.

[7] von Issendorff, B.; Palmer, R. E. A New High Transmission Infinite Range Mass Selector for Cluster and Nanoparticle Beams. *Rev. Sci. Instrum.* **1999**, *70*, 4497–4501.

[8] Pratontep, S.; Carroll, S. J.; Xirouchaki, C.; Streun, M.; Palmer, R. E. Size-Selected Cluster Beam Source Based on Radio Frequency Magnetron Plasma Sputtering and Gas Condensation, *Rev. Sci. Instrum.* **2005**, *76*, 045103.

[9] Clemenger, K.; Heer, W. A. De; Saunders, W. A. Electronic Shell Structure and Abundances of Sodium Clusters. *Phys. Rev. Lett.* **1984**, *52*, 2141–2143.

[10] Echt, O.; Sattler, K.; Recknagel, E. Magic Numbers for Sphere Packings: Experimental Verification in Free Xenon Clusters. Phys. Rev. Lett. **1981**, *47*, 1121–1124.

[11] Kappes, M.M.; Kunz, R.W.; Schumacher, E. Production of Large Sodium Clusters (Na_x, $x \leqslant 65$) by Seeded Beam Expansions. *Chem. Phys. Lett.* **1982**, *91*, 413-418.

[12] Sattler, K.; Mühlbach, J.; Recknagel E. Generation of Metal Clusters Containing from 2 to 500 Atoms, *Phys. Rev. Lett.* **1980**, *45*, 821-824.

[13] Heath, J. R.; Liu, Y.; O'Brien, S. C.; Zhang, Q.; Curl, R. F.; Tittel, F. K.; Smalley, R. E. Semiconductor Cluster Beams: One and Two Color Ionization Studies of Si_x and Ge_x. *J. Chem. Phys.* **1985**, *83*, 5520-5526.

[14] Katakuse, I.; Ichihara, T.; Fujita, Y.; Matsuo, T.; Sakurai, T.; Matsuda H. Mass Distributions of Copper, Silver and Gold Clusters and Electronic Shell Structure. Int. J. Mass Spectrom. *Ion Processes* **1985**, *67*, 229–236.

[15] Heer, W. A. The Physics of Simple Metal Clusters: Experimental Aspects and Simple Models. *Rev. Mod. Phys.* **1993**, *65*, 611-676.

[16] Palmer, R. E.; Cao, L.; Yin, F. Note: Proof of Principle of A New Type of Cluster Beam Source with Potential for Scale-up. *Rev. Sci. Instrum.* **2016**, *87*, 046103.

[17] Oiko, V. T. A.; Mathieu, T.; Cao, L.; Liu, J.; Palmer, R. E. Production of Silver Nanoclusters Using A Matrix-Assembly Cluster Source with A Solid CO_2 Matrix. *J. Chem. Phys*. **2016**, *145*, 166101.

[18] Fayet, P.; Patthey, F.; Roy, H.V.; Detzel, T.; Schneider, W.D. Electronic Structure of Supported Mass-Selected Transition Metal Clusters: A Photoemission Study. *Surface Science* **1992**, *270*, 1101–1108.

[19] Schwentner, N.; Koch, E. E.; Jortner, J. Electronic Excitation in Condensed Rare Gases, Springer Tracts in Modern Physics, Berlin, Springer, **1986**.

[20] Phelps, D. J.; Avci, R.; Flynn, C. P. Metal-Insulator Transition in Metal—Rare-Gas Alloys. *Phys. Rev. Lett.* **1975**, *14*, 5279-5288.

Chapter 4 Exploring the Atomic Structure of 1.8 nm Monolayer-Protected Gold Clusters with Aberration-Corrected STEM

The two $Au_{144}(SR)_{60}$ samples were provide by Prof. Hannu Häkkinen from the University of Jyväskylä, and Prof. Amala Dass from the University of Mississippi. The synthesis and mass spectra of the two samples were conducted by these two groups separately. The STEM HAADF imaging and analysis were performed by me. This work has been published in the paper *Exploring the Atomic Structure of 1.8 nm Monolayer-Protected Gold Clusters with Aberration-Corrected STEM* (*Ultramicroscopy*, 2016, doi: 10.1016/j.ultramic.2016.11.021). Most of the text and figures used are from this paper.

4.1 Introduction to $Au_{144}(SR)_{60}$ clusters

Monolayer-protected (MP) noble metal clusters are attracting considerable interest because of the appearance of magic numbers, which account for the stability of certain sizes, and their applications in bio-imaging, catalysis, sensors and so on [1-4]. It is a key factor to determine the full atomic structure of these MP clusters in understanding their physical and chemical properties in depth. For certain thiolated clusters, single crystal X-ray crystallography has provided reliable details of both the inner gold-core structures and the Au-S ligand units. To date the MP clusters identified by this method are $Au_{25}(SR)_{18}$ [5-7], $Au_{28}(SR)_{20}$ [8], $Au_{36}(SR)_{24}$ [9], $Au_{38}(SR)_{24}$ [10], $Au_{102}(SR)_{44}$ [11], $Au_{130}(SR)_{50}$ [12], and $Au_{133}(SR)_{52}$ [13, 14]. In the case of clusters of nominal composition $Au_{144}(SR)_{60}$, the determination of an ordered atomic structure with single crystal X-ray diffraction has so far proved unsuccessful, even though several research groups have

obtained crystals [15-17]. This might be because the core and/or ligand layers of the clusters are amorphous [41], and/or because the crystals contain clusters of different sizes, for there are reports of many species of closely related composition, such as $Au_{144}(SR)_{59}$ [18], $Au_{146}(SR)_{59}$ [19], $Au_{137}(SR)_{56}$ [20, 21] etc. Recently, nominally $Au_{144}(SR)_{60}$ clusters doped with other metals (Ag [22-26], Pd [27], and Cu [28, 29]) have attracted attention due to their electronic and optical properties. Understanding of the $Au_{144}(SR)_{60}$ cluster is naturally of importance for further studies of these bimetallic clusters.

A theoretical structure for $Au_{144}(SR)_{60}$ was predicted by Lopez-Acevedo et al. [30] in 2009, and was composed of a chiral icosahedral Au_{114} core and 30 linear $Au(SR)_2$ units. Experimental studies by large angle X-ray diffraction (LA-XRD) [31, 32] extended X-ray absorption fine structure (EXAFS) [33] and ^1H NMR [34] techniques showed indirect evidence of agreement with the proposed model. Nevertheless, the failure of single crystal X-ray experiments means that the precise structure of $Au_{144}(SR)_{60}$ remains unresolved.

Structure determination of MP Au clusters by electron microscopy is valuable, since it does not require the growth of high quality single crystals needed for single crystal X-ray crystallography. Nanobeam electron diffraction combined with HAADF-STEM imaging was employed to determine the structure of nominally $Au_{144}(SR)_{60}$ [35] and $Au_{130}(SR)_{50}$ [36] clusters by the Yacaman and Whetten group. The experimental diffraction patterns and HAADF images show agreement with the predicted models [30, 37] in the case of specific individual clusters, but some other information, such as the cluster size distribution, percentage of clusters that fit the predicted model, and

proportion of unidentified structures, is not given. Bruma et al [38] proposed a method of using scanning nanobeam diffraction to determine the structure of MP Au clusters ($Au_{102}(SR)_{44}$). They also reported the effect of electron beam damage of the clusters and found that the structure of thiolated clusters could be modified after a few seconds. Azubel et al [39] determined the structure of a MP Au_{68} cluster at atomic resolution by using low electron dose (~800 $e^-/Å^2$) TEM together with three-dimensional reconstruction of hundreds of TEM images. The advantage of this method, adapted from biological studies, is that the atomic structure of a MP Au cluster can in principle be revealed without any prior knowledge or fitting to model structures. However, this requires that the MP Au clusters should be homogeneous both in structure and size. Statistical investigations of both cluster size and structure by HAADF-STEM have been reported by the Birmingham group, in the case of the MP Au_{38}, MP Au_{40} and MP Au_{55} clusters [40 - 43]. These experiments yielded the cluster nuclearity, aspect ratio, fluxionality and, in the case of MP Au_{55} [43], evidence that the atomic structure matches the theoretical prediction for one isolated size fraction.

Here I report a statistical investigation of nominally $Au_{144}(SR)_{60}$ clusters, synthesised independently by two different groups. The atom counting technique is used to determine the range of cluster sizes in the specimen, and the atomic structures are explored by comparison with multislice simulations of different model structures. We find a very small fraction of clusters (~3%) match the theoretically predicted $Au_{144}(SR)_{60}$ structure [30], while a large proportion of the clusters are amorphous (i.e. did not match any model structure). However, 20% of these clusters are found to exhibit ring-dot features in the atomic images, which is an indication of local icosahedral symmetry.

4.2 Experimental details

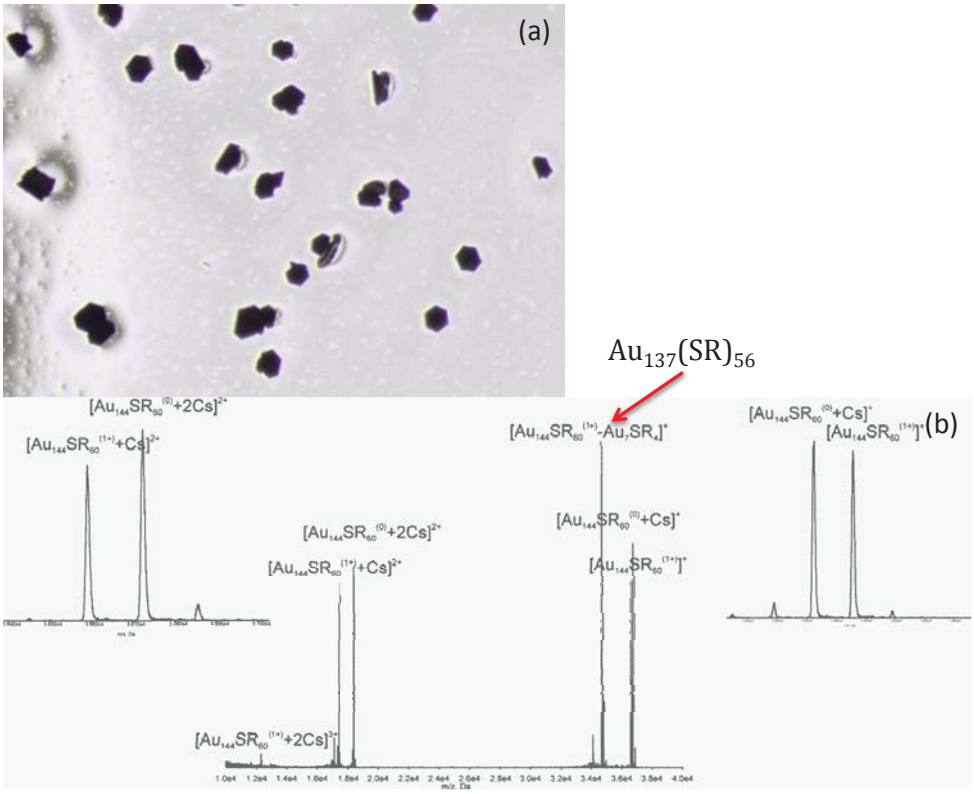

Figure 4.1 (a) Light microscopy image of recrystallized $Au_{144}(PET)_{60}$ clusters from toluene-acetonitrile solvent system showing black plate crystals. The average size of the crystals was approximately 0.050 – 0.100 mm in diameter. (b) ESI-TOF mass spectrum measured from the synthesised clusters (reproduced from ref45). The red arrow indicates the peak of clusters with a composition of $Au_{137}(SR)_{56}$. From reference [44].

The $Au_{144}(SR)_{60}$ (SR stands for 2-phenylethanethiol (PET) ligand) clusters were provided by the group of Prof. H. Häkkinen (University of Jyväskylä, Finland) and the group of Prof. A. Dass (University of Mississippi, USA), respectively. The standard synthesis method and ESI mass spectrum of $Au_{144}(SR)_{60}$ clusters from Finland were reported in ref 45 . The as-prepared clusters were additionally purified by recrystallization from toluene-acetonitrile solvent system. The clusters were sent to Birmingham in crystal form. Figure 4.1(a) shows a light microscopy image of the

recrystallized $Au_{144}(SR)_{60}$ clusters. The crystals are in a hexagonal shape and the diameter of the crystals is approximately 0.050 – 0.100 mm. Figure 4.1(b) is the ESI-TOF mass spectrum measured from the synthesised clusters, in which $Au_{144}(SR)_{60}$ was observed to produce peaks having different charge states and addition of Cs^+ ions. Products of $Au_{137}(SR)_{56}$ was also observed with a high intensity as indicated with a red arrow, which means that different size clusters may be contained in the crystals.

The synthesis method of $Au_{144}(SR)_{60}$ clusters prepared in USA was given as follows. The first step was the synthesis of crude product that contains a wide range of Au cluster sizes. The second step was the etching of the crude product with excess thiol, and the third step was cluster fractionation; both these steps aimed to narrow the size distribution.

Step 1: 30 mL $HAuCl_4$ aqueous solution was mixed with tetraoctylammonium bromide (TOABr) toluene solution (1.1 mmol, 30 mL) and was stirred for 30 min at room temperature. Phenylethane thiol (10 mmol) was then added and stirred for another 30 min. This solution was cooled in ice bath and an aqueous solution of $NaBH_4$ (20 mmol, 20 mL) was rapidly added to the solution under vigorous stirring. After 3 h, the organic layer was extracted and evaporated to dryness. Excess thiol, TOABr and other by-products in the product were washed with methanol. The residual mixture was separated with toluene. Smaller clusters (7–10 kDa) were excluded by acetonitrile (CH_3CN) extraction.

Step 2: The CH_3CN insoluble portion was dissolved in toluene and etched with excess phenylethane thiol at 80 °C under stirring. After 1 day, the reaction was stopped and

washed with methanol to remove excess thiol and the product extracted with toluene. Step 3: The product was then dissolved in toluene and subjected to solvent fractionation using CH_3CN. Several solvent fractionations were performed to remove small clusters such as $Au_{38}(SR)_{24}$.

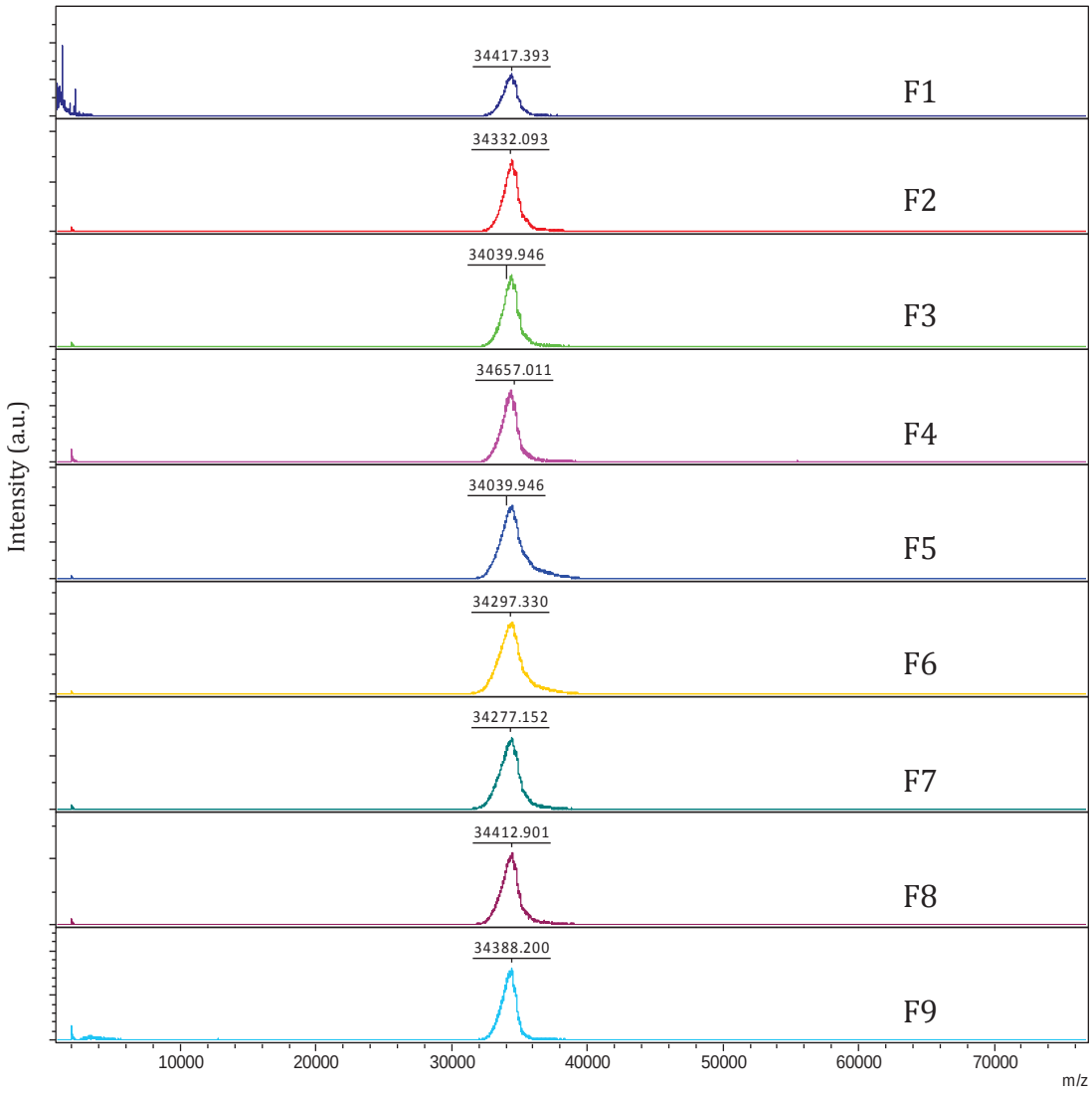

Figure 4.2 MALDI mass spectra of the synthesised clusters after the second SEC process. Fraction F4 and F5 was sent to the University of Birmingham and F5 was used for STEM analysis. From reference [44].

The product so obtained was subjected to further purification using size exclusion chromatography (SEC). Two SEC purifications were performed in THF (0.30 mL).

Several fractions were collected. The resulting product isolated was as characterised by MALDI mass spectra shown in Figure 4.2. The sample F4 and F5 was sent to Birmingham in powder form and F5 was used for STEM imaging. The peak positions of the clusters in the MALDI mass spectra are smaller than the mass of $Au_{144}(SR)_{60}$, which is about 36.6 kDa. The cluster size calculated from the given mass of F5 is 131 ± 6 Au atoms assuming sixty (SCH_2CH_2Ph) ligands attached.

Both of the samples were dissolved in toluene and drop cast onto a TEM grid covered with an amorphous carbon film for further STEM analysis. HAADF-STEM imaging was performed in a 200 kV JEM2100F STEM (JEOL) with spherical aberration corrector (CEOS). HAADF images were acquired with inner and outer detector angles of 62 and 164 mrad (camera length of 10 cm), and probe convergence angle of 19 mrad. The scanning time for each frame was ~2.6 seconds and the electron dose was 7.9×10^4 $e^-/Å^2$/frame.

The QSTEM software package [46] was utilised to simulate the HAADF images of candidate structures for comparison The parameters used in the image simulation are as follow: spherical aberration (C_s) is 1 μm and defocus (C_1) is -19 Å. The acceleration voltage, probe convergence angle, and detector inner and outer collecting angles are the same as described above. The simulation atlases are presented in detail in the Appendix. The structural identification of the MP Au clusters was then performed by comparing the experimental images with multislice simulations. Even clusters of a single isomer deposited on the carbon film of a TEM grid would have random orientations and thus present a variety of projection patterns in HAADF-STEM images. Therefore, a "simulation atlas" which covers the full range of orientations was calculated for each

candidate cluster structure investigated. Considering the experimental size range of the clusters in Figure 1b, models of $Au_{102}(SR)_{44}$ [11], $Au_{130}(SR)_{50}$ [37], $Au_{133}(SR)_{52}$ [14], and $Au_{144}(SR)_{60}$ [30] were chosen for comparison with the experimental images. These cluster models have either been theoretically proposed [37, 30] or experimentally measured [11, 14]. Figure 2 shows some examples of simulations based on the models.

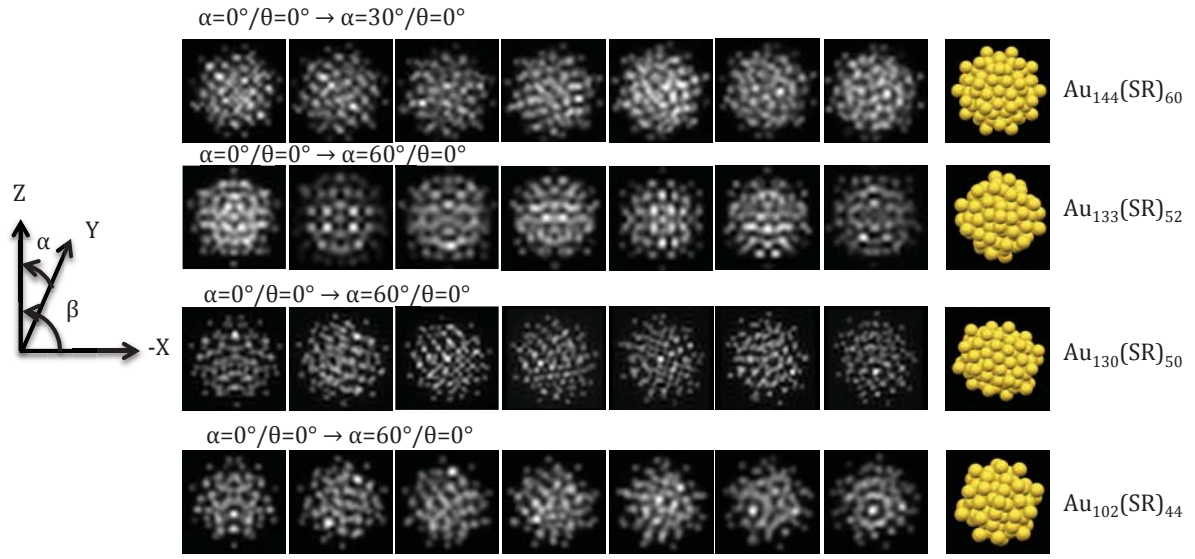

Figure 4.3 Atomic models and multislice simulations examples of $Au_{144}(SR)_{60}$, $Au_{133}(SR)_{52}$, $Au_{130}(SR)_{50}$ and $Au_{102}(SR)_{44}$. The ligands are not shown. From reference [44].

4.3 Results and discussion

4.3.1 Crystallised "$Au_{144}(SR)_{60}$" sample

In STEM *Z*- (atomic number) contrast images, the HAADF intensity of an atom is proportional to Z^n, where n= 1.46 ± 0.18 according to our previous calibration [47], therefore, the HAADF intensity contributed by the nominal sixty (SCH_2CH_2Ph) ligands is equivalent to 17.9 ± 7.6 Au atoms. The Au core size (i.e. the total number of Au atoms including any in the $Au(SR)_2$ staples) is then derived on the assumption (for

convenience) that every MP cluster has sixty ligands. Single Au atoms are ejected by purposely scanning of a cluster for an extended time; an example of a HAADF-STEM image containing these reference single atoms is shown in Figure 4.4a. The integrated HAADF intensity of Au single atoms and undamaged MP clusters are shown in Figure 4.4b and 4.4c. The corresponding diameter distribution of the MP Au clusters is shown in Figure 4.4d; the average diameter of the clusters is 1.8 ± 0.1 nm.

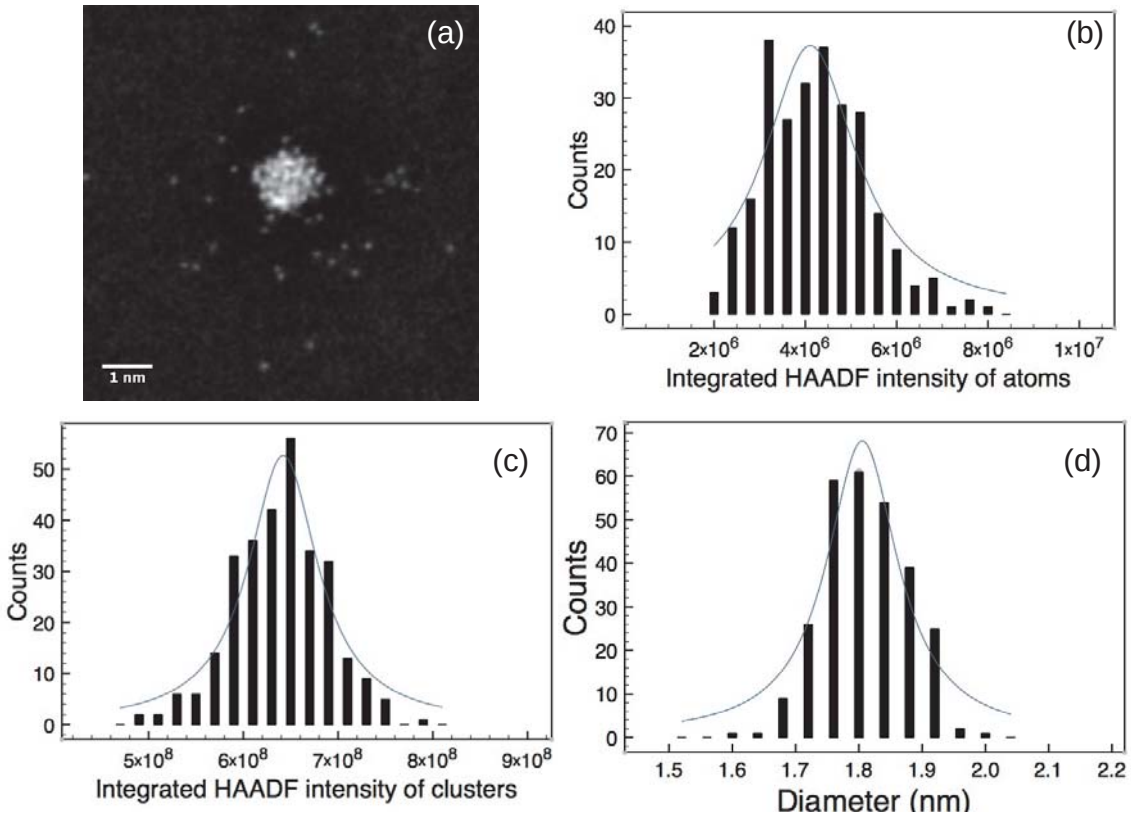

Figure 4.4 (a) An example HAADF image of "$Au_{144}(SR)_{60}$" clusters; (b) HAADF intensity distribution of "$Au_{144}(SR)_{60}$" clusters. (c) Integrated HAADF intensity of single atoms; (d) Diameter distribution of the clusters. The average diameter is 1.8 ± 0.1 nm. From reference [44].

Au atom numbers in the MP Au clusters were calibrated with the intensity of Au single atoms from this atom counting approach and the resulting histogram of Au core size is presented in Figure 4.5. As we can see that the average size of the MP clusters is 137 ±

11 Au atoms, rather than 144. The size distribution is broad and for the purpose of illustration (only), we also show in Figure 4.5 a multiple Gaussian fit with three peaks at 128 ± 7, 137 ± 2 and 144 ± 9. The fit is chosen because it is compatible with the electrospray ionisation (ESI) mass spectrum in Figure 4.1b (ref [45]), in which both $Au_{144}(SR)_{60}$ and $Au_{137}(SR)_{56}$ peaks are identified. The existence of clusters at the peak of 128, may be because of losing a number of $Au_4(SR)_4$ fragments, which was observed in the collision induced dissociation studies [48, 49]. The size distribution of Figure 4.5 indicates that the sample synthesised contains different size clusters, although it can still form crystals. This may well explain why well-defined single crystal X-ray diffraction patterns have not been obtained for nominal $Au_{144}(SR)_{60}$ single crystals.

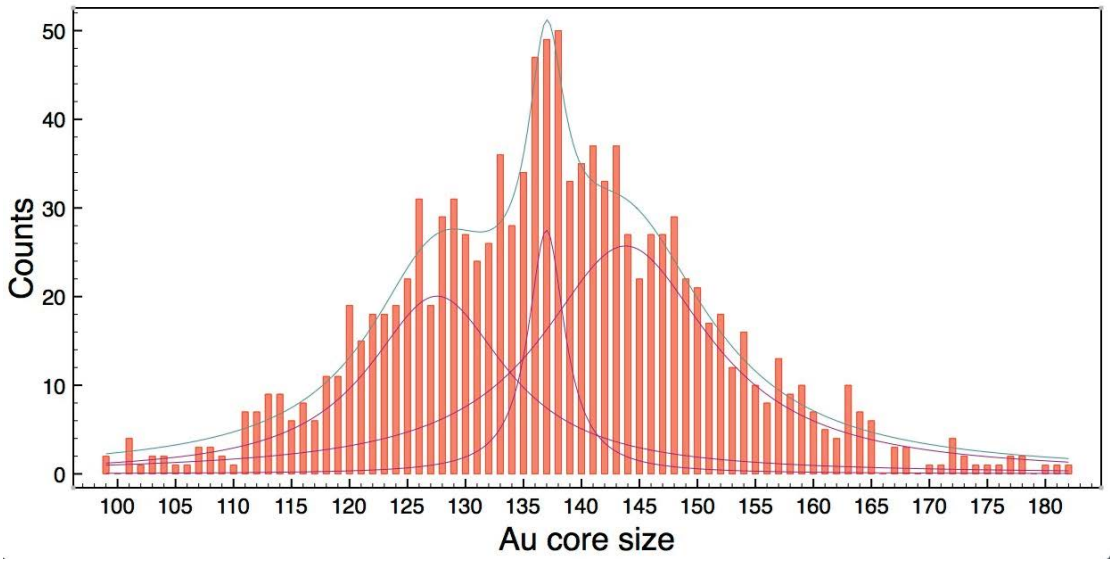

Figure 4.5 Au core size for the MP Au clusters calibrated with HAADF intensity of single atoms by assuming that each cluster has sixty ligands. From reference [44].

The comparison with the simulations was carried out for 849 experimental cluster images. This systematic investigation demonstrates that only about 3% of the clusters match the predicted $Au_{144}(SR)_{60}$ structure [30]. (Even if we restrict analysis to clusters in

the size fraction 139 to 149 Au atoms, only 4% of the experimental images match the theoretical structure.) The fraction of images, which matches the other models, is even lower. Idealised bare Au_{147} (no ligands) clusters with icosahedral, decahedral and face-centred cubic structures were also used for comparison. They are not explicit in the thesis because of the low match to the simulations and the fact that they were not ligand-protected. Figures 4.6(a-d) show some examples of HAADF-STEM images of the MP Au clusters that are found to fit the $Au_{144}(SR)_{60}$ simulations. As we can see that the main motif in these clusters (ring-dot or straight line features) is in line with the simulations (including the location of the motif). However, the matches between experiment and simulation are not perfect at the detailed level.

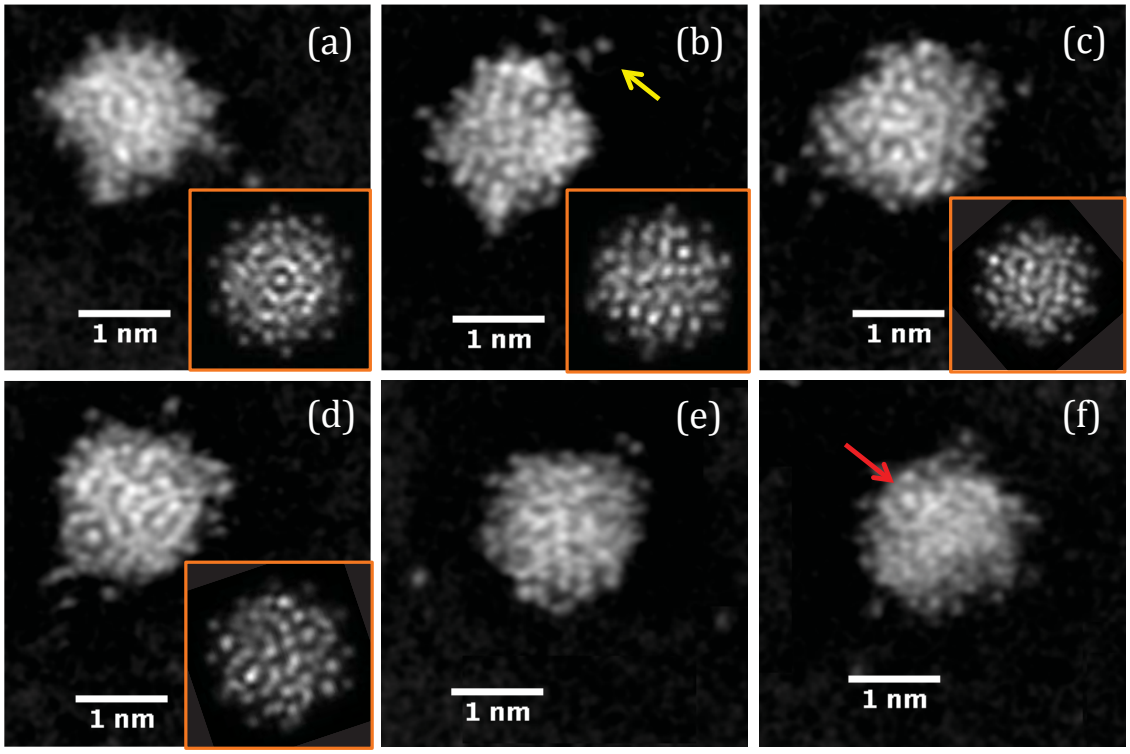

Figure 4.6 (a-f) are HAADF-STEM images of MP Au clusters. (a-d) are MP Au clusters found to be similar to the $Au_{144}(SR)_{60}$ model. Examples of ejected atoms are indicated by a yellow arrow. The insets are the corresponding simulations along the orientations of

(a) α=40°, β=70°; (b) α=20°, β=50°; (c) α=15°, β=20°; (d) α=10°, β=30°. (e) An example of unidentified cluster and (f) a cluster with a ring-dot feature (indicated by the red arrow). From reference [44].

This deviation may arise because of the instability of the clusters, at the atomic level, under the electron beam irradiation. Firstly, radiation-induced atom diffusion [50] may cause atom smearing during image acquisition. Secondly, the surface structure of thiolated clusters is expected to be sensitive to the state of the ligands [51, 52], so any radiation damage to the ligands may induce cluster structure modification. Thirdly, less strongly bound Au atoms can be ejected during a normal imaging scan, as we observe individual atoms a few angstroms away from the cluster (indicated by the yellow arrow in Figure 3b). However, our previous study on MP Au_{55} [43] clusters found that over 40% of the cluster images matched the simulations. Thus we think that the electron beam has a limited effect on the core structure of the clusters. Additionally, the $Au_{144}(SR)_{60}$ cluster may have several possible isomeric structures of similar energy. Tian et al. [53] showed two isomers of $Au_{38}(SR)_{24}$ and the less stable isomer transformed irreversibly to the more stable isomer when heated to 50 °C. These four reasons may explain the imperfect detailed match between experimental and simulated cluster structure, even in generally well-matched cases. Most of the cluster images were found to be amorphous (Figure 4.6e). However, amongst these clusters, we found that a good proportion (~20%) of clusters presented ring-dot features, as highlighted in Figure 4.6f.

4.3.2 Powder "$Au_{144}(SR)_{60}$" sample

To check the generality of our result, in addition to the MP Au cluster crystals from Jyväskylä, we also explored a batch of nominally $Au_{144}(SR)_{60}$ clusters (with ligands of

SCH_2CH_2Ph) synthesised by the group of Prof. A. Dass of the University of Mississippi. The HAADF-STEM imaging conditions employed for these powder samples were the same as the sample described above. An example of high-resolution HAADF image of powder form "$Au_{144}(SR)_{60}$" clusters is shown in Figure 4.7a and the measured average diameter of clusters is 1.8 ± 0.1 nm (Figure 4.7b), which is the same as the sample prepared by the group in Finland. The cluster size derived from the peak in the MALDI spectrum (F5 in Figure 4.2) is 131 ± 6 Au atoms assuming sixty (SCH_2CH_2Ph) ligands attached.

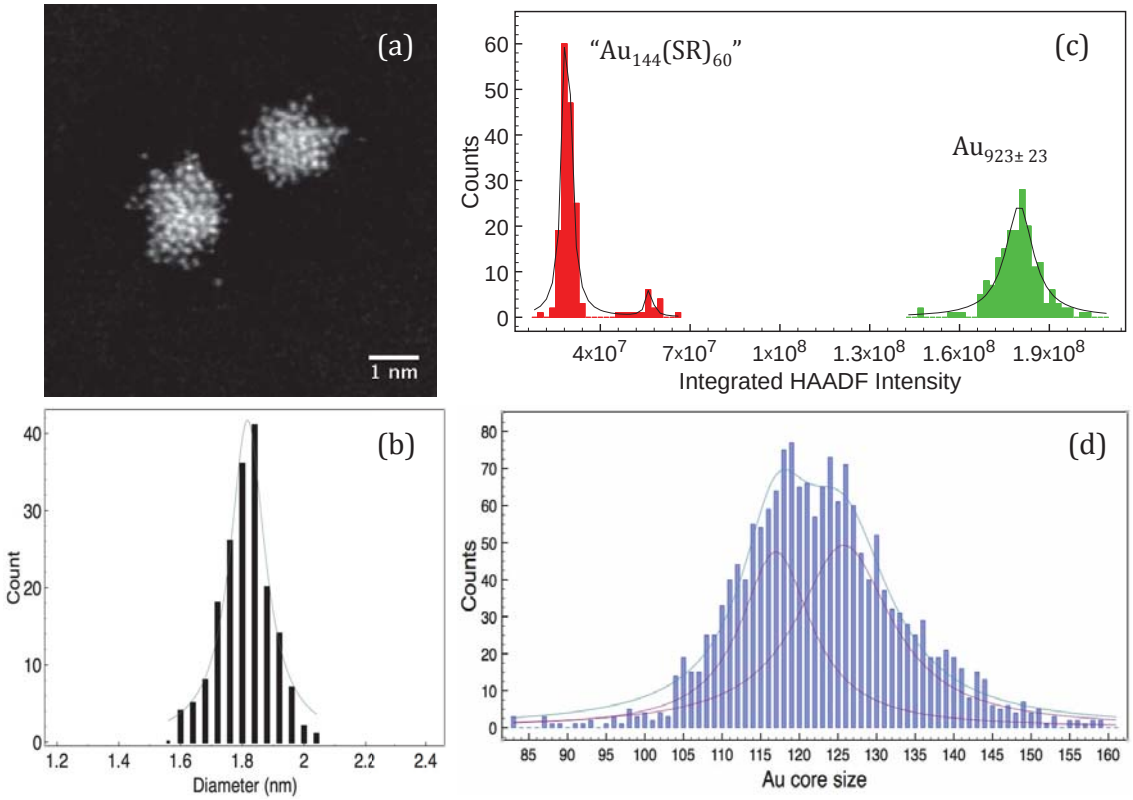

Figure 4.7 (a) An example of HAADF image of "$Au_{144}(SR)_{60}$" clusters; (b) Diameter distribution of the clusters. The average diameter is 1.8 ± 0.1 nm. (c) The integrated HAADF intensity of "$Au_{144}(SR)_{60}$" and size-selected $Au_{923\pm23}$ clusters (923±23 Au atoms). (d) Au core size distribution calibrated with HAADF intensity of $Au_{923\pm23}$ clusters by assuming that each cluster has sixty (SCH_2CH_2Ph) ligands. From reference [44].

Sized-selected $Au_{923\pm23}$ clusters were utilised as a mass balance to count the atom number of the "$Au_{144}(SR)_{60}$" clusters. The clusters were dissolved in toluene and drop cast onto half of a TEM grid covered with an amorphous carbon film. The other half of the TEM grid contained pre-deposited size-selected $Au_{923\pm23}$ clusters, which were generated in a magnetron sputtering, gas condensation cluster source with a lateral time-of-flight (TOF) mass selector [54, 55]. Figure 4.7c shows the integrated HAADF intensity of "$Au_{144}(SR)_{60}$" and $Au_{923\pm23}$ clusters, and the deviated Au core size distribution histogram is shown in Figure 4.7d. As we can see in Figure 4d, there is a slight discrepancy between the mean nuclearity of the MP Au clusters derived from our STEM atom counting method (122 ± 9) and the peak of the MALDI-MS spectrum (131 ± 6), but it is notable that the error bars do overlap. One possible cause of the offset could be that the integrated HAADF intensity of size-selected $Au_{923\pm23}$ clusters may be overestimated because of electron multi-scattering and channelling effect. However, the fitting peaks at 117 ± 6 and 126 ± 8 indicate that the sample is not pure $Au_{144}(SR)_{60}$ clusters, but a mixture of different sizes.

The structure identification was performed in the whole size range, and some comparison examples are presented in Figure 4.8. Figure 4.8a-d are the HAADF images of the clusters that are found similar to the simulations of the $Au_{144}(SR)_{60}$ model (shown in the insets). About 7% of the clusters are found match the predicted $Au_{144}(SR)_{60}$ model simulations. The percentage is slightly higher than that obtained from the sample prepared in Finland, but still over 90% of the clusters are unidentified or amorphous (Figure 4.8e). Additional to the fit to the $Au_{144}(SR)_{60}$ models, about 30% of the clusters exhibit a ring-dot feature.

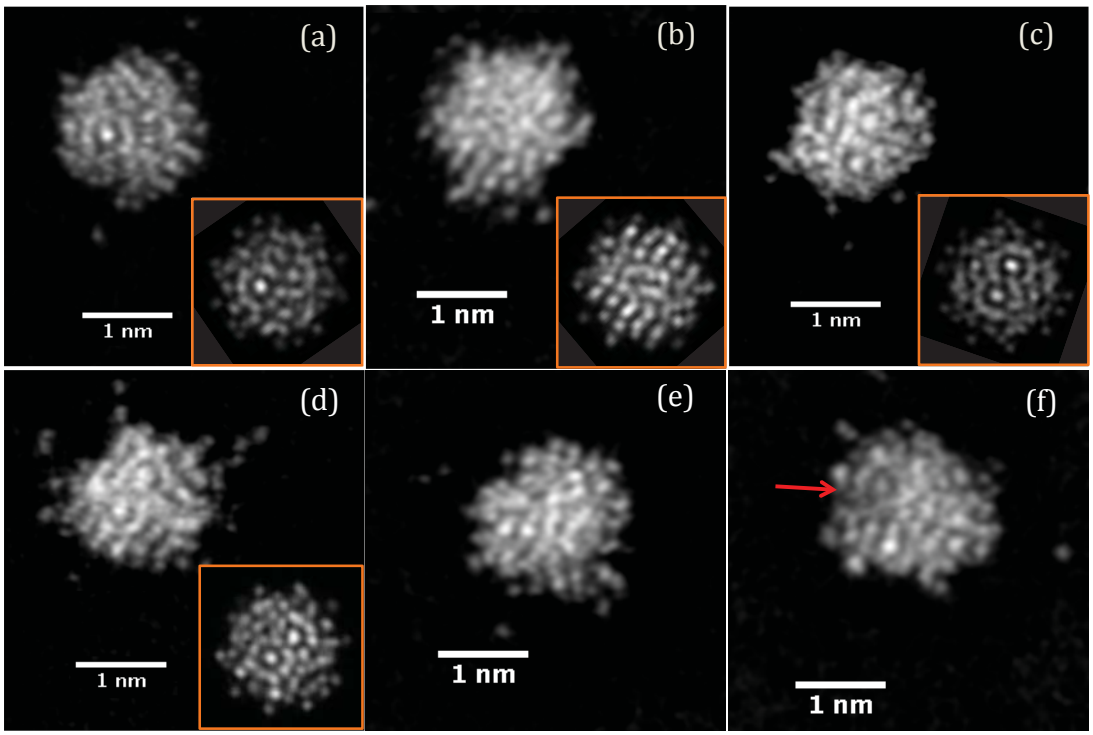

Figure 4.8. (a-f) are HAADF-STEM images of MP Au clusters that match the predicted $Au_{144}(SR)_{60}$ structure. The insets are the corresponding simulations along the orientations of (a) α=30°, β=10°; (b) α=10°, β=20°; (c) α=5°, β=70°; (d) α=40°, β=20°. (e) An example of the unidentified cluster and (f) a cluster with a ring-dot feature (indicated by the red arrow). From reference [44].

In both of the cases, the ring-dot feature appears frequently in the HAADF images. The appearance of this feature is consistent with the existence of local icosahedral symmetry in the clusters. A simulation atlas of an icosahedral, decahedral, and cuboctahedral bare Au_{147} is presented in Figure A7-9. The ring-dot feature can be seen in the simulations of $Au_{144}(SR)_{60}$ (Figure A1-2), and $Au_{133}(SR)_{52}$ (Figure A6) as well as $Au_{102}(SR)_{44}$ (Figure A3) and $Au_{130}(SR)_{50}$ (Figure A4-5). Both $Au_{102}(SR)_{44}$ and $Au_{130}(SR)_{50}$ have decahedral cores, but those are encapsulated by two five-fold symmetry caps [11, 37] and a ring-dot feature occurs at certain orientations in the simulations. Thus the observed ring-dot motifs may be traceable either to an icosahedral core or, in a few

cases, to a five-fold cap. Worth noting is that not all of the orientations show a ring-dot feature, so a higher percentage of clusters may contain similar structural elements. For example, in the case of $Au_{144}(SR)_{60}$and $Au_{133}(SR)_{52}$, if 20% of the images present a ring-dot feature, and assume the clusters are randomly orientated, then 40% of the clusters may contain an icosahedral core (around 50% of atlas simulations present the ring-dot feature).

4.4 Summary and conclusions

In summary, we have employed aberration-corrected STEM to characterise the size and provide insights into the structure of nominally $Au_{144}(SR)_{60}$ clusters. We find the samples synthesised contain a range of cluster sizes, which is also indicated in the mass spectra. Image comparison with multislice simulations of model structures of all orientations shows that only about 3% of clusters fit the predicted $Au_{144}(SR)_{60}$ structure. Nevertheless, the experimental images exhibited a ring-dot feature, characteristic of a local icosahedral order, in a further 20 to 30% of clusters. Based on the simulation atlases, it may be that an even higher proportion of clusters, perhaps 40%, contain icosahedral elements. Electron beam damage at the atomic scale may account for the imperfect matches between simulations and experiments, and no doubt both low doses and low beam energy would be desirable for minimising the electron beam effect on the thiolated clusters, but there is no doubt that the ability of HAADF-STEM both to size and to analyse individual clusters is a powerful tool in the structure resolution problem. In the present case, the rather broad size distribution obtained from the atom counting is consistent with the absence of well-ordered X-ray diffraction patterns from the cluster crystals.

References

[1] Tsukuda, T.; Häkkinen, H.; Protected Metal Clusters: From Fundamentals to Applications. *Elsevier*, Amsterdam, 2015.

[2] Polavarapu, L.; Manna, M.; Xu, Q. Biocompatible Glutathione Capped Gold Clusters as One- and Two-Photon Excitation Fluorescence Contrast Agents for Live Cells Imaging. *Nanoscale* **2011**, *3*, 429-434.

[3] Ma, G.; Binder, A.; Chi, M.; Liu, C.; Jin, R.; Jiang, D.; Fan, J.; Dai, S. Stabilizing Gold Clusters by Heterostructured Transition-Metal Oxide-Mesoporous Silica Supports for Enhanced Catalytic Activities for CO Oxidation. *Chem. Commun.* **2012**, *48*, 11413–11415.

[4] Shivhare, A.; Ambrose, S. J.; Zhang, H.; Purves, R.W.; Scott, R.W.J. Stable and Recyclable Au_{25} Clusters for the Reduction of 4-Nitrophenol. *Chem. Commun.* **2013**, *49*, 276–278.

[5] Heaven, M.W.; Dass, A.; White, P.S.; Holt, K.M.; Murray, R.W. Crystal Structure of the Gold Nanoparticle $[N(C_8H_{17})_4][Au_{25}(SCH_2CH_2Ph)_{18}]$. *J. Am. Chem. Soc.* **2008**, *130*, 3754–3755.

[6] M. Zhu, C.M. Aikens, F.J. Hollander, G.C. Schatz, R. Jin, Correlating the Crystal Structure of a Thiol-Protected Au_{25} Cluster and Optical Properties. *J. Am. Chem. Soc.* **2008**, *130*, 5883–5885.

[7] Zhu, M.; Eckenhoff, W.T.; Pintauer, T.; Jin, R. Conversion of Anionic $[Au_{25}(SCH_2CH_2Ph)_{18}]^-$ Cluster to Charge Neutral Cluster via Air Oxidation. *J. Phys. Chem. C* **2008**, *112*, 14221–14224.

[8] Zeng, C.; Li, T.; Das, A.; Rosi, N.L.; Jin, R. Chiral Structure of Thiolate-Protected 28-Gold-Atom Nanocluster Determined by X-ray Crystallography. *J. Am. Chem. Soc.* **2013**, *135*, 10011–10013.

[9] Zeng, C.; Qian, H.; Li, T.; Li, G.; Rosi, N.L.; Yoon, B.; Barnett, R.N.; Whetten, R.L.; Landman, U.; Jin, R. Total Structure and Electronic Properties of the Gold Nanocrystal $Au_{36}(SR)_{24}$. *Angew. Chem. Int. Ed.* **2012**. *51*, 13114–13118.

[10] Qian, H.; Eckenhoff, W.T.; Zhu, Y.; Pintauer, T.; Jin, R. Total Structure Determination of Thiolate-Protected Au_{38} Nanoparticles. *J. Am. Chem. Soc.* **2010**, *132*, 8280–8281.

[11] Jadzinsky, P.D.; Calero, G.; Ackerson, C.J.; Bushnell, D.A.; Kornberg, R.D. Structure of a Thiol Monolayer-Protected Gold Nanoparticle at 1.1 Å Resolution. *Science* 2007, *318*, 430–433.

[12] Chen, Y.; Zeng, C.; Liu, C.; Kirschbaum, K.; Gayathri, C.; Gil, R.R.; Rosi, N.L.; Jin, R. Crystal Structure of Barrel-Shaped Chiral $Au_{130}(P\text{-}MBT)_{50}$ Nanocluster, *J. Am. Chem. Soc.* **2015**, *137*, 10076–10079.

[13] Zeng, C.; Chen, Y.; Kirschbaum, K.; Appavoo, K.; Sfeir, M.Y.; Jin, R. Structural Patterns at All Scales in a Nonmetallic Chiral $Au_{133}(SR)_{52}$ Nanoparticle. *Sci. Adv.* **2015**, *1*, e1500045.

[14] Dass, A.; Theivendran, S.; Nimmala, P.R.; Kumara, C.; Jupally, V.R.; Fortunelli, A.; Sementa, L.; Barcaro, G.; Zuo, X.; Noll, B.C. $Au_{133}(SPh\text{-}tBu)_{52}$ Nanomolecules: X-Ray Crystallography, Optical, Electrochemical, and Theoretical Analysis. *J. Am. Chem. Soc.* **2015**, *137*, 4610–4613.

[15] Schaaff, T.G.; Shafigullin, M.N.; Khoury, J.T.; Vezmar, I.; Whetten, R.L. Properties of a Ubiquitous 29 kDa Au:SR Cluster Compound. *J. Phys. Chem. B* **2001**, *105*, 8785–8796.

[16] Ackerson, C.J.; Jadzinsky, P.D.; Sexton, J.Z.; Bushnell, D.A.; Kornberg, R.D. Synthesis and Bioconjugation of 2 and 3 nm-Diameter Gold Nanoparticles. *Bioconjugate Chem.* **2010**, *21*, 214–218.

[17] Koivisto, J.; Salorinne, K.; Mustalahti, S.; Lahtinen, T.; Malola, S.; Pettersson, M. Vibrational Perturbations and Ligand–Layer Coupling in a Single Crystal of $Au_{144}(SC_2H_4Ph)_{60}$ Nanocluster. *J. Phys. Chem. Lett.* **2014**, *144*, 1–6.

[18] Chaki, N.K.; Negishi, Y.; Tsunoyama, H.; Shichibu, Y.; Tsukuda, T. Ubiquitous 8 and 29 kDa Gold: alkanethiolate Cluster Compounds: Mass-Spectrometric Determination of Molecular Formulas and Structural Implications. *J. Am. Chem. Soc.* **2008**, *130*, 8608–8610.

[19] Fields-zinna, C.A.; Sardar, R.; Beasley, C.A.; Murray, R.W.; Carolina, N. Electrospray Ionization Mass Spectrometry of Intrinsically Cationized Nanoparticles, $[Au_{144/146}(SC_{11}H_{22}N(CH_2CH_3)_3^+)_x(S(CH_2)_5CH_3)_y]^{x+}$. *J. AM. Chem. Soc.* **2009**, *146*, 16266–16271.

[20] Salorinne, K.; Lahtinen, T.; Koivisto, J.; Kalenius, E.; Nissinen, M.; Pettersson, M.; Häkkinen, H. Non-destructive Size Determination of Thiol-Stabilized Gold Nanoclusters in Solution by Diffusion Ordered NMR Spectroscopy. *Anal. Chem.* **2013**, *85*, 3489–3492.

[21] Jupally, V.R.; Dharmaratne, A.C.; Crasto, D.; Huckaba, A.J.; Kumara, C.; Nimmala, P.R.; Kothalawala, N.; Delcamp, J.H.; Dass, A. $Au_{137}(SR)_{56}$ Nanomolecules: Composition, Optical Spectroscopy, Electrochemistry and Electrocatalytic Reduction of CO_2. *Chem. Commun.* **2014**, *50*, 9895–9898.

[22] Kumara, C.; Dass, A. $(AuAg)_{144}(SR)_{60}$ Alloy Nanomolecules. *Nanoscale* **2011**, *3*, 3064–3067.

[23] Malola, S.; Häkkinen, H. Electronic Structure and Bonding of Icosahedral Core Shell Gold-Silver Nanoalloy Clusters $Au_{144-x}Ag_x(SR)_{60}$. *J. Phys. Chem. Lett.* **2011**, *2*, 2316–2321.

[24] Koivisto, J.; Malola, S.; Kumara, C.; Dass, A.; Pettersson, M. Experimental and Theoretical Determination of the Optical Gap of the $Au_{144}(SC_2H_4Ph)_{60}$ Cluster and the $(Au/Ag)_{144}(SC_2H_4Ph)_{60}$ Nanoalloys. *J. Phys. Chem. Lett.* **2012**, *3*, 3076-3080.

[25] Malola, S.; Lehtovaara, L.; Häkkinen, H. TDDFT Analysis of Optical Properties of Thiol Monolayer-Protected Gold and Intermetallic Silver–Gold $Au_{144}(SR)_{60}$ and $Au_{84}Ag_{60}(SR)_{60}$ Clusters. *J. Phys. Chem. C* **2014**, *118*, 20002–20008.

[26] Barcaro, G.; Sementa, L.; Fortunelli, A.; Stener, M. Comment on "$(Au–Ag)_{144}(SR)_{60}$ Alloy Nanomolecules" by C. Kumara and A. Dass, Nanoscale, 2011, 3 , 3064. *Nanoscale* **2015**, *7*, 8166–8167.

[27] Kothalawala, N.; Kumara, C.; Ferrando, R.; Dass, A. $Au_{144-x}Pd_x(SR)_{60}$ Nanomolecules. *Chem. Commun*. **2013**, *49*, 10850-10852.

[28] Dharmaratne, A.C.; Dass, A. $Au_{144-x}Cu_x(SC_6H_{13})_{60}$ Nanomolecules: Effect of Cu Incorporation on Composition and Plasmon-like Peak Emergence in Optical Spectra. *Chem. Commun.* **2014**, *50*, 1722–1724.

[29] Malola, S.; Hartmann, M.J.; Häkkinen, H. Copper Induces a Core Plasmon in Intermetallic $Au_{(144,145)-X}Cu_X(SR)_{60}$ Nanoclusters. *J. Phys. Chem. Lett.* **2015**, *6* 515–520.

[30] Lopez-acevedo, O.; Akola, J.; Whetten, R.L.; Grönbeck, H.; Häkkinen, H. Structure and Bonding in the Ubiquitous Icosahedral Metallic Gold Cluster $Au_{144}(SR)_{60}$. *J. Phys. Chem. C* **2009**, *144*, 5035–5038.

[31] Cleveland, C.L.; Landman, U.; Schaaff, T.G.; Shafigullin, M.N.; Stephens, P.W.; Whetten, R.L. Structural Evolution of Smaller Gold Nanocrystals: The Truncated Decahedral Motif. *Phys. Rev. Lett*. **1997**, *79*, 1873–1876.

[32] Schaaff, T.G.; Shafigullin, M.N.; Khoury, J.T.; Vezmar, I.; Whetten, R.L.; Cullen, W.G.; First, P.N.; Gutiérrez-Wing, C.; Ascensio, J.; Jose-Yacamán, M. Isolation of Smaller

Nanocrystal Au Molecules: Robust Quantum Effects in Optical Spectra. *J. Phys. Chem. B* **1997**, *101*, 7885–7891.

[33] MacDonald, M.A.; Zhang, P.; Qian, H.; Jin, R. Site-Specific and Size-Dependent Bonding of Compositionally Precise Gold–Thiolate Nanoparticles from X-Ray Spectroscopy. *J. Phys. Chem. Lett.* **2010**, *1*, 1821–1825.

[34] Wong, O.A.; Heinecke, C.L.; Simone, A.R.; Whetten, R.L.; Ackerson, C.J. Ligand Symmetry-Equivalence on Thiolate Protected Gold Nanoclusters Determined by NMR Spectroscopy. *Nanoscale* **2012**, *4*, 4099–4102.

[35] Bahena, D.; Bhattarai, N.; Santiago, U.; Tlahuice, A.; Ponce, A.; Bach, S.B.H.; Yoon, B.; Whetten, R.L.; Landman, U.; Jose-Yacamán, M. STEM Electron Diffraction and High-Resolution Images Used in the Determination of the Crystal Structure of the $Au_{144}(SR)_{60}$ Cluster. *J. Phys. Chem. Lett.* **2013**, *4*, 975–981.

[36] Tlahuice-flores, A.; Santiago, U.; Bahena, D.; Vinogradova, E.; Conroy, C.V.; Ahuja, T.; Bach, S.B.H.; Ponce, A.; Wang, G.; Jose-Yacamán, M.; Whetten, R.L. Structure of the Thiolated Au_{130} Cluster. *J. Phys. Chem.* A **2013**, *117*, 10470–10476.

[37] Negishi, Y.; Sakamoto, C.; Tatsuya, O.; Tsukuda, T. Synthesis and the Origin of the Stability of Thiolate-Protected Au_{130} and Au_{187} Clusters. *J. Phys. Chem. Lett.* **2012**, *3*, 1624–1628.

[38] Bruma, A.; Santiago, U.; Alducin, D.; Villa, G.P.; Whetten, R.L.; Ponce, A.; Mariscal, M.; José-Yacamán, M. Structure Determination of Superatom Metallic Clusters Using Rapid Scanning Electron Diffraction. *J. Phys. Chem. C* **2015**, *102*, 1902–1908.

[39] Azubel, M.; Koivisto, J.; Malola, S.; Bushnell, D.; Hura, G.L.; Koh, A.L.; Tsunoyama, H.; Tsukuda, T.; Pettersson, M.; Häkkinen, H.; Kornberg, R.D. Electron Microscopy of Gold Nanoparticles at Atomic Resolution. Science **2014**, *345*, 909–912.

[40] Wang, Z.W.; Toikkanen, O.; Quinn, B.M.; Palmer, R.E. Real-Space Observation of Prolate Monolayer-Protected Au_{38} Clusters Using Aberration-Corrected Scanning Transmission Electron Microscopy. *Small* **2011**, *7*, 1542–1545.

[41] Malola, S.; Lehtovaara, L.; Knoppe, S.; Hu, K.J.; Palmer, R.E.; Bürgi, T.; Häkkinen, H. $Au_{40}(SR)_{24}$ Cluster as A Chiral Dimer of 8-Electron Superatoms: Structure and Optical Properties*. J. Am. Chem. Soc.* **2012**, *134*, 19560–19563.

[42] Wang, Z.W.; Toikkanen, O.; Yin, F.; Li, Z.Y.; Quinn, B.M.; Palmer, R.E. Counting the Atoms in Supported, Monolayer-Protected Gold Clusters. *J. Am. Chem. Soc.* **2010**, *132*, 2854–2855.

[43] Jian, N.; Stapelfeldt, C.; Hu, K.J.; Fröba, M.; Palmer, R.E. Hybrid Atomic Structure of the Schmid Cluster $Au_{55}(PPh_3)_{12}Cl_6$ Resolved by Aberration-Corrected STEM. *Nanoscale* **2015**, *7*, 885–888.

[44] Liu J; Jian N; Ornelasa I; Pattisona A. J.; Lahtinen T., Salorinne K.; Häkkinen H.; Palmer, R. E. Exploring the Atomic Structure of 1.8 nm Monolayer-Protected Gold Clusters with Aberration-Corrected STEM. Ultramicroscopy, 2016, doi: 10.1016/j.ultramic.2016.11.021

[45] Salorinne, K.; Lahtinen, T.; Koivisto, J.; Kalenius, E.; Nissinen, M.; Pettersson, M.; Häkkinen, H. Non-destructive Size Determination of Thiol-Stabilized Gold Nanoclusters in Solution by Diffusion Ordered NMR Spectroscopy. *Anal. Chem.* **2013**, *85*, 3489–3492.

[46] Koch, C. Determination of Core Structure Periodicity and Point Defect Density Along Dislocations, Ph.D. Thesis, Arizona State University, Arizona, 2002.

[47] Wang, Z. W.; Palmer, R. E. Intensity Calibration and Atomic Imaging of Size-Selected Au and Pd Clusters in Aberration-Corrected HAADF-STEM. *J. Phys. Conf. Ser.* **2012**, *371*, 012010.

[48] Hamouda, R.; Bertorelle, F.; Rayane, D.; Antoine, R.; Broyer, M.; Dugourd, P. Glutathione Capped Gold $Au_N(SG)_M$ Clusters Studied by Isotope-Resolved Mass Spectrometry. *Int. J. Mass Spectrom*. **2013**, *335*, 1–6.

[49] Black, D. M.; Bhattarai, N.; Whetten, R. L.; Bach, S. B. H. Collision-Induced Dissociation of Monolayer Protected Clusters Au_{144} and Au_{130} in an Electrospray Time-of-Flight Mass Spectrometer. *J. Phys. Chem. A* **2014**, *118*, 10679– 10687

[50] Egerton, R.F.; McLeod, R.; Wang, F.; Malac, M. Basic Questions Related to Electron-Induced Sputtering in the TEM. *Ultramicroscopy* **2010**, *110*, 991–997.

[51] Zeng, C.; Chen, Y.; Das, A.; Jin, R. Transformation Chemistry of Gold Nanoclusters: From One Stable Size to Another. *J. Phys. Chem. Lett.* **2015**, *6*, 2976–2986.

[52] Chen, Y.; Zeng, C.; Kauffman, D.R.; Jin, R. Tuning the Magic Size of Atomically Precise Gold Nanoclusters via Isomeric Methylbenzenethiols. *Nano Lett.* **2015**, *15*, 3603–3609.

[53] Tian, S.; Li, Y.Z.; Li, M.B.; Yuan, J.; Yang, J.; Wu, Z.; Jin, R. Structural Isomerism in Gold Nanoparticles Revealed by X-Ray Crystallography. *Nat. Commun.* **2015**, *6*, 8667.

[54] Von Issendorff, B.; Palmer, R. E. A New High Transmission Infinite Range Mass Selector for Cluster and Nanoparticle Beams. *Rev. Sci. Instrum.* **1999**, *70*, 4497–4501.

[55] Pratontep, S.; Carroll, S. J.; Xirouchaki, C.; Streun, M.; Palmer, R. E. Size-Selected Cluster Beam Source Based on Radio Frequency Magnetron Plasma Sputtering and Gas Condensation. *Rev. Sci. Instrum.* **2005**, *76*, 045103.

Chapter 5 Oxidation State Analysis of Metal Oxide Nanoparticles by EELS

The CeO_x and CuO_x samples investigated in the chapter were prepared by Sophie. Briffa from the School of Geography, Earth and Environmental Sciences, University of Birmingham. The hydrothermally synthesised CoO_x and FeO_x nanoparticles were provided by Selina Tang of the Promethean Particles Ltd., Nottingham. The XRD data of the FeO_x samples were collected by Isabella Römer, from the School of Geography. All the STEM images and EELS data were taken and analysed by me. Some of the presented work pertaining to CeO_x and CuO_x has been published in the paper *Development of Scalable and Versatile Nanomaterial Libraries for Nanosafety Studies: Polyvinylpyrrolidone (PVP) Capped Metal Oxide Nanoparticles* (*RSC Adv.* 2017, *7*, 3894–3906). [Ref 16] Some text and figures about the EELS and STEM images are adapted from this paper.

5.1 Introduction to metal oxide nanoparticles

Metal oxide nanoparticles attract considerable interest in the field of catalysis, energy storage and optics [1-3], due to the large diversity of oxide compounds and their unique chemical and physical properties. The interplay between factors such as morphology, crystal structure, size and valence state affords intriguing activities in various applications. However, the active performance of nanoparticles may also bring side effects to humans and other organisms when they are released into the environment unintentionally or intentionally. Some nanoparticles, such as copper oxide (CuO_x), cobalt oxide (CoO_x), Cerium oxide (CeO_x), have been found to be toxic [4-6]. Metal oxide

nanoparticles are already used in many industrial and everyday fields such as electronics, cosmetics, and medical applications [7, 8]. Humans are more likely to be exposed via the environment and consumer products as the use of nanomaterial increases rapidly. In 2015, an investigation of 1814 consumer products shows that about 29% of the products contain nanomaterials [9].

Many studies demonstrate that transition metals act as catalysts in the oxidative deterioration of biological macromolecules [10, 11]; therefore the toxicities of these metal oxide nanoparticles may be due at least in part to oxidative tissue damage. Oxidation state of the metals seems to a key factor for the toxic effects. It has been reported that transition metals undergo redox cycling reactions, resulting in the production of reactive oxygen species, such as the superoxide ion, hydrogen peroxide, and hydroxyl radical [10, 12]. The reactive oxygen species will then enhance the lipid peroxidation and DNA damage. Reaney et al [13] reported that Mn^{3+} is more effective than Mn^{2+} on inhibiting the cellular aconitase enzyme activity. Pulido-Reyes et al [6] showed that the main factor of toxicity of Cerium oxide is related to the percentage of surface content of Ce^{3+} sites. Cerium oxide nanoparticles were found to be toxic when the percentage of Ce^{3+} is higher than 40%. It has been found that the release of ions often accompanied by the generation of reactive oxygen species [14]. Puzyn et al. [15] reported that the toxicity of metal oxide NMs decreased in the order $Me^{2+} > Me^{3+} > Me^{4+}$, because the release of cations Me^{n+} having a smaller charge is more energetically favourable than the release of cations with a larger n.

Characterising the oxidation state of the metal oxide nanoparticles is essential to study the origin of their toxic effects. Compared to the ensemble average information given by

X-ray photoelectron spectroscopy (XPS), STEM EELS can provide chemical information of individual nanoparticles [16]. In this chapter, we studied the oxidation states of CeO_x, CuO_x, CoO_x and FeO_x using STEM EELS. The Ce oxidation state of the CeO_x nanoparticles was found to be 3.41±0.39. The O K-edge of over half of the CuO_x nanoparticles is close to that of Cu_2O reference spectra, indicating that the oxidation state of over 50% CuO_x nanoparticles are at 1+, while others have a different O K-edge from the CuO and Cu_2O reference spectra. The investigation of CoO_x and FeO_x shows that the average oxidation state changes with the particles size and synthesis precursor.

5.2 Experimental details

Colloidal CeO_x and CuO_x nanoparticles were synthesised by a reflux reaction method. CoO_x and FeO_x nanoparticles were prepared by a continuously hydrothermal method. The preparation details for CeO_x nanoparticles are given as follows and was reported by Merrifield et al[17]. 130 mg of cerium nitrate were dissolved in 60 mL of a 3 mmol solution of polyvinylpyrrolidone (PVP) with a molecule weight of 10,000 amu, and the mixture was then heated for 3 hours at 105 °C. After heating, the reaction was quenched with cold water. The excess PVP was removed using acetone by centrifuging at 4000 rpm for 10 min. The yellow pellet was retained and re-suspended in ultra high purity water (UHP, resistivity 18.2 MΩ-cm). CuO_x nanoparticles were synthesised in the same way by substituting the cerium nitrate reagent with equimolar amounts of copper nitrate.

The CoO_x and FeO_x nanoparticles were prepared by a hydrothermal method. A continuous-flow hydrothermal reactor [18-20] was used to prepare the CoO_x and FeO_x nanoparticles. Figure 5.1a shows the schematic of the hydrothermal reactor system and

the design of the nozzle reactor (Figure 5.1b). Deionized water was pumped through the preheater (P3) by a High Performance Liquid Chromatography (HPLC) pump (P1) to the reactor at a rate of 20 ml/min. The flow was heated to 400 °C. Aqueous cobalt salt solution or iron salt solution (at ambient temperature) was fed to the reactor at a rate of 10 ml/min by another HPLC pump, P2. The preheated water was fed downwards into the reactor (R1) through the internal pipe while the salt solution flowed in a counter-current direction. The mixed fluids were pumped to the cooler (P4) through the reactor outlet. The pressure in the system was kept at 240 bar by a back-pressure regulator (V3).

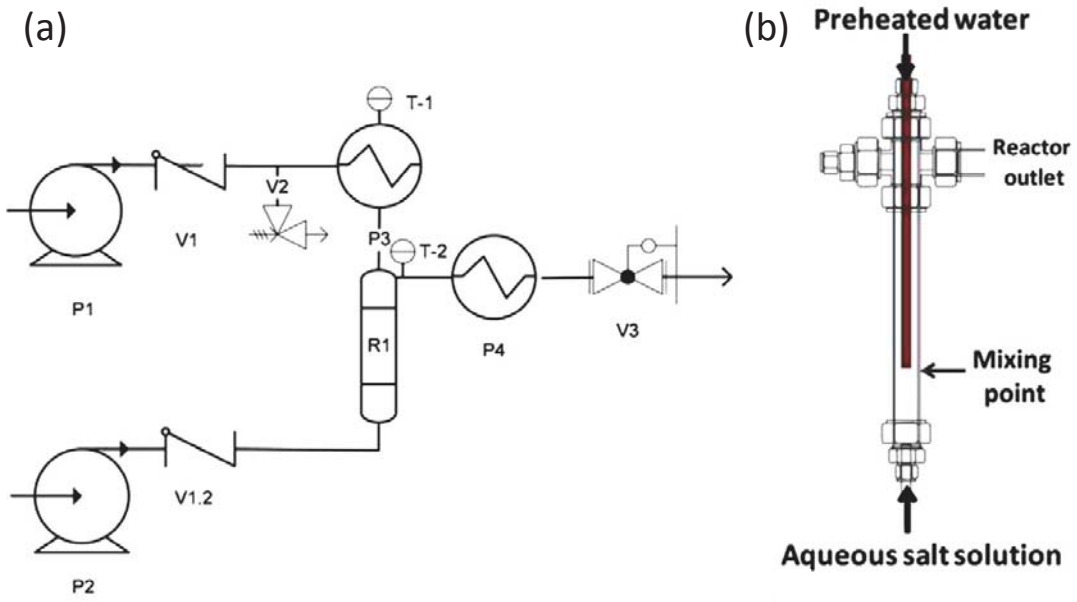

Figure 5.1 (a) A schematic of the continuous-flow hydrothermal reactor system; P1 and P2 stand for Gilson HPLC pumps, P3 water preheater, R1 nozzle reactor, P4 cooler, V1, V1.2 check valves, V2 pressure relief valve, V3 Tescom back-pressure regulator, T-1,2 thermocouples. (b) Nozzle reactor design. From reference [16].

For the sample of cobalt oxide nanoparticles, cobalt (II) acetate tetrahydrate ($Co(C_2H_3O_2)_2{\cdot}4H_2O$, Sigma-Aldrich, UK) was used as the precursor where the concentration was 0.05 mol. The down flow water feed contained 0.25% v/v hydrogen peroxide (H_2O_2, Fisher Scientific, UK). H_2O_2 is used here to drive oxidation of the cobalt precursor to oxidise the Co^{2+} since Co oxide nanoparticles could not precipitate from cobalt nitrate solutions in the absence of a base [21, 22]. For the iron oxide samples, two different precursors were used, which are iron (III) nitrate nonahydrate ($Fe(NO_3)_3{\cdot}9H_2O$, Sigma Aldrich) and ammonium iron (III) citrate ($C_6H_8O_7{\cdot}xFe^{3+}{\cdot}yNH_3$, Sigma-Aldrich). No H_2O_2 was used during the synthesis, as the nitrate and citrate ions can act as the oxidising and reducing agent on the iron, respectively. On the other hand, the solubility of iron ions is several orders of magnitude lower than the Co ions [21], therefore, FeO_x is easier to precipitate than CoO_x. The FeO_x nanoparticles synthesised by iron (II) nitrate nonahydrate and ammonium iron (III) citrate are labelled as N-FeO_x and C-FeO_x, respectively. The collected samples were black aqueous dispersions and washed by centrifugation or filtration and then were sent to the University of Birmingham for characterisation.

The samples were deposited on Cu grids for electron microscopy analysis. The HAADF (High-angle annular dark field)-STEM imaging was performed in a 200 kV JEM2100F STEM (JEOL) with a spherical aberration corrector (CEOS). HAADF images were acquired with inner and outer detector angles of 62 and 164 mrad, respectively, at a probe convergence angle of 19 mrad. The electron energy loss spectra (EELS) were recorded with an Enfina detector attached to the JEM2100F STEM. The aperture size used is 3 mm and the camera length is 2 cm corresponding to a collection semi-angle of 57.8mrad. The energy dispersion is 0.3 eV/channel and the acquisition time is 5s for

each spectrum. The valence state of the transition metal oxides has a relationship with the intensity ratio of the M_4/M_5 or L_2/L_3 edges, and a number of methods have been developed to determine the valence state. Here we chose the multiple linear least-square (MLLS) fitting and the white line intensity ratios to calculate the valence states. The second derivative method was used to determine the white line ratio for the spectra. One advantage of this method is that the measurements do not depend on background removal and is not dependent on the method used to determine the continuous M or L edge contribution. The raw spectra were smoothed with the Savitzky-Golay method [23] to eliminate the channel-to-channel fluctuations. The Savitzky-Golay method has an advantage of smoothing the spectrum without loss of resolution. The spectra were analysed with the DigitalMicrograph software. The X-ray diffraction (XRD) patterns were collected using a Bruker D8 powder diffractometer using Cu Kα radiation (λ = 1.5406 Å).

5.3 Results and discussion

5.3.1 PVP-capped CeO_x nanoparticles

Figure 5.2a shows the HAADF image of CeO_x ($1.5<x<2$) nanoparticles. The peak of the diameter distribution of the nanoparticles is at 3.3 ± 0.8 nm (Figure 5.2b). Figure 5.2c is a high-resolution HAADF image of a CeO_x nanoparticle showing an orientation of <0-11>, and the measured interplanar space for the {111} plane is 0.324 nm, which is a little bit bigger than that in bulk CeO_2 (0.312 nm) because of lattice expansion as the particle size decreases [24,25]. The particle shown in Figure 5.2d is hexagonal in shape and the interplanar space of 0.277 nm corresponds to the {200} plane.

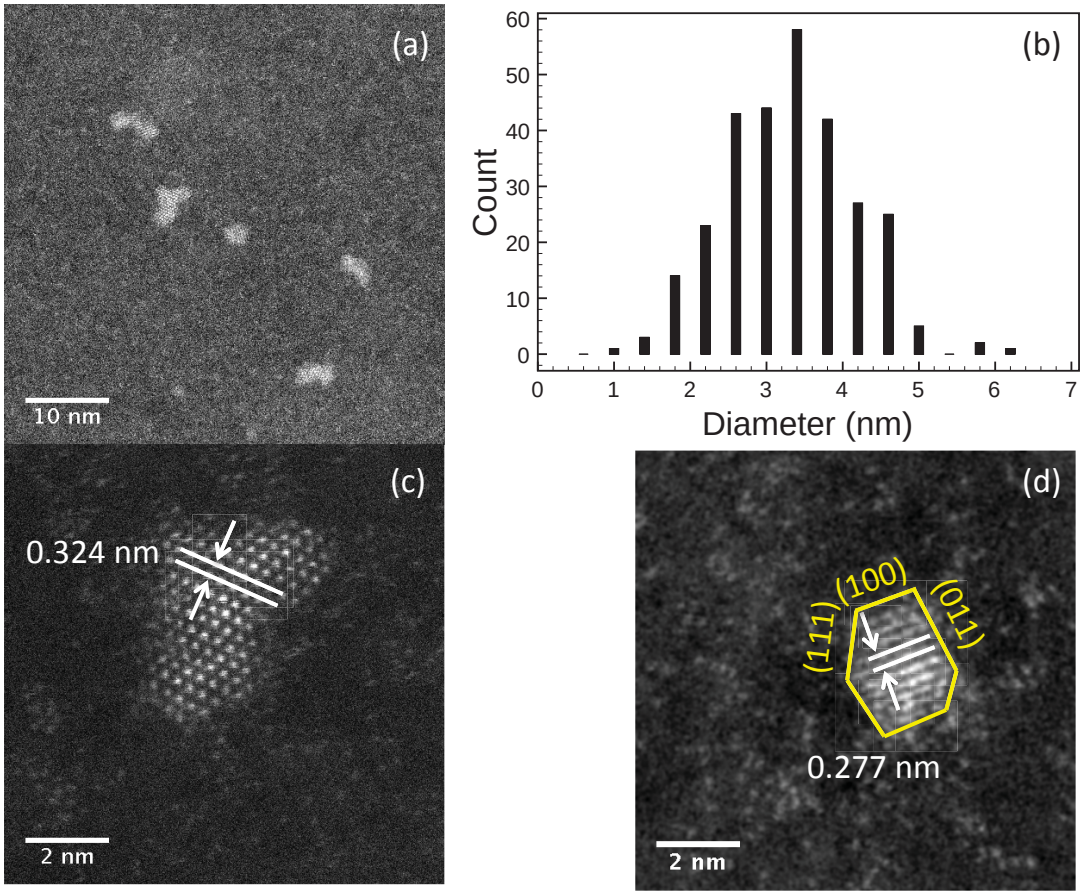

Figure 5.2 (a) A low magnification HAADF image of PVP-capped CeO_x nanoparticles; (b) Diameter distribution of the nanoparticles. The average value of the diameter is 3.3 ± 0.8 nm. (c, d) High-resolution HAADF image of CeO_x nanoparticles

The oxidation state of cerium oxide can be studied by EELS or X-ray photoelectron spectroscopy (XPS) in its M-edge region, which carries information on the initial state 4f occupancy. In the EELS spectrum of ceria, the M-edge white lines occur as two sharp peaks due to the $3d_{3/2} \rightarrow 4f_{5/2}$ transition (M_4) and the $3d_{5/2} \rightarrow 4f_{7/2}$ transition (M_5). The intensity of M_4 edge is higher than that of M_5 edge in Ce^{4+}, and reversed in Ce^{3+} (Figure 5.3a). The white line ratio in EELS has been used to determine the valence state of Ce ions, since the M_5/M_4 ratio has a linear relationship with the combinations of Ce^{3+} and Ce^{4+}. To determine the valence state of the synthesised colloidal CeO_x nanoparticles,

multiple linear least-square (MLLS) fitting and M_5/M_4 ratio methods were performed. In both methods, reference spectra are needed. Here we used CeO_2 nanoparticles and $CeCl_3$ salt as the reference material of Ce^{4+} and Ce^{3+} ions, respectively.

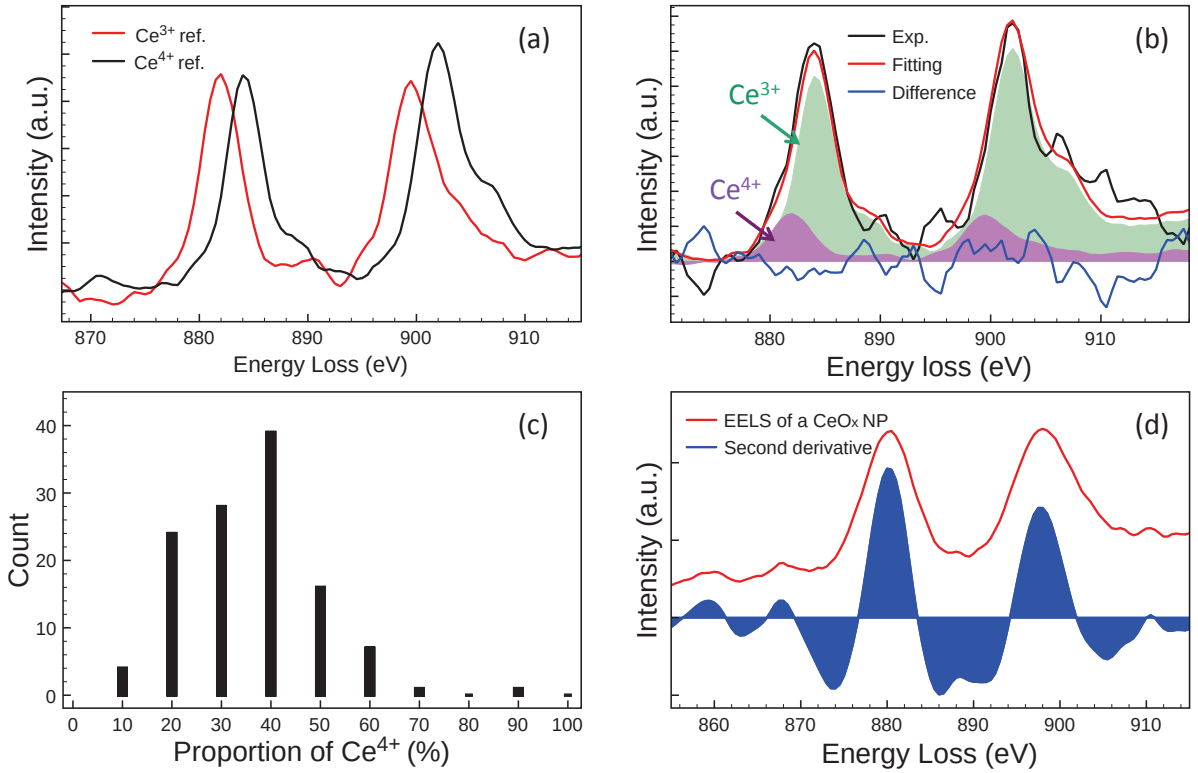

Figure 5.3 (a) Reference EELS spectra of Ce^{3+} and Ce^{4+} materials; (b) An example of MLLS fitting result; (c) The histogram of Ce^{4+} proportion in the CeO_x nanoparticles; (d) An EELS spectrum of CeO_x nanoparticle and its second derivative.

Figure 5.3a shows the reference EELS spectra of Ce^{3+} and Ce^{4+}. The Ce^{3+} M_5 and M_4 edges are separated by about 17.5 eV and the two main peaks of are at 882 and 899.5 eV, respectively. There is a chemical shift of about 2 eV between the Ce^{3+} and Ce^{4+} M_5 edges and the main peaks of the Ce^{4+} M_5 and M_4 edges are at 884 and 902 eV, respectively. MLLS fitting was performed in the energy range from 870 to 915 eV with the two reference spectra, and an example of the fitting result is presented in Figure 5.3b. The fraction of Ce^{4+} ions' distribution in the CeO_x nanoparticles is shown in Figure

5.3c, which indicates that the oxidation state of the CeO_x nanoparticles is not homogeneous and the average value of the oxidation state calculated from 120 nanoparticles is 3.38 ± 0.13 (the error is calculated from the spread of the distribution), which is consistent with a previous report [17].

Several techniques have been proposed to determine The M_5/M_4 ratio by measuring the intensity ratio of M_5 and M_4 peaks on background subtracted spectra or the intensity of the positive peaks on its second derivative [26-28]. In this study, we determined the M_5/M_4 ratio by measuring the area under the positive peaks in the second derivative spectra, since the calculated ratio is rather stable and is not sensitive to the specimen thickness. Figure 5.3d represents an example of an EELS spectrum (red curve) and its second derivative. The M_5/M_4 ratios calculated from the Ce^{3+} and Ce^{4+} reference spectra are 1.11 ± 0.05 and 0.85 ± 0.02 (standard deviation), respectively. The average M_5/M_4 ratio calculated from 31 spectra is 1.00 ± 0.10, and because of the linear relationship between the white ratio and the oxidation state, the corresponding average oxidation state is found to be 3.41 ± 0.36, which agrees with the result obtained from the MLLS fitting. The result shows that most of the ceria nanoparticles have a higher proportion of Ce^{3+} than Ce^{4+}. Oxygen loss on the particle surface is accompanied by a valence change from Ce^{4+} to Ce^{3+}. Haigh et al. [29] reported that oxygen-vacancy diffusion into the particle is favoured. Therefore, as the particle size decreases, the fraction of Ce^{3+} ions increased rapidly.

5.3.2 PVP-capped CuO_x nanoparticles

To avoid the effect of the Cu grid, PVP-capped CuO_x NPs were drop-casted onto a Mo TEM grid covered with amorphous carbon film and were then imaged in the ac-STEM.

Figure 5.4 (a, c) present the low and high magnification HAADF images of the CuO_x NPs. Interestingly, we found that CuO_x particles are surrounded by less bright bands as indicated by the red arrows. Figure 5.4d is a false colour image of Figure 5.4c to increase the visual contrast. We think that the less bright bands in the HAADF images may consist of some PVPs and CuO_x fragments since we can see some atoms (indicated in the yellow circles) near the CuO_x particles. The size distribution of the CuO_x nanoparticles is shown in Figure 5.4b and the average diameter is 2.6±0.4 nm.

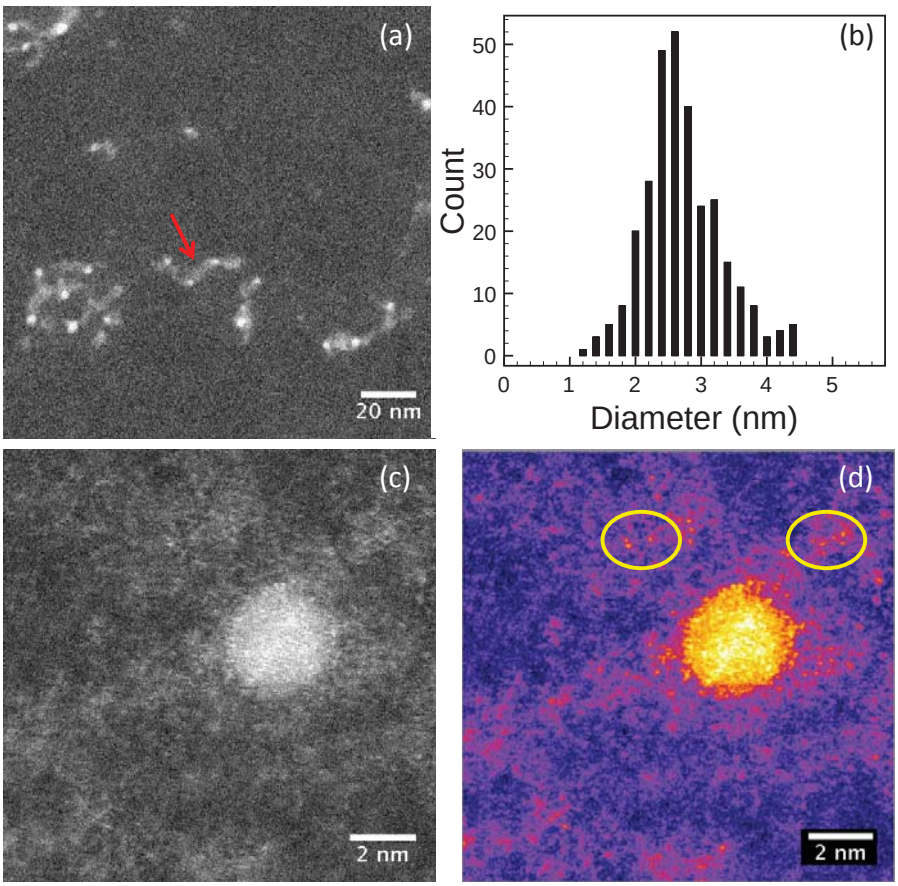

Figure 5.4 (a, c) Low and high magnification HAADF images of PVP-capped CuO_x nanoparticles; (b) Size distribution of the CuO_x NPs; (d) A false colour image of (c) to increase the visual contrast. Red arrow indicates the less bright bands and the yellow circles indicate atoms.

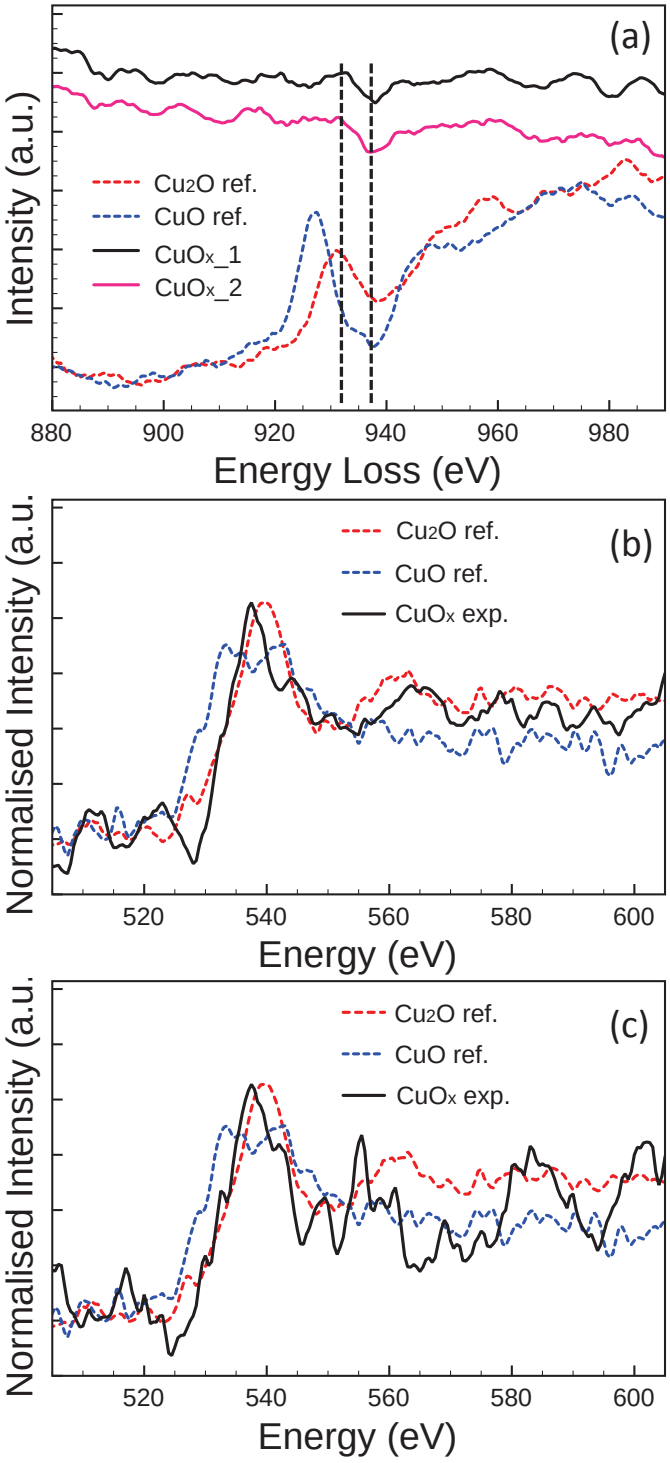

Figure 5.5 (a) EELS spectra of Cu L edges from Cu_2O, CuO and PVP-capped CuO_x nanoparticles; (b, c) O K-edge comparison between the reference spectra (Cu_2O and CuO) and the spectrum of the CuO_x nanoparticles. Reproduced from reference [16].

Figure 5.5a shows the Cu L-edges in the EELS spectra of the CuO_x nanoparticles and the reference materials (Cu_2O, < 50 nm; CuO, < 5 μm; bought from SIGMA-ALDRICH). From this diagram, we can see the difference between the L-edges of Cu_2O and CuO. The first main peaks (Cu L_3 edges) of the Cu_2O and CuO are located at 931 and 927.5 eV, respectively, and there is a chemical shift of about 3.5 eV between these two spectra. The Cu L-edges of the synthesised CuO_x nanoparticles are very weak and have a very poor signal-to-noise (S/N) ratio shown in Figure 5.5a. It's possible to see that the energy position of a valley (indicated by the right dash line) occurs at the same position as the reference spectra and that a small hump appears at around 931 eV, which is similar to the L_3 edge of the Cu_2O spectra. The poor S/N ratio might be because of the very small size of nanoparticles, and it's not possible to perform MLLS fitting to determine the oxidation state of the CuOx nanoparticles quantitatively.

The energy-loss near-edge structure (ELNES) of O K-edge is another fingerprint on the variation in the valence state and structure. The ELNES of O K-edges from the CuO_x nanoparticles were compared to the spectra taken from CuO (blue dashed line) and Cu_2O (red dashed line) reference materials shown in Figure 5.5b, c. The comparison was performed in thirteen spectra and eight of them showed some similarity both in the shape and the onset of the O K-edge to the ELNES of Cu_2O (Figure 5.5b), which means that the valence state of over 60% of the CuOx nanoparticles might be 1+. The rest of the spectra are different in structure from the O K-edge of either Cu_2O or CuO (Figure 5.5c), however, the onset of the O K-edge is similar to the Cu_2O spectra, which may indicate a complicated mixture of valence states or a different structure of copper oxides (such as $Cu(OH)_2$).

5.3.3 CoO_x nanoparticles

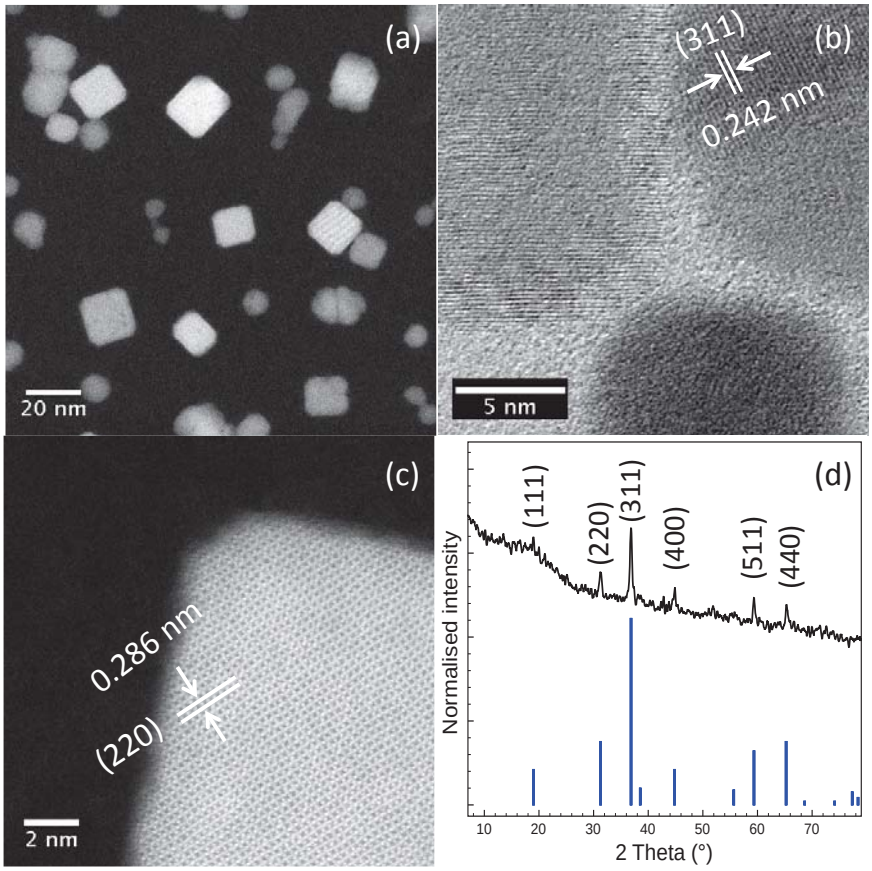

Figure 5.6 (a) A HAADF image of CoO_x NPs; Example HAADF images of a spherical (b) and a cubic (c) cobalt oxide nanoparticles; (d) XRD pattern of the CoO_x sample. The blue lines are the reflections from a standard XRD pattern of FCC Co_3O_4 (JCPDS 42-1467).

Figure 5.6(a) shows the HAADF image of the hydrothermally synthesised CoO_x nanoparticles. These particles have two different shapes; examples of spherical and cubic nanoparticles are presented in Figure 5.6(b, c). I measured the interplanar spacings of these two kinds of particles to check the structural homogeneity of the particles. The interplanar spacing of 0.242 nm and 0.286 nm indicated in figure 5.6b and 5.6c are corresponding to the (311) and (220) planes of structure Co_3O_4, respectively [30]. Figure 5.6(d) is a XRD pattern of this sample; no other diffraction peaks are found,

indicating that the CoO_x nanoparticle is Co_3O_4, a mixed valence compound of $Co^{II}O \bullet Co^{III}_2O_3$.

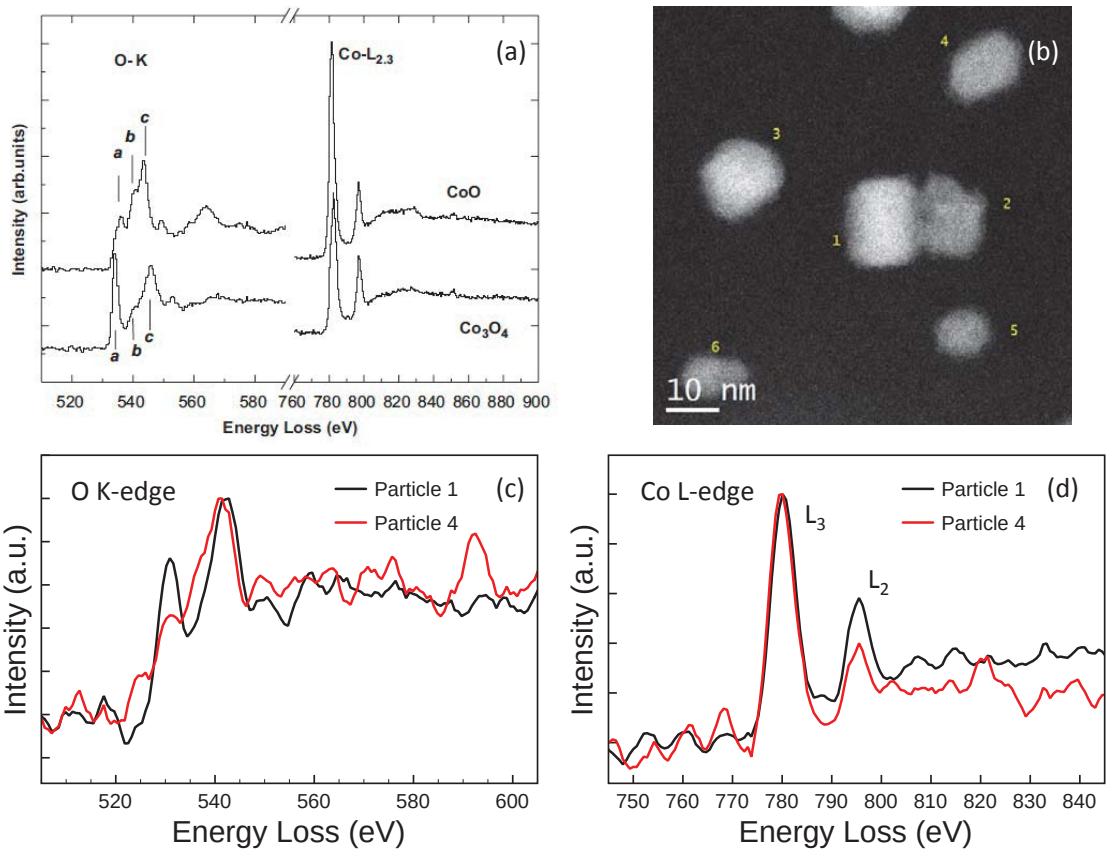

Figure 5.7 (a) Reference spectra of O K-edge and Co L-edge of CoO and Co_3O_4 [31]; (b) HAADF image of CoO_x NPs; (c, d) O K-edge and Co L-edge of particle 1 and particle 4 shown in (b).

The shapes of the O K-edge and Co L-edge from CoO and Co_3O_4 reference materials [31] are shown in Figure 5.7a. It's worthy to note that the O K-edge ELNES of CoO appears as a broad peak (c) and some small features (a, c). While the O K-edge ELNES of Co_3O_4 has two sharp and separated peaks. The variation of the Co L-edge ELNES is not obvious, but we can still see that the white line ratio (L_3/L_2) of CoO is bigger than that of Co_3O_4. Figure 5.7 (c) and (d) show the O K-edge and Co L-edge ELNES comparison between Particle 1 and 4 indicated in Figure 5.6(b). The spectra of these two particles have a different feature in their O ELNES and the spectrum of Particle 1 is similar to the

reference spectrum of Co_3O_4 and the spectrum of Particle 4 is closer to that of CoO. Particle 4 has a higher L_3/L_2 ratio than that of Particle 1, which is also consistent with the Co L-edge ELNES of CoO reference spectrum.

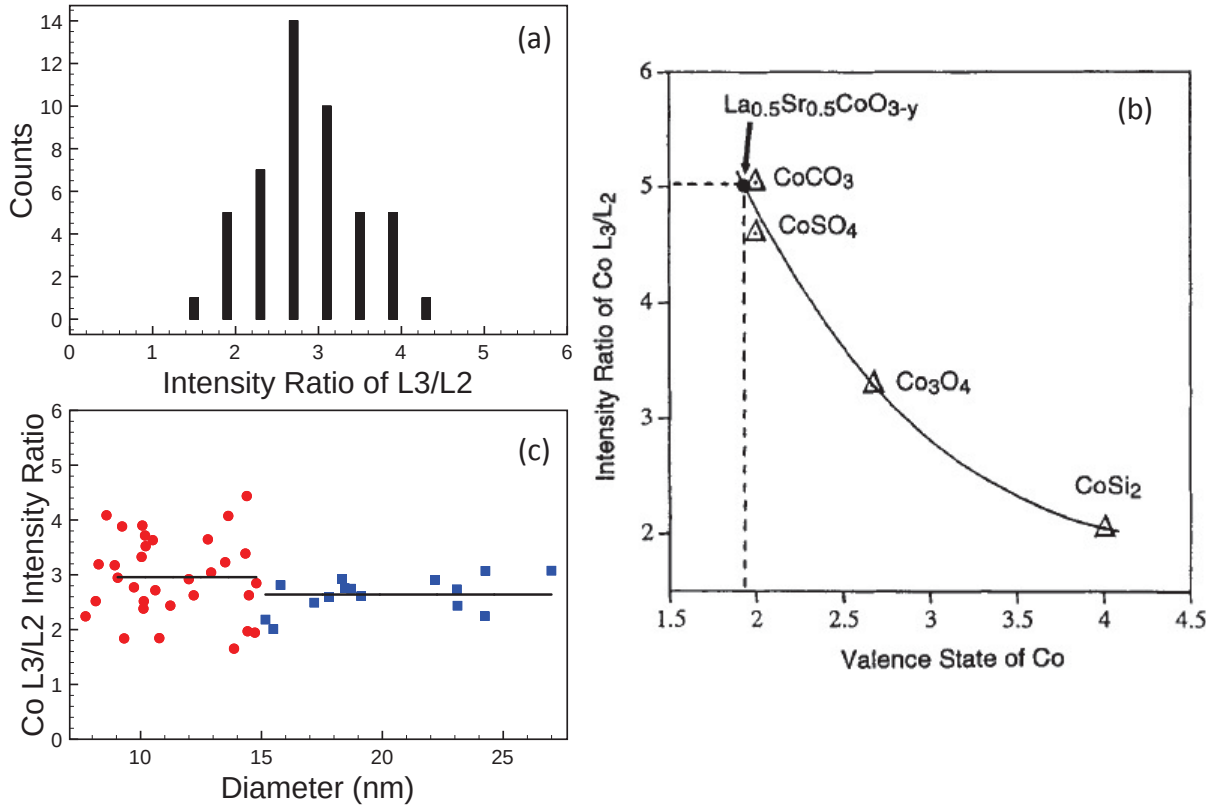

Figure 5.8 (a) L_3/L_2 ratio distribution of the CoO_x NPs; (b) A diagram of the intensity ratio of Co L_3/L_2 against valence state of Co [35]; (c) A diagram of L_3/L_2 ratio against the diameter.

Since the variations of the L_3/L_2 ratio are intrinsically related to the changes in the Co valence state, the L_3/L_2 ratio was measured by using the second deviation method. The L_3/L_2 ratio distribution of CoO_x nanoparticles is shown in Figure 5.7a, and the average value of the white ratio is 2.86 ± 0.64. The relationship between the white-line ratio and the Co valence state was referred to previous studies [32-35] and it is reported that the relationship is not linear. According to the diagram shown in Figure 5.8b, the estimated average valence state of Co is close to 3.0, which is higher than 2.67+. This may indicate

that the CoO_x nanoparticles are O rich [35]. The diagram of white-line ratio against nanoparticle diameter (Figure 5.8c) demonstrates that the white-line ratio of nanoparticles of a diameter less than 15 nm has a big variation from about 1.8 to 4.2 and that the L_3/L_2 ratio of nanoparticles larger than 15 nm is relatively constant. The average L_3/L_2 ratio of the smaller CoO_x particles (< 15 nm) is found to be 2.95 ± 0.72 corresponding to a lower oxidation state and the larger particles is at 2.64 ± 0.31 (about 3.1+ in oxidation state). This indicates that the bigger CoO_x nanoparticles have an O richer surface than the smaller ones.

5.3.4 FeO_x nanoparticles

Figure 5.9a,b and 5.9d,e show the HAADF and BF images of the N-FeO_x and C-FeO_x nanoparticles synthesised with $Fe(NO_3)_3{\cdot}9H_2O$ and $C_6H_8O_7{\cdot}xFe^{3+}{\cdot}yNH_3$ precursors, respectively. In both cases, the nanoparticles agglomerate because there is no stabiliser attached to the surface of the hydrothermally prepared nanoparticles. The C-FeO_x nanoparticles are bigger than the N-FeO_x nanoparticles. The size distribution histograms are shown in Figure 5.9c and e, and the average diameters of the two samples are 17.5 ± 4.2 nm and 6.5± 1.4 nm, respectively.

The crystallinity of these two samples seems to be different. Figure 5.9b shows that lattice fringes are clearly visible in the C-FeO_x nanoparticles, while the lattice fringes in the N-FeO_x nanoparticles are disordered. XRD patterns were collected to check the crystallinity of these two samples. Similar to the STEM result, we found the C-FeO_x nanoparticles are crystallized and the XRD pattern (Figure 5.10) indicates that the C-FeO_x nanoparticles are Fe_3O_4. This result agrees with some previous report that Fe_2O_3 is usually the product of a ferric salt except in the case of ferric ammonium citrate, when

the product is Fe_3O_4 [22, 36]. No distinct peak was observed in the N-FeO_x sample indicating that these particles are amorphous.

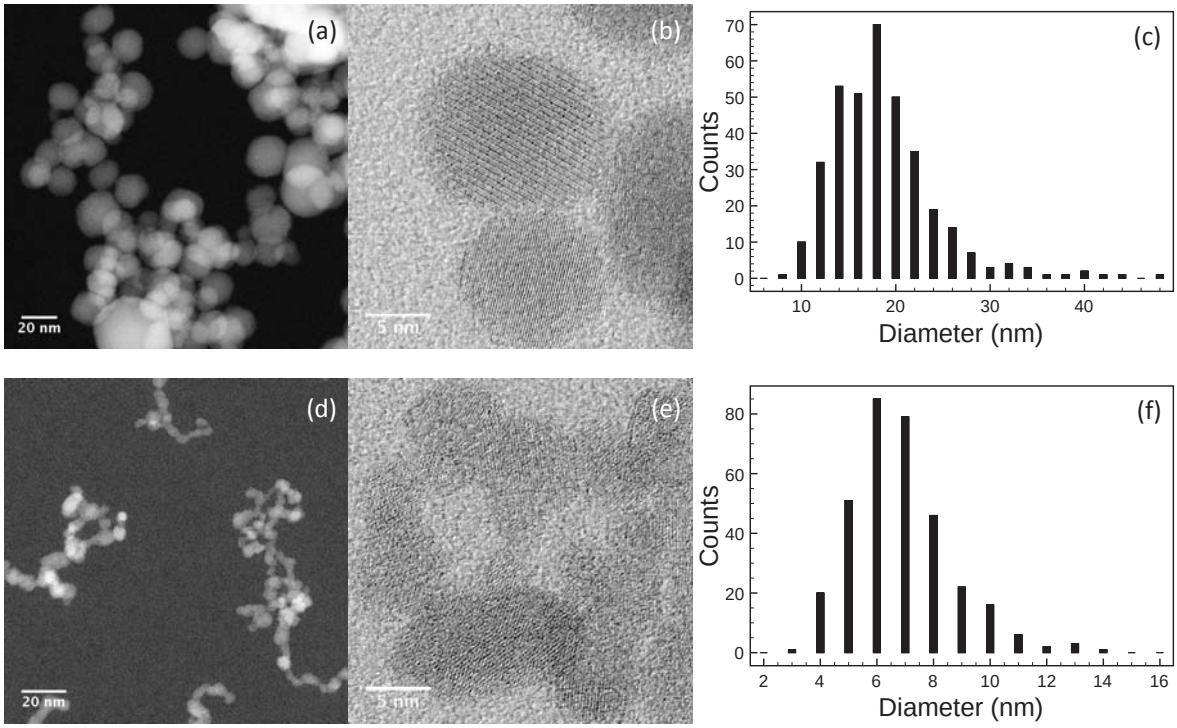

Figure 5.9 HAADF (a) and BF (b) images of C-FeOx nanoparticles, and size distribution histogram (c); HAADF (d) and BF (e) images of N-FeOx nanoparticles, and size distribution histogram (f).

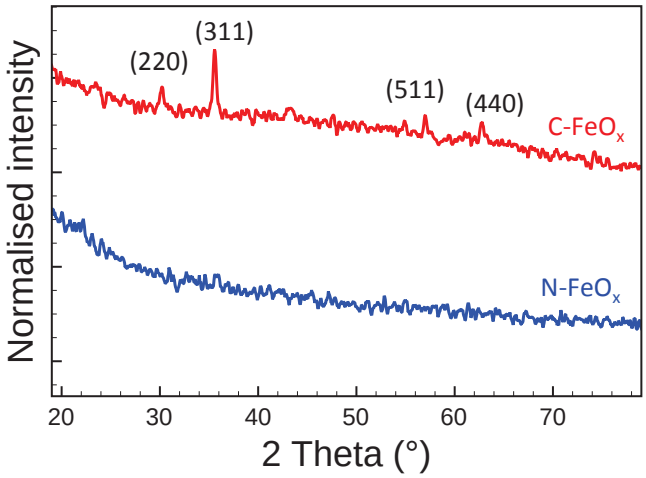

Figure 5.10 XRD patterns of C-FeO_x and N-FeO_x nanoparticles

The EELS spectra of the synthesised N-FeO_x and C-FeO_x nanoparticles are shown in Figure 5.11. There are three distinct features labelled A-C in the detailed structure of the O K-edge (Figure 5.11a). The O K-edges of reference materials are presented in Chapter 1 (Figure 23 [37]). The relative intensity of peak A at around 528 eV gradually increases from FeO to Fe_2O_3; B is a dominant feature around 537 eV, which remains rather similar for all iron oxide phases; C is a broad and featureless peak at about 558 eV. The measured relative intensity ratio of peak A to B (I_A/I_B) is 0.57 for N-FeO_x and 0.71 for the C-FeO_x sample. This indicates that the concentration of Fe^{3+} in N-FeO_x is less than that in the C-FeO_x nanoparticles. Comparing the ELNES of the Fe L-edges of these two samples, no significant difference is observed, except that the L_3 peak position of C-FeO_x sample is at 0.5-1 eV lower energy loss than that of the the N-FeO_x sample. However, the chemical shift from Fe^{2+} to Fe^{3+} is about 1.8 eV [38], the discrepancy of the energy shift at L_3 peak may be due to a complex mixture of iron oxide phases in the N-FeO_x sample.

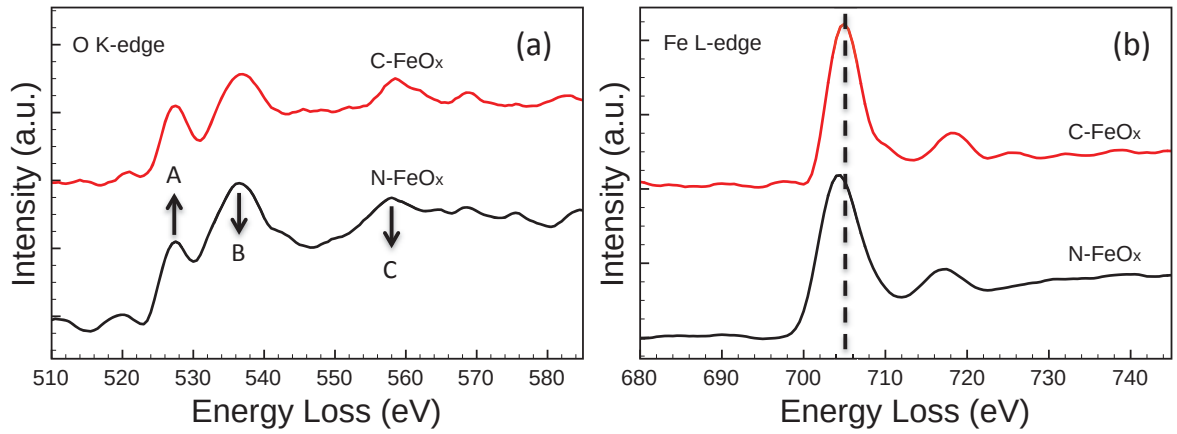

Figure 5.11 (a) O K-edge and (b) Fe L-edge ELNES of N-FeOx and C-FeOx nanoparticles.

The white-line intensity ratio was measured from the second derivative of over 40 EELS spectra of each sample, and the average L_3/L_2 values for N-FeO_x and C-FeO_x are 5.1±0.7

and 6.1 ± 0.8, respectively. The error was calculated from standard deviation. The relationship between the white-line intensity ratio and the valence state is not linear. Previous studies [39, 40, 37] demonstrate that the L_3/L_2 ratio is larger when the valence state of Fe is higher. From the XRD result, we know that the C-FeO_x nanoparticles are Fe_3O_4 with an average oxidation state of 2.67+, while the N-FeO_x nanoparticles have a lower oxidation state, which is consistent with the O K-edge analysis. The N-FeO_x could be FeO or a mixture of Fe and Fe_3O_4 since FeO is thermodynamically unstable tending to disproportionate to metal and Fe_3O_4 [41].

5.4 Summary and conclusions

In summary, in this chapter I considered the oxidation states of metal oxide nanoparticles, CeO_x, CuO_x, CoO_x and FeO_x, by STEM-EELS. The oxidation state was investigated by measuring the white-line ratio or performing MLLS fitting or comparing the O K-edge near structure with reference materials. We found about 60% of Ce^{3+} and 40% of Ce^{4+} in the CeO_x nanoparticles with an average diameter of 3.3 ± 0.8 nm. The average oxidation state of Ce ions was about 3.40+, and the results obtained from MLLS fitting and the white-line ratio calculation agreed with each other. Due to the small size of the CuO_x nanoparticles, the EELS spectra had a very poor signal-to-noise ratio at the Cu L-edge. O K-edges of the CuO_x particles were compared to the Cu_2O and CuO reference spectra. It has been found that over 60% of the CuO_x particles exhibited a similar shape and onset to Cu_2O in their O K-edge near structure, which means that the oxidation state of over half of the CuO_x particles is 1+. The XRD pattern of the CoO_x sample shows that the structure of the nanoparticles corresponds to Co_3O_4. The average oxidation state of small CoO_x nanoparticles (<15 nm) is lower than the bigger ones (>15 nm) indicating that the smaller CoO_x nanoparticles are O deficient comparing to the

bigger ones. The oxidation state of FeO_x nanoparticles varies when using different iron salts as precursors. The C-FeO_x nanoparticles synthesised with ammonium iron citrate correspond to Fe_3O_4 as confirmed by the XRD result. In contrast the N-FeO_x nanoparticles prepared with iron nitrate have lower oxidation state, which may reflect FeO or a mixture of Fe and Fe_3O_4. This study provides oxidation states of these metal oxide nanoparticles for further toxicity test, which can help to understand the relationship between oxidation states and the toxic properties of these nanoparticles.

References

[1] Zhang, M.; Respinis, M.; Frei, H. Time-resolved observations of water oxidation intermediates on a cobalt oxide nanoparticle catalyst. *Nat. Chem.* **2014**, *6*, 362–367

[2] Frey, N. A.; Peng, S.; Cheng, K.; Sun, S. Magnetic nanoparticles: synthesis, functionalization, and applications in bioimaging and magnetic energy storage. *Chem. Soc. Rev.* **2009**, *38*, 2532-2542

[3] Clavero, C. Plasmon-induced hot-electron generation at nanoparticle/metal-oxide interfaces for photovoltaic and photocatalytic devices. *Nat. Photon.* **2014**, *8*, 95–103.

[4] Karlsson, H. L.; Cronholm, P.; Gustafsson, J.; Moeller, L. Copper Oxide Nanoparticles Are Highly Toxic: A Comparison between Metal Oxide Nanoparticles and Carbon Nanotubes. *Chem. Res. Toxicol.* **2008**, *21*, 1726–1732.

[5] Chattopadhyay, S.; Dash, S. K.; Tripathy, S.; Das, B.; Mandal, D.; Pramanik, P.; Roy, S. Toxicity of Cobalt Oxide Nanoparticles to Normal Cells; An in Vitro and in Vivo Study. *Chem. Biol. Interact.* **2015**, *226*, 58–71.

[6] Pulido-Reyes, G.; Rodea-Palomares, I.; Das, S.; Sakthivel, T. S.; Leganes, F.; Rosal, R.; Seal, S.; Fernández-Piñas, F. Untangling the Biological Effects of Cerium Oxide Nanoparticles: The Role of Surface Valence States. *Sci. Rep.* **2015**, *5*, 15613.

[7] M. Tejamaya, I. Romer, R. C. Merrifield and J. R. Lead, Stability of Citrate, PVP, and PEG Coated Silver Nanoparticles in Ecotoxicology Media, *Environ. Sci. Technol.*, **2012**, *46*, 7011–7017

[8] V. V. Nikodinovska, K. Mladenovska, A.Grozdanov, Risks and health effects from exposure to engineered Nanostructures: A critical review, *J. Chem. Technol. Metall.*, **2015**, *50*, 117-134

[9] Vance, M. E.; Kuiken, T.; Vejerano, E. P.; McGinnis, S. P.; Hochella, M. F.; Hull, D. R. Nanotechnology in the Real World: Redeveloping the Nanomaterial Consumer Products Inventory. *Beilstein J. Nanotechnol.* **2015**, *6*,1769–1780.

[10] Stohs, S. J.; Bagchi, D. Oxidative Mechanisms in the Toxicity of Metal Ions. *Free Radic. Biol. Med.* **1995**, *18*, 321–336.

[11] Farina, M.; Avila, D. S.; Da Rocha, J. B. T.; Aschner, M. Metals, Oxidative Stress and Neurodegeneration: A Focus on Iron, Manganese and Mercury. *Neurochem. Int.* **2013**, *62*, 575–594.

[12] Valko, M.; Morris, H.; Cronin, M. T.D. Metals, Toxicity and Oxidative Stress. Curr. Med. Chem., **2005**, *12*, 1161-1208.

[13] Reaney, S. H.; Kwik-uribe, C. L.; Smith, D. R. Manganese Oxidation State and Its Implications for Toxicity. *Chem. Res. Toxicol.,* **2002**, *15*, 1119–1126.

[14] Auffan, M., Rose, J.,Wiesner, M. R. and Bottero, J. Y. Chemical stability of metallic nanoparticles: a parameter controlling their potential cellular toxicity in vitro. *Environ. Pollut*. **2009**, *157*, 1127–1133.

[15] Puzyn, T.; Rasulev, B.; Gajewicz, A.; Hu, X.; Dasari, T. P.; Michalkova, A.; Hwang, H.-M.; Toropov, A.; Leszczynska, D.; Leszczynski, J. Using Nano-QSAR to Predict the Cytotoxicity of Metal Oxide Nanoparticles. *Nat. Nanotechnol.* **2011**, *6*, 175–178.

[16] Briffa, S. M.; Lynch, I.; Trouillet, V.; Bruns, M.; Hapiuk, D.; Liu, J.; Palmer, R. E.; Valsami-Jones, E.; Valsami-Jones, E.; Lynch, I.; et al. Development of Scalable and Versatile Nanomaterial Libraries for Nanosafety Studies: Polyvinylpyrrolidone (PVP) Capped Metal Oxide Nanoparticles. *RSC Adv.* **2017**, *7*, 3894–3906.

[17] Merrifield, R. C.; Wang, Z. W.; Palmer, R. E.; Lead, J. R. Synthesis and Characterization of Polyvinylpyrrolidone Coated Cerium Oxide Nanoparticles. *Environ. Sci. Technol. Lett.* **2013**, *47*, 12426-12433.

[18] Lester, E.; Aksomaityte, G.; Li, J.; Gomez, S.; Gonzalez-Gonzalez, J.; Poliakoff, M. Controlled continuous hydrothermal synthesis of cobalt oxide (Co_3O_4) nanoparticles. *Prog. Cryst. Growth Ch.* **2012**, *58*, 3-13.

[19] Lester, E.; Tang, S.; Khlobystov, A.; Rose, V. L.; Buttery, L.; Roberts, C. J. Producing nanotubes of biocompatible hydroxyapatite by continuous hydrothermal synthesis. *CrystEngComm*. **2013**, *15*, 3256-3260.

[20] Moro, F.; Tang, S. Y.; Tuna, F.; Lester, E. Magnetic properties of cobalt oxide nanoparticles synthesized by a continuous hydrothermal method. *J. Magn. Magn. Mater.* **2013**, *348*, 1–7.

[21] Cote, L. J.; Teja, A. S.; Wilkinson, A. P.; Zhang, Z. J. Continuous hydrothermal synthesis of $CoFe_2O_4$ nanoparticles. *J. Mater. Res.* **2003**, *210*, 307–317.

[22] Cote, L. J.; Teja, A. S.; Wilkinson, A. P.; Zhang, Z. J. Continuous hydrothermal synthesis and crystallization of magnetic oxide nanoparticles. *J. Mater. Res.* **2002**, *19*, 2410–2416.

[23] Savitzky, A.; Golay, M.J.E. Smoothing and differentiation of data by simplified least-squares procedures. *Anal. Chem.* **1964**, *36*,1627–1639.

[24] Tsunekawa, S.; Sahara, R.; Kawazoe, Y.; Ishikawa, K. Lattice relaxation of monosize CeO_{2-x} nanocrystalline particles. *Appl. Surf. Sci*. **1999**, *152*, 53-56.

[25] Wu, L.; Wiesmann, H. J.; Moodenbaugh, A. R.; Klie, R. F.; Zhu, Y.; Welch, D. O.; Suenaga, M. Oxidation State and Lattice Expansion of CeO_{2-x} Nanoparticles as a Function of Particle Size. *Phys. Rev. B* **2004**, *69*, 125415.

[26] Manoubi, T.; Colliex, C.; Rez, P.; Quantitative electron energy loss spectroscopy on M_{45} edges in rare earth oxides. *J. Electron Spectrosc. Relat. Phenom.* **1990**, *50*, 1-18.

[27] Kurata, H.; Colliex, C. Electron-energy-loss core-edge structures in manganese oxides. *Phys. Rev. B* **1993**, *48*, 2102-2018.

[28] Pearson, D. H.; Ahn, C. C.; Fultz, B. White lines and d-electron occupancies for the 3d and 4d transition metals. *Phys. Rev. B* **1993**, *47*, 8471-8478.

[29] Haigh, S. J.; Young, N. P.; Sawada, H.; Takayanagi, K.; Kirkland, A. I. Imaging the Active Surfaces of Cerium Dioxide Nanoparticles. *ChemPhysChem* **2011**, *12*, 2397– 2399.

[30] Liu, X.H.; Qiu, G. Z.; Li, X. G. Shape-controlled synthesis and properties of uniform spinel cobalt oxide nanocubes. *Nanotechnology* **2005**, *16*, 3035–3040.

[31] Zhang, Z. L. Surface effects in the energy loss near edge structure of different cobalt oxides. *Ultramicroscopy* **2007**, *107*, 598–603.

[32] Verelst, M.; Ely, T. O.; Amiens, C.; Snoeck, E.; Lecante, P.; Mosset, A.; Respaud, M. Broto, J. M.; Chaudret, B. Synthesis and Characterization of CoO, Co_3O_4, and Mixed Co/CoO Nanoparticules. *Chem. Mater.* **1999**, *11*, 2702-2708.

[33] Stemmer, S.; Sane, A.; Browning, N. D.; Mazanec, T. J. Characterization of oxygen-deficient $SrCoO_{3-\delta}$ by electron energy-loss spectroscopy and Z-contrast imaging. *Solid State Ionics* **2000**, *130*, 71-80.

[34] Wang, Z. L.; Yin, J. S. Cobalt valence and crystal structure of $La_{0.5}Sr_{0.5}CoO_{2.25}$. *Philos. Mag. B* **1998**, *77*, 49-65.

[35] Zhang, Z. Surface effects in the energy loss near edge structure of different cobalt oxides, *Ultramicroscopy* **2007**, *107*, 598-603.

[36] Adschiri, T.; Kanazawa, K.; Arai, K. Rapid and Continuous Hydrothermal Crystallization of Metal Oxide Particles in Supercritical Water. *J. Am. Ceram. Soc.* **1992**, *75*, 1019–1022.

[37] Colliex, C.; Manoubi, T.; Ortiz, C. Electron-Energy-Loss-Spectroscopy near-Edge Fine Structures in the Iron-Oxygen System. *Phys. Rev. B* **1991**, *44*, 11402–11411.

[38] Van Aken, P.; Liebscher, B.; Styrsa, V. J. Quantitative Determination of Iron Oxidation States in Minerals Using Fe $L_{2,3}$-Edge Electron Energy-Loss near-Edge Structure Spectroscopy. *Phys. Chem. Miner.* **1998**, *25*, 323–327.

[39] Cosandey, F.; Su, D.; Sina, M.; Pereira, N.; Amatucci, G. G. Fe Valence Determination and Li Elemental Distribution in Lithiated $FeO_{0.7}F_{1.3}$/C Nanocomposite Battery Materials by Electron Energy Loss Spectroscopy (EELS). *Micron* **2012**, *43*, 22–29.

[40] Van Aken, P. A.; Liebscher, B. Quantification of Ferrous/ferric Ratios in Minerals: New Evaluation Schemes of Fe L23 Electron Energy-Loss near-Edge Spectra. *Phys. Chem. Miner.* **2002**, *29*, 188–200.

[41] Okada, T.; Saiki, T.; Taniguchi, S.; Ueda, T.; Nakamura, K.; Nishikawa, Y.; Iida, Y. Hydrogen Production Using Reduced-Iron Nanoparticles by Laser Ablation in Liquids. *ISRN Renew. Energy* **2013**, *2013*, 1–7.

Chapter 6 Characterisation of Pt-Cr Bimetallic Nanoparticles

In this chapter, the Pt-Cr samples investigated were prepared by G. Gupta of the School of Chemical Engineering, who also conducted the TEM, XPS and EDX. The STEM HAADF intensity analysis was conducted by the author and F. Yin. The synthesis procedure, TEM, EDX and XPS data are described in this chapter because the STEM HAADF analysis was based on these results. This work has been published in the paper *Pt Diffusion Dynamics for the Formation Cr–Pt Core–Shell Nanoparticles* (*Langmuir*, 2015, 31, 6917–6923 [Ref. 13]). Most of the text and figures are taken from this paper.

6.1 Introduction to bimetallic nanoparticles

Bimetallic nanoparticles attract great attention in the field of catalysts because of the possibility to enhance the catalytic performance and achieve new novel properties, which may not be obtained from monometallic particles [1-3]. The enhanced catalytic activity of bimetallic nanoparticles was usually interpreted by geometric effects (core-shell, coordination number and lattice spacing) and the change of electronic structures [4, 5]. Bimetallic nanoparticles constructed with noble and abundant metal elements provides a potential way to significantly reduce the use of noble metals and retain similar or superior catalytic activity at the same time.

The characterisation of bimetallic nanoparticles usually includes the elemental composition and distribution, which is quite challenging, especially for small particles (< 3 nm). In an electron microscope, small nanoparticles are very sensitive to the high-energy electron beam, they can either be damaged due to the knock-on and radiolysis

effects [6, 7] or generated very low signal for EDX and EELS analysis. STEM uses Z-contrast imaging, and the intensity in HAADF images is proportional to Z^n (n<2). It is possible to analyse the elemental distribution of small nanoparticles using HAADF images, since the acquire time is short and the signal-to-noise ratio is relatively high [8,9]. In this chapter, we studied the elemental distribution of wet-chemically synthesised Pt-Cr nanoparticles by analysing their HAADF intensity. Based on the average HAADF intensity analysis, we found that small nanoparticles are pure Pt and the large nanoparticles are Pt-Cr. Comparison between the experimental and simulated HAADF intensity profiles indicates that a Pt-Cr alloy is formed.

6.2 Experimental details

The synthetic strategy for the preparation of core-shell Pt-Cr nanoparticles was based on the pre-formation of Cr nanoparticles and later reduction of an intermediate Pt ion-containing supramolecular complex onto the Cr cores. This strategy aims at producing nanoparticles with a Pt monolayer shell on a Cr core. Synthesis procedure involves four steps as is shown in Figure 6.1: (1) the synthesis of a bipyridine Pt-chelating moiety [10, 11, 12] containing a diazonium cation (**D-BiPy**); (2) the formation of **D-BiPy-**functionalised Cr core nanoparticles stabilised by Cr-carbon bonds via diazonium reduction; (3) complexation of Pt(II) metal ions with the bipyridine chelating moieties of the **D-BiPy-**functionalised Cr core nanoparticles; (4) reduction of the Pt(II) metal ions on the pre-formed Cr nanoparticles [13].

The details of synthesising the layered Pt-Cr nanoparticles are as follow. First, a solution of D-BiPy in ethanol (10mL, 6mL) was mixed with $CrCl_3 \cdot 6H_2O$ ethanol solution (5mL, 6mM) under a continuous stirring condition for 10 min. Second, a $NaBH_4$ solution in

ethanol (5mL, 0.4M) was added to the mixture slowly; The colour changed to dark green, indicating the reduction of Cr precursor. Third, 30 min later, a solution of dichloro(1,5-cyclooctadiene) platinum(II) in ethanol (5mL, 6 mM) was added to the mixture prepared in the second step. Acetone was used to purify the nanoparticle precipitates and the black solid was dried in a vacuum oven at 40 °C.

In the one-pot synthesis, the reducing agent ($NaBH_4$) is present throughout but with diminished reducing power in the complexation stage. The deposition of Pt on the pre-formed Cr nanoparticles can be guided by two possible complexation routes. One route is the complexation of **BiPy** groups with Pt(II) metal ions and the other is the complexation with minuscule clusters consisting of very few Pt(II) metal ions and Pt(0) atoms [14, 15]. The pure Pt nanoparticles can be formed from the Pt precursor that is not involved in complex formation with the bipyridine chelating moieties.

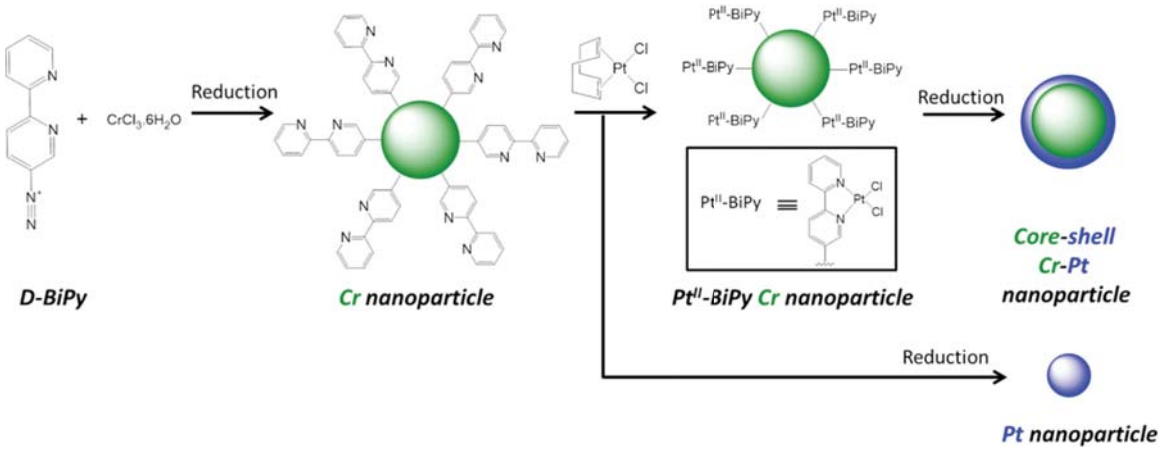

Figure 6.1 Schematic of synthesising procedures of layered core–shell bimetallic Cr–Pt nanoparticles in one pot. From reference [13].

The synthesised Pt-Cr nanoparticles were precipitated and then deposited on Cu grid coated with an amorphous carbon film and examined in a JEOL JEM2100F STEM with a

spherical aberration corrector (CEOS). HAADF images of the nanoparticles were acquired with inner and outer angles of 62 and 164 mrad at a probe convergence angle of 19 mrad and camera length of 10 cm. The integrated intensities and intensity line profiles were obtained using ImageJ software. The Cr core nanoparticles were characterised by TEM (FEI Tecnai TF20 coupled with an Oxford Instruments INCA 350 EDX system operated at an acceleration voltage of 200 kV) and the oxidation states of the Pt-Cr nanoparticles were characterised by X-ray photoelectron spectroscopy (XPS) using an AXIS Nova instrument. High resolution scans of Pt 4f, C 1s, N 1s, and Cr 2p were carried out using a monochromatic Al Kα X-ray source with a step size of 0.1 eV.

6.3 Results and discussion

6.3.1 TEM and XPS analysis

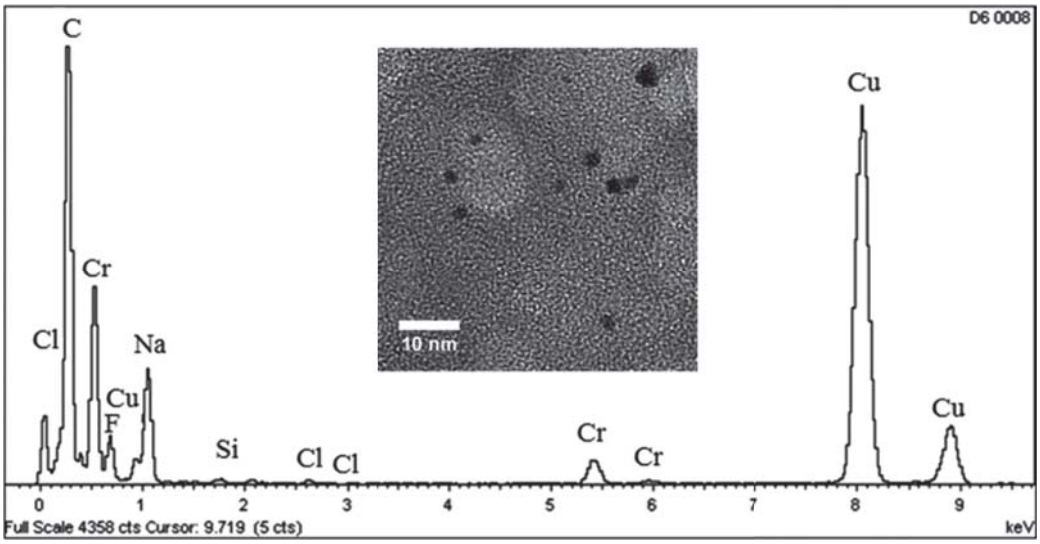

Figure 6.2 TEM image (inset) and TEM EDX spectrum of pre-formed Cr nanoparticles. From reference [13].

The preformed Cr nanoparticles were characterised by TEM and EDX (Figure 6.2). The TEM image (inset of Figure 6.2) confirms the formation of monodispersed Cr

nanoparticles, which have an average size of 1.8 ± 0.3 nm. The element composition of the nanoparticles was determined by the EDX spectrum in Figure 6.2 and the nanoparticles are confirmed to be Cr. Other elements (Na, Si, F) are also detected because of the residuals from the preparation procedure.

Figure 6.3 shows the high-resolution XPS spectra of the Pt-Cr nanoparticles. Several samples were analysed, and the results presented herein are based on the samples in which both Cr and Pt are presented. It is worth noting that XPS analysis of some sample areas showed only the presence of Pt and not Cr. This indicates that the Pt precursor, which did not form a complex with the bipyridine chelating moieties, had undergone reduction and formation of pure Pt nanoparticles during the preparation of the layered core-shell Pt-Cr nanoparticles.

The XPS N 1s peak (Figure 6.3a) centred at 399.7 eV can be ascribed to the pyridine nitrogen in the **D-BiPy** molecules. The O 1s spectrum is a single peak at 531.4 eV, which indicates the presence of metal (either Cr or Pt) oxide and/or hydroxide on the Pt-Cr nanoparticles. The presence of two doublets in the Cr 2p spectrum (Figure 3c) means that Cr exists in metallic as well as oxidised form. The doublet with peaks centred at 576.4 and 585.6 eV is assigned to the metallic Cr. The other doublet at 577.5 and 587.3 eV is attributed to the Cr oxide in its oxidised state (III) [16,17]. The oxidised to metallic Cr ratio is 4:1 measured by the integrated intensities of the two doublet peaks. The Pt 4f spectrum indicates the existence of metallic Pt with binding energy values of 71.6 and 74.9 eV. A similar amount of $Pt(OH)_2$, whose doublet peaks area at 72.8 and 76.1 eV [16], was also extracted from the Pt spectrum.

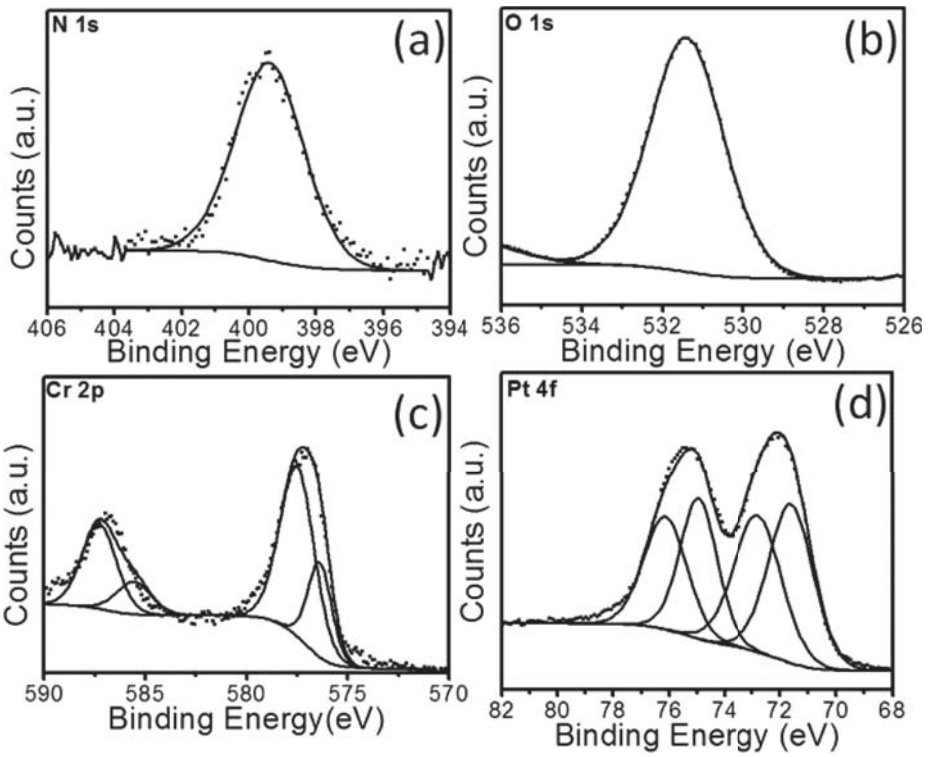

Figure 6.3 XPS spectra of the synthesised Pt-Cr nanoparticles from the peak regions of N 1s (a), O 1s (b), Cr 2p (c), and Pt 4f (d). From reference [13].

6.3.2 STEM-HAADF analysis

The formation of core-shell Pt-Cr nanoparticles can't be determined from the XPS analysis. However, the XPS results reveal that the nanoparticles consist of Pt and Cr and that a high percentage of Cr is in its oxidised form. To determine the atomic structure of the Pt-Cr nanoparticles, STEM-HAADF studies were applied. Because STEM uses Z (atomic number) contrast imaging, the intensity (I) in the HAADF images is proportional to Z^n, where n=1.46 ± 0.18 based on our previous calibration [18]. Therefore, the HAADF intensity of a Pt atom (Z=78) is about 5.6 times brighter than that of one Cr atom (Z=24). Hence, structural and chemical information can be obtained simultaneously by analysing the HAADF intensity of the bimetallic nanoparticles.

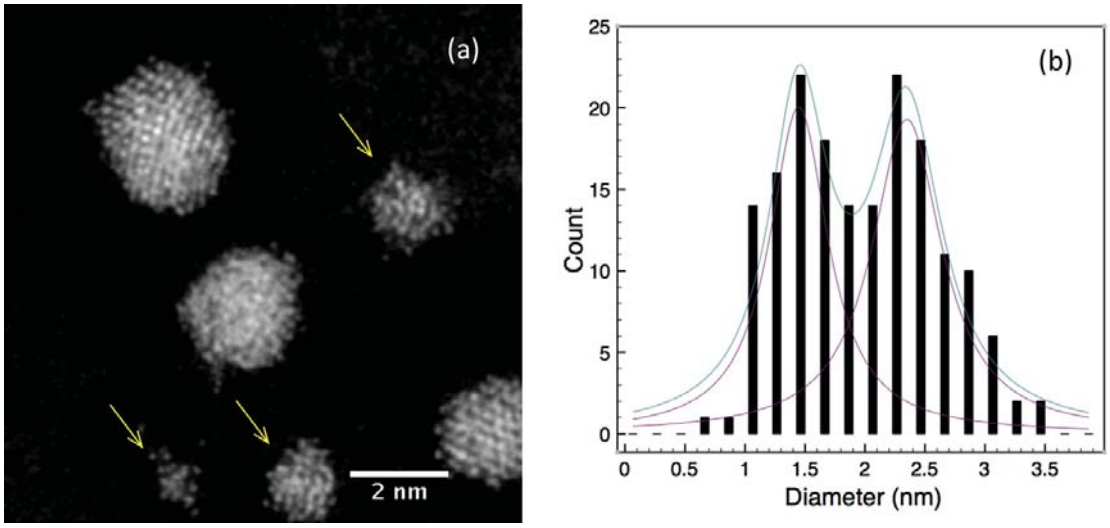

Figure 6.4 A representative STEM-HAADF image (a) and a size distribution (b) of Pt-Cr nanoparticles. Gaussian fitting was performed in the size distribution histogram, which shows two fitting peaks at 1.45 ± 0.25 and 2.35 ± 0.30 nm, respectively. Small particles are indicated with arrows. From reference [13].

An example STEM-HAADF image is shown in Figure 6.4a, and the size distribution is presented in Figure 6.4b. Two kinds of nanoparticles (small and large) are observed in the STEM images, and the statistical data show that the diameter of the small nanoparticles (indicated by yellow arrows in Figure 6.4a) is 1.45 ± 0.25 nm and that the large ones is 2.35 ± 0.30 nm. Comparing with the size of the pre-formed Cr core nanoparticles (~1.8 nm determined by TEM), the size of the small nanoparticles is even smaller. This observation suggests that the smaller nanoparticles are neither pure Cr nor bimetallic nanoparticles but pure Pt nanoparticles considering the size and HAADF intensity, which is also supported by the XPS data. Further to the XPS data, the relationships of the HAADF intensity versus the volume of the nanoparticles were drawn in Figure 6.5. In the diagram (Figure 6.5a) of integrated HAADF intensity versus the nanoparticle volume (R^3), there are more data points below the fitting line when R^3

> 2, demonstrating a lower percentage of Pt in the larger nanoparticles. The change of intensity against the nanoparticle size can be seen clearly in the diagram of the average HAADF intensity (I/R^3) versus R^3 in Figure 6.5b. The smaller nanoparticles (R^3 > 2) have the highest I/R^3 value, enabling us to assign them as pure Pt nanoparticles.

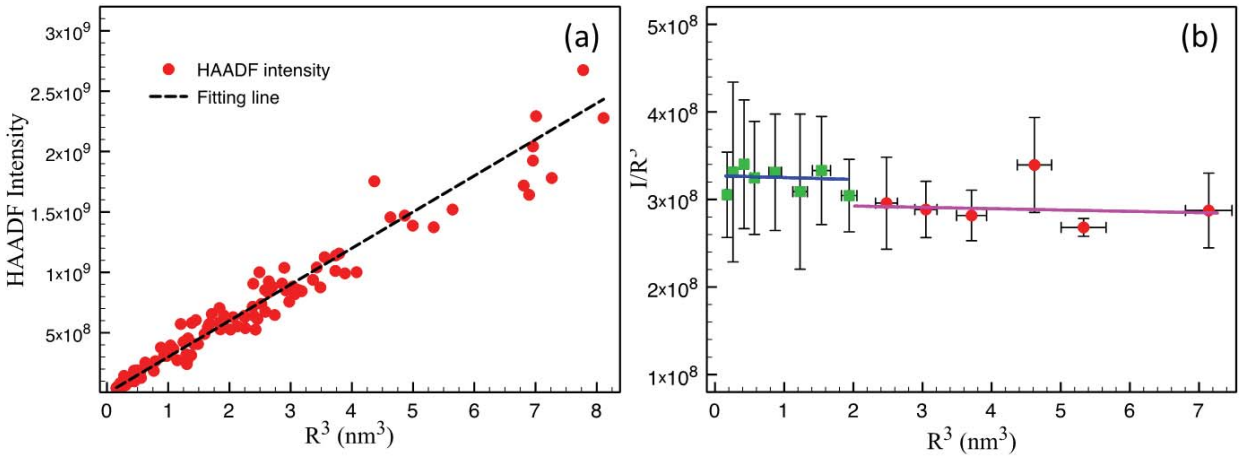

Figure 6.5 (a) A diagram of integrated HAADF intensity against the nanoparticle volume; (b) A diagram of average HAADF intensity versus the nanoparticle volume. From reference [13].

6.3.3 HAADF intensity line profiles simulations

The larger nanoparticles are expected to be the Pt-Cr nanoparticles, since the average diameter of the larger nanoparticles is 0.55 nm (as thick as a single layer of Pt atoms) bigger than the pre-formed Cr core nanoparticles. In order to identify the structure of the Pt-Cr nanoparticles, we simulated the HAADF intensity line profiles of different core-shell models. The models we employed were based on a simple geometrical structure, which is a spherical core with a concentric spherical shell. The HAADF intensities at different positions depend on the height of the projected atomic column, with each atom contributing a $Z^{1.46}$-dependent intensity. Based on the TEM, XPS and

STEM results, the model size of the Pt-Cr nanoparticles was set to be 2.35 nm with a 1.8 nm core in diameter. Since 80% of the Cr atoms are in oxide form suggested by XPS analysis and that Cr_2O_3 is the most stable form [19] among the different chromium oxides, Cr_2O_3 was considered in the HAADF intensity simulations. The total number of Pt atoms is constrained with the assumption that a single layer of Pt shell is formed and the number of Cr atoms is determined by the size of the pre-formed Cr core. The densities used in the calculation are the bulk densities of Pt (21.45 g/cm^3), Cr (7.19 g/cm^3) and Cr_2O_3 (5.22 g/cm^3). Because of the big intensity contrast between the O and Pt atoms in the HAADF images, the intensity of O atoms in the Pt oxides was ignored.

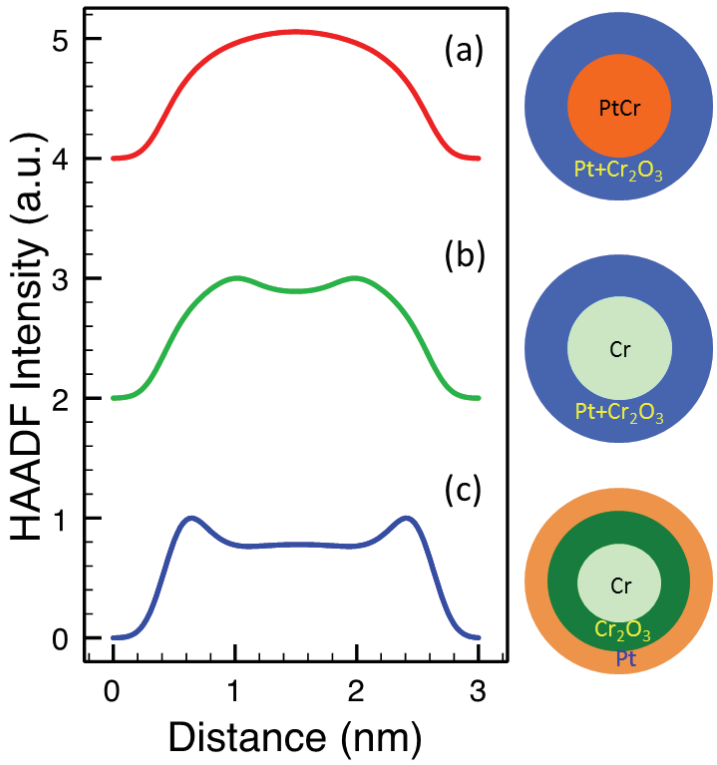

Figure 6.6 Simulated HAADF intensity line profiles for three types of structures: (a) Pt–Cr/Cr_2O_3–Pt, (b) Cr/Cr_2O_3–Pt and (c) Cr–Cr_2O_3/Pt. The corresponding models are presented on the right. The calculated line profiles were convolved with a Gaussian function for smoothing process. From reference [13].

Figure 6.6 shows the simulated HAADF intensity line profiles of three different configurations. The intensity line profiles of Cr-core and Pt-shell configurations (Figure 6.6b, c) are concave in the centre indicating a dark core and a bright shell. Line profiles having brighter core or a nearly flat contrast in the centre indicates a mixture of Cr and Pt atoms in the nanoparticles (Figure 6.6a). The negligible intensity change at the Cr/Cr_2O_3 and the $Pt–Cr/Pt–Cr_2O_3$interface proves that the ignorance of the O HAADF intensity in the Pt oxide is acceptable.

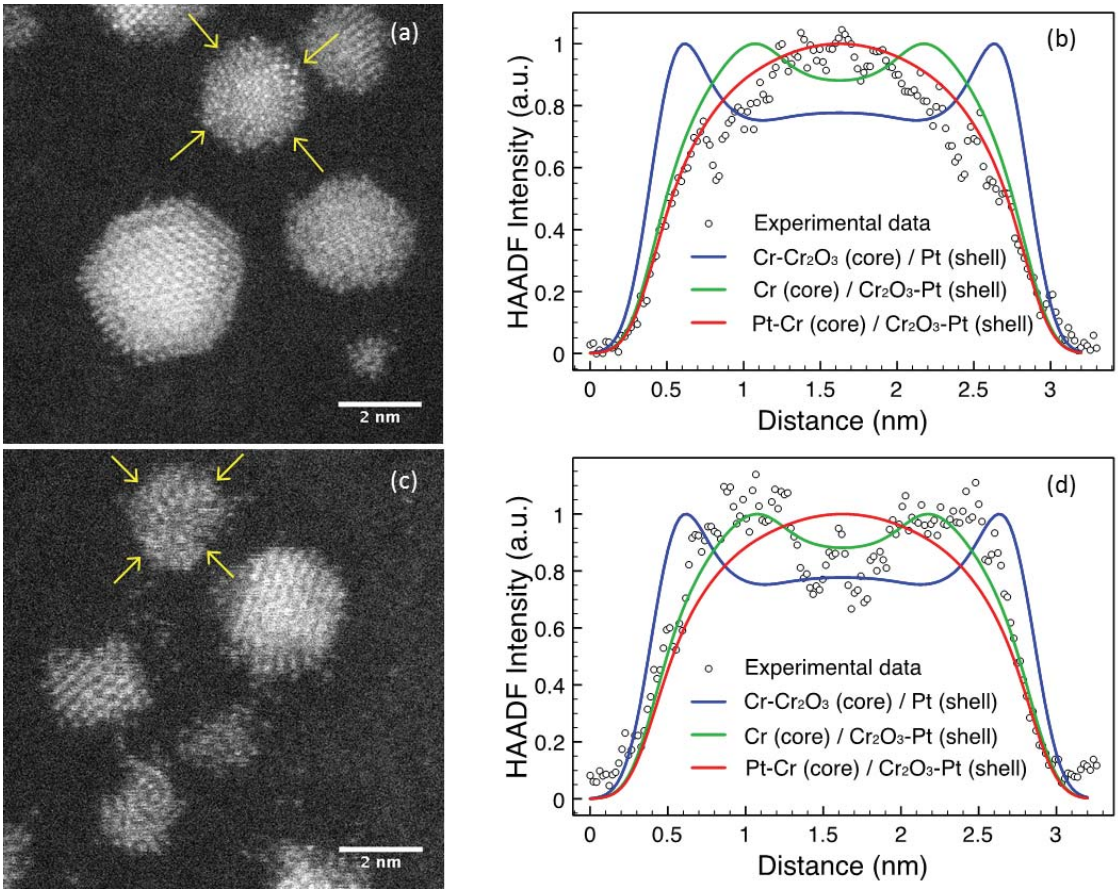

Figure 6.7 (a, c) High-resolution STEM images and (b, d) experimental and simulated HAADF intensity line profiles for Pt-Cr nanoparticles. The experimental average profiles (hollow circles) were measured along the lines indicated by the yellow arrows with 4.1-Å-wide bands. From reference [13].

Comparison between the experimental and simulated HAADF line profiles is shown in Figure 6.7. From the typical STEM-HAADF images, we find that most of the Pt-Cr nanoparticles do not display typical core-shell structures as the intensity line profiles shown in Figure 6.6b, c. An example of the experimental HAADF intensity profiles is presented in Figure 6.7b (hollow circle curve) and its line profile shows a brighter or a nearly flat contrast central area, which is consistent with the intensity profile (the red curve) calculated from the structure of Pt–Cr (core)/Cr_2O_3–Pt (shell). Statistical analysis of 182 Pt-Cr nanoparticles has revealed that ~98% of the studied nanoparticles presents a profile similar to this model. Only about 2% of the nanoparticles exhibited concave HAADF line profiles (i.e., Pt-rich shell) as indicated in Figure 6.7 c, d.

These observations suggest that Pt atoms have diffused from the surface into the core and formed a Pt-Cr alloy core and shell. The diffusion of Pt atoms can be explained by Cabrera–Mott theory. Based on the theory, the Mott potential built up across the oxide layer due to a contact potential difference between metal and adsorbed oxygen can drive both anion and cation transport across the oxide film at low temperature [20]. The Pt atoms will tend to diffuse into the core of the bimetallic nanoparticles through the established field-assisted diffusion mechanism [21], when the Pt atom deposits on the oxide layer, due to its high electron affinity. This behaviour leads to the formation of Pt-Cr alloyed core and shell nanoparticles.

6.4 Summary and Conclusions

In summary, I characterized the layered core-shell bimetallic Pt-Cr nanoparticles synthesised by the reduction of an intermediate Pt-ion-containing complex onto pre-formed Cr nanoparticles. The composition and structure of the bimetallic Pt-Cr nanoparticles were studied by STEM analysis, and compared with XPS and TEM data of

collaborations. The HAADF intensity analysis shows that the small nanoparticles observed in STEM-HAADF images with a diameter of 1.45 ± 0.25 nm are pure Pt nanoparticles, and that the larger nanoparticles whose diameter is 2.35 ± 0.30 nm are ascribed to Pt-Cr bimetallic nanoparticles. The HAADF intensity line profile results indicate the formation of Pt and Cr mixed core and shell. Field-assisted diffusion of the Pt atoms is tentatively attributed to be the main reason for the formation of the Pt-Cr mixed nanoparticles.

References

[1] Park, J. Y.; Zhang, Y.; Grass, M.; Zhang, T.; Somorjai, G. A. Tuning of Catalytic CO Oxidation by Changing Composition of Rh–Pt Bimetallic Nanoparticles. *Nano Lett.* **2008**, *8*, 673–677.

[2] Wang, A. Q.; Chang, C. M.; Mou, C. Y. Evolution of Catalytic Activity of Au-Ag Bimetallic Nanoparticles on Mesoporous Support for CO Oxidation. *J. Phys. Chem. B* **2005**, *109*, 18860–18867.

[3] Hou, W.; Dehm, N. A.; Scott, R. W. J. Alcohol Oxidations in Aqueous Solutions Using Au, Pd, and Bimetallic AuPd Nanoparticle Catalysts. *J. Catal.* **2008**, *253*, 22–27.

[4] Koffi, R. C.; Coutanceau, C.; Garnier, E.; Léger, J. M.; Lamy, C. Synthesis, Characterization and Electrocatalytic Behaviour of Non-Alloyed PtCr Methanol Tolerant Nanoelectrocatalysts for the Oxygen Reduction Reaction (ORR). *Electrochim. Acta* **2005**, *50*, 4117–4127.

[5] Zhang, J.; Lima, F. H. B.; Shao, M. H.; Sasaki, K.; Wang, J. X.; Hanson, J.; Adzic, R. R. Platinum Monolayer on Nonnoble Metal–Noble Metal Core–Shell Nanoparticle Electrocatalysts for O2 Reduction. *J. Phys. Chem. B*, **2005**, 109, 22701–22704

[6] Banhart, F. Irradiation Effects in Carbon Nanostructures Irradiation Effects in Carbon Nanostructures. *Rep. Prog. Phys.* **1999**, *62*, 1181–1221.

[7] Egerton, R. F.; Li, P.; Malac, M. Radiation Damage in the TEM and SEM. *Micron* **2004**, *35*, 399–409.

[8] Yin F.; Wang Z. W.; Palmer R. E. Controlled Formation of Mass-Selected Cu–Au Core–Shell Cluster Beams. *J. Am. Chem. Soc.*, **2011**, *133*, 10325–10327

[9] Jian, N.; Palmer, R. E. Variation of the Core Atomic Structure of Thiolated ($Au_xAg_{1-x})_{312\pm55}$ Nanoclusters with Composition from Aberration-Corrected HAADF STEM. *J. Phys. Chem. C* **2015**, *119*, 11114–11119.

[10] Weinstein, J. A.; Zheligovskaya, N. N.; Mel'nikov, M. Y.; Hartl, F. Spectroscopic (UV/VIS, resonance Raman) and spectroelectrochemical study of platinum(II) complexes with 2,2 '-bipyridine and aromatic thiolate ligands. *J. Chem. Soc., Dalton Trans.* **1998**, 2459– 2466

[11] Tang, W. S.; Lu, X. X.; Wong, K. M. C.; Yam, V. W. W.Synthesis, photophysics and binding studies of Pt(II) alkynyl terpyridine complexes with crown ether pendant. Potential luminescent sensors for metal ions. *J. Mater. Chem.* **2005**, *15*, 2714– 2720.

[12] Muro, M. L.; Diring, S.; Wang, X. H.; Ziessel, R.; Castellano, F. N. Photophysics in Platinum(II) Bipyridylacetylides. *Inorg. Chem.* **2009**, *48*, 11533– 11542.

[13] G. Gupta, P. Iqbal, F. Yin, J. Liu, R. E. Palmer, S. Sharma, K. C.-F. Leung, P. M. Mendes. Pt diffusion dynamics on the formation Pt-Cr core-shell nanoparticles. *Langmuir* **2015**, *31*, 6917–6923.

[14] West, J. L.; Halas, N. J.Engineered Nanomaterials for Biophotonics Applications: Improving Sensing, Imaging, and Therapeutics. *Annu. Rev. Biomed. Eng.* **2003**, *5*, 285–292.

[15] Frey, N. A.; Peng, S.; Cheng, K.; Sun, S. Magnetic Nanoparticles: Synthesis, Functionalization, and Applications in Bioimaging and Magnetic Energy Storage. *Chem. Soc. Rev.* **2009**, *38*, 2532– 2542.

[16] Moulder, J. F.; Stickle, W. F.; Sobol, P. E.; Bomben, K. D. Handbook of X-ray Photoelectron Spectroscopy; Physical Electronics: Minnesota, 1995.

[17] Biesinger, M. C.; Brown, C.; Mycroft, J. R.; Davidson, R. D.; McIntyre, N. S. X-Ray Photoelectron Spectroscopy Studies of Chromium Compounds. *Surf. Interface Anal.* **2004**, *36*, 1550–1563.

[18] Wang, Z. W.; Palmer, R. E. Intensity Calibration and Atomic Imaging of Size-Selected Au and Pd Clusters in Aberration-Corrected HAADF-STEM. *J. Phys.: Conf. Ser.* **2012**, *371*, 012010.

[19] Brady, P. V. The Physics and Chemistry of Mineral Surfaces; CRC Press, 1996.

[20] Subramanian, N. D.; Moreno, J.; Spivey, J. J.; Kumar, C. Copper Core-Porous Manganese Oxide Shell Nanoparticles J. Phys. Chem. C 2011, 115, 14500– 14506

[21] Barnhart, J.Occurrences, Uses, and Properties of Chromium Regul. Toxicol. Pharmacol. 1997, 26, S3– S7

Chapter 7 Internal Order Determined by Choice of Iron Salt Precursor in Continuous Hydrothermally Prepared Fe-Co Bimetallic Nanoparticles

The Fe-Co oxide nanoparticles considered here were synthesised by Selina Vi Yu Tang of Promethean Particles Ltd in Nottingham. The XRD data were collected by Isabella R. Roche in the School of Geography. The STEM-HAADF, -EDX, and -EELS measurements and analysis were done by me.

7.1 Introduction to Fe-Co nanoparticles

Magnetic nanoparticles have attracted considerable attention in the recent decades, not only because of the fundamental research interest concerning the shape/size effects, but also for their many important technological applications in the fields of biomedicine [1,2], information storage [3], ferrofluid technology [4, 5] etc. Fe-Co oxide nanoparticles are one of the most interesting and important magnetic materials because of their chemical stability, mechanical hardness, high magnetic anisotropy and moderate saturation magnetisation [6-8].

There are many factors, such as size, morphology, composition, and cation distributions, which can affect the magnetic properties of the Fe-Co nanoparticles. Joshi et al. [9] reported that the saturation magnetisation of the cobalt ferrite nanoparticles increased with an increase in size, and that the faceted irregular nanoparticles exhibit lower saturation magnetisation than the spherical ones, possibly because of the preferential growth of crystal toward the easily magnetized crystallographic direction induces the

higher shape anisotropy. Sathya et al. [10] studied the effect of composition stoichiometry on the magnetic properties of cobalt ferrite nanoparticles. They reported that the specific absorption rate (relevant for magnetic hyperthermia) and the relaxivity value (significant for magnetic resonance imaging, MRI) of the cobalt ferrite ($Co_xFe_{3-x}O_4$) NPs could be tuned not only by the NP's size, but also by the Fe/Co ratio. They concluded that particles of 20 ± 2 nm in size and Co stoichiometry (x) in the x=0.5–0.7 range are promising candidates as heat mediators for both hyperthermia and MRI applications. Fe-Co oxide NPs usually have a spinel structure with unit formula AB_2O_4, where *A* and *B* stand for tetrahedral and octahedral cation sites within the close packed array of oxygen atoms [11]. The metal ion distribution in different sites also has a strong influence on its magnetic properties. The information of cations (Fe^{3+}, Co^{3+}, Fe^{2+}, Co^{2+}) distribution in the $Co_{1+x}Fe_{2-x}O_4$ ($0 \leq x \leq 1$) nanoparticle can be obtained by the Mössbauer spectroscopy [12-14]. Liu et al [15] reported that the migration of Co^{2+} ions from A to B sites could result in an increase in the saturation magnetization and coercivity.

The hydrothermal method is one of the most widely used synthesis protocols for the preparation of metal oxide NPs [16, 17]. By adjusting the synthesis conditions, such as pH, reaction temperature, Co to Fe ratio and surfactants, the particle morphology and Co to Fe ratio in the NPs can be adjusted [16,18,19] The control of cation distribution can be achieved by changing the reaction time [15] or the post-annealing and quenching conditions [20, 21]. However, the effect of synthesis conditions on the elemental distribution of the Fe ad Co in the nanoparticles is rarely discussed. Undoubtedly, the inhomogeneous alloying in Fe-Co nanoparticles will affect their magnetic properties. Antoniak et al [22] reported a 20-30% reduction of magnetic moment of FePt

nanoparticles with respect to the bulk material, because of the composition inhomogeneity in the particles. Additionally, using a seeded growth procedure, López-Ortega et al. [23] synthesised $Mn_xFe_{3-x}O_4/Fe_xMn_{3-x}O_4$ bi-magnetic core/shell nanoparticles, the heterostructured NPs showed a strong exchange coupling between the core and shell resulting in a coercivity increase.

In this Chapter, we studied two batches of Fe-Co oxide nanoparticles synthesised by a continuous-flow hydrothermal method. The samples were well-characterised by XRD, STEM-HAADF, -EDX and -EELS methods. We found that by changing the iron salt, from iron nitrate to ammonium iron citrate, the internal order (crystallinity, elemental distribution, etc.) in the Fe-Co oxide NPs can be changed.

7.2 Synthesis procedure and experimental details

The synthesis of Fe-Co oxide nanoparticles was conducted in a high-pressure equipment using a continuous-flow hydrothermal reactor which is the same equipment as mentioned in the experimental section in Chapter 5. This method has previously been described in the literatures [24-28] and a schematic of the continuous supercritical water reactor system is shown in Figure 7.1.

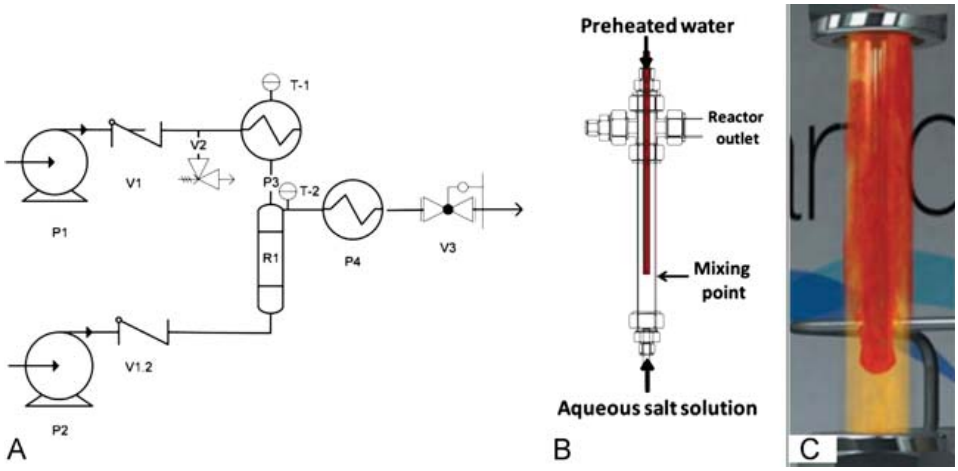

Figure 7.1 (A) A schematic diagram of the continuous hydrothermal reactor system: P1, P2 are Gilson HPLC pumps; P3, water preheater; P4, cooler; R1, nozzle reactor; V1, V1.2 are check valves; V2, pressure relief valve; V3, Tescom backpressure regulator; T1, T2, thermocouples. (B) A schematic of the designed nozzle reactor [25]. (C) An animated depiction of the Nozzle reactor. [26]

Briefly, deionised water is pumped into an electric preheater at a rate of 20 ml/min and is heated up to 400 °C. The supercritical water then flows into the Nozzle reactor section of the system. At the same time, a flow of aqueous metal salt solution is pumped up from the bottom at a rate of 10 ml/min at ambient temperature. The Co precursor used here is cobalt (II) acetate tetrahydrate ($Co(C_2H_3O_2)_2{\cdot}4H_2O$, Sigma-Aldrich) and Fe precursors are iron (III) nitrate nonahydrate ($Fe(NO_3)_3{\cdot}9H_2O$, Sigma Aldrich) and ammonium iron (III) citrate ($C_6H_8O_7{\cdot}xFe^{3+}{\cdot}yNH_3$, Sigma-Aldrich). Depending on samples, different Fe to Co ratio is employed in the metal salt solutions and the total concentration of cations was 0.05 mol/L. A summary of sample codes and precursor concentrations is given in Table 1.

Table 7.1 Summary of precursor concentrations used for each sample.

Sample code	Fe/Co ratio	Cobalt acetate (M)	Ammonium iron citrate (M)	Iron nitrate (M)
INN-1	1:3	0.0375	-	0.0125
INN-2	1:1	0.0250	-	0.0250
INN-3	3:1	0.0125	-	0.0375
AIC-1	1:3	0.0375	0.0125	-
AIC-2	1:1	0.0250	0.0250	-
AIC-3	3:1	0.0125	0.0375	-

For the AIC-1 sample, the water flow feed also contained 0.25% v/v hydrogen peroxide (H_2O_2, Fisher Scientific, UK). Hydrogen peroxide was used here to drive oxidation of the

cobalt precursor. A reaction temperature of 400 °C was chosen to keep a high rate of conversion and the whole system pressure was maintained at 240 bar by a backpressure regulator. The collected samples were washed by centrifugation or filtration.

The nanoparticles were deposited on Cu grids covered with continuous amorphous carbon film and were then characterised in a 200 kV JEM2100F scanning transmission electron microscope (STEM) with a spherical aberration probe corrector (CEOS). HAADF images were acquired at camera length of 10 cm. The inner and outer collection angles of the Gatan HAADF detector are 62 and 164 mrad, respectively and the convergence angle of the probe is 19 mrad. EDX mapping (obtained with a Bruker XFlash 4030 detector) was employed to determine the average elemental compositions of a certain area. EELS single spectra and mapping were recorded with a Gatan Enfina detector (1340 channels) at camera length 2 cm and collection semi-angle 57.8 mrad on the Enfina detector. The aperture size is 3 mm and the energy dispersion is 0.5 eV/channel. The acquisition time for single EELS spectrum is 5s. A Jeol ADF detector was used to acquire the ADF images. The spectra were analysed with the DigitalMicrograph software. The X-ray diffraction (XRD) patterns were collected using a Bruker D8 powder diffractometer using Cu Kα radiation (λ = 1.5406 Å).

7.3 Results and discussion

7.3.1 Morphology and crystallisation

Figure 7.2 shows the HAADF images and corresponding histograms of NP diameter for the samples from the INN and AIC batches. In both cases, the NPs were aggregated.

However, the level of agglomeration of the NPs in the AIC sample series was higher than that in the INN series. From the size distribution histograms, it can be seen that the diameter ranged from around 5 to 30 nm, and that the AIC sample series had more large particles (>15 nm). Overall, the average diameters of the two batches of samples were close to each other. Changing the iron salt in the solution seems to have an effect on the dispersion of the hydrothermally synthesised Fe-Co NPs.

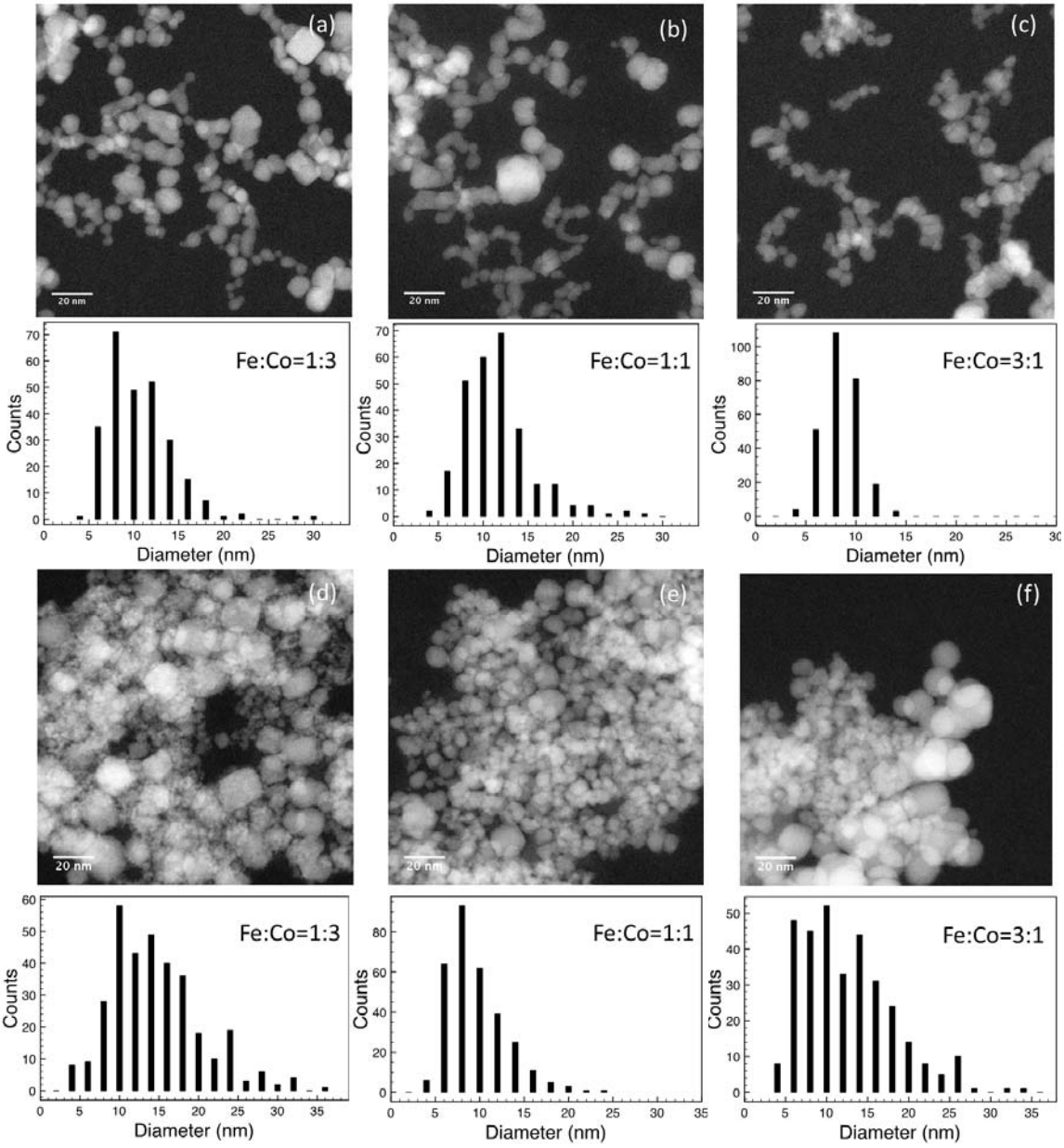

Figure 7.2 HAADF images of sample (a) INN-1, (b) INN-2, (c) MINN-3, (d) AIC-1, (e) AIC-2 and (f) AIC-3. The corresponding diameter histograms are underneath and the

measured average diameter are 10.6±3.6 nm, 11.5±3.8 nm, 8.6±1.7 nm, 13.0±5.2 nm, 8.3±2.5 nm, and 10.2±6.2 nm, respectively.

The morphology difference between the two batches of samples can also be seen in the two pure iron oxide nanoparticle samples synthesised with $Fe(NO_3)_3{\cdot}9H_2O$ and $C_6H_8O_7{\cdot}xFe^{3+}{\cdot}yNH_3$ precursors, respectively (Figure 5.9 in Chapter 5). A similar agglomeration was observed. The XRD data (Figure 5.10) demonstrated that the FeO_x nanoparticles synthesised with $Fe(NO_3)_3{\cdot}9H_2O$ is amorphous, while the other one is crystallised. Therefore, the nanoparticles dispersion and crystallinity seem to be controlled by the iron salt precursors in the solutions. In the case of pure iron oxide samples, the diameter of nanoparticles prepared with $C_6H_8O_7{\cdot}xFe^{3+}{\cdot}yNH_3$ precursor (17.5 ± 4.2 nm) is bigger than that synthesised with $Fe(NO_3)_3{\cdot}9H_2O$ precursor (6.5± 1.4 nm). This is different from what we observed in the Fe-Co oxide samples, which means that the nanoparticle size of the Fe-Co oxide sample may be related not only to the anion species, but also to the co-existence of Co cations in the solution.

The XRD results from the INN and AIC sample series are shown in Figure 7.3. The XRD spectra of the INN samples (Figure 7.3a) suggested that the Fe-Co oxide NPs from INN-2 and -3 are not well crystallised, since the diffraction peaks are weak and broad. The crystallite sizes of Fe-Co nanoparticles in the INN series are calculated using the Scherer equation and are found to be about 6.9 nm, 4.2 nm, and 4.4 nm for sample INN-1, -2 and -3, respectively. These values are smaller than those measured from the STEM-HAADF images, which suggests that the Fe-Co NPs probably have segregated Fe-rich and Co-rich regions since these regions have different lattice parameters when the Fe/Co ratio varies [15, 29]. This was also supported by the EELS mapping analysis shown below.

Figure 7.3b shows clear XRD patterns from the AIC samples, which correspond to the AB_2O_4 structure [30,31]. The sharp peaks indicated that these particles were more crystallised than those in the INN sample series. The average crystallite sizes calculated from XRD patterns of AIC-1, -2 and -3 are around 13.3 nm, 9.2 nm and 10.6 nm, respectively, which agree with the microscope measurements, indicating a high level of crystallinity.

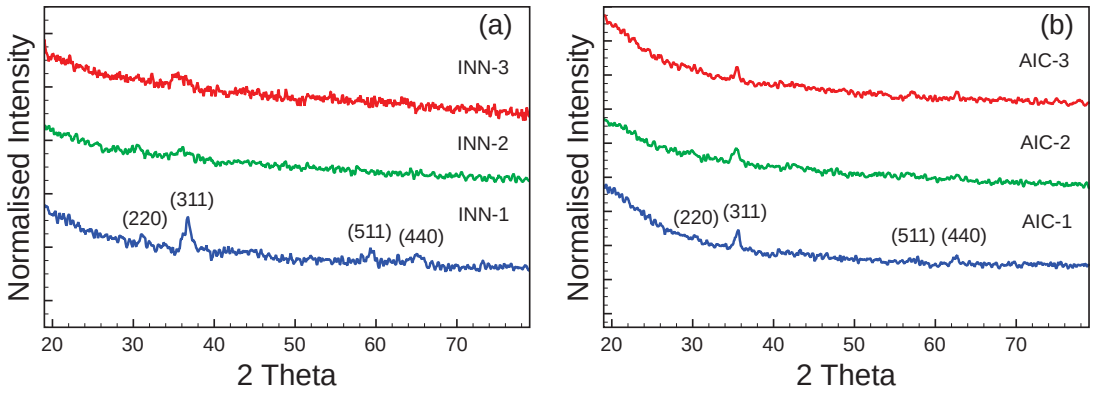

Figure 7.3 XRD patterns of the sample series (a) INN and (b) AIC.

7.3.2 Elemental composition by EDX and EELS

Table 2 shows the elemental compositions of each sample in the INN and AIC series. It is important to note that the Fe/Co ratios of the synthesised INN samples are close to the ratios in the metal salt solutions. In the case of the AIC samples, these two ratios are very different, and the Fe/Co ratios detected in the particles are always higher than in the solutions. This may be caused by the ammonium citrate in the solutions. In the hydrothermal synthesis of iron oxide particles from ammonium iron citrate, it has been reported that the Fe^{3+} can be reduced to Fe^{2+} by the carbon monoxide formed from the thermal decomposition of ammonium citrate in the supercritical water [32,33]. In a reducing environment, the oxidation of Co^{2+} to Co^{3+} will also be highly suppressed and

the precipitation of Co ions from the solution will become more difficult [16]. This could explain why the Co content detected in the AIC samples was always lower than expected. For the samples in the INN series, where iron nitrate was used as the precursor, the nitrate ions might act as an oxidation agent to drive the Co^{2+} to Co^{3+}.

Table 7.2 Elemental compositions of the samples from INN and AIC batches determined by STEM-EDX mapping. The elemental compositions are an average value of the nanoparticles in a certain area. The errors are calculated from 1-Sigma uncertainty of the corresponding elemental peak in the EDX spectra.

Sample code	Fe/Co ratio	Element (at.%)		
		O	Fe	Co
INN-1	0.37±0.02	62.2±2.4	10.2±0.4	27.6±1.0
INN-2	0.91±0.05	61.0±2.7	18.6±0.8	20.5±0.8
INN-3	3.17±0.15	66.4±2.4	25.6±0.8	8.1±0.3
AIC-1	1.87±0.08	58.4±1.9	27.1±0.8	14.5±0.5
AIC-2	2.56±0.11	62.6±1.9	26.9±0.8	10.5±0.3
AIC-3	3.22±0.12	51.5±1.4	37.0±1.0	11.5±0.3

7.3.3 Elemental distribution by EELS mapping

Knowing the elemental distribution of Fe and Co is of great value, since the physical and chemical properties of the Fe-Co nanoparticles can be greatly affected. STEM-EELS was employed here to study the elemental distribution in the particles. Some mapping results of the three INN samples are shown in Figure 7.4. As we can see that the elemental distribution in the Fe-Co nanoparticles synthesised with iron nitrate (INN batch) is not uniform and that the Co- and Fe- rich regions can be clearly seen in all the three samples. As the Fe/Co ratio increases, the signal of Co (green) is gradually decreasing.

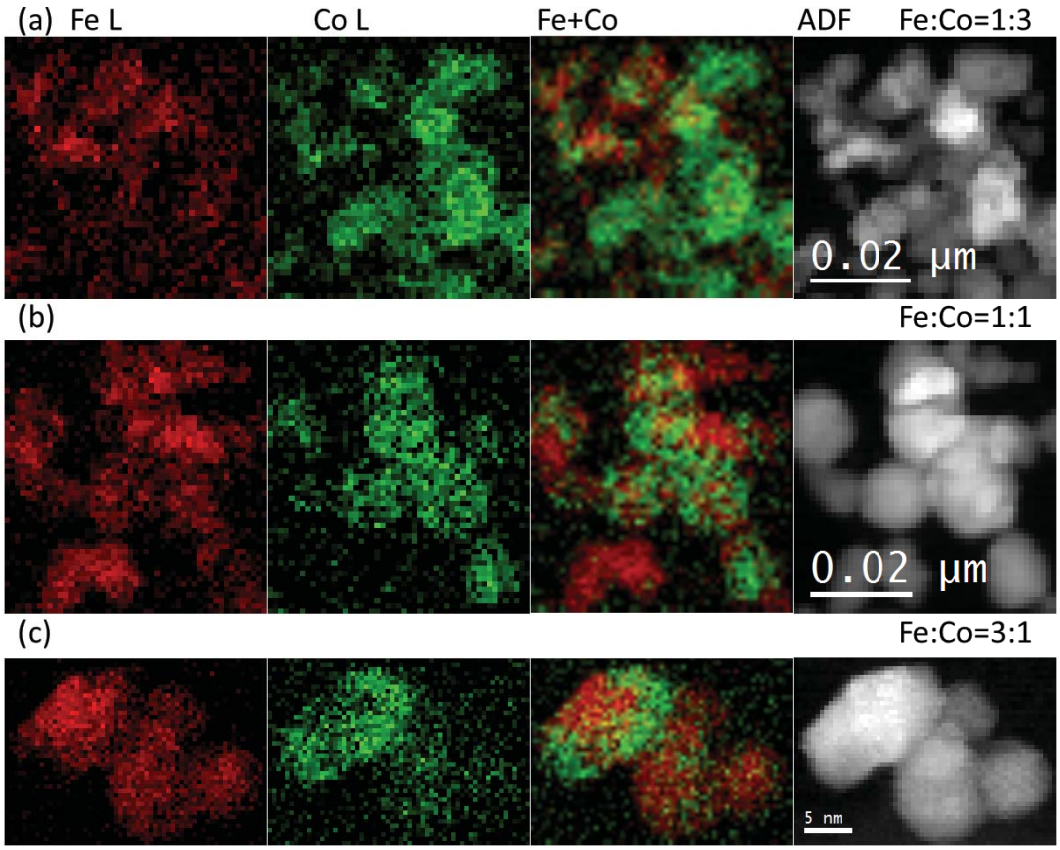

Figure 7.4 EELS mapping examples of the Fe-Co oxide nanoparticles from sample (a) INN-1, (b) INN-2 and (c) INN-3. From the left to the right are the Fe and Co L edge maps, mix of the Fe and Co maps and the corresponding ADF images. The scanning step is about 1 nm/pixel.

The inhomogeneity of elemental distribution in single Fe-Co oxide nanoparticles (INN batch) presents a different distribution morphology as is shown in Figure 7.5. Elemental distribution with uncomplete core-shell (Figure 7.5a), onion-layered (Figure 7.5b) and "dumbbell" structures are observed. We find that the Fe-rich areas are likely to be in the core (Figure 7.5a and 7.5b) and the Co-rich regions lie at the surface (Figure 7.5a) or on the top of the Fe-rich regions (Figure 7.5c). The non-uniform elemental distribution in the NPs of INN samples may be caused by the nitrate anions in the iron salt and the solubility of the Fe and Co ions in the solutions.

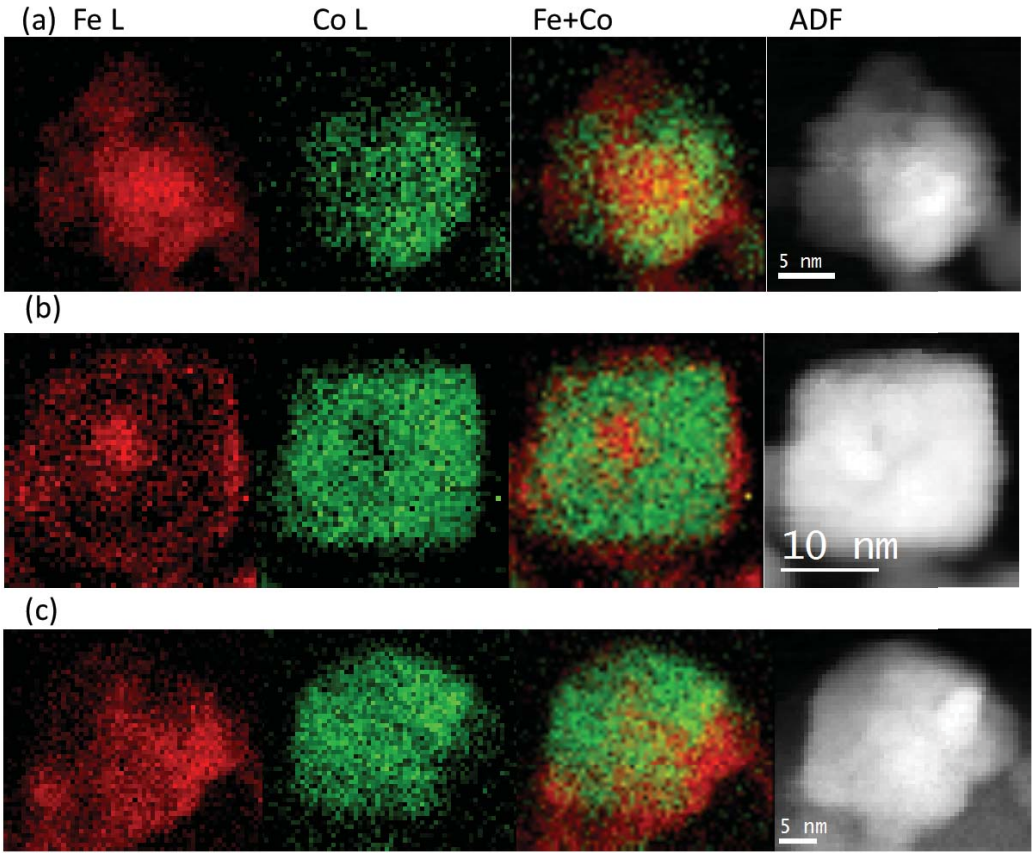

Figure 7.5 STEM-EELS mapping of single Fe-Co nanoparticles from the INN samples with different distribution structures (a) uncomplete core-shell, (b) onion-layer structure and (c) "dumbbell" structure.

It has been reported [16, 34] that cobalt oxide particles cannot be precipitated from cobalt nitrate solutions in the absence of a base because of its high solubility in the water or that only a few large particles can be produced when cobalt nitrate contacts with supercritical water [35]. On the other hand, the solubility of Fe ions in iron nitrate solution is several orders of magnitude lower than that of Co in its nitrate solution [16]. Therefore, it is easier for Fe oxide or hydroxide to nucleate than that of Co oxide or hydroxide during the hydrothermal processing. Co oxide can then proceed to precipitate on the surface of Fe oxide nucleus and form different distribution morphologies. This also explains why the iron-rich regions tend to be in the core and

cobalt-rich regions on the surface or top of the Fe-rich particles. These observations suggest that a Fe nucleus forms first and then Co grows up on the Fe nucleus. Because of the ion diffusion in the solution, Fe- and Co- rich layers could appear alternatively and form onion-layered structure.

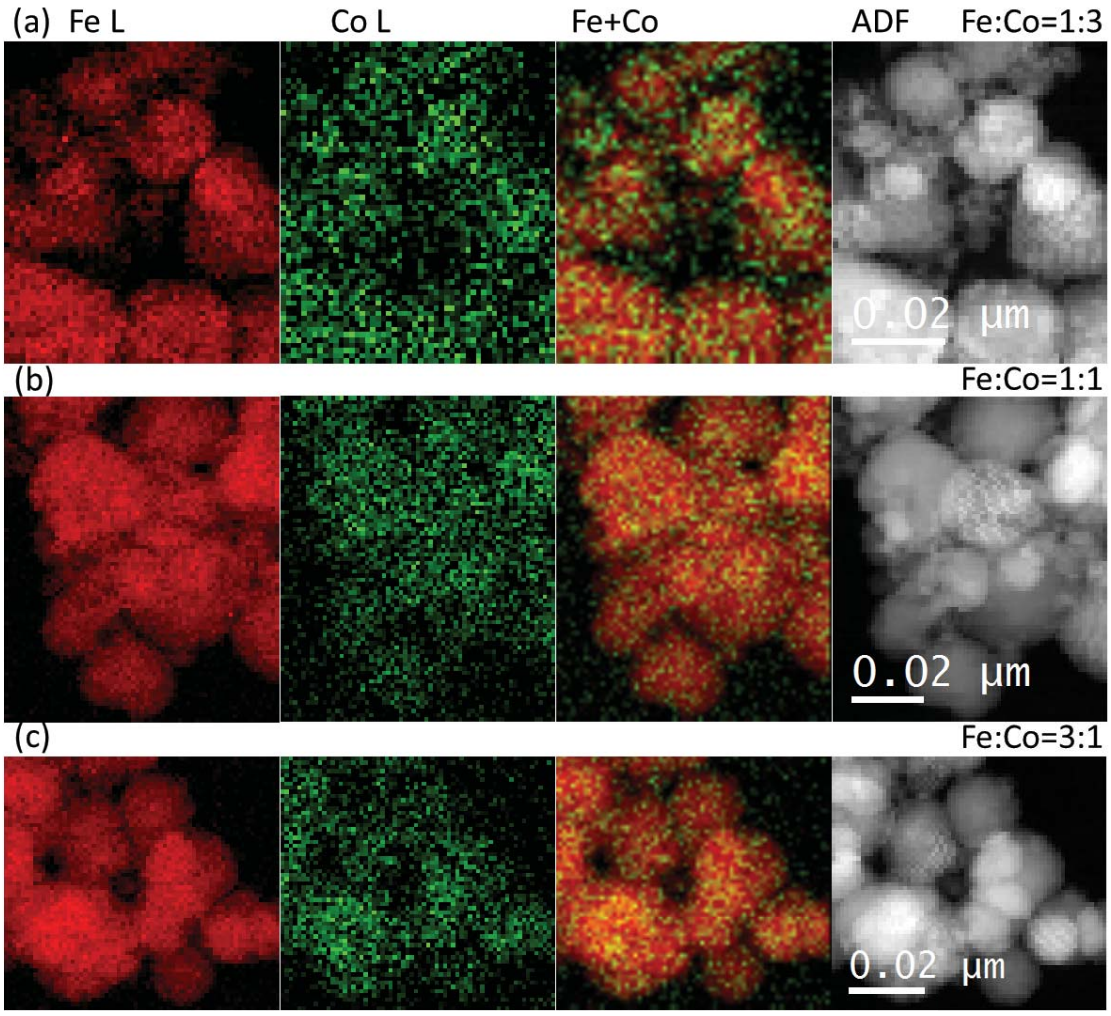

Figure 7.6 STEM-EELS mapping examples of the Fe-Co oxide nanoparticles from sample (a) AIC-1, (b) AIC-2 and (c) AIC-3. From the left to the right are the Fe and Co L edge maps, mix of the Fe and Co maps and the corresponding ADF images.

For the AIC sample series, we found that the Fe and Co spatial distributions in these NPs were very uniform (Figure 7.6). In this case, cobalt ferrite is likely to be formed as the XRD results indicate. There are two possible reasons for the uniform elemental

distribution. First, carbon monoxide produced by the thermal decomposition of citrate [32,36] is expected to be miscible with supercritical water and provide a homogeneous reaction atmosphere promoting the oxidizing and reducing capability [33]. Second, citrate anions can form complexes with both Fe and Co cations. Citrate complexes of Fe and Co have been reported elsewhere in the literature [37, 38], which indicate that the citrate ligand binds to Fe or Co atoms through the O atom of the hydroxyl group and the carboxyl group. The formation of these complexions (among iron ions, cobalt ions and citrate) in the solution will promote the simultaneous precipitation of Fe and Co ions during the thermal decomposition process [36,39], resulting in a uniform elemental distribution.

Controlling the elemental arrangement in magnetic alloy NPs is of great importance, not only because it can change the magnetic properties of the particles [22] but also because it might influence their toxicities and biocompatibilities. Iron oxide NPs are widely used in in vivo applications because of their low toxicity and biocompatibility [40, 41]. For the Fe-Co oxide NPs, the non-uniform distribution of Co oxide (especially when the Co rich region is on the surface of the NPs) may increase the toxicity of the particles, since it has been reported that Co NPs can induce cytotoxicity and genotoxicity in cells [42-44]. A toxicity investigation of the Fe-Co oxide NPs reported in this work is in progress, and may shed light on the effect of the spatial distributions of the metals in the NPs on the toxicity.

7.4 Summary and conclusions

In summary, in this chapter I have described a STEM analysis of two series of Fe-Co oxide nanoparticles with iron nitrate or citrate as precursors using a continuous

hydrothermal synthesizing method. The STEM-HAADF, -EDX, and -EELS results, like the XRD, show that the crystallisation, morphology, elemental composition and atomic arrangement of the nanoparticles are very different when the anion species in the solution changes from nitrate to citrate. The Fe-Co nanoparticles prepared with ammonium iron citrate are well crystallised and have a uniform elemental distribution. However, the nanoparticles synthesised with iron nitrate tend to be more amorphous and the elemental distribution is also inhomogeneous. It seems that the presence of citrate anions in the precursor solutions can inhibit the precipitation of Co ions, but promote the crystallisation and uniform atomic arrangement of the Fe-Co nanoparticles. Overall, this investigation into the effect of the salt anions in continuous hydrothermal synthesis sheds light upon the mechanism of the hydrothermal reactions, possibly allowing for a better control of the nanoparticles produced in future.

References

[1] Rosi, N. L.; Mirkin, C. A. Nanostructures in Biodiagnostics. *Chem. Rev.*, **2005**, *105*, 1547–1562.

[2] Jain, P. K.; Huang, X.; El-Sayed, I. H.; El-Sayed, M. A. Noble Metals on the Nanoscale: Optical and Photothermal Properties and Some Applications in Imaging, Sensing, Biology, and Medicine. *Acc. Chem. Res.*, **2008**, *41*, 1578–1586.

[3] Nikumbh, A. K.; Pawar, R. A.; Nighot, D. V.; Gugale, G. S.; Sangale, M. D.; Khanvilkar, M. B.; Nagawade, A. V. Structural, electrical, magnetic and dielectric properties of rare-earth substituted cobalt ferrites nanoparticles synthesized by the co-precipitation method. *J. Magn. Magn. Mater.* **2014**, *355*, 201-209.

[4] Clark, N. A.; Soft-matter physics: Ferromagnetic ferrofluids. *Nature*, **2013**, *504*, 229–230.

[5] Verberck, B. Quantum ferrofluids: Made to order. *Nat. Phys.* **2016**, *12*, 205.

[6] Tihay, F.; Pourroy, G.; Richard-Plouet, M.; Roger, A. C.; Kiennemann, A. Effect of Fischer–Tropsch Synthesis on the Microstructure of Fe–Co-Based Metal/spinel Composite Materials. *Appl. Catal. A Gen.*, **2001**, *206*, 29–42.

[7] Mathew, D. S.; Juang, R. S. An Overview of the Structure and Magnetism of Spinel Ferrite Nanoparticles and Their Synthesis in Microemulsions. *Chem. Eng. J.*, **2007**, *129*, 51–65.

[8] Toksha, B. G.; Shirsath, S. E.; Patange, S. M.; Jadhav, K. M. Structural Investigations and Magnetic Properties of Cobalt Ferrite Nanoparticles Prepared by Sol–gel Auto Combustion Method. *Solid State Commun.*, **2008**, *147*, 479–483.

[9] Joshi, H. M.; Lin, Y. P.; Aslam, M.; Prasad, P. V.; Schultz-Sikma, E. A.; Edelman, R.; Meade, T.; Dravid, V. P. Effects of Shape and Size of Cobalt Ferrite Nanostructures on Their MRI Contrast and Thermal Activation. *J. Phys. Chem. C*, **2009**, *113*, 17761–17767.

[10] Sathya, A.; Guardia, P.; Brescia, R.; Silvestri, N.; Pugliese, G.; Nitti, S.; Manna, L.; Pellegrino, T. $Co_xFe_{3-x}O_4$ Nanocubes for Theranostic Applications: Effect of Cobalt Content and Particle Size. *Chem. Mater.*, **2016**, *28*, 1769–1780.

[11] Sawatzky, G. A. Cation Distributions in Octahedral and Tetrahedral Sites of the Ferrimagnetic Spinel $CoFe_2O_4$. *J. Appl. Phys.*, **1968**, *39*, 1204.

[12] Kawano, S.; Yamamoto, N.; Achiwa, N. Determination of Metal Ion Distribution in Cubic Spinel $FeCO_2O_4$. *Jpn. J. Appl. Phys.*, **1974**, *13*, 1891–1892.

[13] Murray, P. J.; Linnett, J. W. Cation Distribution in the Spinels $Co_xFe_{3-x}O_4$. *J. Phys. Chem. Solids* **1976**, *37*, 1041–1042.

[14] Smith, P. A.; Spencer, C. D.; Stillwell, R. P. Co^{57} and Fe^{57} Mössbauer Studies of the Spinels $FeCo_2O_4$ and $Fe_{0.5}Co_{2.5}O_4$. *J. Phys. Chem. Solids* **1978**, *39*, 107–111.

[15] Liu, M.; Lu, M.; Wang, L.; Xu, S.; Zhao, J.; Li, H. Mössbauer Study on the Magnetic Properties and Cation Distribution of $CoFe_2O_4$ Nanoparticles Synthesized by Hydrothermal Method. *J. Mater. Sci.* **2016**, *51*, 5487–5492.

[16] Cote, L. J.; Teja, A. S.; Wilkinson, A. P.; Zhang, Z. J. Continuous Hydrothermal Synthesis of $CoFe_2O_4$ Nanoparticles. *J. Mater. Res.* **2003**, *210*, 307–317.

[17] Daou, T. J.; Pourroy, G.; Begin-Colin, S.; Greneche, J. M.; Ulhaq-Bouillet, C.; Legare, P.; Bernhardt, P.; Leuvrey, C.; Rogez, G. Hydrothermal Synthesis of Monodisperse Magnetite Nanoparticles, *Chem. Mater.* **2006**, *18*, 4399-4404.

[18] Zhao, D.; Wu, X.; Guan, H.; Han, E. Study on Supercritical Hydrothermal Synthesis of $CoFe_2O_4$ Nanoparticles. *J. Supercrit. Fluids* **2007**, *42*, 226–233.

[19] Zhao, L.; Zhang, H.; Xing, Y.; Song, S.; Yu, S.; Shi, W.; Guo, X.; Yang, J.; Lei, Y.; Cao, F. Studies on the Magnetism of Cobalt Ferrite Nanocrystals Synthesized by Hydrothermal Method, *J. Solid State Chem.* **2008**, *181*, 245–252.

[20] Sawatzky, G. A. Cation Distributions in Octahedral and Tetrahedral Sites of the Ferrimagnetic Spinel $CoFe_2O_4$. *J. Appl. Phys.* **1968**, *39*, 1204.

[21] Sawatzky, G. A.; Van Der Woude, F.; Morrish, A. H. Mössbauer Study of Several Ferrimagnetic Spinels. *Phys. Rev.* **1969**, *187*, 747–757.

[22] Antoniak, C.; Spasova, M.; Trunova, A.; Fauth, K.; Wilhelm, F.; Rogalev, A.; Minár, J.; Ebert, H.; Farle, M.; Wende, H. Inhomogeneous Alloying in FePt Nanoparticles as a Reason for Reduced Magnetic Moments. *J. Phys. Condens. Matter* **2009**, *21*, 336002.

[23] López-Ortega, A.; Estrader, M.; Salazar-Alvarez, G.; Estradé, S.; Golosovsky, I. V.; Dumas, R. K.; Keavney, D. J.; Vasilakaki, M.; Trohidou, K. N.; etc. Strongly Exchange Coupled Inverse Ferrimagnetic Soft/hard, $Mn_xFe_{3-x}O_4/Fe_xMn_{3-x}O_4$, Core/shell Heterostructured Nanoparticles. *Nanoscale* **2012**, *4*, 5138–5147.

[24] Hobbs, H.; Briddon, S.; Lester, E. The Synthesis and Fluorescent Properties of Nanoparticulate ZrO_2 Doped with Eu Using Continuous Hydrothermal Synthesis. *Green Chem.* **2009**, *11*, 484-491.

[25] Lester, E.; Aksomaityte, G.; Li, J.; Gomez, S.; Gonzalez-Gonzalez, J.; Poliakoff, M. Controlled Continuous Hydrothermal Synthesis of Cobalt Oxide (Co_3O_4) Nanoparticles. *Prog. Cryst. Growth Charact. Mater.* **2012**, *58*, 3–13.

[26] Moro, F.; Tang, S. V. Y.; Tuna, F.; Lester, E. Magnetic Properties of Cobalt Oxide Nanoparticles Synthesised by a Continuous Hydrothermal Method. *J. Magn. Magn. Mater.* **2013**, *348*, 1–7.

[27] Lester, E.; Tang, S. V. Y.; Khlobystov, A.; Rose, V. L.; Buttery, L.; Roberts, C. J. Producing Nanotubes of Biocompatible Hydroxyapatite by Continuous Hydrothermal Synthesis. *CrystEngComm*. **2013**, *15*, 3256.

[28] Wang, Q.; Tang, S. V. Y.; Lester, E.; O'Hare, D. Synthesis of Ultrafine Layered Double Hydroxide (LDHs) Nanoplates Using a Continuous-Flow Hydrothermal Reactor. *Nanoscale* **2013**, *5*, 114–117.

[29] Ferreira, T. A. S.; Waerenborgh, J. C.; Mendonça, M. M.; Nunes, M. R.; Costa, F. M. Structural and Morphological Characterization of $FeCo_2O_4$ and $CoFe_2O_4$ Spinels Prepared by a Coprecipitation Method. *Solid State Sci.* **2003**, *5*, 383–392.

[30] Kim, Y. I.; Kim, D.; Lee, C. S. Synthesis and Characterization of $CoFe_2O_4$ Magnetic Nanoparticles Prepared by Temperature-Controlled Coprecipitation Method. *Phys. B Condens. Matter* **2003**, *337*, 42–51.

[31] Ma, Z.; Ren, L.; Xing, S.; Wu, Y.; Gao, Y. Sodium Dodecyl Sulfate Modified $FeCo_2O_4$ with Enhanced Fenton-Like Activity at Neutral pH. *J. Phys. Chem. C* **2015**, *119*, 23068–23074.

[32] Adschiri, T.; Kanazawa, K.; Arai, K.; Rapid and Continuous Hydrothermal Crystallization of Metal Oxide Particles in Supercritical Water. *J. Am. Ceram. Soc.* **1992**, *75*, 1019–1022.

[33] Adschiri, T.; Hakuta, Y.; Arai, K.; Hydrothermal Synthesis of Metal Oxide Fine Particles at Supercritical Conditions. *Ind. Eng. Chem. Res.* **2000**, *39*, 4901–4907.

[34] Cote, L. J.; Teja, A. S.; Wilkinson, A. P.; Zhang, Z. J. Continuous hydrothermal synthesis and crystallization of magnetic oxide nanoparticles. *J. Mater. Res.* **2002**, *19*, 2410–2416.

[35] Hao, Y.; Teja, A. Continuous Hydrothermal Crystallization of Fe_2O_3 and Co_3O_4 Nanoparticles. *J. Mater. Res.* **2003**, *18*, 415-422.

[36] Gajbhiye, N. S.; Prasad, S. Thermal Decomposition of Hexahydrated Nickel Iron Citrate. *Thermochim. Acta* **1996**, *285*, 325–336.

[37] Birsa Čelič, T.; Jagličič, Z.; Lazar, K.; Zabukovec Logar, N. Structure and Magnetic Properties of a New iron(II) Citrate Coordination Polymer. *Acta Cryst* **2013**, *69*, 490–495.

[38] Zhou, Z.; Deng, Y.; Wan, H. Structural Diversities of Cobalt(II) Coordination Polymers with Citric Acid. *Cryst. Growth Des.* **2005**, *5*, 1109–1117.

[39] Prasad, S.; Vijayalakshmi, A.; Gajbhiye, N. S. Synthesis of Ultrafine Cobalt Ferrite by Thermal Decomposition of Citrate Precursor. *J. Therm. Anal. Calorim.* **1998**, *52*, 595–607.

[40] Weissleder, R.; Stark, D. D.; Engelstad, B. L.; Bacon, B. R.; Compton, C. C.; White, D. L.; Jacobs, P.; Lewis, J. Superparamagnetic Pharmacokinetics Iron Oxide : Pharmacokinetics and Toxicity. *Am. J. Roentgenol.* **1989**, *152*, 167–173.

[41] Wu, Y.; Wang, Y.; Luo, G.; Dai, Y. In Situ Preparation of Magnetic Fe_3O_4-Chitosan Nanoparticles for Lipase Immobilization by Cross-Linking and Oxidation in Aqueous Solution. *Bioresour. Technol.* **2009**, *100*, 3459–3464.

[42] Papis, E.; Rossi, F.; Raspanti, M.; Dalle-Donne, I.; Colombo, G.; Milzani, A.; Bernardini, G.; Gornati, R. Engineered Cobalt Oxide Nanoparticles Readily Enter Cells. *Toxicol. Lett.* **2009**, *189*, 253–259.

[43] Ponti, J.; Sabbioni, E.; Munaro, B.; Broggi, F.; Marmorato, P.; Franchini, F.; Colognato, R.; Rossi, F. Genotoxicity and Morphological Transformation Induced by Cobalt

Nanoparticles and Cobalt Chloride: An in Vitro Study in Balb/3T3 Mouse Fibroblasts. *Mutagenesis* **2009**, *24*, 439–445.

[44] Chattopadhyay, S.; Dash, S. K.; Tripathy, S.; Das, B.; Mandal, D.; Pramanik, P.; Roy, S. Toxicity of Cobalt Oxide Nanoparticles to Normal Cells; An in Vitro and in Vivo Study. *Chem. Biol. Interact.* **2015**, *226*, 58–71.

Chapter 8 Conclusions

In this thesis, a variety of nanomaterials were investigated by ac-STEM, including Ag clusters produced in the reflection mode MACS, thiol-protected Au clusters, metal oxide nanoparticles and bimetallic nanoparticles. We explored the capability of ac-STEM in the characterisation of cluster size, atomic structure, oxidation states, and elemental analysis.

Ag clusters produced in the newly designed MACS were investigated using STEM HAADF images. I found that the Ag clusters collected with different incident and collection angles had similar size distributions. The cluster size decreases a lot when the metal concentration in the matrix increases to 3.56%. The cluster flux decreases when the incident angle increases. The optimal collection angle for a high cluster flux is when the angle between the incident beam and cluster flux is at 110°. The sputtering yield of the MACS is about 1%, which shows a great potential to scale up the production of nanoclusters.

A statistical investigation is conducted to characterise the size and atomic structure of nominally $Au_{144}(SR)_{60}$ clusters synthesised by two different groups. By weighing the clusters with single atoms and size-selected Au_{923} clusters, we found that the clusters were not monodispersed in size. Structure identification was performed by comparing the images with model structure simulations. Only about 3% to 7% of clusters were found to fit the predicted $Au_{144}(SR)_{60}$ model, nevertheless, a ring-dot feature, characteristic of a local icosahedral order, was frequently (~20% of the clusters) observed.

STEM-EELS was used to characterise the oxidation states of CeO_x, CuO_x, CoO_x and FeO_x nanoparticles. The white line ratio and near edge structure analysis showed that the average oxidation state of CeO_x nanoparticles was ~3.4+ and that the valence state of over half of the CuO_x nanoparticles was 1+. The investigation of CoO_x and FeO_x nanoparticles shows that the oxidation state varies when the particles size and synthesis precursor change. These studies will provide oxidation state information of these particles for further toxicity test to have a good understanding of the relationship between the toxicity and the oxidation state of the material.

Elemental distributions in Pt-Cr bimetallic nanoparticles were studied by analysing their HAADF intensities. The average HAADF intensity of smaller nanoparticles (1.45±0.25 nm) was brighter than the larger ones (2.35±0.3 nm), indicating that the smaller nanoparticles were pure Pt, which was also supported by the XPS data. The larger nanoparticles were assigned as Pt-Cr bimetallic nanoparticles. Comparison between the experimental and simulated HAADF intensity profiles indicated that most of the Pt-Cr nanoparticles had a mixed core and shell. Field-assisted diffusion is tentatively attributed to be the main reason for the formation of Pt and Cr mixed nanoparticles.

STEM-EDX and EELS were utilised to investigate the elemental compositions and distributions of a series of hydrothermally prepared Fe-Co oxide nanoparticles. I found that the crystallinity, Fe/Co composition and element spatial distribution in the synthesised NPs had a strong dependence on the choice of iron salts. The Fe-Co nanoparticles synthesised with ammonium iron citrate were well crystallised and had a homogeneous elemental distribution. While the nanoparticles prepared with iron

nitrate were more amorphous and the metal atoms distribution were not uniform. The composition analysis showed that the presence of ammonium citrate seems to inhibit the precipitation of Co ions in solution, and promotes the crystallisation of the NPs.

Appendix Simulation atlases

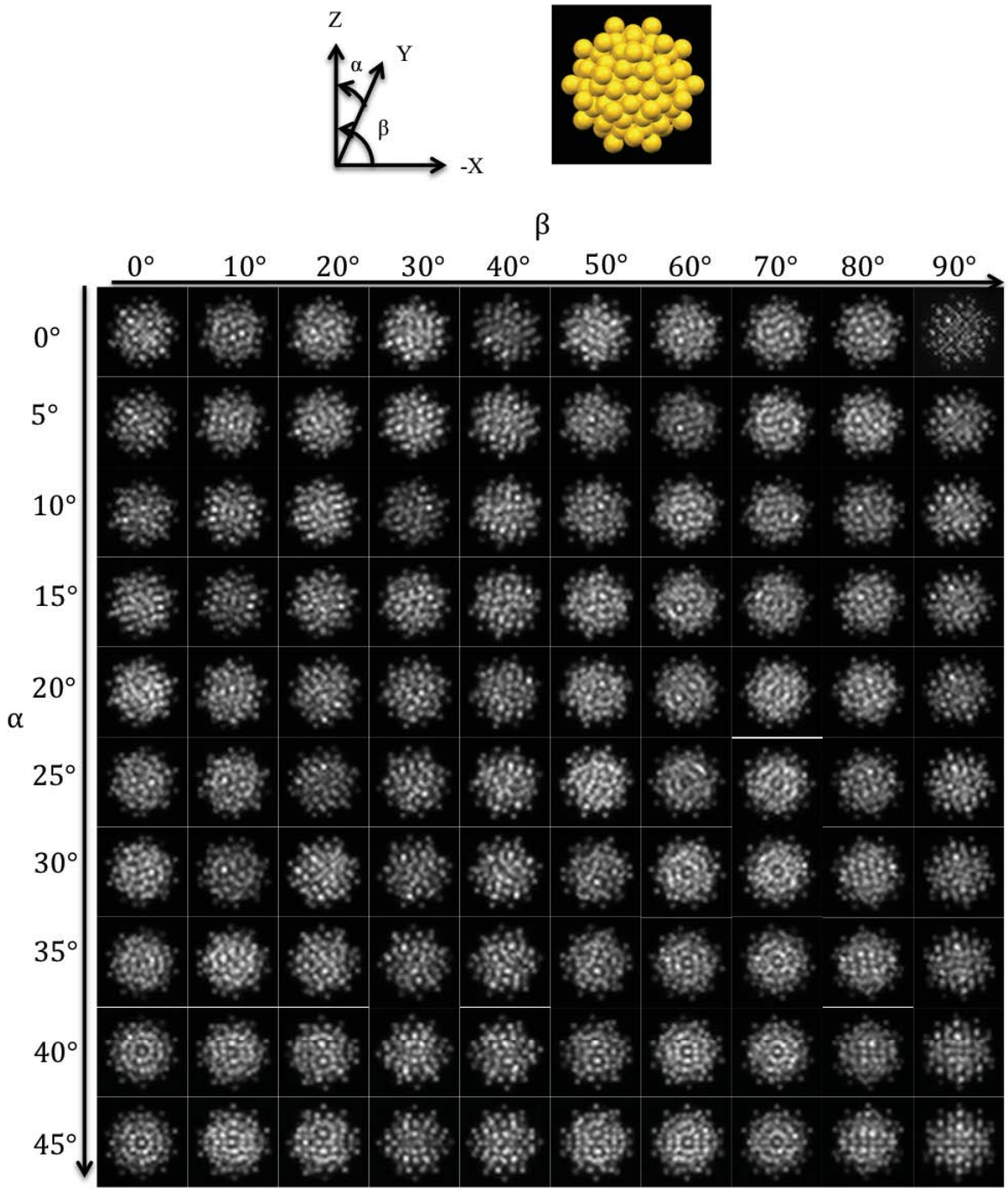

Figure A1. STEM simulation images for the predicted $Au_{144}(SR)_{60}$ cluster (α=0~45°, β=0~90°).

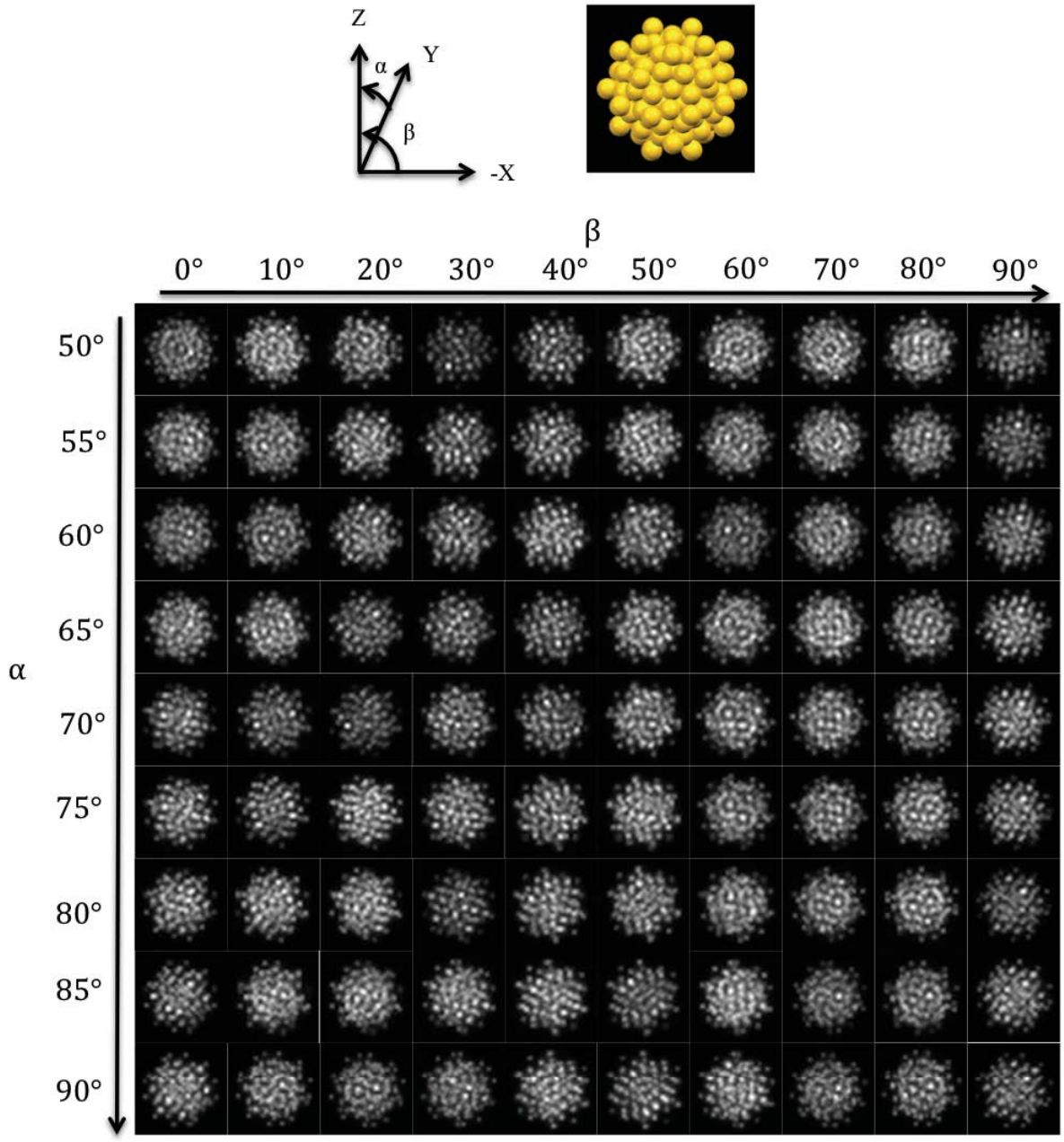

Figure A2. STEM simulation images for the predicted $Au_{144}(SR)_{60}$ cluster (α=50~90°, β=0~90°).

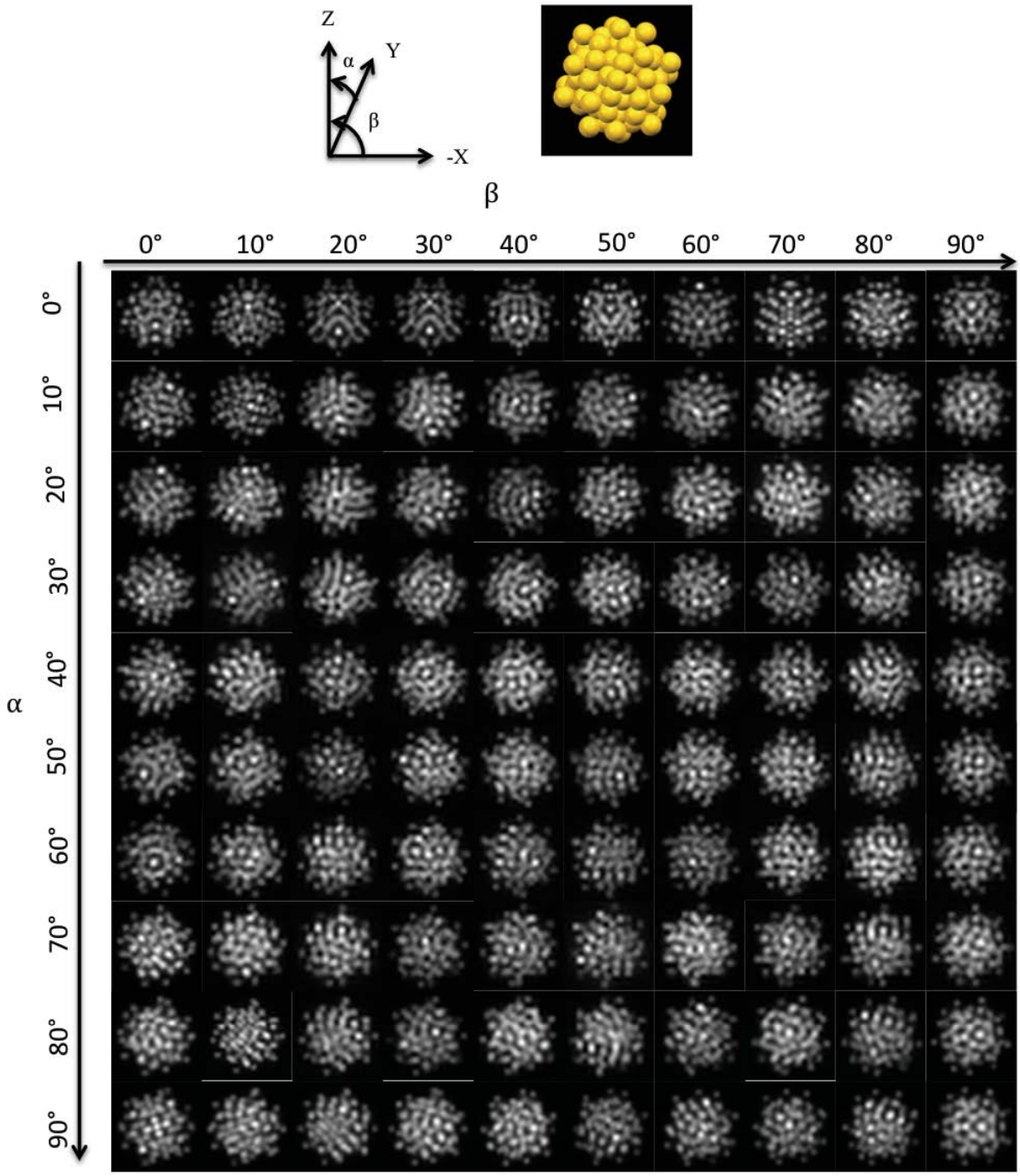

Figure A3. STEM simulation images for the $Au_{102}(SR)_{44}$ cluster (α=0~90°, β=0~90°).

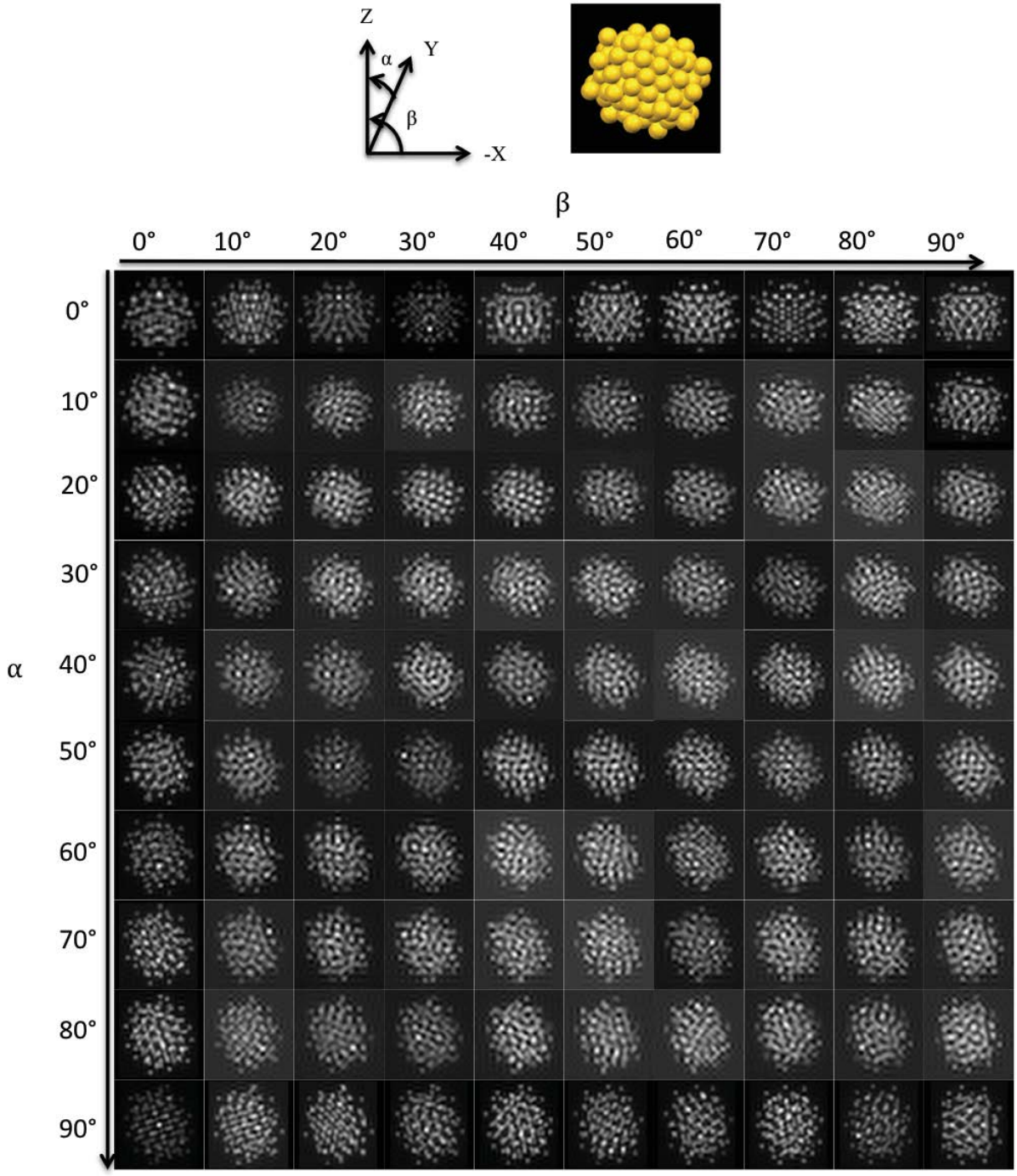

Figure A4. STEM simulation images for the $Au_{130}(SR)_{50}$ cluster (α=0~90°, β=0~90°).

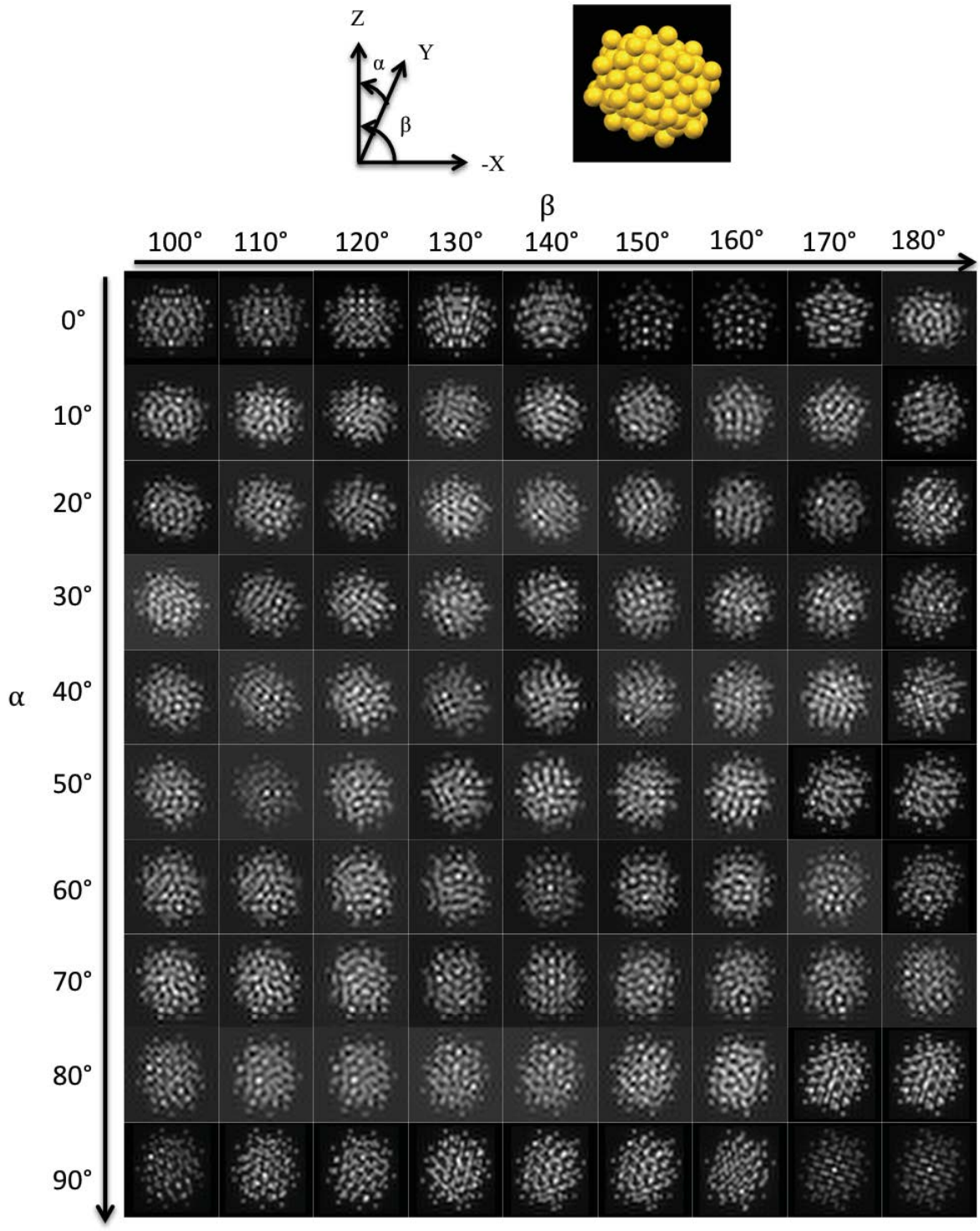

Figure A5. STEM simulation images for the $Au_{130}(SR)_{50}$ cluster (α=0~90°, β=100~180°).

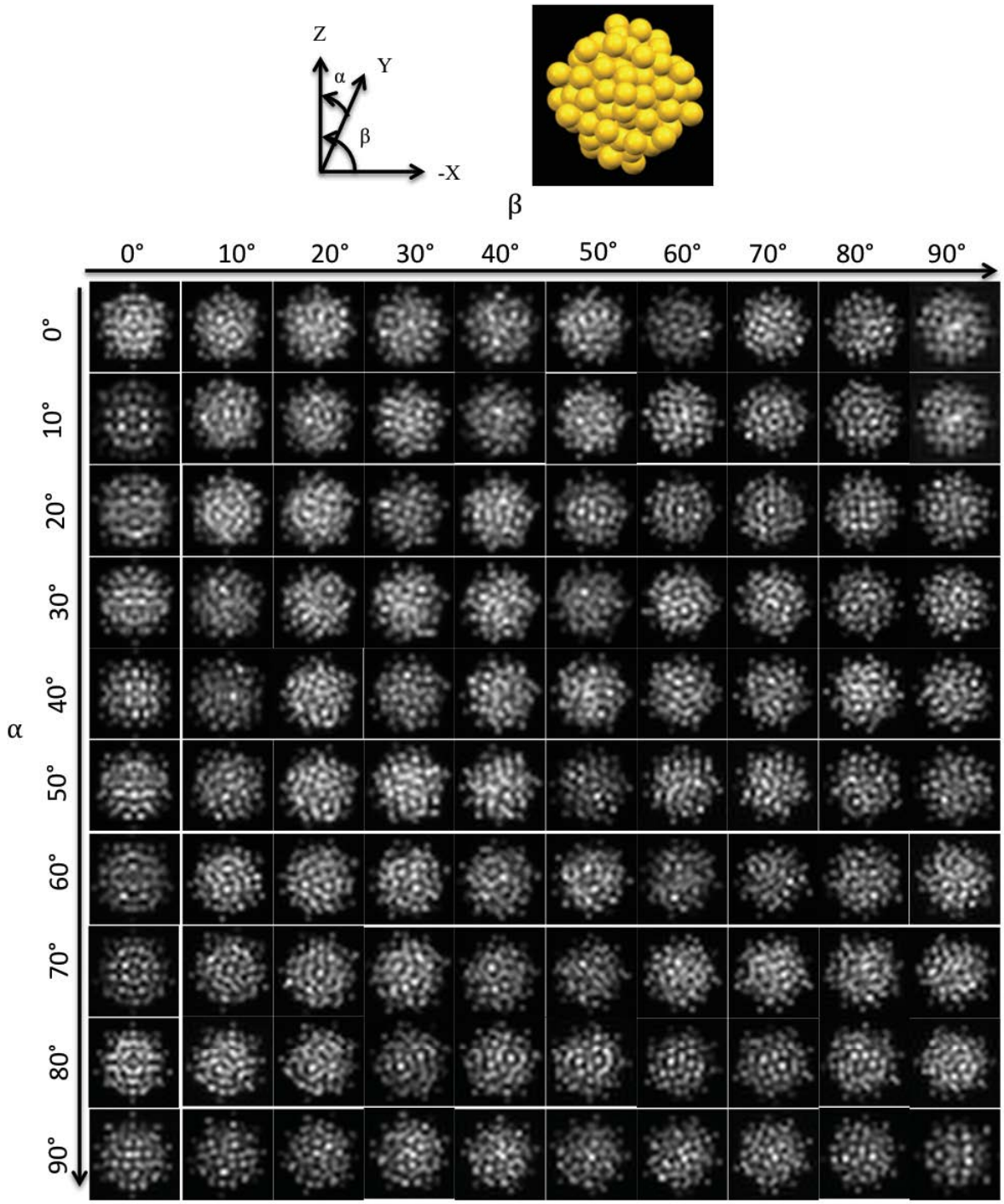

Figure A6. STEM simulation images for the $Au_{133}(SR)_{52}$ cluster (α=0~90°, β=90~90°).

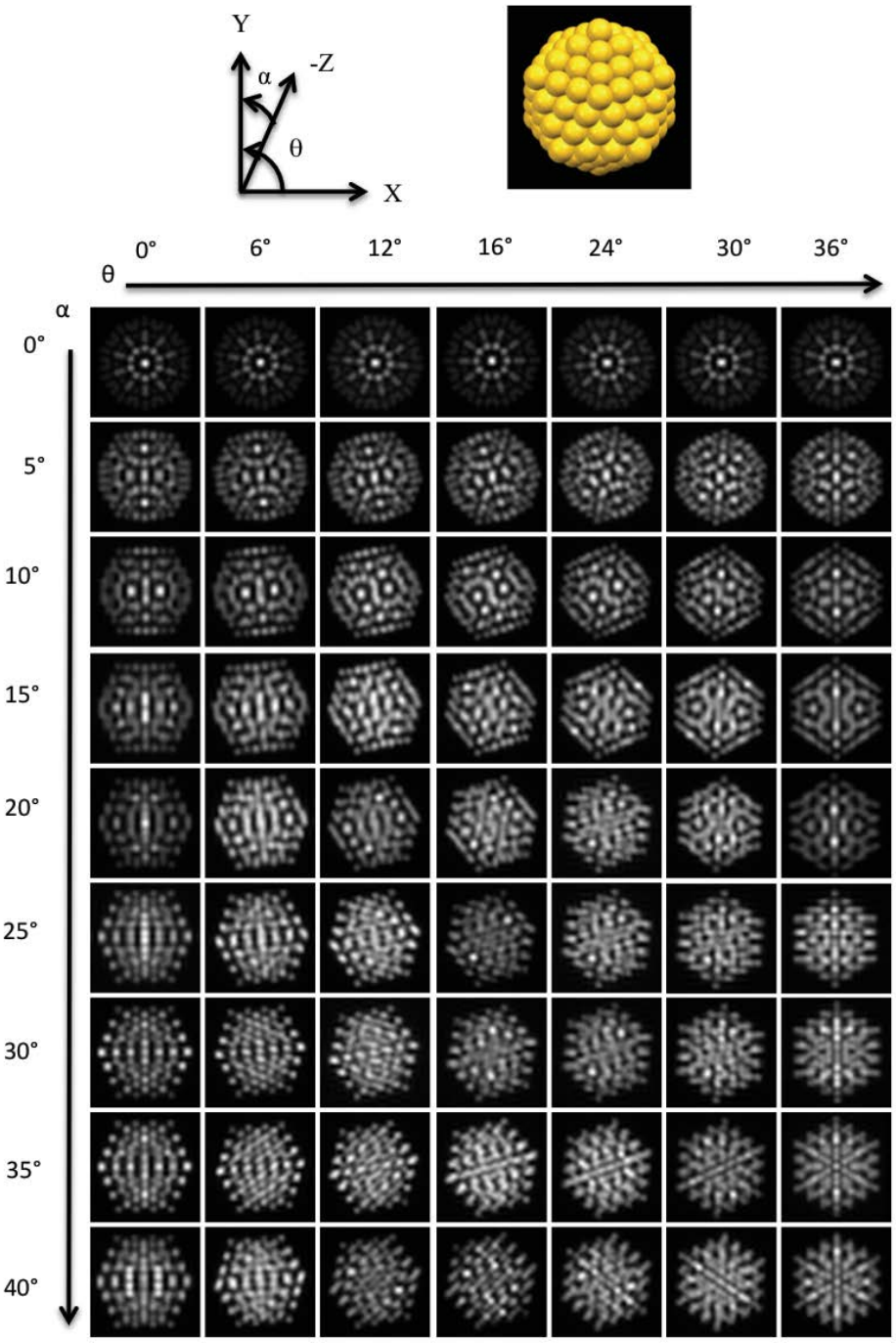

Figure A7. STEM simulation images for an Icosahedral Au_{147} cluster (α=0~40°, θ=0~36°).

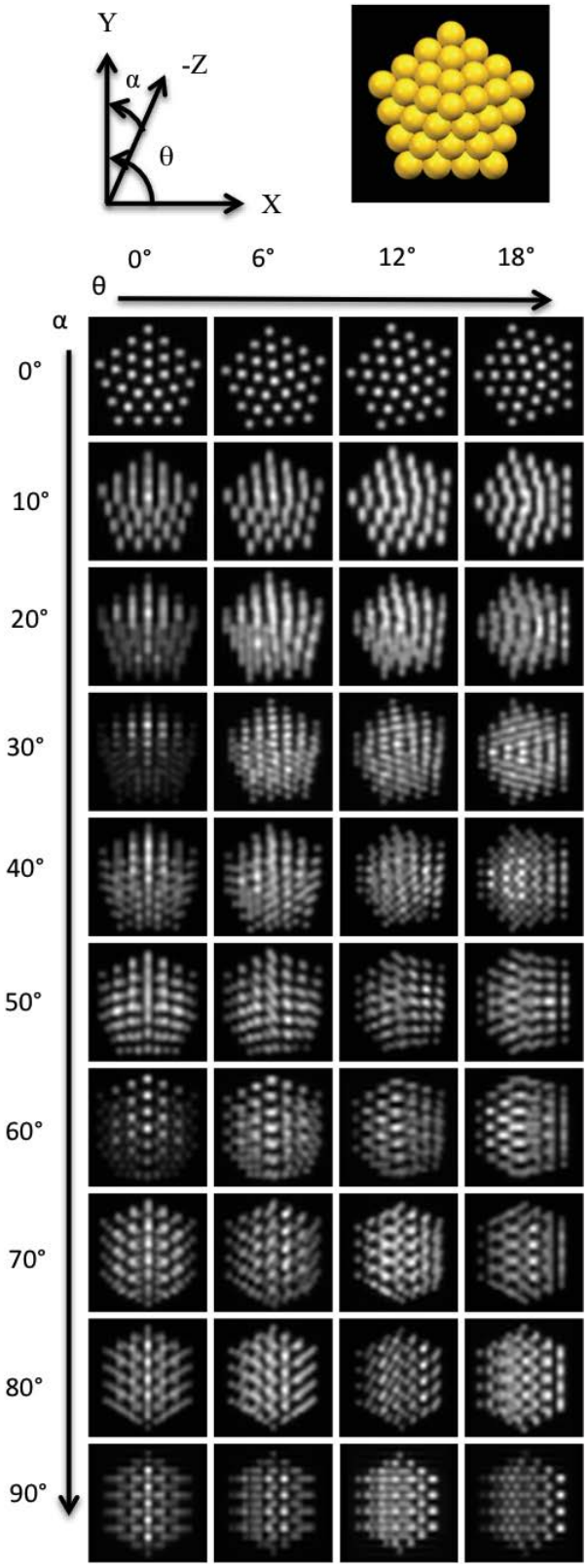

Figure A8. STEM simulation images for an Decahedral Au_{147} cluster (α=0~90°, θ=0~18°).

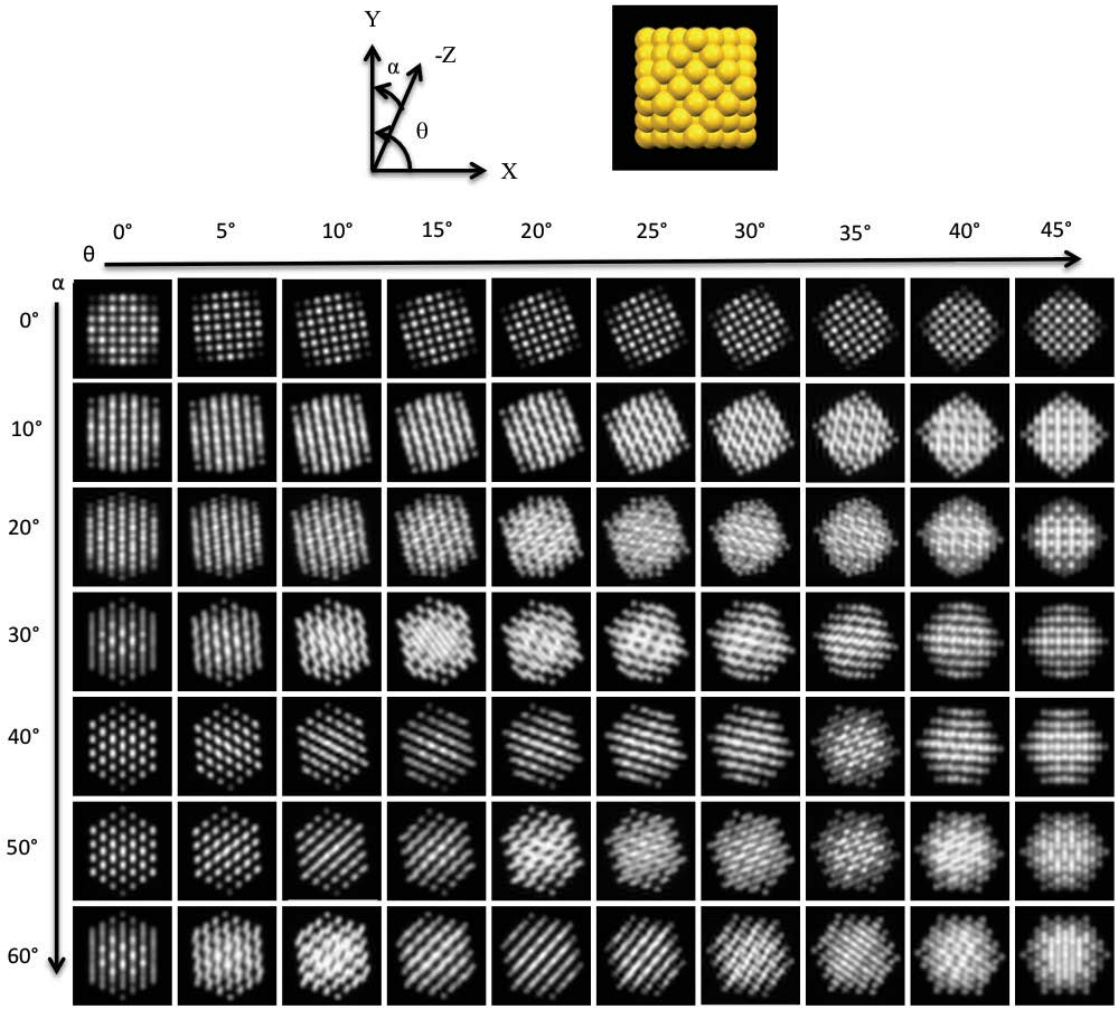

Figure A9. STEM simulation images for a Cuboctahedral Au_{147} cluster (α=0~60°, θ=0~45°).

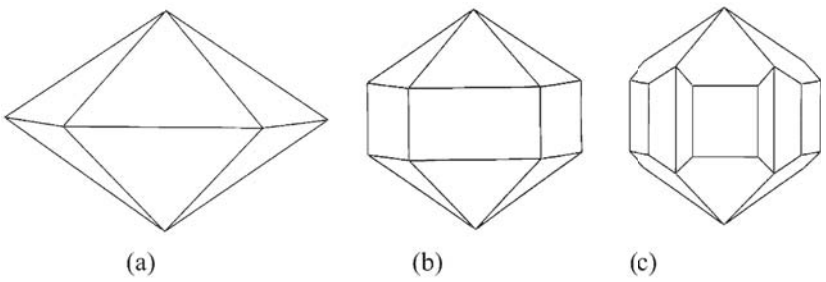

Figure A10 Structural schemes of classic decahedron (a), Ino's decahedron (b), and Marks' decahedron (c).